NASA Contractor Report 2965

Closed Loop Models for Analyzing Engineering Requirements for Simulators

Sheldon Baron, Ramal Muralidharan,
and David Kleinman

CONTRACT NAS1-14449
FEBRUARY 1980

NASA

NASA Contractor Report 2965

Closed Loop Models for Analyzing Engineering Requirements for Simulators

Sheldon Baron, Ramal Muralidharan,
and David Kleinman
Bolt Beranek and Newman, Inc.
Cambridge, Massachusetts

Prepared for
Langley Research Center
under Contract NAS1-14449

National Aeronautics
and Space Administration

**Scientific and Technical
Information Office**

1980

TABLE OF CONTENTS

LIST OF FIGURES

LIST OF FIGURES

LIST OF FIGURES

LIST OF TABLES

Symbols

A, B, C, D, E	general system matrices
$D^*(s)$	transfer function of discrete system
$\tilde{D}(s)$	transfer function of continuous approximation to discrete system
E[ ]	expected value
e	base for natural logarithms
$F_1(s)$	transfer function of dealiasing filter
$F_2(s)$	transfer function of data hold/visual servo combination
f_i	fraction of attention devoted to i^{th} variable
G(s)	system function of simulation
g	acceleration of gravity, m/sec^2
H(s)	transfer function of data hold
h	altitude, m
L^*	optimal feedback gains
n	normal acceleration, g's
p	roll rate, rad/sec.
q	pitch rate, rad/sec.
R	target range, m.
r	yaw rate, rad/sec.
s	Laplace transform variable
T	sample period, sec.
T_N	"neuromotor-lag", matrix, sec.
u(t)	control-vector
V(s)	transfer function of visual servo
V_{u_i}	motor-noise covariance
V_{y_i}	observation noise covariance

Symbols

α	angle of attack, rad.
β	sideslip angle, rad.
γ	flight path angle, rad.
Δ	fast sample period for mybrid model, sec.
δ_a	aileron deflection, rad.
δ_e	elevator deflection, rad.
$\delta(.)$	Dirac delta function
ε	tracking error, rad.
ζ	damping coefficient
θ	pitch angle, rad.
ρ_{u_i}	motor noise/signal ratio
ρ_{y_i}	observation noise/signal ratio
τ	delay of human operator
$\tau_{(.)}$	effective delay of corresponding simulation element
Φ_c	transfer function of continuous system
ϕ	roll angle, rad.
ψ	heading angle, rad.
Ω	sampling frequency, Hz
ω_c	cutoff frequency of analog-digital prefilter, rad/s
ω_n	natural frequency of visual servo, rad/s
$(\dot{})$	time derivative
$(\,)^*$	Laplace transform of impulse sampled signals
$\lvert\ \rvert$	absolute value

Symbols

$v_u(t)$	operator motor noise
$v_y(t)$	operator observation noise
$w(t)$	disturbance- or command-vector
$x(t)$	state-vector
$\hat{\underline{x}}(t)$	estimate of system state vector
$\underline{y}(t)$	output-vector
$\underline{y}_p(t)$	perceived output-vector
z	z-transform variable

SUMMARY

The development of engineering requirements for man-in-the loop simulation is a complex task involving numerous trade-offs between simulation fidelity and costs, accuracy and speed, etc. The design of the simulation model has become increasingly important and difficult as digital computers play a more central role in the simulations. For real-time digital simulation with a pilot in the loop the design problem involves specification of conversion equipment (A-D and D-A) as well as of the discrete model of the system dynamics.

The objective of the work reported here was to develop a closed loop analytic model, incorporating a model for the human pilot, (namely, the optimal control model) that would allow certain simulation design tradeoffs to be evaluated quantitatively and to apply this model to analyze a realistic flight control problem. The effort concentrated on the dynamic, closed loop aspects of the simulation. Problems associated with perceptual issues in cue generation are not considered. However, the limitations imposed by the dynamics of visual cue generation equipment are considered.

The human pilot in closed loop control will operate on essentially continuous outputs to generate continuous control inputs. Thus, even when digital computers are used in an aircraft simulation, it is meaningful to consider a continuous transfer function approximation to the open loop simulation dynamics. Such an approximation is developed in this study. It consists of a rational transfer function multiplied by a

transportation lag. The rational transfer function approximates the amplitude distortions introduced by discrete integration of the flight dynamics. The delay accounts for all the phase lags introduced by the simulator components. These phase lags are the major source of degraded performance and increased workload in closed loop tasks. However, the amplitude distortions can be significant for open-loop responses.

The approximate model is then incorporated in the standard optimal control model for the human operator. The resulting continuous closed-loop model is used to analyze both overall simulation effects and the effects of individual elements. The results show that, as compared to an ideal continuous simulation, the discrete simulation can result in significant performance and/or workload penalties. The magnitude of the effects depends strongly on sample period as expected.

In addition to the continuous model, a hybrid model is developed to investigate situations that could not be treated adequately with the continuous model. The hybrid model is used to investigate the effects of improper pilot adaptation to the simulator configuration and to explore the interactions between closed loop performance and the design parameters in the dealiasing filter and data reconstructor.

A preliminary validation of the continuous model is performed by comparing model results with data obtained in an independent experiment. The model proves capable of predicting the effects of computational delays in generating visual cues, once model parameters are chosen to match basic conditions.

1. INTRODUCTION

The development of engineering requirements for man-in-the-loop digital simulation is a complex task involving numerous trade-offs between simulation fidelity and costs, accuracy and speed, etc. The principal issues confronting the developer of a simulation involve the design of the cue (motion and visual) environment so as to meet simulation objectives and the design of the digital simulation model to fulfill the real-time requirements with adequate accuracy.

In specifying the cue environment the designer must establish the need for particular cues as well as the requisite fidelity of presentation. The choices made here are highly important because the validity and utility of the simulation results can be critically dependent upon them and because the decisions involve major costs in the simulation. (Cue generation equipment is generally very expensive to buy and maintain and, even when available, its inclusion will involve additional cost because of the added simulation complexity.) Unfortunately, the decisions are quite difficult to arrive at rationally, inasmuch as the choices depend on complex psychological as well as engineering factors. The requirements will be governed by the purpose of the simulation: training simulators have different needs than research simulators. They will also be problem dependent (e.g., the need for motion cues in the analysis of aircraft control in a gusty environment will depend on the gust response of the aircraft). Finally, the capabilities of the human controller both help and compound the problem. The human pilot may be able to compensate for simulator shortcomings and maintain system performance at the expense of

workload (assuming the real cues are helpful, an assumption that is not always valid). In such a situation, the pilot could give a degraded evaluation of the system that would be unwarranted.

The design of the simulation model has become increasingly important and difficult as digital computers play a more central role in the simulations. For real-time digital simulation with a pilot in the loop the design problem involves specification of conversion equipment (A-D and D-A) as well as of the discrete model of the system dynamics. The design of an adequate discrete simulation is also related closely to the cue generation problem inasmuch as the errors and, in particular, the delays introduced by the simulation will be present in the information cues utilized by the pilot. The significance of this problem has been amply demonstrated, most recently in the ASUPT experience [1]. Of course, human pilots can compensate for model shortcomings as well as for those of cue generation, again with possible effects on the subjective evaluation of the simulation.

"Rules of thumb", open loop response measurements and subjective feedback from pilots are all helpful in developing the engineering requirements for simulators. However, for simulations in which the operator's principal task is flight control, it would be most useful to have analytic models that would allow one to explore the inevitable tradeoffs quantitatively in a closed loop control context. There has been considerable research into the problems of developing digital models that simulate adequately continuous control systems. Models have been proposed based on standard numerical methods for integration of dynamical equations of motion, the use of operational methods (particularly z-transforms) and the use of specialized integration schemes [2-4]. The thrust of this research has been to develop techniques that will allow the digital simulation to respond in the same fashion

as the continuous system being simulated without requiring inordinate computation times (as might ordinarily be dictated by the relatively high bandwidths of many control systems). These studies have considered both open- and closed-loop systems, but they have ignored the problems associated with a human closing the loop. Insofar as the human controller differs from those considered previously (in adaptivity, noise injection properties and in an ability and propensity to trade performance and workload), prior analytic work on digital simulations of control systems is inadequate for defining requirements for piloted simulations.

The objective of the work reported here was to develop a closed loop analytic model, incorporating a model for the human pilot, that would allow certain simulation design tradeoffs to be evaluated quantitatively and to apply this model to analyze a realistic flight control problem. The effort concentrated on the dynamic, closed loop aspects of the simulation. Problems associated with perceptual issues in cue generation were not considered. However, the limitations imposed by the dynamics of cue generation equipment and the effects of adding or omitting information are amenable to treatment by the resulting model.

The optimal control model of the human operator [5-7] is central to the closed loop analysis techniques to be employed. This model has been validated and applied extensively and has a structure that is well-suited to analysis of the simulation problems of interest. The model can be used to generate predictions of attentional workload as well as of closed-loop performance. This is significant because, as noted earlier, pilots may compensate for simulation shortcomings but with a workload penalty; such simulation-induced operator tradoffs need to be explored.

Two approaches to the development of a closed-loop model have been employed in this study. First, a continuous approximation to the open-loop dynamics of the digital simulation was developed. This approximation can be used with the existing implementation of the optimal control model to explore performance/workload penalties associated with the simulation. Although it was believed that such an approach would be satisfactory for most applications, a second, more exact, approach to model development was also considered to assure that the approximations of the continuous model were valid. In particular, a simulation version of the optimal control model was used to control an exact representation of the discrete simulation dynamics; in this model, those portions of the closed loop simulation that correspond to continuous elements (including the human) operate at a significantly higher sample rate than those corresponding to discrete elements (which operate at simulation sample rates). We have called this latter model the hybrid model for obvious reasons.

In the remainder of the report we develop and apply the two models. In Chapter 2, the elements of the discrete simulation are described and the continuous model approximation for the closed-loop simulation is developed. The hybrid model is described in Chapter 3. Results of applying the closed-loop models to a potential simulation of an F8 target tracking problem are presented in Chapter 4 along with a preliminary validation of the model. Chapter 5 contains concluding remarks.

2. CONTINUOUS CLOSED-LOOP MODEL OF SIMULATION

Figure 1 is a generalized block diagram of a digital closed-loop, piloted simulation. The analysis of the implications of various options and tradeoffs on closed-loop performance and workload is the problem of interest here. Below, we discuss in general terms the elements of the loop and then develop a continuous model for the simulation that can be used in conjunction with the optimal control model for the pilot.

2.1 Simulation Description

2.1.1 Analog to Digital Conversion

The human controller is assumed to generate a continuous control input (or vector of inputs). This continuous or analog signal must be converted into a discrete variable for utilization in the digital simulation of the vehicle dynamics. This process, usually referred to as sampling, produces errors in the simulation. Some errors arise because actual samplers are non-ideal (e.g., sampler jitter, aperture errors). For well-designed samplers, errors that are inherent in the sampling operation itself are most important.

The well-known sampling theorem states that the sampling frequency must be at least twice the highest frequency component of the analog signal being sampled. In applying the theorem, the highest frequency occurring in the signal (and not the highest frequency of interest) determines the required sampling frequency. For reasonable accuracy of the reconstructed signal

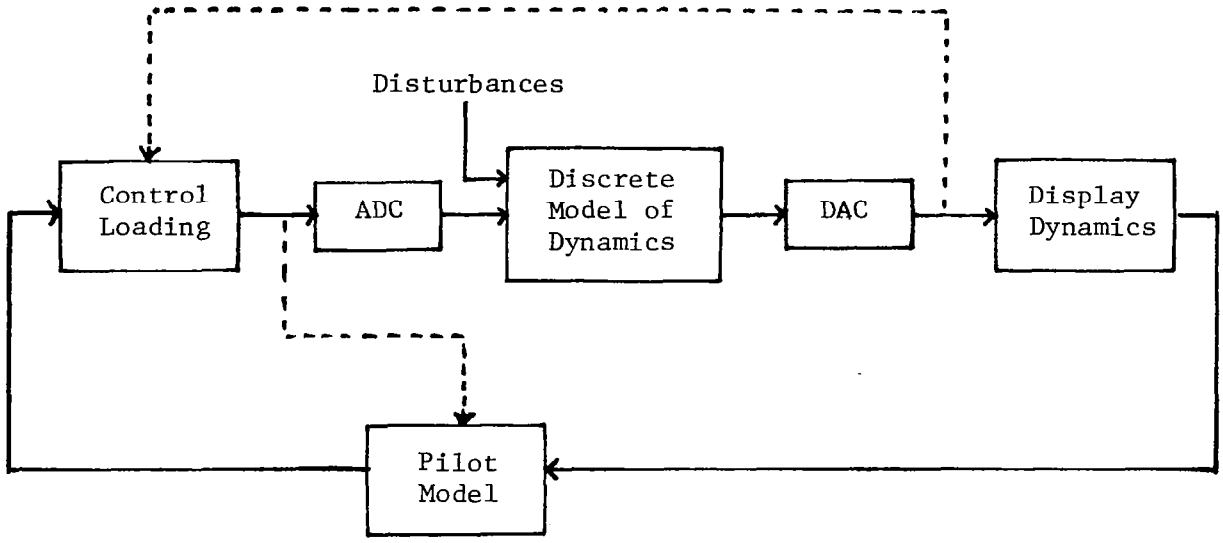

Figure 1.- Simplified Model for Closed Loop Analysis of Digital Simulation.

a much larger sampling frequency is frequently used ([8] suggests a value of at least ten times the highest frequency component). Nevertheless, to prevent aliasing of unwanted high frequency signals (e.g., from noise in the analog portions of the system or from wide-band remnant injected by the human controller), the input to the sampler is normally low-pass filtered. The design of this filter is part of the simulation design. A common choice for the ADC pre-filter is a Butterworth filter which has the desirable property of a flat amplitude response out to the filter cut-off frequency ω_c. This cut-off frequency (and the filter-order) are design parameters. One would like to select ω_c to minimize aliasing problems while passing the frequencies of interest. However, the filter introduces phase shift and the lower the value of ω_c the greater the phase lag of the frequencies of interest. This unwanted lag adds to the computation time lags in the digital simulation and could exacerbate an already serious problem.

2.1.2 Discrete System Modeling

For the problems of interest, differential equations of motion will have to be "integrated" using discrete methods; i.e., by replacing the differential equations by appropriate difference equations. Methods for accomplishing this in general and for the special case of modeling continuous control systems have been

the subject of extensive research. Principally, the approaches have involved numerical methods, operational methods (particularly z-transforms) and, to a lesser extent, sampled-data control theory. Whatever the approach, the major concerns are accuracy, stability, speed and programming ease. Generally speaking, two types of errors are introduced by one step of the integration process, namely round-off and truncation errors. Truncation error is a function of the integration method used, whereas round-off error is a function of the word length of the computer. The manner in which these errors propagate is determined by the stability of the numerical method, the computer program and the problem itself.

While in non-real time applications computation time is a practical consideration, in the problems of interest here it is a design specification. The necessity for matching the simulation time-base to that of the human controller limits the complexity of the numerical integration schemes that can be employed. On the other hand, given the feedback nature of the system and the sampling frequencies that must be used because of the human, numerical accuracy errors are usually of secondary importance.

Of primary importance for closed-loop control problems are the phase-shift (or delay) and amplitude distortion introduced by the integration process. Many integrators have been analyzed to determine their phase and amplitude characteristics (see e.g., [2]) and methods for compensating such integrators, both continuously and discretely, have also been studied (e.g., [3]). Many of the methods have considered matching the total digital simulation loop to that of the continuous control system.

Thus, the integration scheme is considered in conjunction with the data reconstruction process and other system elements. The overall digital simulation system is "compensated" so as to achieve some desired goal such as matching the static gain and closed-loop eigenvalues of the continuous system [4].

Here, we will be primarily interested in the overall distortions introduced by discrete integration of aircraft dynamic equations of motion and in developing continuous models reflecting those distortions. This will be discussed in detail in Section 2.2.

2.1.3 Digital to Analog Conversion (Data Reconstruction)

The discrete simulation model produces outputs at discrete times which must be converted to continuous inputs for processing by the human operator. This involves some sort of data reconstruction process. Based on sampling theory, an ideal low pass filter is needed to recover the wanted information while eliminating the undesirable high frequency outputs that are a result of the sampling. Such filters cannot be achieved practically, and data reconstruction is accomplished by some form of "data-holding". The choice of the data reconstructor is open to the designer, with the tradeoffs involving complexity, accuracy and speed. In general, the higher the order of the data reconstruction process the sharper the amplitude characteristic cuts off. However, distortion of high frequencies in the band of interest and increased phase lag also usually result from increased order reconstruction. In our subsequent analysis, we will limit consideration to zero-order and first-order holds for data reconstruction.

2.1.4 Cue Generation (Display Dynamics and Control Loading)

The cue generation simulation is simplified considerably in Figure 1, in keeping with the limits of this program. In particular, we show only a servo system that might be associated with generating visual cues. The basic idea is to attempt to consider the effects of dynamics in generating visual cues without getting deeply involved in problems related to the perception of these or other cues. Thus, the model accounts for the information available and the dynamics involved in presenting that information.*

A block modeling control loading is also included in Figure 1. The analysis of control loading will be limited to examining the effects of digital generation of the loading forces on closed-loop performance. The subtleties associated with perception of force feedback or of subjective evaluations of control loading will not be explored. These problems are, of course, of major importance in deciding on the requisite cue simulation but they are left to future study.

2.1.5 Optimal Control Model for Pilot

The optimal control model (OCM) of the human operator is illustrated in Figure 2. The model has been documented extensively [e.g., 5-7]. Here some of the features of the model that are particularly relevant to subsequent discussions are reviewed briefly. Figure 2 illustrates the structure of the OCM.

---

* One may also treat motion cues in a similar manner [9]. However, to limit the scope of this effort we have concentrated on fixed-base simulation, leaving the inclusion of motion to later study.

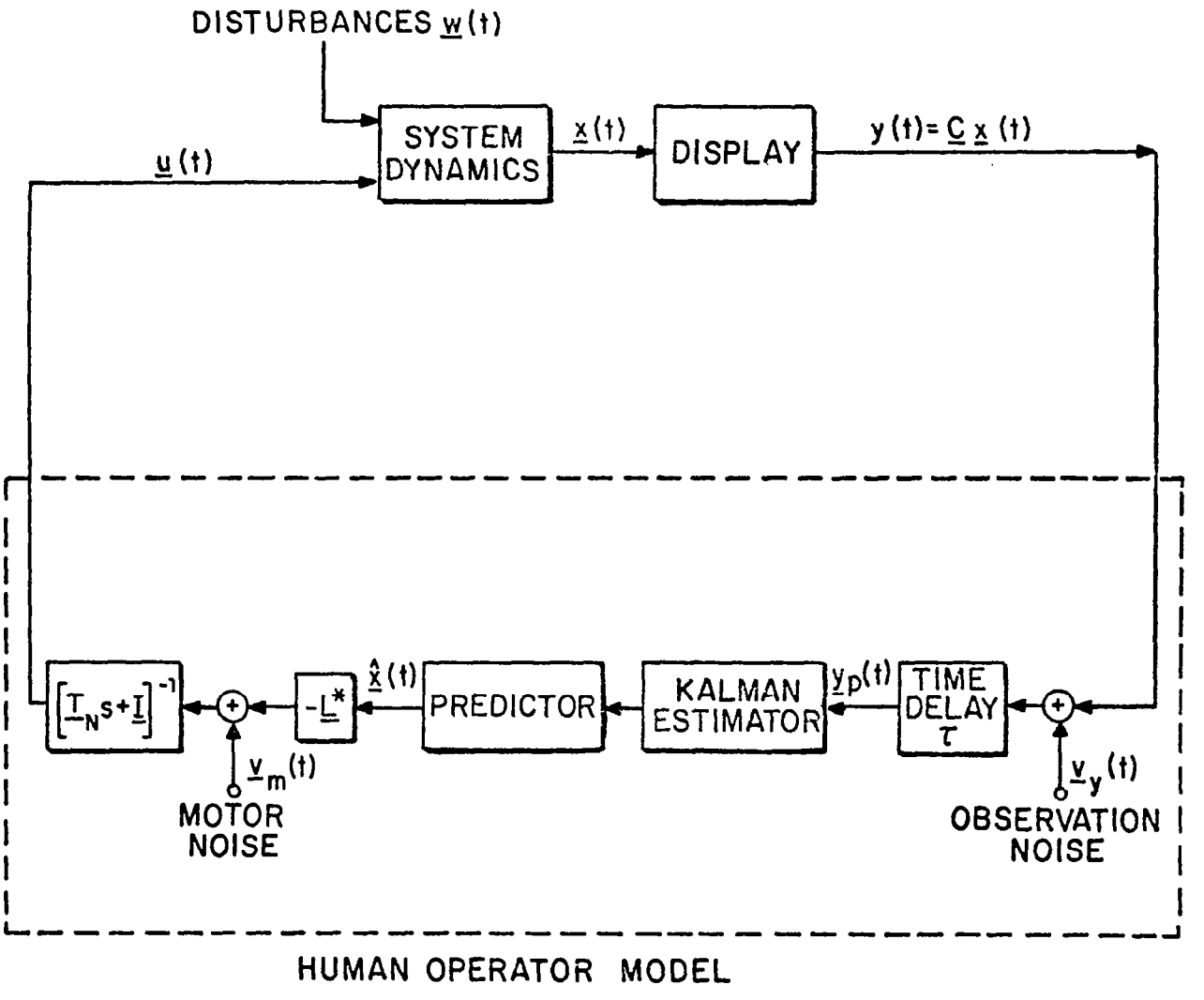

Figure 2.- Structure of the Optimal Control Model.

The OCM as originally conceived and developed presupposes that the system dynamics, corresponding to the element to be controlled, may be expressed in state variable format

$$\dot{\underline{x}}(t) = \underline{\underline{A}}_c \underline{x}(t) + \underline{\underline{B}}_c \underline{u}(t) + \underline{\underline{E}}_c \underline{w}(t) \qquad (1)$$

$$\underline{y}(t) = \underline{\underline{C}}_c \underline{x}(t) + \underline{\underline{D}}_c \underline{u}(t)$$

where $\underline{x}$ is the n-dimensional state-vector, $\underline{y}$ is an m-dimensional vector of displayed outputs, $\underline{u}$ is the r-dimensional control input vector and $\underline{w}$ is a vector of disturbance and/or command inputs. The system matrices ($\underline{\underline{A}}_c, \underline{\underline{B}}_c, \underline{\underline{C}}_c, \underline{\underline{D}}_c, \underline{\underline{E}}_c$) are generally assumed to be time-invariant, although this restriction has been relaxed in recent investigations [10,11]. The above system dynamics include the linearized dynamics of the aircraft (or other controlled element) and any dynamics associated with measurement, control and display systems. The subscript c on the system matrices is included to emphasize that the dynamics are assumed to represent a continuous system.

For purposes of discussion it is convenient to consider the model for the pilot as being comprised of the following: (i) an "equivalent" perceptual model that translates displayed variables into noisy, <u>delayed</u> perceived variables denoted by $\underline{y}_p(t)$*;

---

* A threshold is also considered part of the perceptual process, but may actually be used to model the effects of non-idealized displays. The threshold is treated by statistical linearization techniques.

(ii) an information processing model that attempts to estimate the system state from the perceived data. The information processor consists of an optimal (Kalman) estimator and predictor and it generates the minimum-variance estimate $\hat{x}(t)$ of $x(t)$; (iii) a set of "optimal gains", L^*, chosen to minimize a quadratic cost functional that expresses task requirements; and (iv) an equivalent "motor" or output model that accounts for "bandwidth" limitations (frequently associated with neuromotor dynamics) of the human and an inability to generate noise-free control inputs.

The time-delay, observation- and motor-noises and the neuromotor-lag matrix are included to account for inherent limitations on human processing and perceptual-motor activity. Methods for choosing values for these quantities have been determined by matching experimental data and these values have been found to be generally independent of task parameters [5].

The time delay or transport lag is intended to model delays associated with the human. All displayed variables are assumed to be delayed by the same amount, viz. τ seconds. Delays introduced by the simulation can be added to the human's delay without any problem, so long as all outputs are delayed by the same amount. If such is not the case, then all outputs can be delayed by τ, where τ is now the sum of the minimal delay introduced by the simulation and the operator's delay, and additional delays for the outputs requiring them can be modeled via inclusion of Padé approximations in the output path.

The observation and motor noises model human controller remnant [12] and involve injection of wide-band noise into the system. This noise is "filtered" by the other processes in the

pilot model and by the system dynamics. It should be emphasized that the injected remnant is a legitimate (if unwanted) part of the pilot's input to the system and, therefore, significant amounts of remnant power should not be filtered out in the de-aliasing process of a valid simulation.

The neuro-motor lag matrix limits the bandwidth of the model response. Typically, for wide-band control tasks, involving a single control variable, a bandwidth limitation of about 10-12 rad/sec gives a good match to experimental results (i.e., a neuro-motor time constant of $T_N \approx .08 - .10$). For many aircraft control tasks there is no significant gain (i.e., reduction in error) to be obtained by operating at this bandwidth, and there can be some penalty in unnecessary control activity. For such tasks larger time constants (lower bandwidths) have been observed. In these cases, if the neuro-motor time constant is arbitrarily set at the human's limit (say $T_N \approx .1$) good predictions of tracking or regulation performance are usually obtained; but the control activity and pilot bandwidth tend to be overestimated.

It may be useful to have more accurate estimates of pilot bandwidth for making decisions concerning approximations to the discrete simulations. Therefore, T_N was chosen in this study on the basis of a model analysis of the tradeoff between error and control-rate scores. The procedure is illustrated by Figure 3, which is a curve showing the tradeoff between error and control-rate for the F-8 longitudinal short-period dynamics, and the target tracking input to be analyzed later in this report. Shown on the curve is the rate-limit for the F-8 actuator; T_N must be chosen so that this limit is not reached or violated a

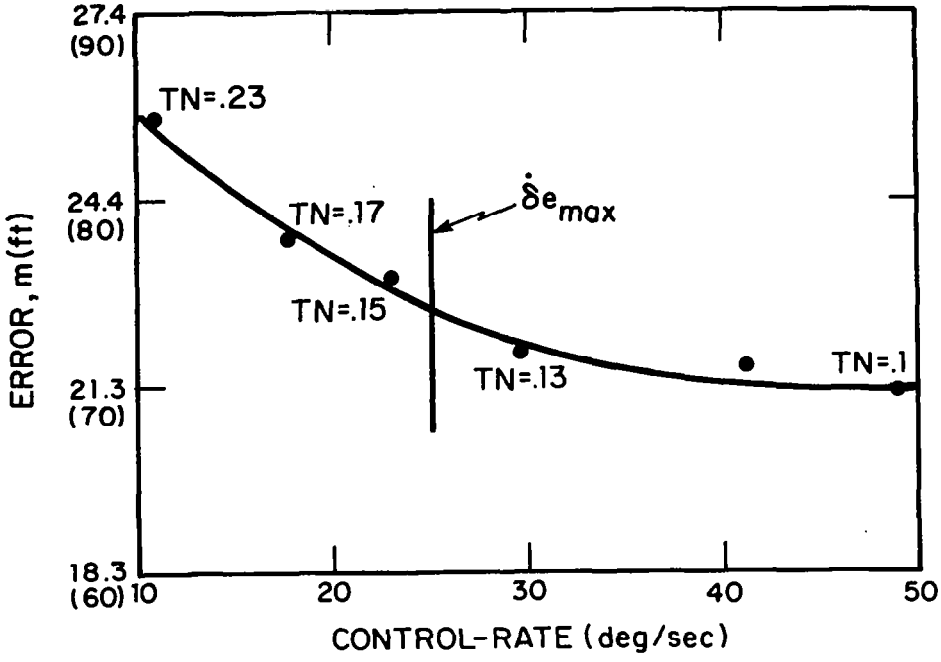

Figure 3. - Error/Control-Rate Tradeoff.

significant portion of the time (so the linearized analysis is valid). A value for T_N of approximately .15 (an operator bandwidth of about 1 Hz) was chosen on the basis of this curve. This value gives an rms control rate that is less than the maximum. The error score exceeds that obtained with T_N = .1 by less than 10%, while the control rate is less than half of that obtained with the wider bandwidth.

The optimal estimator, predictor and gain matrix represent the set of "adjustments" or "adaptations" by which the human attempts to optimize his behavior. The general expressions for these model elements depend on the system and task and are determined by solving an appropriate optimization problem according to well-defined rules. Of special interest here is that, in the basic continuous OCM, the estimator and predictor contain "internal models" of the system to be controlled and the control gains are computed based on knowledge of system dynamics. The assumption is that the operator learns these dynamics during training.*

The question arises as to the appropriate internal model when the human controls a discrete simulation of a nominally continuous system. It would appear that if the operator is trained on the simulation, then the appropriate model corresponds to the simulation model.** This will be the assumption employed with the continuous model.

---

* This is generally more convenient than assuming that the external model differs from the true model and also leads to good performance prediction [13]

** If the simulation model is poor, a control strategy that is inappropriate for the actual system could be learned with negative results in, say, transfer of training. This issue can be addressed with the hybrid model described later.

Finally, it should be mentioned that the solution to the aforementioned optimization problem yields predictions of the complete closed-loop performance statistics of the system. Predictions of pilot describing functions and control and error spectra are also available. All statistical computations are performed using covariance propagation methods, thus avoiding costly Monte Carlo simulations. This is not the case for the hybrid model described later in Chapter 3.

2.2 Open-Loop Simulator Dynamics

As noted above, the application of the standard OCM to closed loop analysis requires a continuous state representation of the complete controlled element. This state-variable description can be arrived at from basic derivations of dynamical equations, or it can be developed to "match" or approximate the input/output characteristics of the controlled element. We shall develop a continuous model for the simulation utilizing each approach to some extent. In particular, approximate transfer functions for the simulation will be developed first. Inasmuch as there is not a unique state representation corresponding to the transfer function, we will choose the form that corresponds to that which would be derived based on aircraft dynamical equations of motion. This procedure, we believe, provides the most insight into the changes in open-loop characteristics introduced by the discrete simulation of continuous aircraft dynamics.

2.2.1 System Function From Stick Input to Displayed Output

Figure 4 is an elaborated diagram of the simulator portion of Figure 1*. Note that the output of the visual servo, $y(t)$, is a continuous signal as is the input, $u(t)$, to the A-D dealiasing pre-filter.** We begin by deriving the system function that relates these two continuous quantities.

---

* Control loading is neglected in this analysis, but will be considered in the hybrid model.

** For simplicity, we consider single-input, single-output systems. The results obtained here can be generalized to more complex situations.

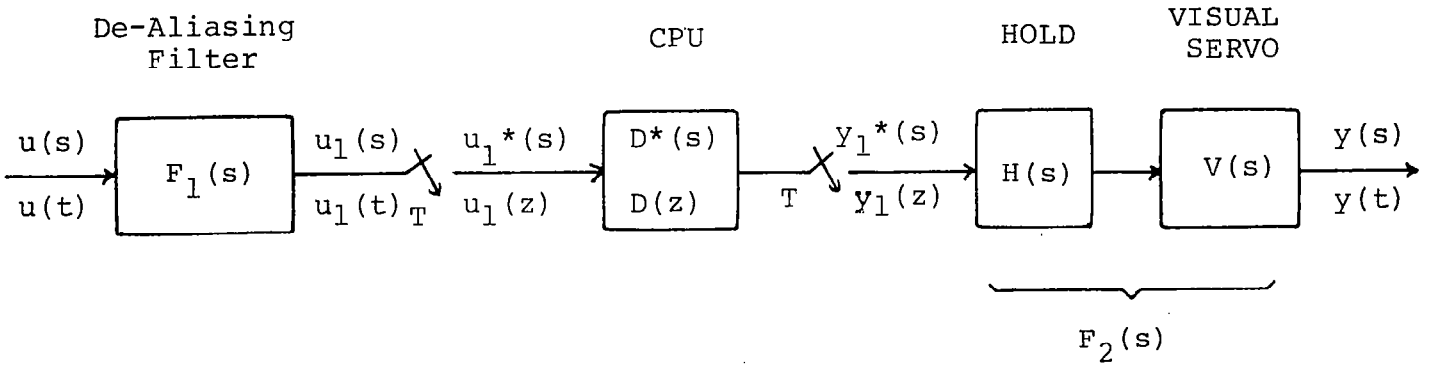

Figure 4. - Open Loop Simulator Dynamics.

For analysis purposes we use the notation implied in Figure 4. Variables or functions with argument s represent Laplace transforms and those with argument z correspond to z-transforms. The starred quantities correspond to Laplace transforms of impulse sampled signals or of functions of z and are defined, e.g., by [2]

$$u_1^*(s) \triangleq u_1(z)\Big|_{z=e^{sT}} = \frac{1}{T}\sum_{n=-\infty}^{\infty} u_1(s+jn\Omega) \tag{2}$$

or

$$D^*(s) = D(z)\Big|_{z=e^{sT}} \tag{3}$$

where

$$\Omega = \frac{2\pi}{T} = \text{sampling frequency.} \tag{4}$$

From Figure 4, we obtain

$$\begin{aligned} y(s) &= F_2(s)y_1^*(s) = F_2(s)D^*(s)u_1^*(s) \\ y(s) &= F_2(s)D^*(s)\left\{\frac{1}{T}\sum_{n=-\infty}^{\infty} F_1(s+jn\Omega)u(s+jn\Omega)\right\} \end{aligned} \tag{5}$$

Equation (5) gives the exact transfer relation between u(s) and y(s). However, it is not a useful expression from the standpoint of closed-loop modeling because of the infinite summation.

The system function, G(s), for a linear system (such as the simulation system under analysis) may be obtained by computing the steady-state response of the system to an input of the form e^{st}. That is,

$$G(s) = \left.\frac{y(t)}{u(t)}\right|_{u(t) = e^{st}}$$

It is shown in Appendix A that the system function from u(s) to y(s) (in steady-state) is given by*

$$\left.\frac{y_{ss}(t)}{u(t)}\right|_{u(t) = e^{st}} \triangleq G(s;t)$$

$$= \left\{ \frac{1}{T} \sum F_2(s+jn\Omega) D^*(s+jn\Omega) e^{jn\Omega t} \right\} F_1(s)$$

and, since D*(s) is periodic in s with period $j\Omega$,

$$G(s;t) = \left\{ \frac{1}{T} \sum_{n=-\infty}^{\infty} F_2(s+jn\Omega) e^{jn\Omega t} \right\} D^*(s) F_1(s) \qquad (6)$$

We note that, as a result of the sampling, the system function between continuous output and continuous input is periodic in time with a period equal to the sampling period.

If the output y(t) is considered only at sampling instants, which amounts to introducing a "fictitious" sampler at the output as is done for instance in [2] or [14], then a time-independent transfer function is obtained, viz.

$$G(s;t)\Big|_{\substack{\text{sample} \\ \text{times}}} = G(s) = F_2^*(s) D^*(s) F_1(s) \qquad (7)$$

We shall consider G(s) defined in (7) to be the "exact" transfer function for the simulation. Note that $F_2^*(s) = (VH_i)^*(s)$.

---

* The notation G(s;t) is used to emphasize the time varying nature of the system function.

2.2.2 Approximations for the Open-Loop Transfer Function

Equation (7) is intractable for use with the continuous OCM. Therefore, it will be necessary to approximate (7) for closed-loop analysis. A straightforward approximation is to ignore all but the n=0 term in the expression for F_2^* which results in

$$G(s) \approx \frac{F_2(s)D^*(s)F_1(s)}{T} \tag{8}$$

In utilizing (8) it will be necessary to approximate $D^*(s)$; the procedure for doing this will be discussed in a subsequent section*.

The approximation of Equation (8) will be good provided that the de-aliasing filter $F_1(s)$ is effective and that only the "low"-frequency range is of interest. Note, too, that this approximation can also be obtained by neglecting all but the first order terms in the exponentials in $u_1^*(s) = u_1(z)\Big|_{z=e^{sT}}$; this is clearly valid for "small" T.

An alternative method of approximating G(s) is suggested by [2]. This method is based on introducing a fictitious sampler and hold following the continuous input (u(t) in Figure 4) and another fictitious sampler at the output. Then the Bode response between the envelopes of the sampled output and input is given by

$$\frac{y^*(s)}{u^*(s)} = F_2^*(s)D^*(s)(F_1F_h)^*(s) \triangleq G^*(s) \tag{9}$$

---

* Suffice to say, for now, that $D^*(s)$ will be approximated by a rational transfer function multiplied by a pure delay so as to yield a good match to the Bode response for $D^*(s)$ in the frequency range of interest.

where $F_h(s)$ is the hold used to reconstruct the sampled u. Since the hold has been introduced to facilitate the analysis, the transfer function from u(s) to the envelope of y*(s) is then approximated by

$$G(s) \simeq \frac{G^*(s)}{F_h(s)} \simeq G^*(s)e^{\tau_h s} \tag{10}$$

where τ_h is the delay introduced by the hold.

The last, and simplest, approximation we will consider is dictated by the response characteristics of the de-aliasing filters and data reconstruction elements that are of interest here. In particular, the transfer functions for the de-aliasing filter and servo are, respectively,

$$F_1(s) = \frac{\omega_c^3}{s^3+2\omega_c s^2+2\omega_c^2 s + \omega_c^3} \tag{11}$$

$$V(s) = \frac{\omega_n^2}{s^2+2\zeta\omega_n s+\omega_n^2} \tag{12}$$

The hold transfer function is either

$$H_o(s) = \frac{1-e^{-sT}}{s} \tag{13}$$

or

$$H_1(s) = T(1+Ts)\left(\frac{1-e^{-Ts}}{Ts}\right)^2 \tag{14}$$

For the simulation studies to be analyzed subsequently sample periods, T, of 1/32, 1/16, 1/10 will be considered. Therefore, if the cutoff of the de-aliasing filter is chosen on the basis of the sampling theorem, $\omega_c > 5$Hz. The visual servo dynamics to be used are those of the visual system of the NASA LRC Differential Maneuvering Simulator (DMS) [15]. For that system, $\omega_n = 25$ rad/sec and $\zeta = .707$.

With the parameter values as just specified, each of the transfer functions of (11) - (14) may be approximated reasonably well by a pure transport lag in the frequency region of interest for manual control ($\omega < \sim 10$ rad/sec). That is,

$$\begin{aligned} F_1(s) &\simeq e^{-\tau_F s} \\ V(s) &\simeq e^{-\tau_V s} \\ H_o(s) &\simeq e^{-\tau_o s} \\ H_1(s) &\simeq e^{-\tau_1 s} \end{aligned} \tag{15}$$

where

$$\begin{aligned} \tau_F &\simeq \frac{2}{\omega_c} = \frac{2T}{\pi} \\ \tau_V &\simeq (\zeta\omega_n)^{-1} = .057 \text{ sec} \\ \tau_o &= T/2 \\ \tau_1 &= T \end{aligned} \tag{16}$$

Substitution of (15) into (8) yields

$$\begin{aligned} F_1(s)D^*(s)F_2(s) &= F_1(s)D^*(s)V(s)\ H(s) \\ &\simeq D^*(s) \exp\left\{-(\tau_F + \tau_V + \tau_i)s\right\} \end{aligned} \tag{17}$$

where i = o or 1 for the zero-order or first-order hold, respectively.

The three approximations (8), (9) and (17) are compared with the exact expression of (7) in Figure 5, for T = 1/10 and $H_i(s) = H_o(s)$. The D* in these figures corresponds to Euler integration of the F8 short period dynamics. In the

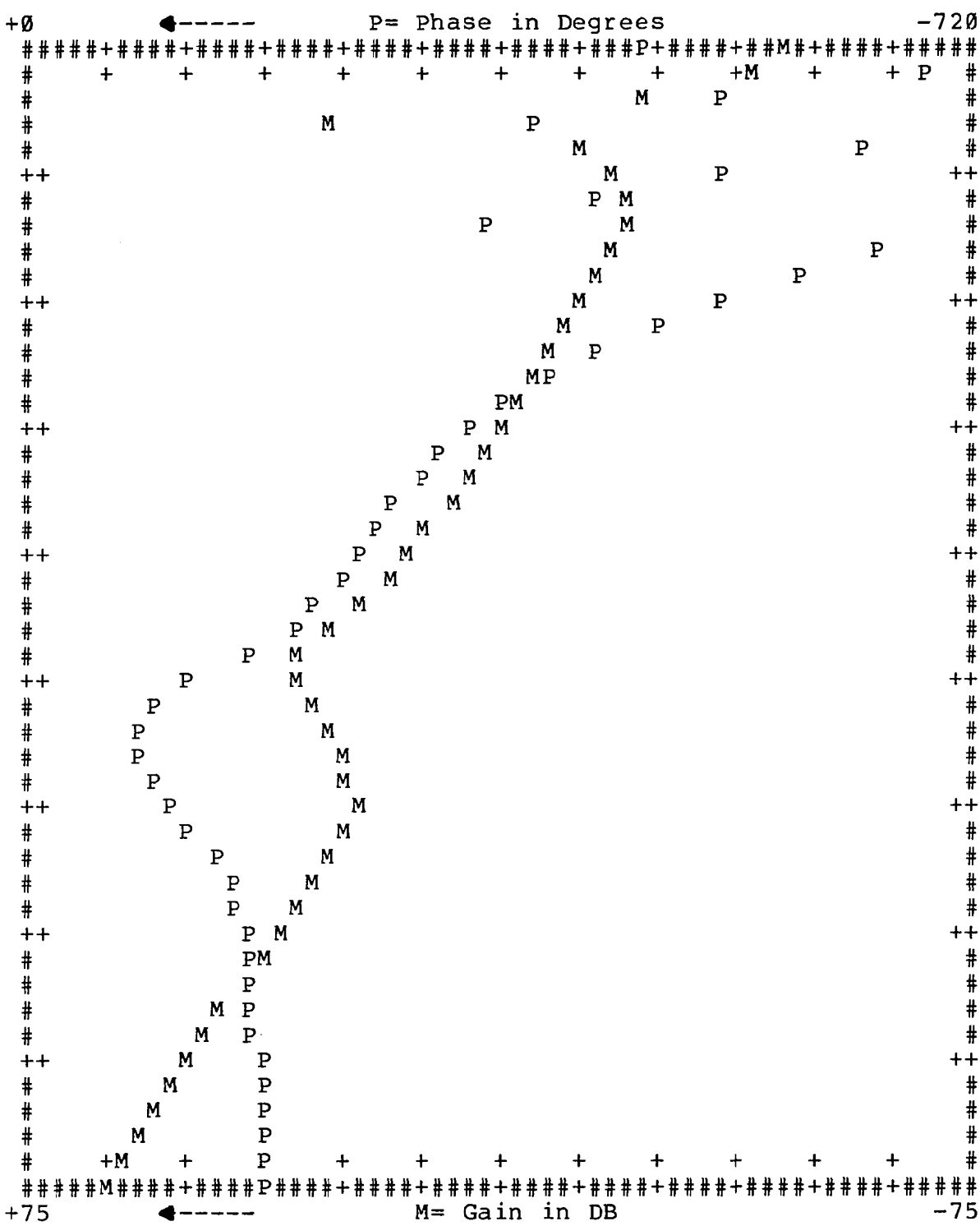

Figure 5. - Approximations to Open Loop Simulator Dynamics.
a) Exact Bode Response $F_2^* D^* F_1^*$.

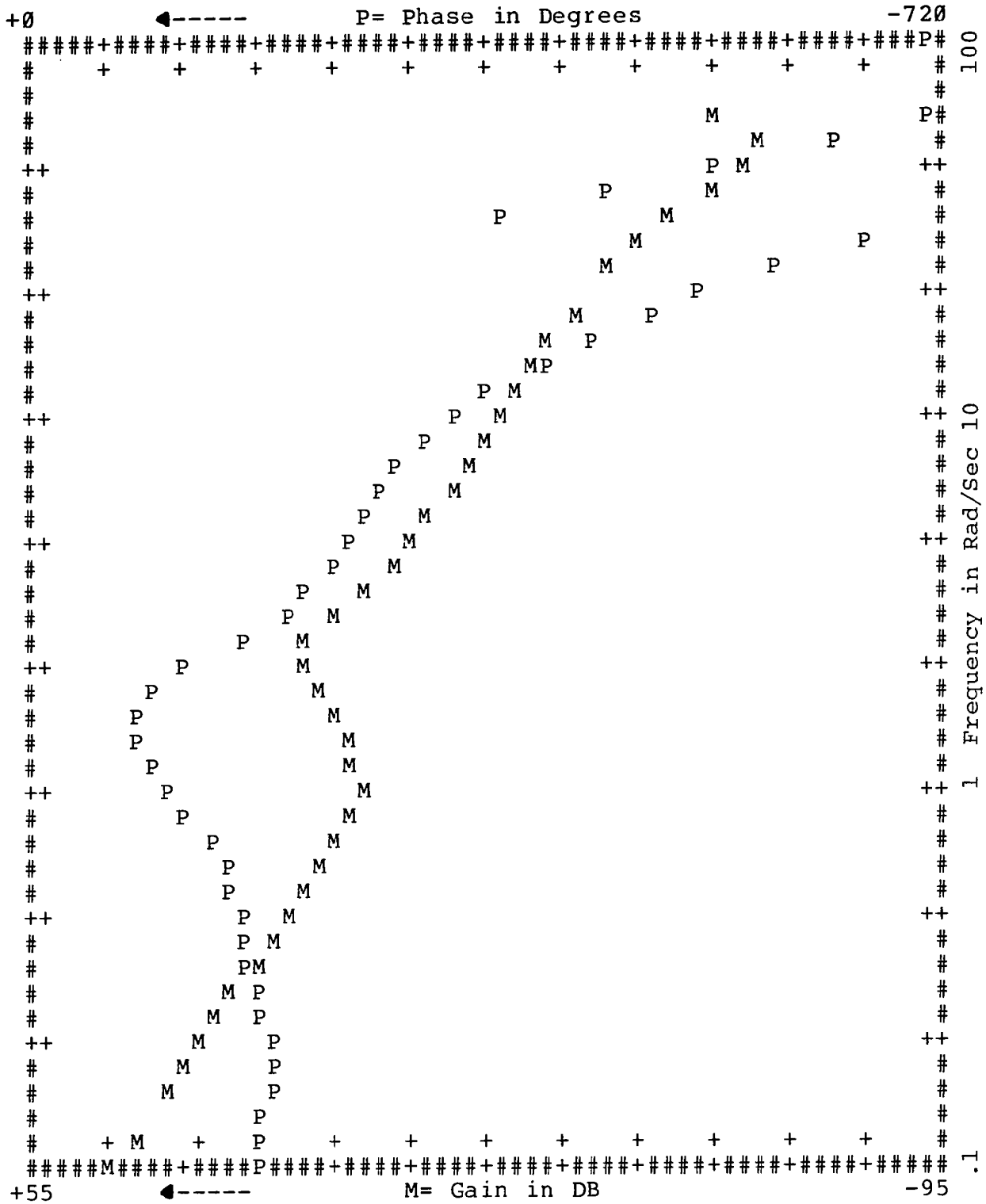

Figure 5. - Approximations to Open Loop Simulator Dynamics.
b) $F_2*D*F_1 \approx F_2D*F_1$.

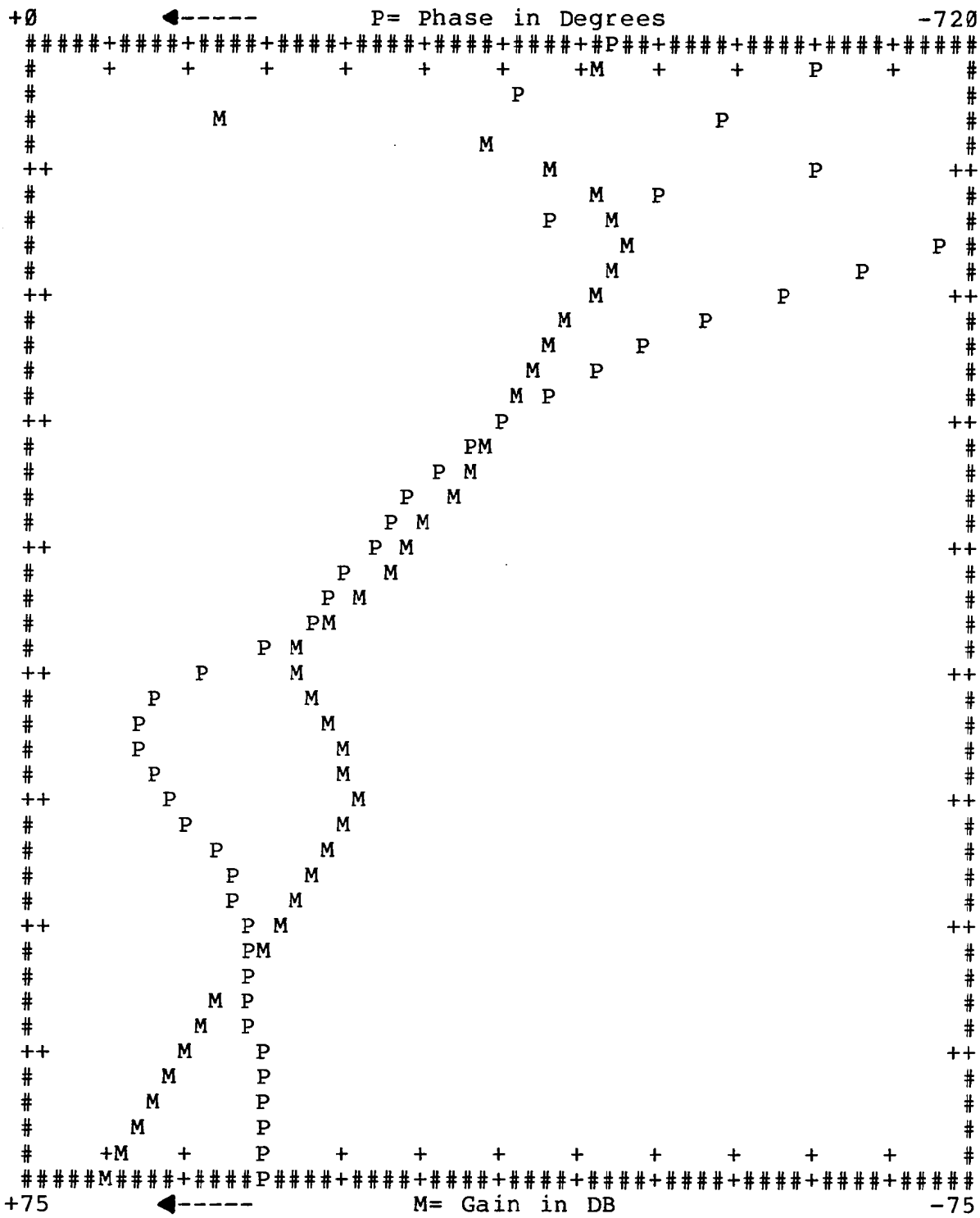

Figure 5.- Approximations to Open Loop Simulator Dynamics.
c) $F_2 * D * F_1 \quad F_2 D * (F_1 H_1) * T_{HS}$.

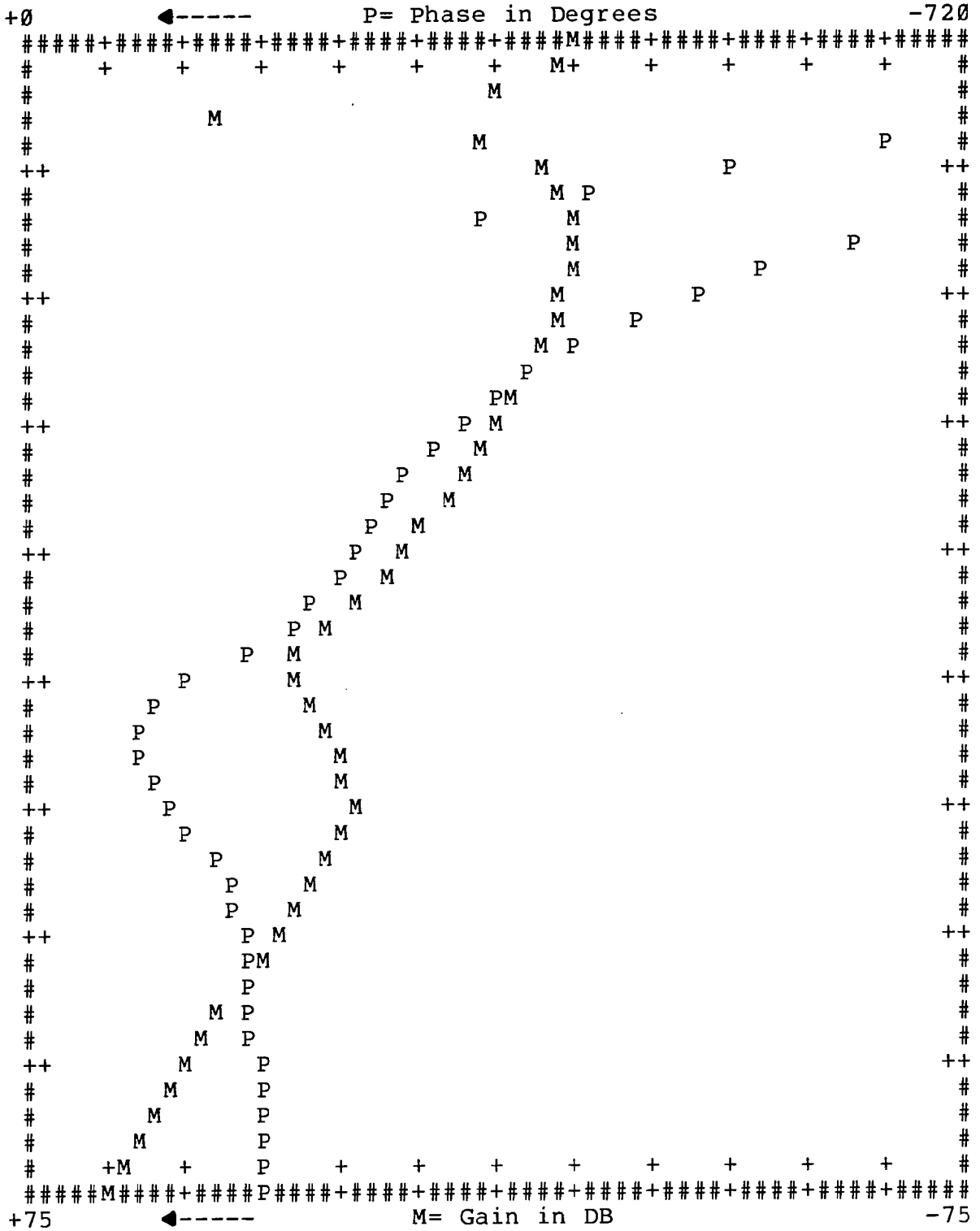

Figure 5. - Approximatins to Open Loop Simulator Dynamics.

d) $F_2*D*F_1 \approx D*e^{-.17s}$.

region $\omega < 10$ rad/sec all three approximations appear to be adequate. Equation (17) will, therefore, be used to model the effects of the A-D, hold and servo dynamics, inasmuch as this expression is both simple and cost-effective to employ in the continuous model. The cost-effectiveness arises from the fact that with Equation (17) no more states are required to model the open loop simulator dynamics than are needed for the continuous problem being simulated; all that is changed is the time delay associated with the human operator. Although the results are not shown here, it was verified that including the exact transfers for the de-aliasing filter and visual servos in the closed loop analysis produces results that are virtually the same as those obtained with the time delay approximation.

2.3 Effects of Discrete Integration

In the previous section the transfer function D*(s) was left unspecified as was the manner in which it was to be approximated for continuous closed-loop analysis with the OCM. In general, D*(s) will be a "distorted" version of the continuous system dynamics that are to be simulated. Some general features of the distortions introduced by various integration schemes are analyzed and presented in Appendix B. Here, we present results pertinent to the F-8 dynamics that are to be analyzed later. Specifically, after a brief discussion of the basic effects of discrete simulation, we show how two integration schemes that are of particular interest for real-time simulation, Euler and Adams-Bashforth (A-B), effect the open-loop F-8 dynamics. We then develop suitable approximations for D*(s) to be used in the closed-loop analysis.

2.3.1 Basic Considerations

Consider the continuous vehicle-dynamics as described in the state-variable form of Equation (1). For constant system matrices, the transfer matrix between system outputs and control inputs is given by

$$\begin{aligned} \underline{y}(s) &= \underline{\Phi}_c(s)\ \underline{u}(s) \\ \underline{\Phi}_c(s) &= \underline{C}_c(s\underline{I}-\underline{A}_c)^{-1}\ \underline{B}_c + \underline{D}_c \end{aligned} \tag{18}$$

When Equations (1) are "integrated" digitally, they lead to a discrete approximation with the following transfer matrix [see Appendix B]

$$\underline{D}^*(s) = \{\underline{c}_d[z\underline{I}-\underline{A}_d]^{-1}\ \underline{B}_d + \underline{D}_d\}\Big|_{z=e^{sT}} \tag{19}$$

where the matrices in (19) depend on the particular integration scheme and sample period as well as on the corresponding continuous system matrices. Several points concerning Equation (19) are noteworthy. First, the elements of the discrete transfer matrix, $\underline{D}^*(s)$, cannot, in general, be expressed as the ratio of two polynomials in s of finite degree. Second, the Bode responses corresponding to (19) will differ from the continuous responses in both amplitude and phase; and, further, the responses for the discrete system are periodic in ω with period equal to $\frac{2\pi}{T}$. Third, the poles and zeros of Equation (19) are infinite in number and are given by, for example,

$$P_i = \sigma_i + j(\omega_i + 2\pi k);\ k = 0, \pm 1, \pm 2, \ldots \tag{20}$$

Moreover, the principal values for the poles and zeros, i.e., those with k = 0, are not, in general, equal to the corresponding poles and zeros of the continuous system. Finally, simple integration schemes, such as Euler, will have the same number of principal poles as the continuous system, whereas multi-step integration schemes, like A-B, will introduce principal roots that are spurious.

2.3.2 Effects on Open-Loop F-8 Dynamics

The longitudinal and lateral dynamics for the F8 aircraft that are to be the subject of the closed loop analysis are given in state variable format in Appendix C. The dynamics correspond to a single flight condition, but involve both CAS-ON [16] and CAS-OFF modes. In addition, a simplified set of lateral dynamics corresponding to perfect coordination is included.

Characteristic Modes

The effect of integration scheme and sample period on the characteristic modes of the F8 are shown in Tables 1 and 2. Table 1 is of prime interest here in that it shows how the basic modes are "perturbed" by the discrete simulation; Table 2 lists the "spurious" modes of lowest frequency introduced by A-B integration.

It can be seen from Table 1, that Euler integration has the greater effect on the location of the characteristic modes. In terms of the basic, unaugmented dynamics its main effect is a reduction in the magnitude of the real parts of the characteristic roots. Thus, the damping ratios for the longitudinal short-period mode and for the lateral dutch roll mode are reduced.

Table 1. Effect of Integration Scheme on Vehicle Modes

Integration Scheme		EULER			ADAMS-BASHFORTH		
Sample Period	Continuous	1/32	1/16	1/10	1/32	1/16	1/10
Longitudinal							
CAS-off: Short Period (ζ_{sp}; ω_{nsp})	.291; 2.28	.257; 2.30	.222; 2.32	.18; 2.33	.291; 2.28	.294; 2.30	.300; 2.33
CAS-on: Short Period (ζ_{sp}; ω_{nsp})	.64; 2.78	.616; 2.86	.586; 2.94	.544; 3.03	.65; 2.79	.65 2.79	.67 2.81
CAS Mode (ζ_{c*}; ω_{nc*}) τ_{c*}	.91; 7.42 .79	.885; 8.31 .78	.840; 9.45 .76	.73; 11.0 .74	.918; 7.30 .79	.939; 6.92 .79	.965; 6.14 .80
Lateral							
CAS-off: Dutch Roll (ζ_d; ω_n)	.128; 2.64	.087; 2.65	.045; 2.65	.004; 2.65	.128; 2.65	.130; 2.67	.131; 2.72
Roll Subsidence (τ_R)	.42	.40	.387	.37	.42	.42	.43
Spiral (τ_R)	40.	40.	40.	40.	40.	40.	40.
CAS-on							
Dutch Roll (ζ_d; ω_{hd})	.621; 2.84	.592; 2.91	.56; 2.99	.516; 3.08	.624; 2.84	.632; 2.85	.649; 2.87
Roll Subsidence (τ_R)	.229	.214	.196	.175	.231	.238	.251
Spiral (τ_R)	76.9	76.9	76.9	76.9	69.0	63.3	78.7
CAS Mode (τ_M)	.20	.184	.167	.144	.202	.209	.224
Coordinated							
Roll Subsidence (τ_R)	.388	.373	.356	.336	.389	.392	.400
Spiral (τ_S)	109.4	109.4	109.2	109.2	113.6	113.6	111.7

* This result is suspicious and may reflect numerical error.

For the lowest sampling rate, T = .1 sec, the reduction in damping is quite significant. The effect on the natural frequencies of these modes is minor, with frequency increasing with decreasing T. The reduction in damping will result in a simulated aircraft with short period and dutch-roll handling characteristics that are poorer than those of the "true" aircraft. On the other hand, the reduction in magnitude of the real parts of the characteristic roots leads to an improved roll response. In particular, the time constant of the roll subsidence mode is reduced by Euler integration, thus yielding quicker roll response. For T = .1, the time constant is reduced from .388s to .336s, i.e., by almost 15%. The effect of Euler integration on the spiral mode is negligible.

The effect of A-B integration on the aircraft modes is both smaller and in a different direction. Damping ratios for the short period and dutch-roll modes are increased by A-B integration, although by amounts so small as to probably be negligible. The changes in the natural frequencies of these modes are similar to that observed for Euler integration. The roll-response is degraded slightly in the A-B case and the spiral mode is apparently unaffected by the integration scheme.

The CAS-on configurations show some of the same trends as those above. In particular, the effects on damping ratios and time constants are qualitatively the same as for the CAS-off configuration. However, the pitch CAS-mode natural frequency* is affected to a much larger extent than is the frequency of the short period mode. Euler integration tends to increase the frequency of this mode as before. On the other hand, for A-B integration the CAS-mode natural frequency decreases with sample period, a trend that is opposite to that for the other modes.

---

* The pitch CAS is a C*-model following design and is described in Section 4.1.

As we have seen, the effects of A-B integration on the aircraft and CAS modes is generally less than that for Euler integration, but A-B introduces spurious roots. The frequency and damping for the unwanted roots with lowest frequencies are given in Table 2. It can be seen that the spurious roots are outside the frequency range of interest for closed-loop manual control and, for sample periods as low as .03125, are unlikely to present any problems. However, for the higher sample periods considered, the roots could lead to undesirable or incorrect open-loop responses (e.g., responses to step inputs). In general, the spurious roots could result in an interaction with CAS modes and structural modes (if included) that would be absent in a continuous simulation or in a discrete simulation with a simpler integration scheme. We will not consider this issue further in this report but mention it as a factor when considering multi-step integration schemes for simulation.

Bode Responses

The above analysis ignores zeros and, generally, does not give the full picture with respect to the distortions introduced by digital integration. Indeed, from a closed-loop standpoint, the most important effects of discrete integration are likely to arise from phase distortion (lag) rather than from perturbation of the characteristic modes. To get a better appreciation of the overall effects of discrete integration, and as a prelude to approximating D*(s), selected Bode responses for the F8 dynamics are presented in Figures 6-9. Additional Bode responses for the cases of interest is given in Appendix B.

Figure 6 shows the effect of Euler and A-B integration on the pitch/elevator ($\theta/\delta e$) transfer function for the F8 unaugmented short period dynamics. The continuous transfer function, the

TABLE 2

LOWEST FREQUENCY SPURIOUS MODES
FOR ADAMS-BASHFORTH INTEGRATION

Sample Period	1/32		1/16		1/10	
	ζ	ω_n(rad/s)	ζ	ω_n(rad/s)	ζ	ω_n(rad/s)
Longitudinal						
CAS OFF:	.88	121.	.83	49.9	.79	26.7
CAS ON:	.60	105.	.38	44.4	.15	25.8
	.81	121.	.74	50.6	.65	27.3
Lateral						
CAS OFF:	.89	114.	.85	46.6	.81	24.5
	.72	144.	.62	63.7	.52	36.7
CAS ON:	.82	120.	.74	50.0	.66	26.9
	.60	126.	.44	56.1	.29	32.8
Coordinated						
	.70	142.	.60	62.9	.50	36.2

corresponding discrete transfer function and a curve of the distortion introduced by the discrete integration are all presented. Distortion is defined as the ratio of the discrete Bode response to the continuous response. Thus, in terms of amplitude and phase, it is the difference between the two responses, where amplitude is given in dB. Curves are given for the highest (T = .1) and lowest (T = .03125) integration step of interest. (It has been assumed that the integration step size is equal to the sample period.) Figures 7-9 contain similar plots for the roll angle/aileron (ϕ/δ_A) for the lateral CAS/ON configuration and for the ϕ/δ_A and transverse line-of-sight tracking error/aileron ($R\epsilon_T/\delta_A$) transfers for the "coordinated" lateral dynamics.

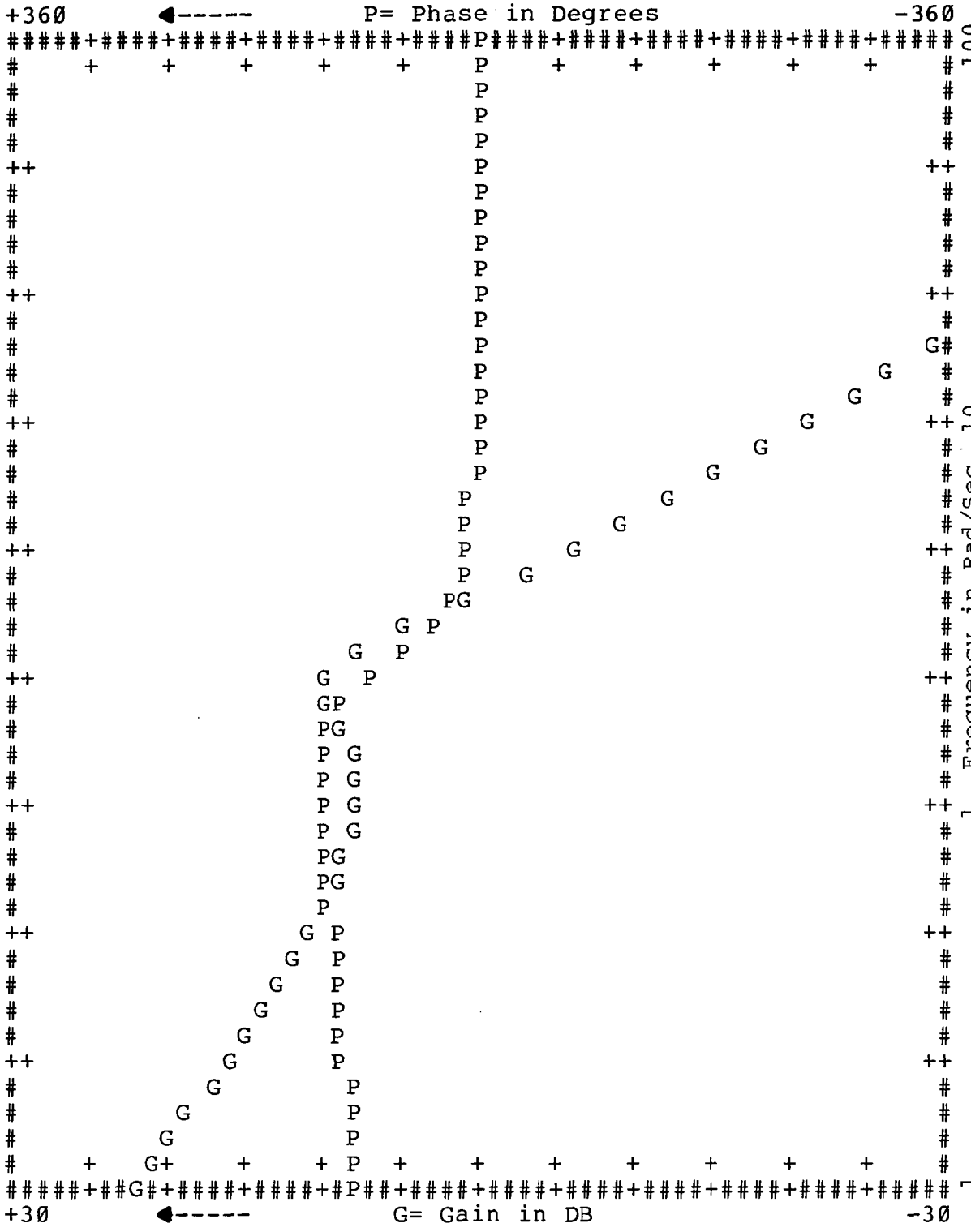

Figure 6. - Pitch/Elevator (θ/δ_e) Bode Responses.
a) Continuous.

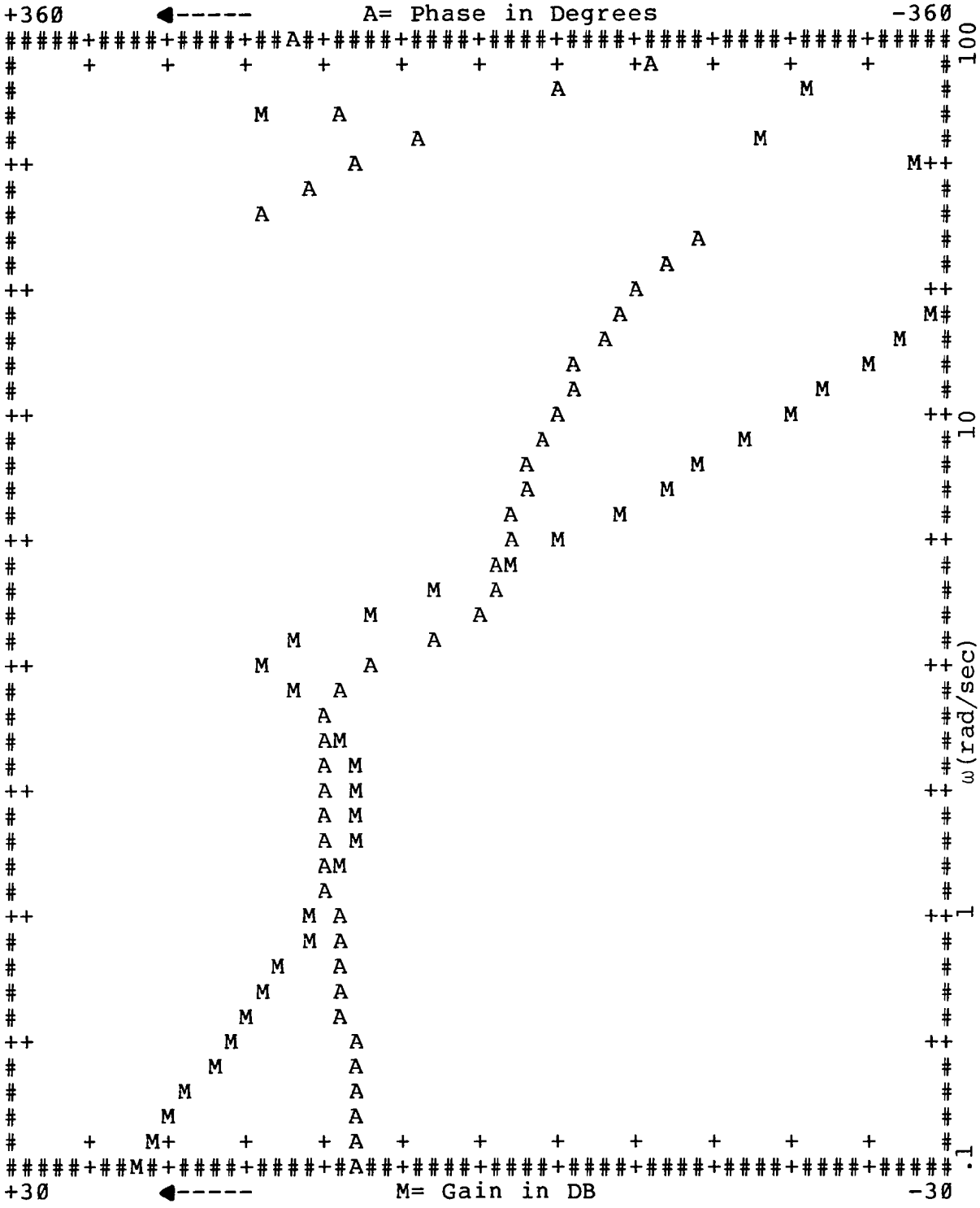

Figure 6. - Pitch/Elevator (θ/δ_e) Bode Responses.
b) θ/δ_e, Euler, T=.1.

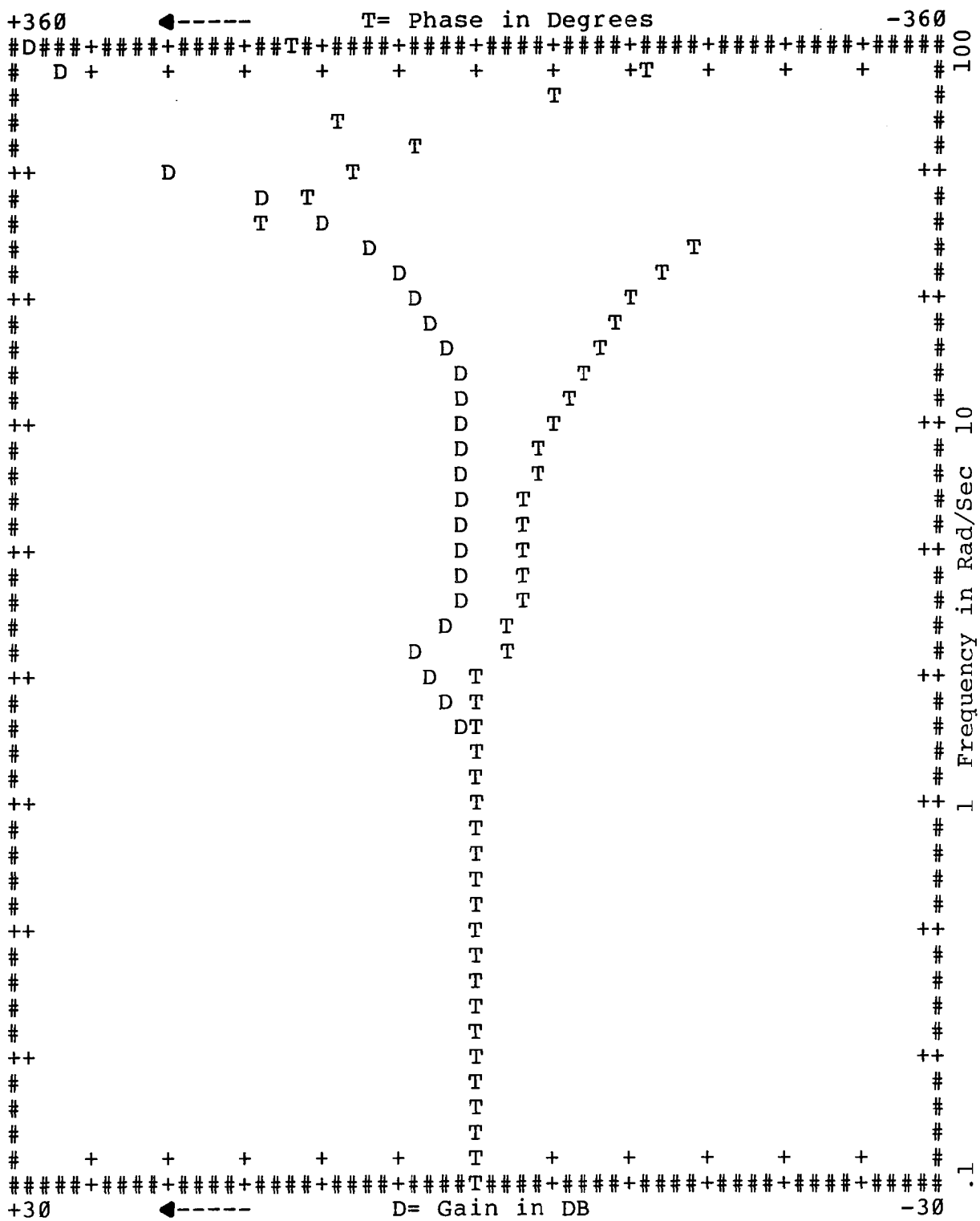

Figure 6. - Pitch/Elevator (θ/δ_e) Bode Responses.
c) θ/δ_e, Euler Distortion, T=.1.

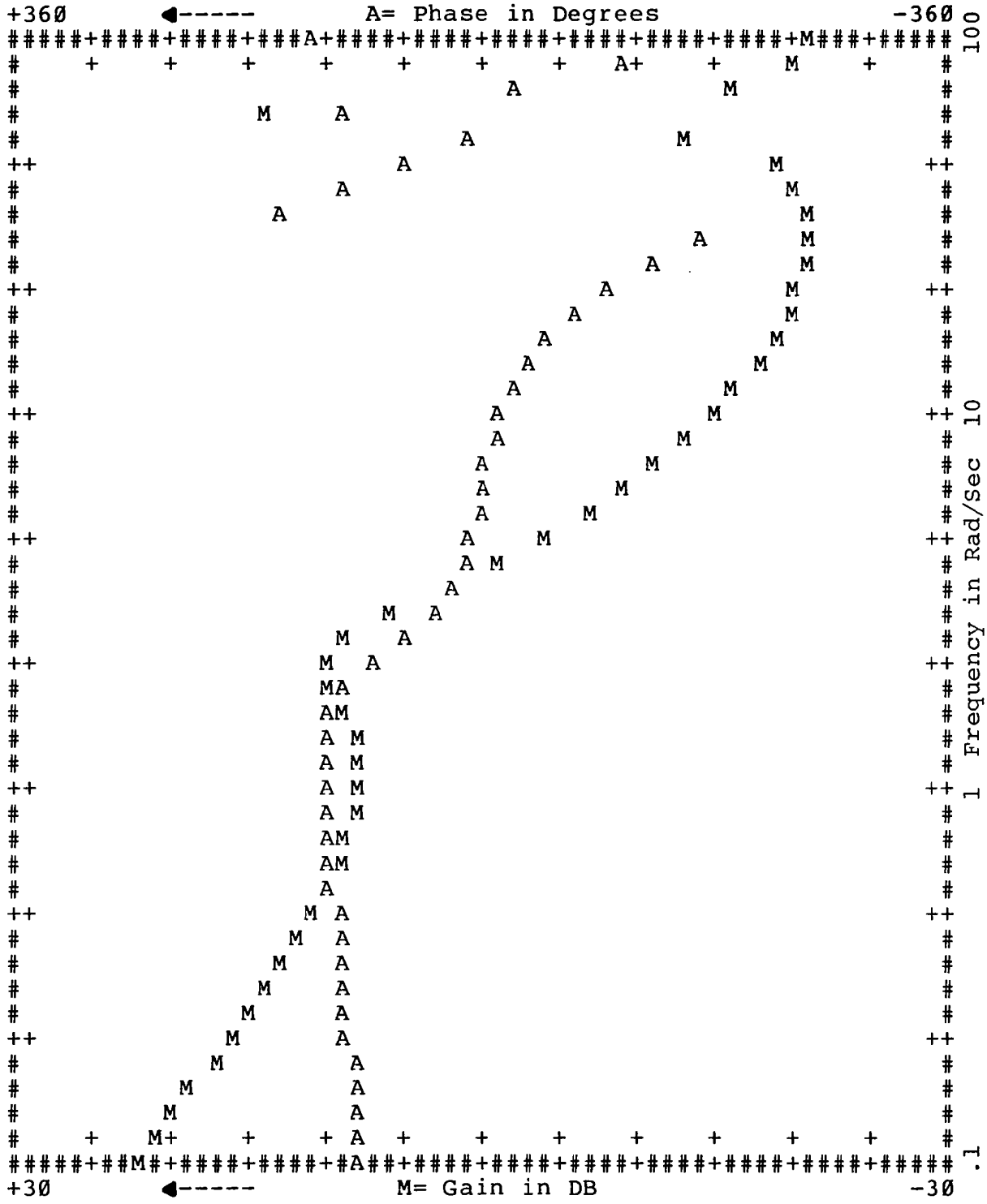

Figure 6.- Pitch/Elevator (θ/δ_e) Bode Responses.
d) θ/δ_e, A-B, T=.1.

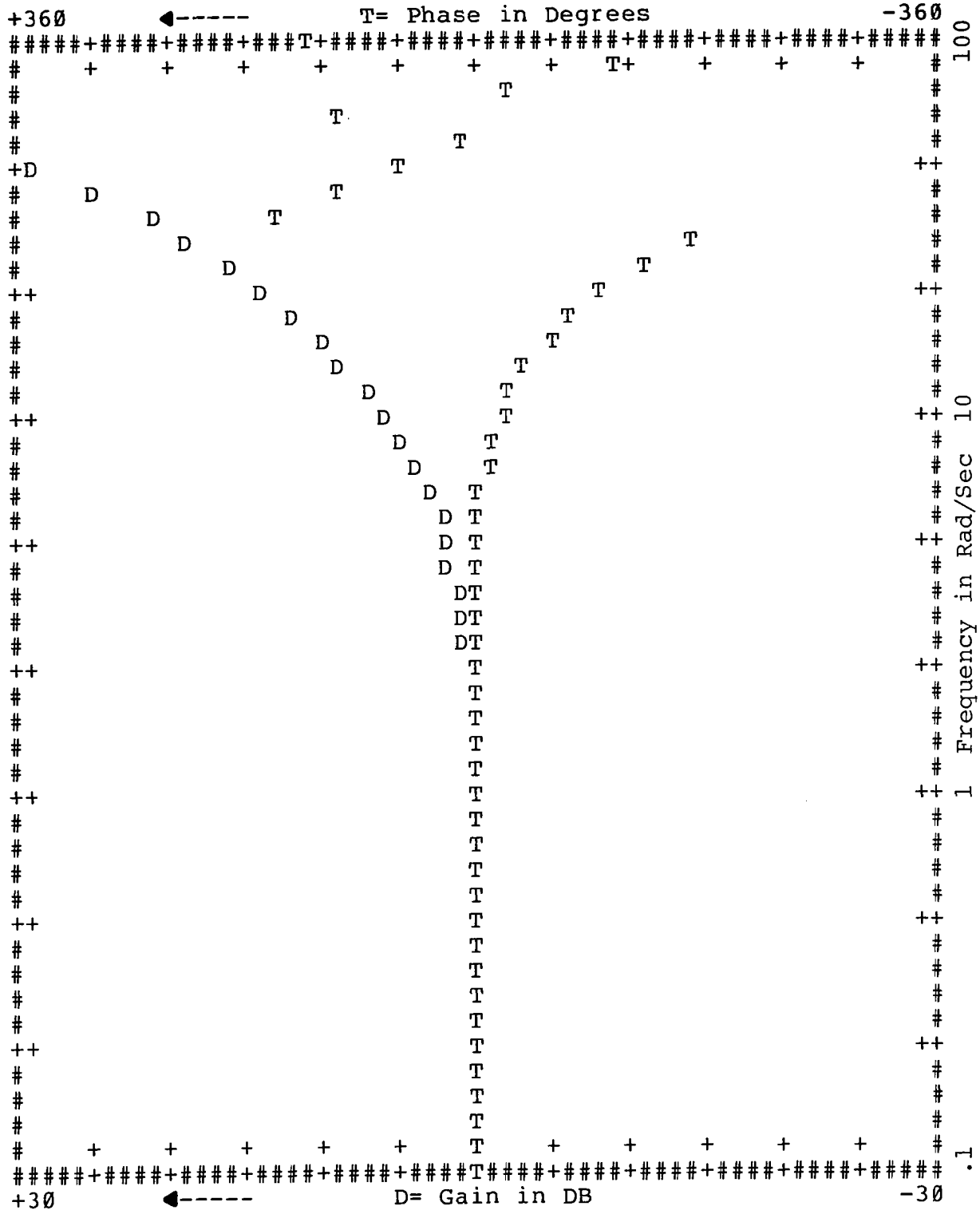

Figure 6.- Pitch/Elevator (θ/δ_e) Bode Responses.
e) θ/δ_e, A-B Distortion, T=.1

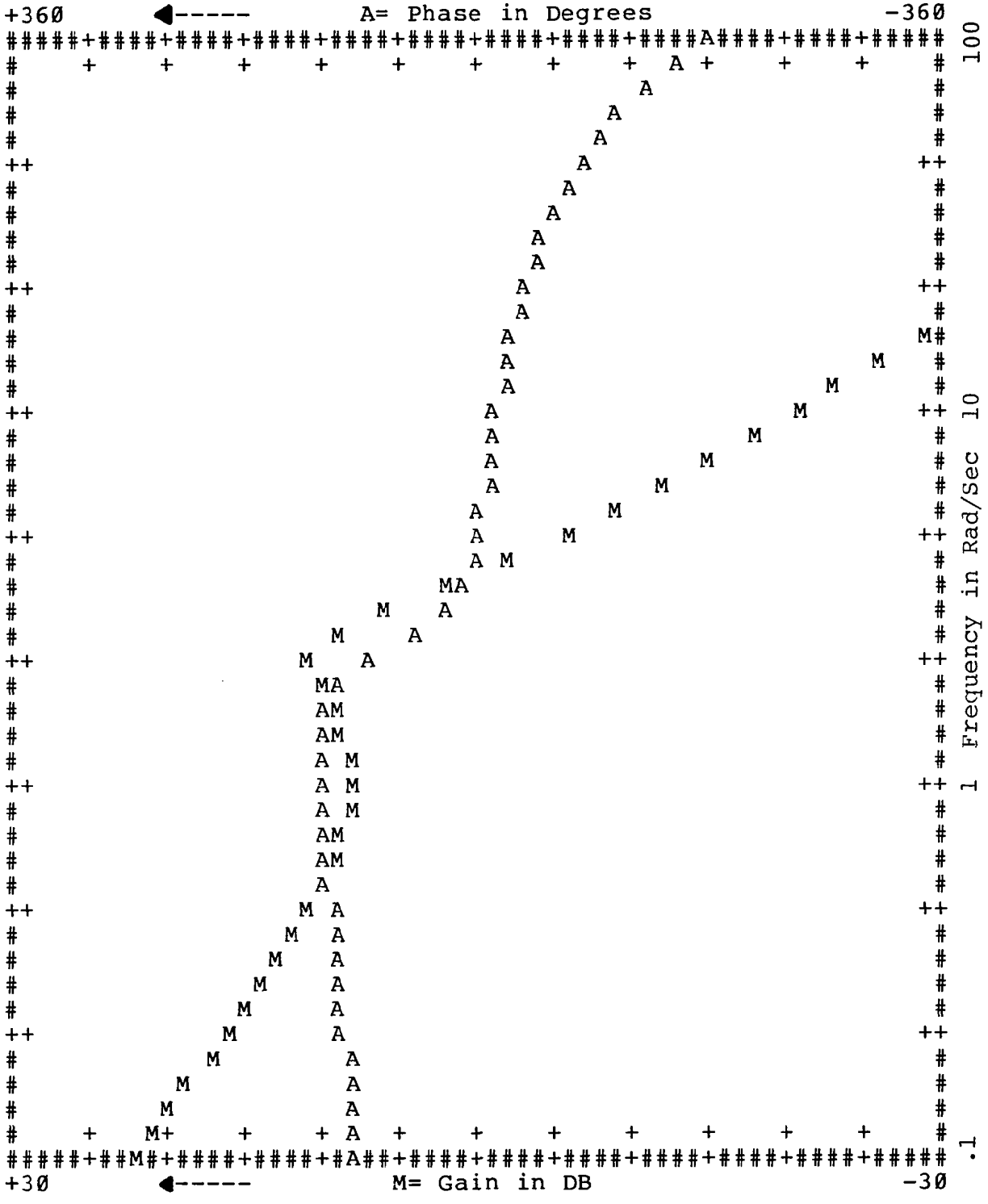

Figure 6.- Pitch/Elevator (θ/δ_e) Bode Responses.
f) θ/δ_e, Euler, T=.03125.

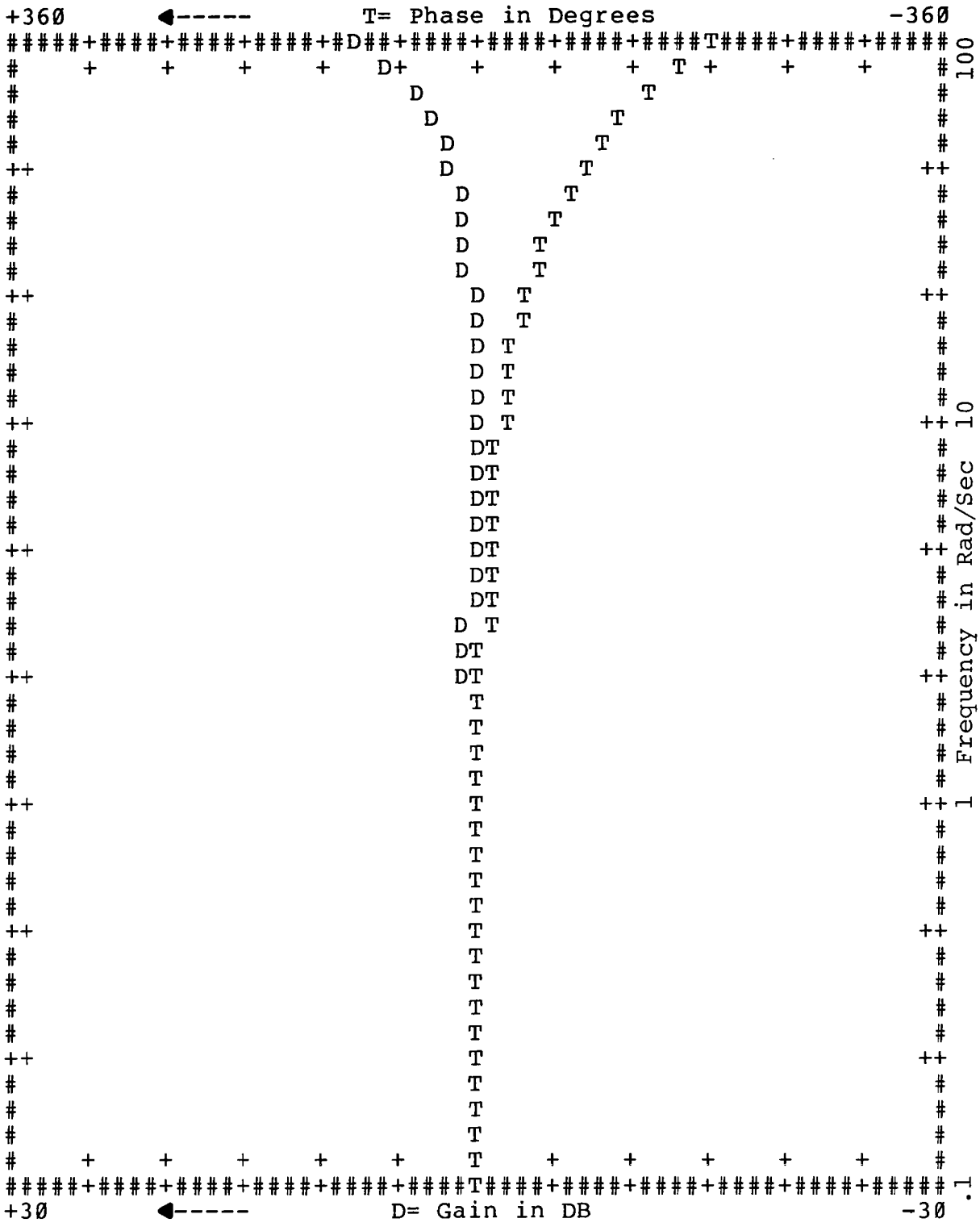

Figure 6.- Pitch/Elevator (θ/δ_e) Bode Responses.
g) θ/δ_e, Euler distortion, T=.03125.

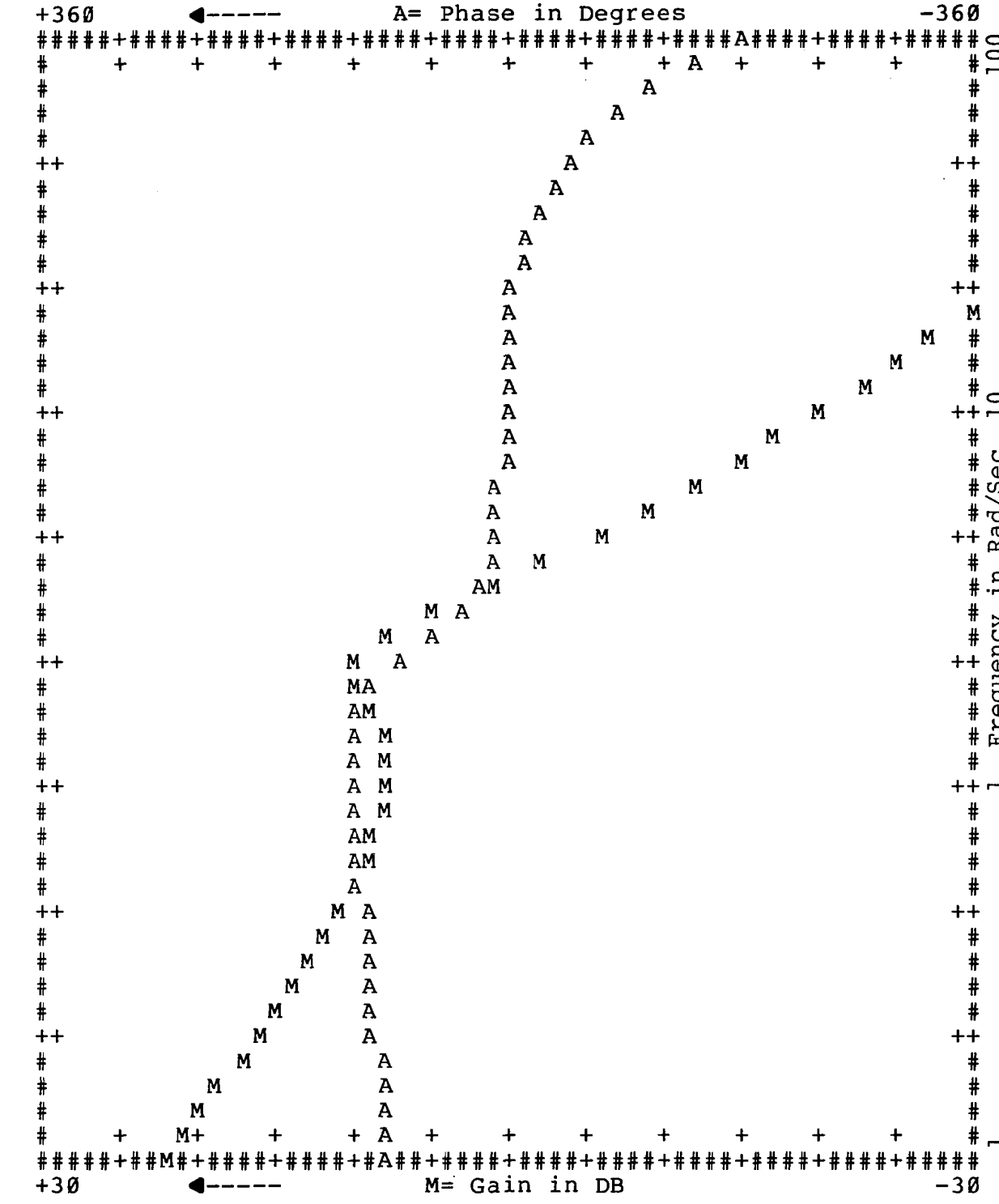

Figure 6.- Pitch/Elevator (θ/δ_e) Bode Responses.
h) θ/δ_e, A-B, T=.03125.

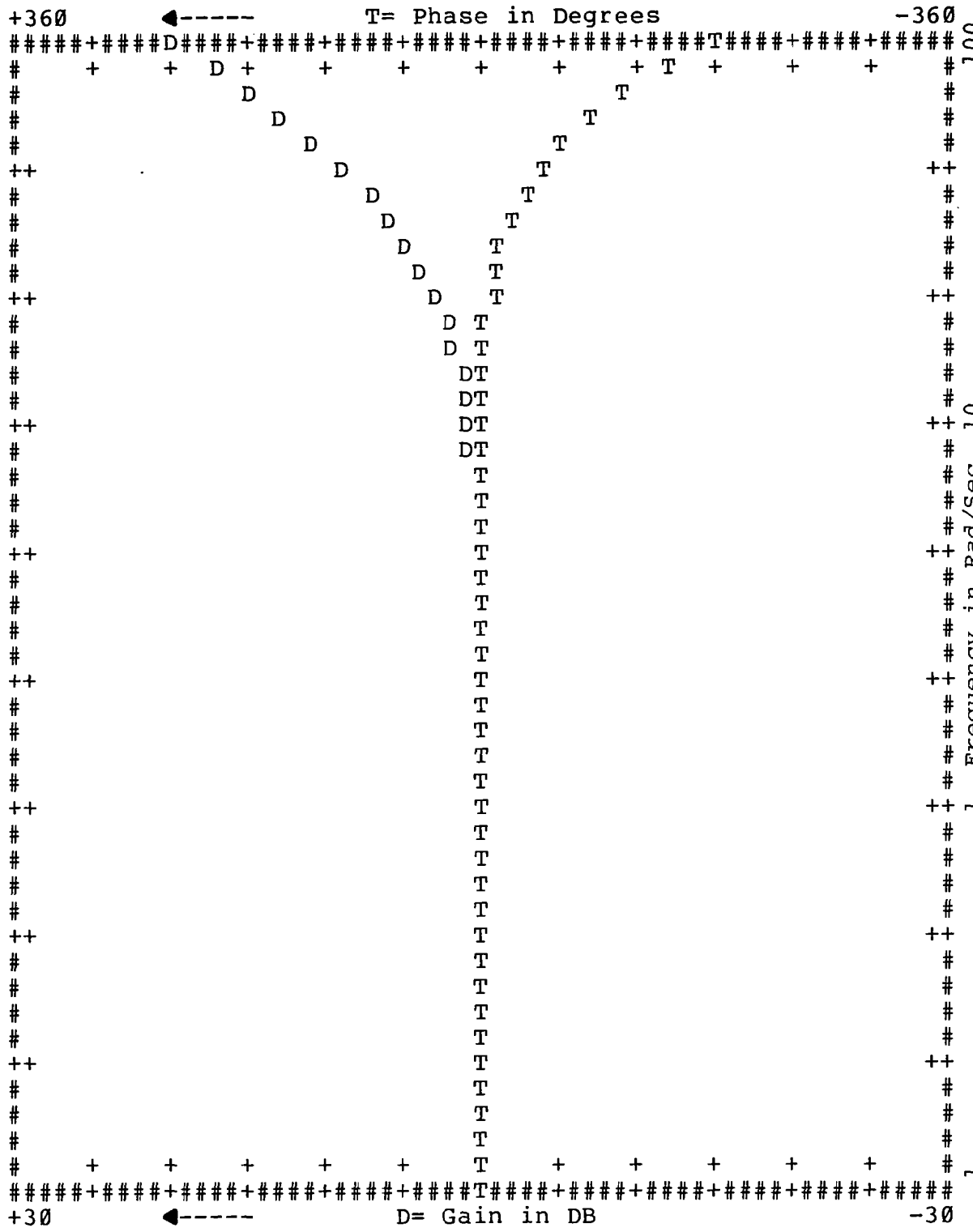

Figure 6. - Pitch/Elevator (θ/δ_e) Bode Responses.
i) θ/δ_e, A-B Distortion, T=.03125.

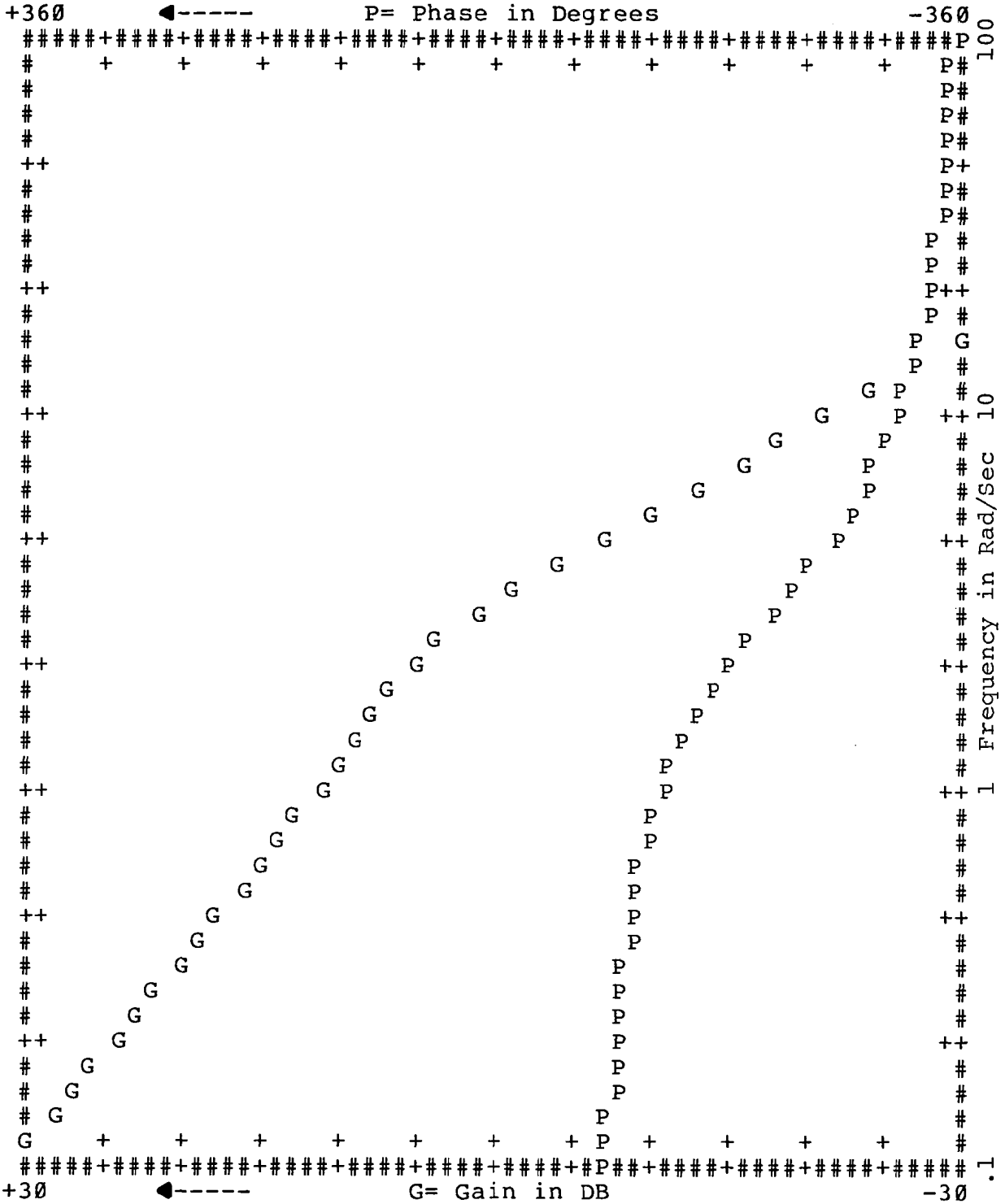

Figure 7. - Roll/Aileron Bode Responses, Lateral CAS-ON Dynamics.
a) Continuous.

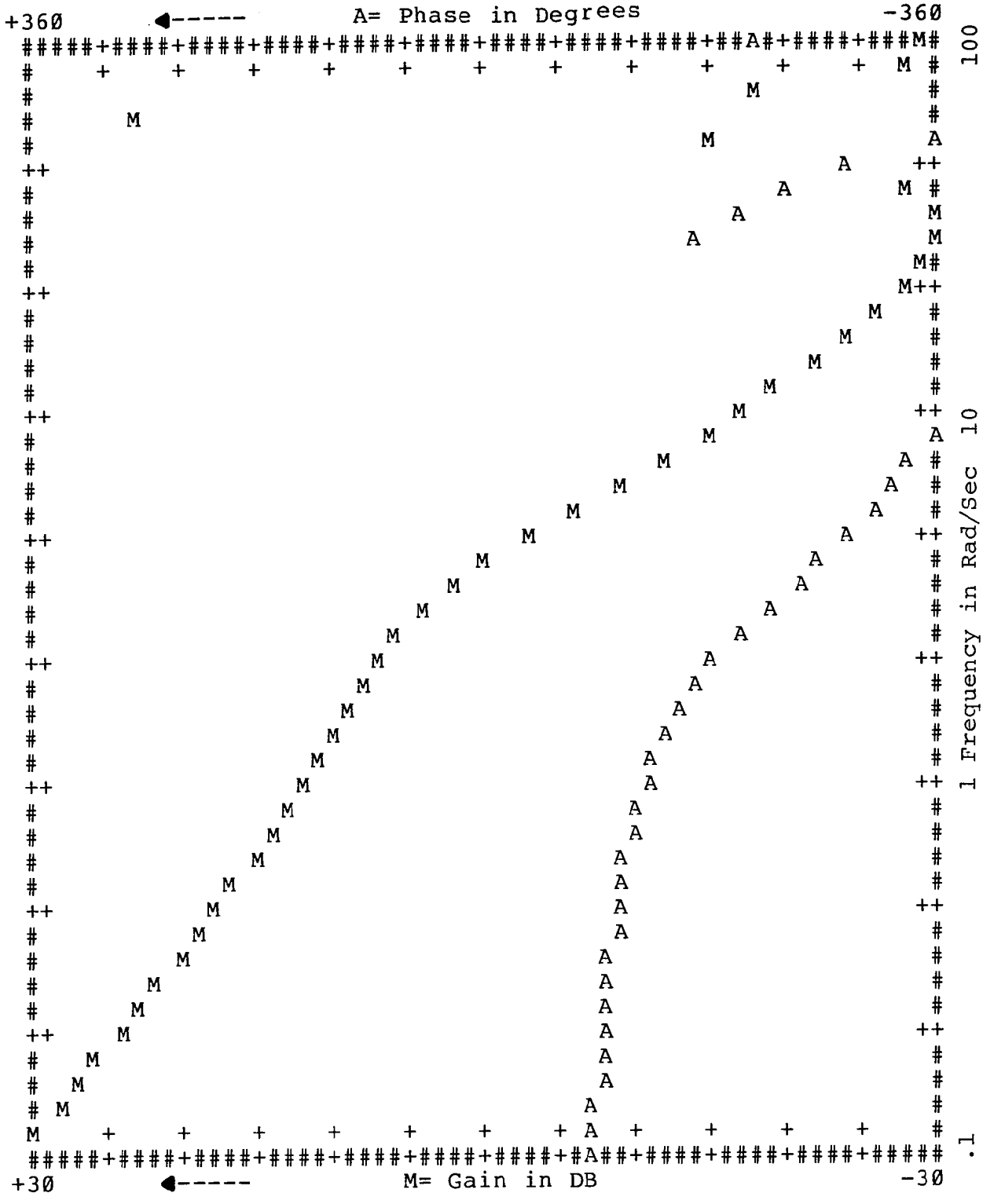

Figure 7. - Roll/Aileron Bode Responses, Lateral CAS-ON Dynamics.
b) ϕ/δ_A, Euler, T=.1.

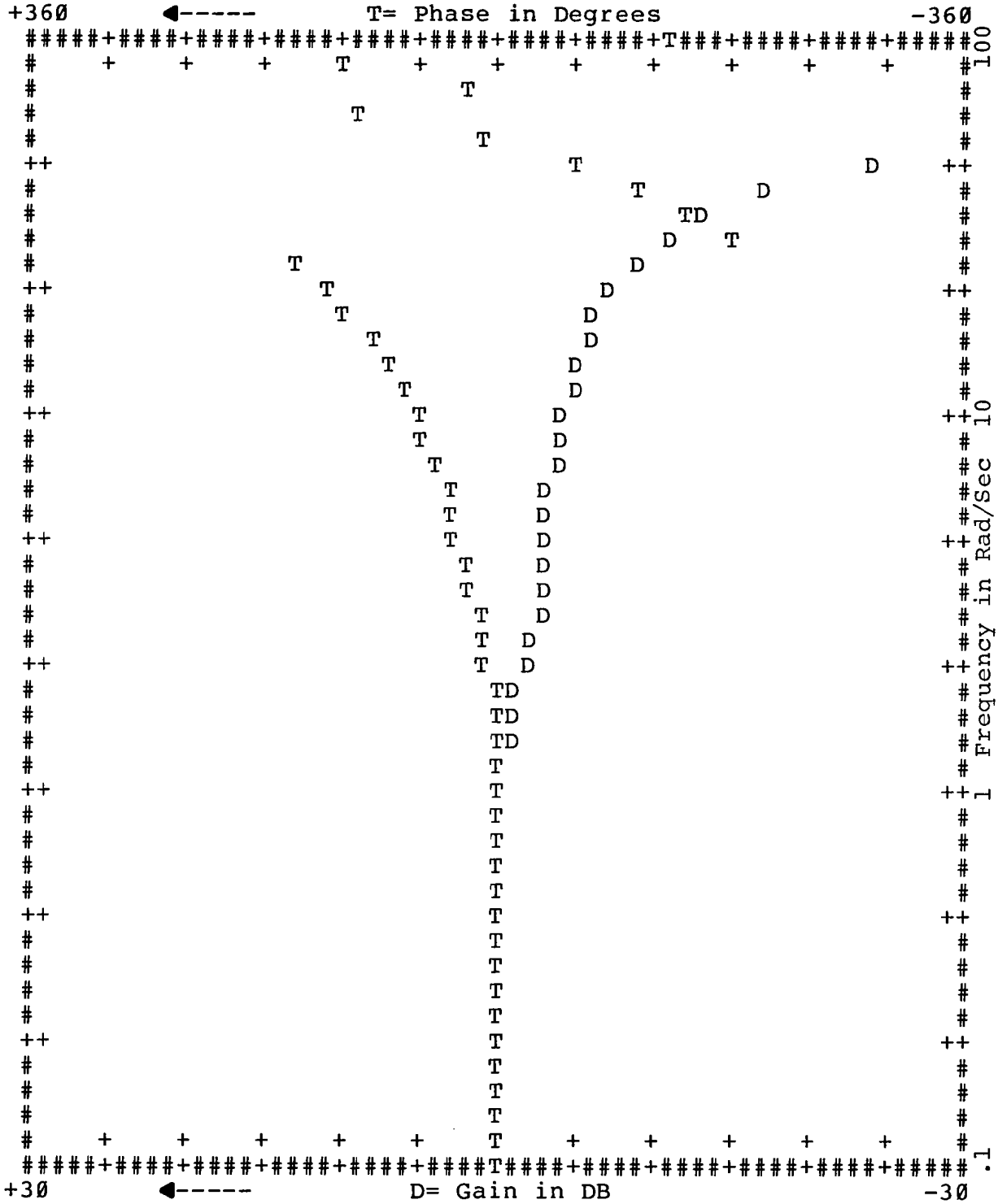

Figure 7. - Roll/Aileron Bode Responses, Lateral CAS-ON Dynamics.
c) ϕ/δ_A, Euler Distortion, T=.1.

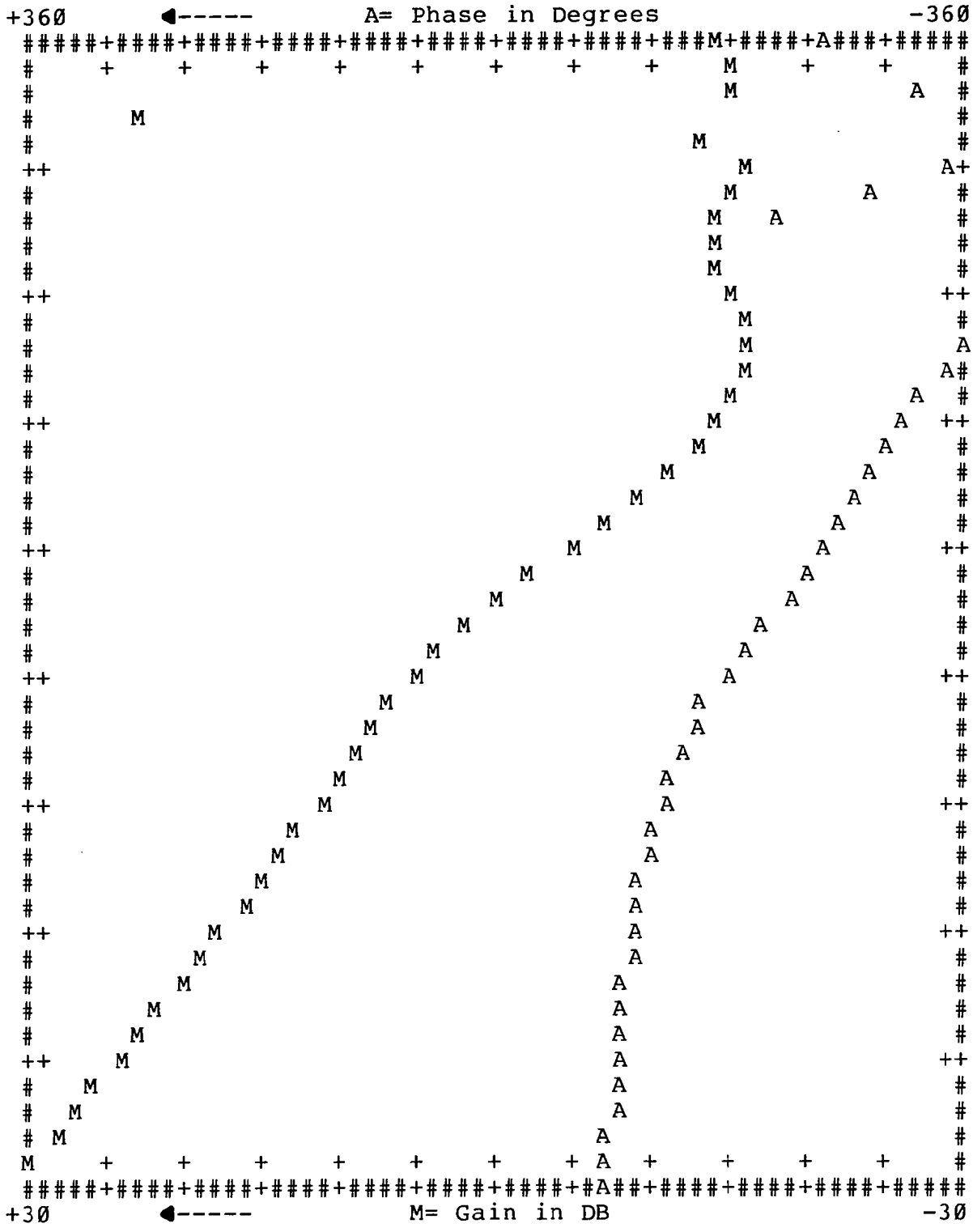

Figure 7.- Roll/Aileron Bode Responses, Lateral CAS-ON Dynamics.
d) ϕ/δ_A, A-B, T=.1.

Figure 7. - Roll/Aileron Bode Responses, Lateral CAS-ON Dynamics.
e) ϕ/δ_A, A-B Distortion, T=.1.

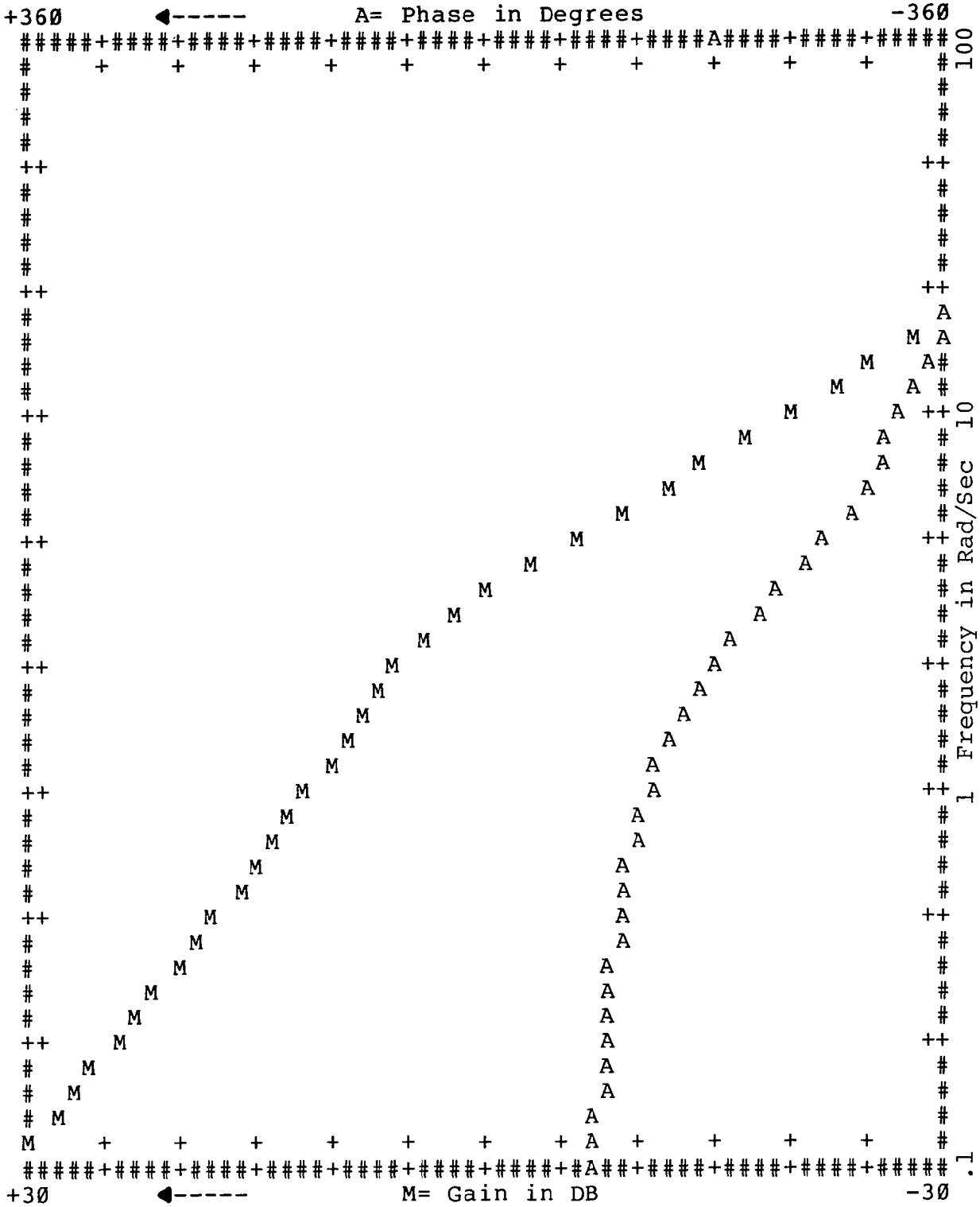

Figure 7. - Roll/Aileron Bode Responses. Lateral CAS-ON Dynamics.
f) ϕ/δ_A, Euler, T=.03125.

Figure 7.- Roll/Aileron Bode Responses, Lateral CAS-ON Dynamics.
g) ϕ/δ_A, Euler Distortion, T=.03125.

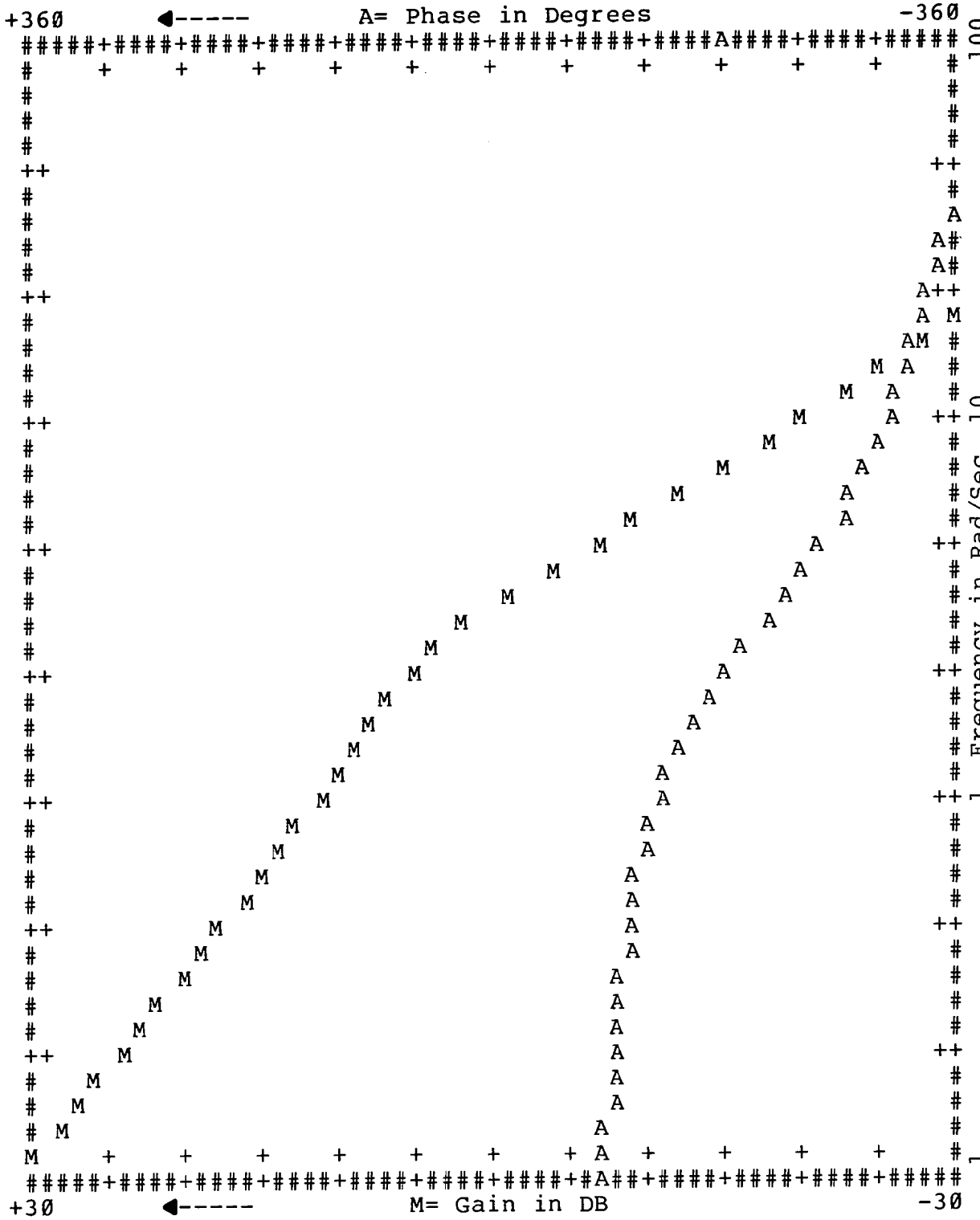

Figure 7. - Roll/Aileron Bode Responses, Lateral CAS-ON Dynamics.
h) ϕ/δ_A, A-B, T=.03125.

Figure 7. - Roll/Aileron Bode Responses, Lateral CAS-ON Dynamics.
i) ϕ/δ_A, A-B Distortion, T=.03125.

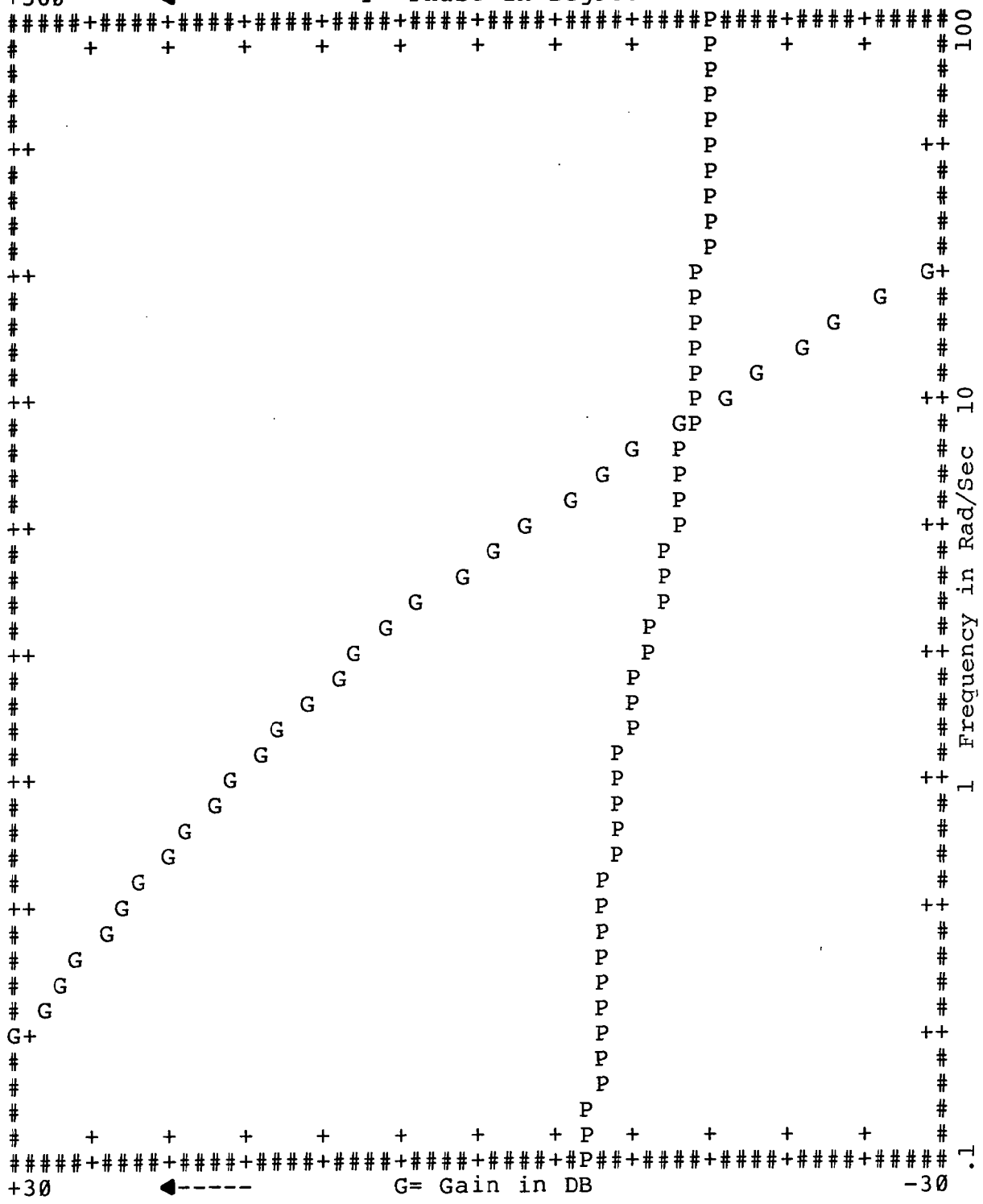

Figure 8. - Roll/Aileron Bode Responses, Coordinated Dynamics.
a) ϕ/δ_A continuous.

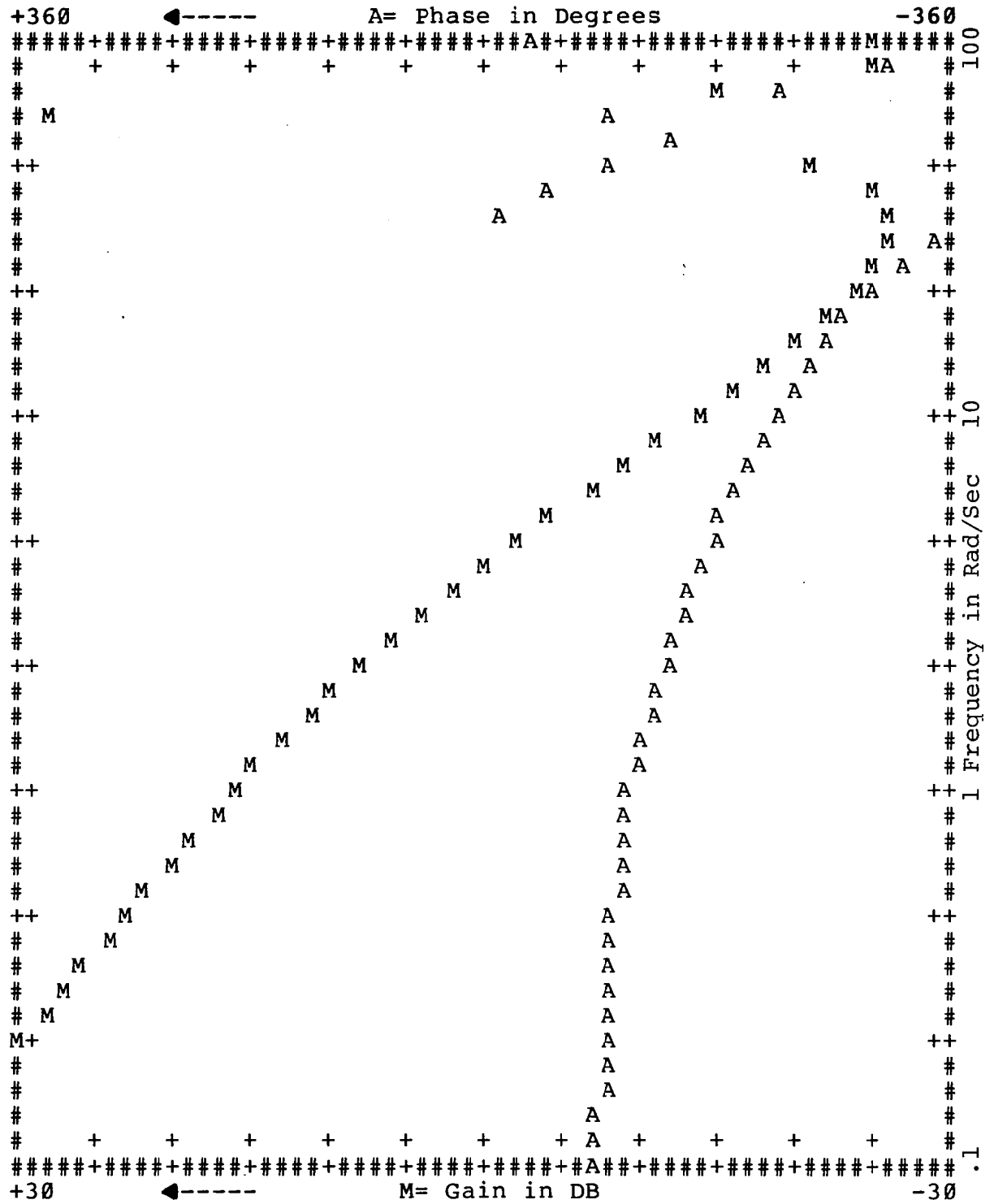

Figure 8. - Roll/Aileron Bode Responses, Coordinated Dynamics.
b) ϕ/δ_A, Euler, T=.1.

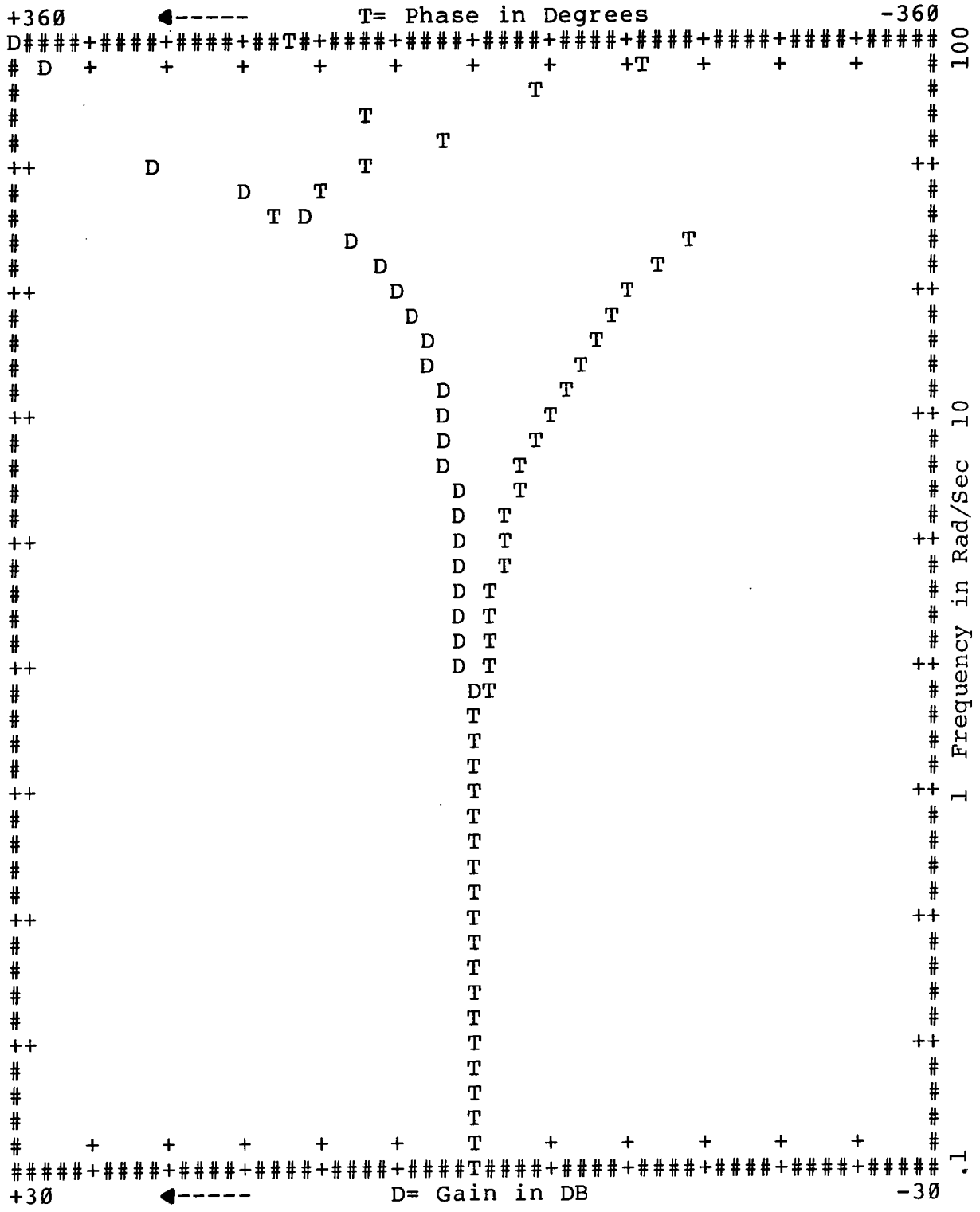

Figure 8.- Roll/Aileron Bode Responses, Coordinated Dynamics.
c) ϕ/δ_A Distortion, Euler, T=.1.

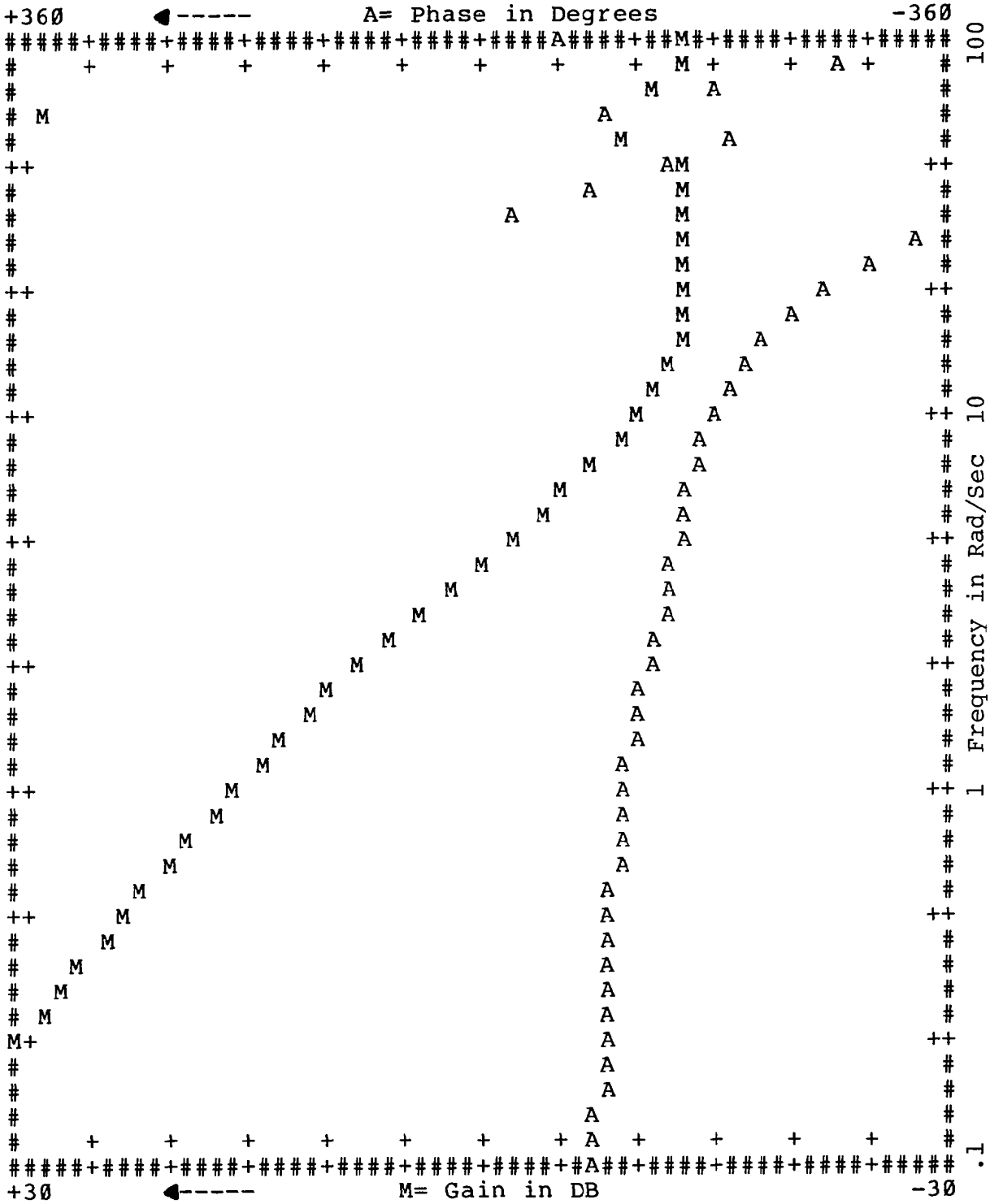

Figure 8. - Roll/Aileron Bode Responses, Coordinated Dynamics.
d) ϕ/δ_A, A-B, T=.1.

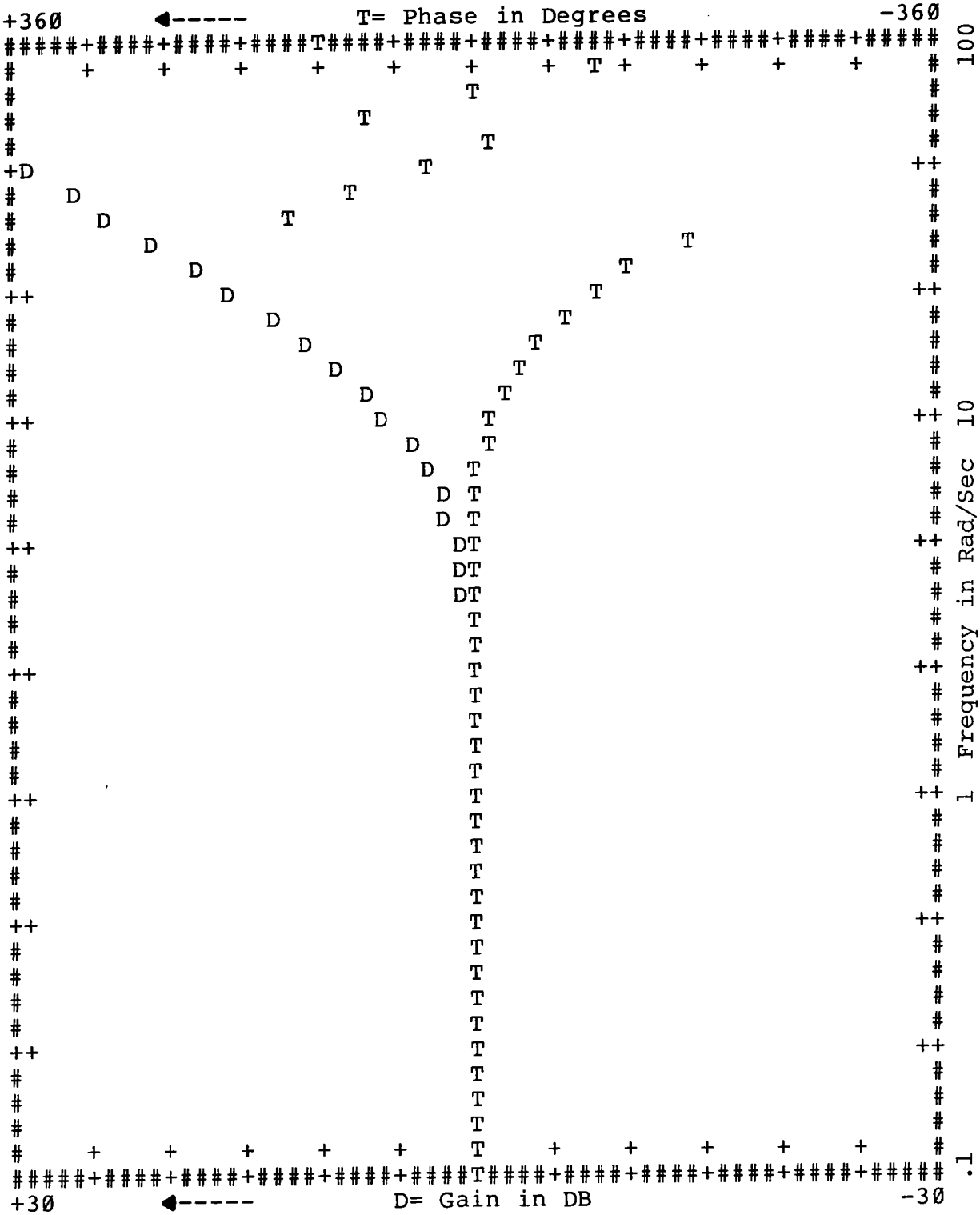

Figure 8.- Roll/Aileron Bode Responses, Coordinated Dynamics.
e) ϕ/δ_A, A-B Distortion, T=.1.

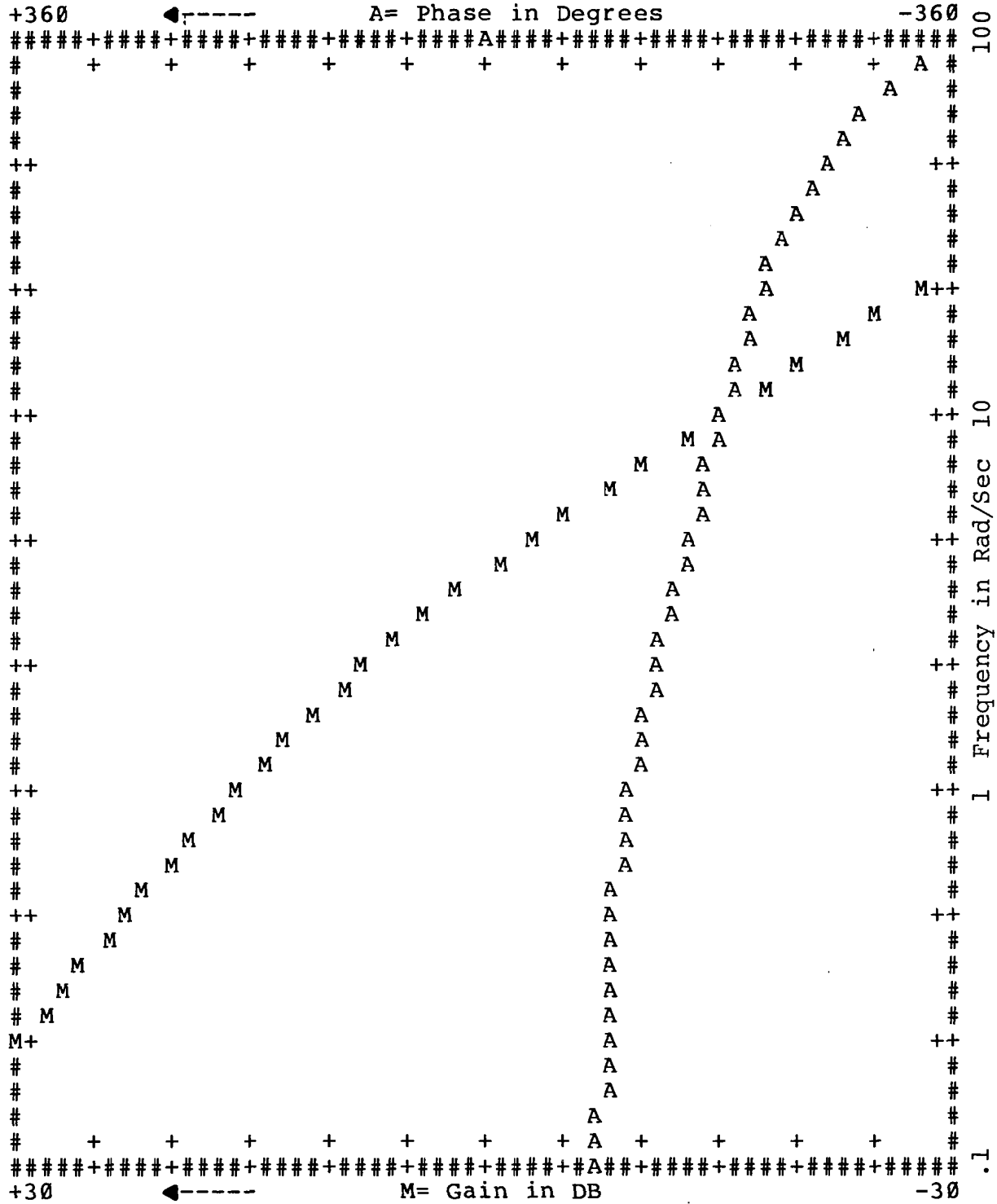

Figure 8. - Roll/Aileron Bode Responses, Coordinated Dynamics.
f) ϕ/δ_A, Euler, T=.03125.

Figure 8. - Roll/Aileron Bode Responses, Coordinated Dynamics.
g) ϕ/δ_A, Euler Distortion, T=.03125.

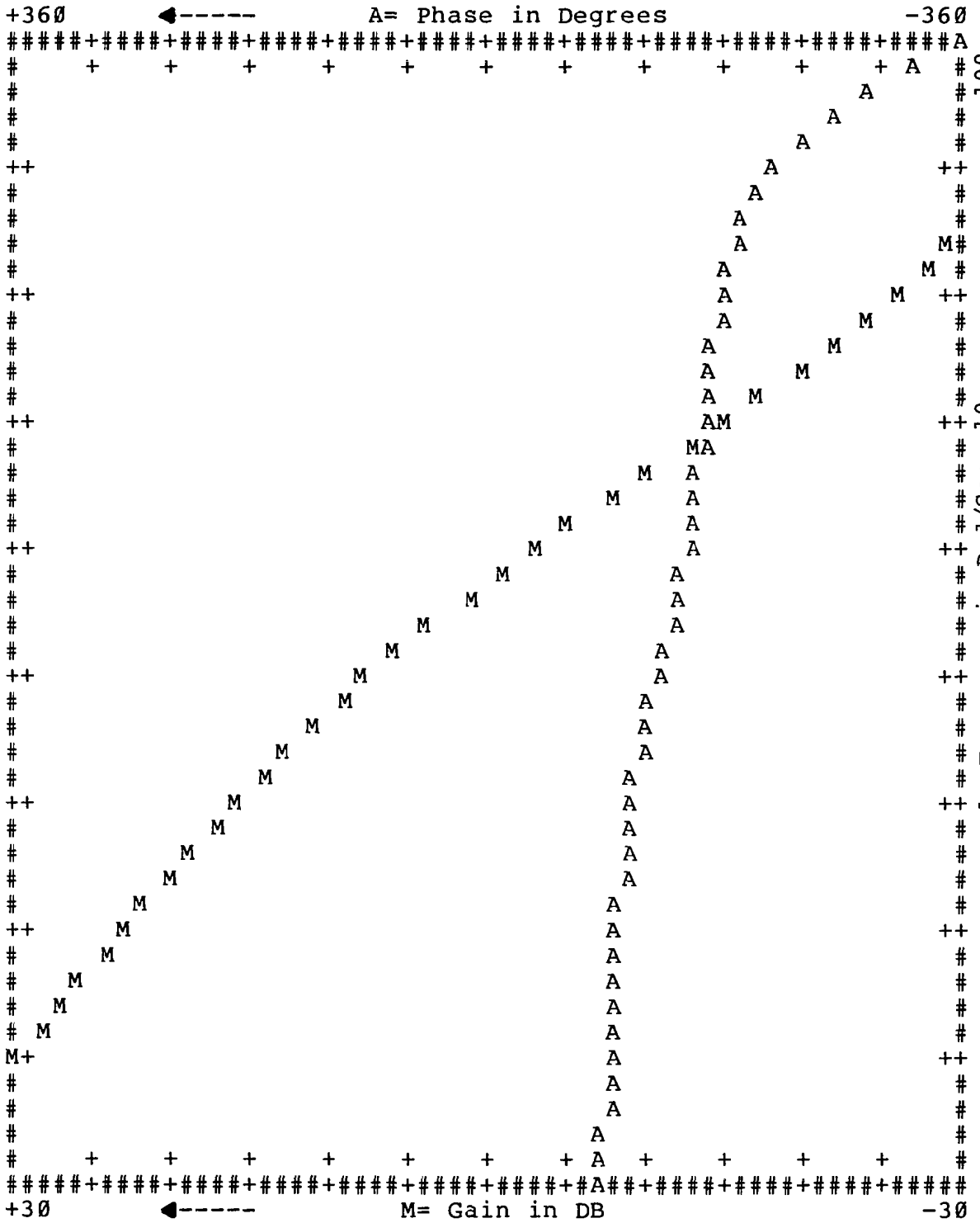

Figure 8. - Roll/Aileron Bode Responses, Coordinated Dynamics.
h) ϕ/δ_A, A-B, T=.03125.

Figure 8. – Roll/Aileron Bode Responses, Coordinated Dynamics.
i) ϕ/δ_A, A-B Distortion, T=.03125.

Figure 9.- Tracking Error/Aileron Bode Responses, Coordinated Dynamics.
a) $R\varepsilon_T/\delta_A$ Continuous.

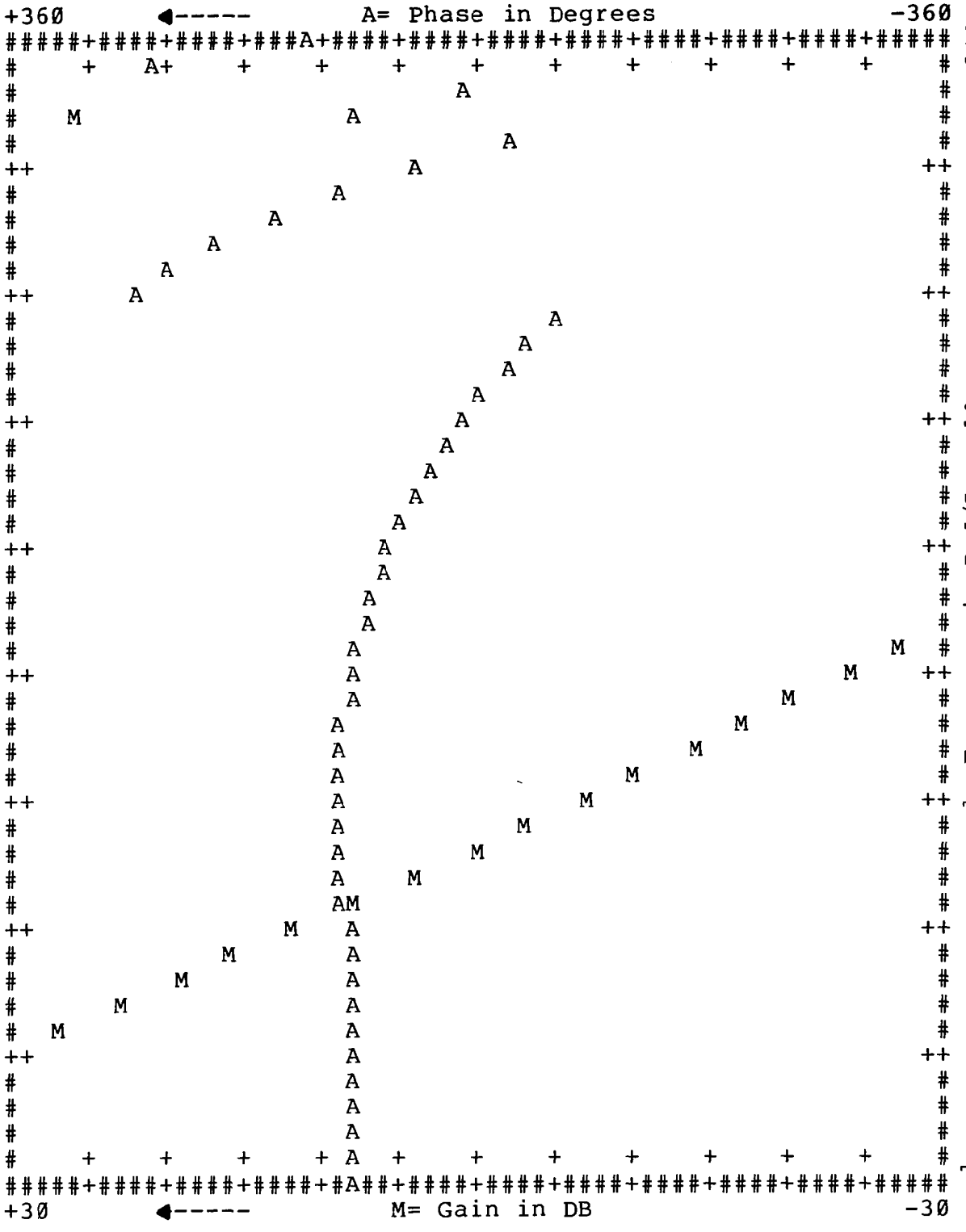

Figure 9.- Tracking Error/Aileron Bode Responses, Coordinated Dynamics.
b) $R\varepsilon_T/\delta_A$, Euler, T=.1.

Figure 9.- Tracking Error/Aileron Bode Responses, Coordinated Dynamics.
c) $R\varepsilon_T/\delta_A$, Euler Distortion, T=.1.

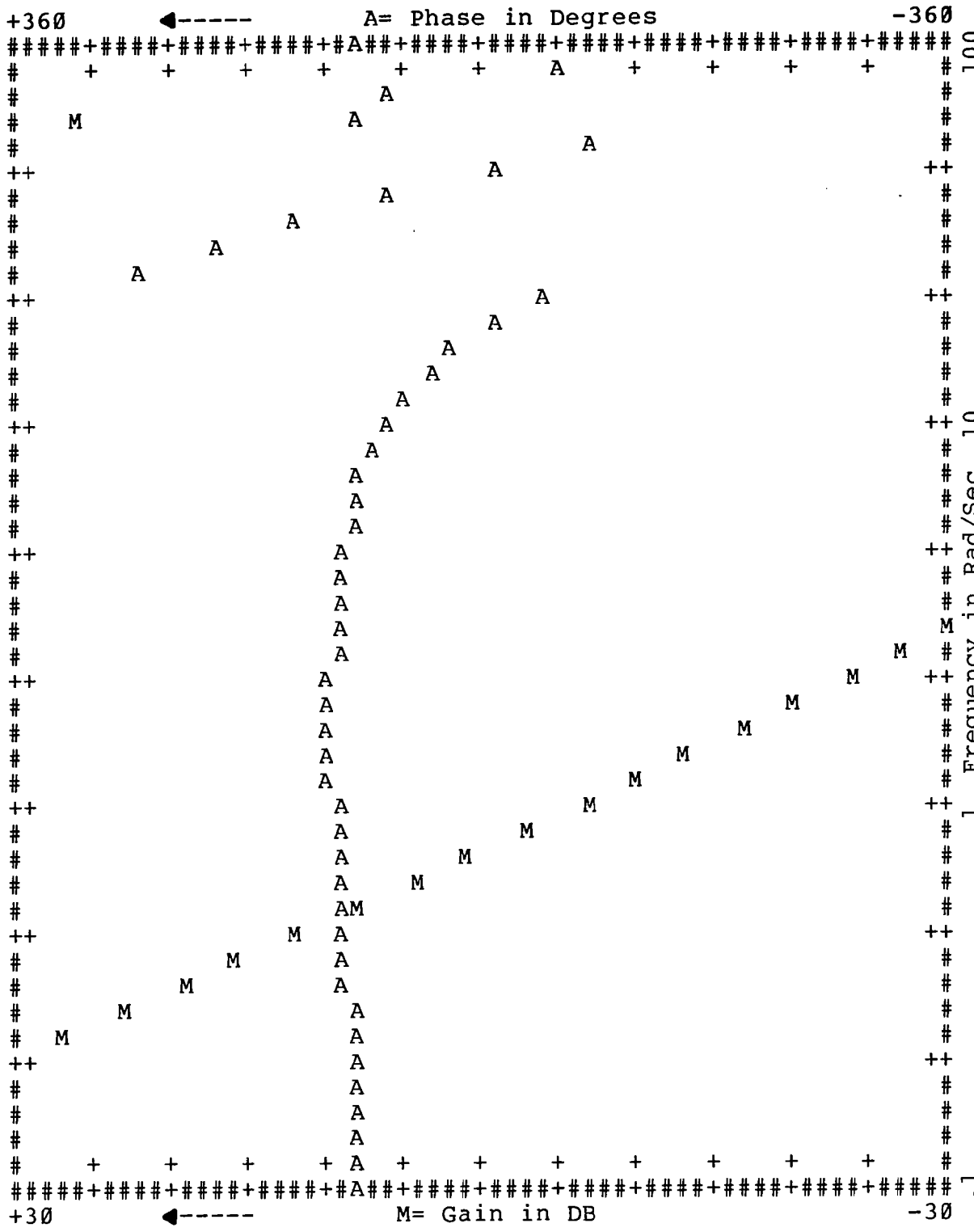

Figure 9. - Tracking Error/Aileron Bode Responses, Coordinated Dynamics.
c) $R\varepsilon_T/\delta_A$, A-B, T=.1.

Figure 9.- Tracking Error/Aileron Bode Responses, Coordinated Dynamics.
d) $R\varepsilon_T/\delta_A$, A-B Distortion, T=.1.

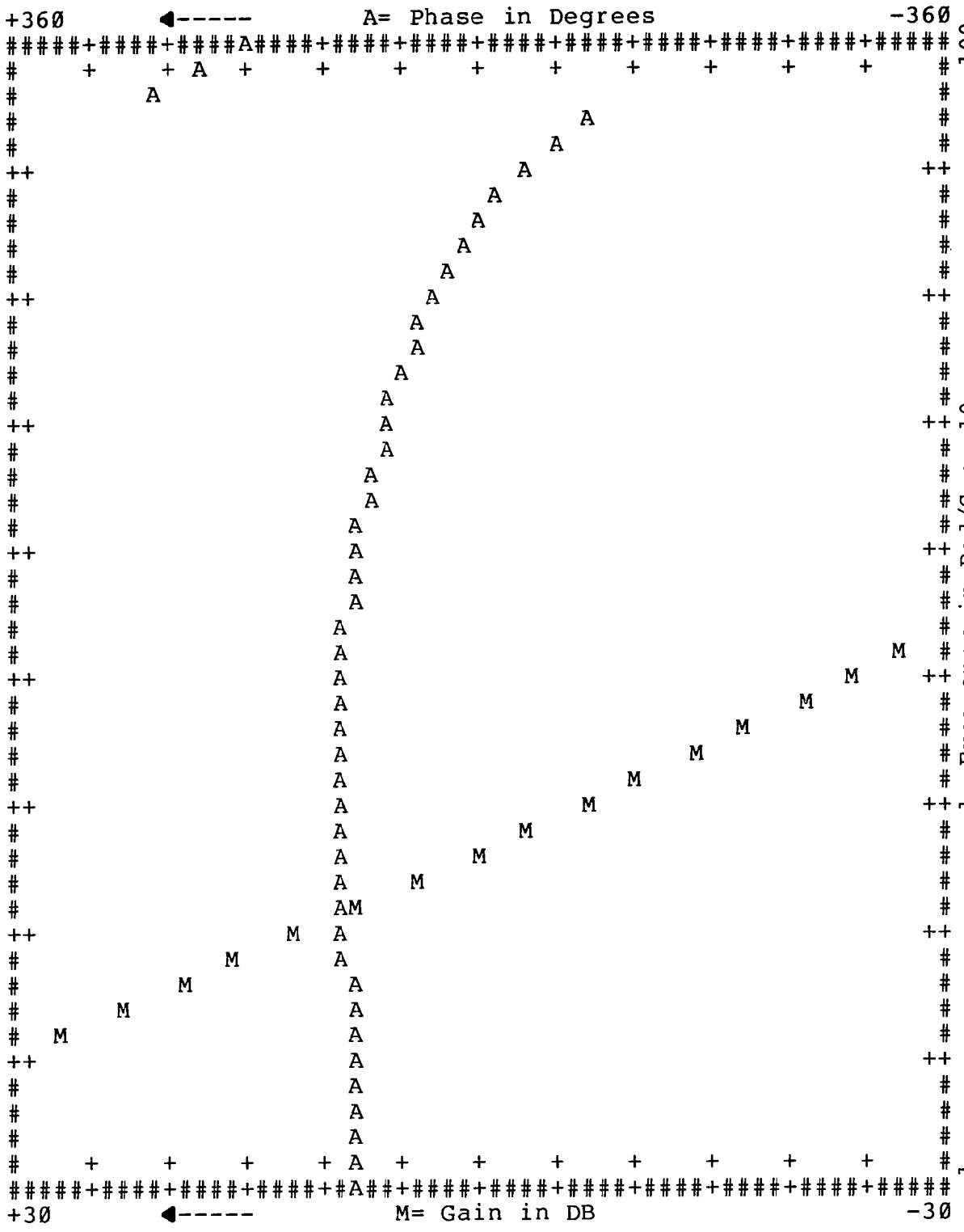

Figure 9.- Tracking Error/Aileron Bode Responses, Coordinated Dynamics.
e) $R\varepsilon_T/\delta_A$, Euler, T=.03125.

Figure 9.- Tracking Error/Aileron Bode Responses, Coordinated Dynamics.
f) $R\varepsilon_T/\delta_A$, Euler Distortion, T=.03125.

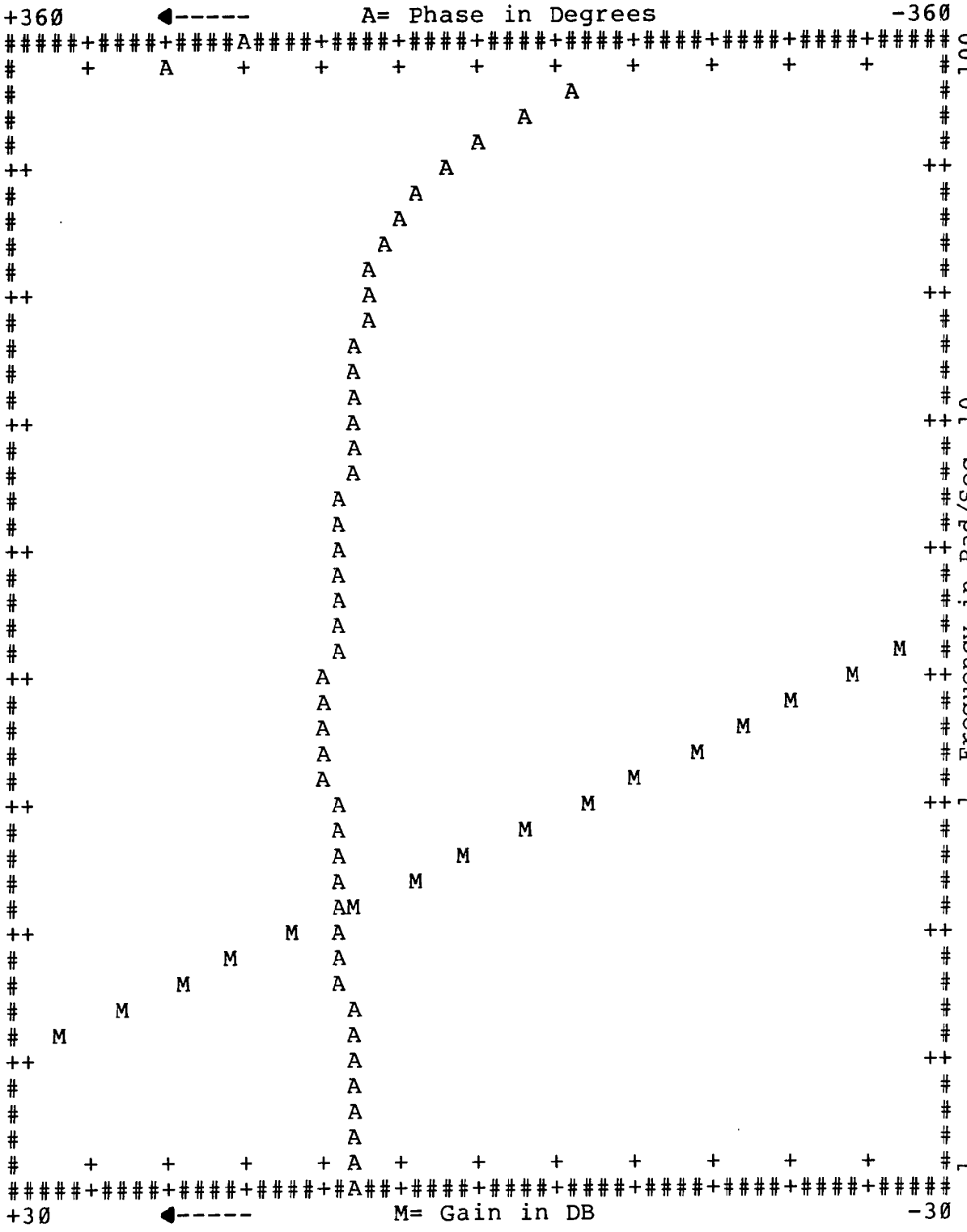

Figure 9. - Tracking Error/Aileron Bode Responses, Coordinated Dynamics.
g) $R\varepsilon_T/\delta_A$, A-B, T=.03125.

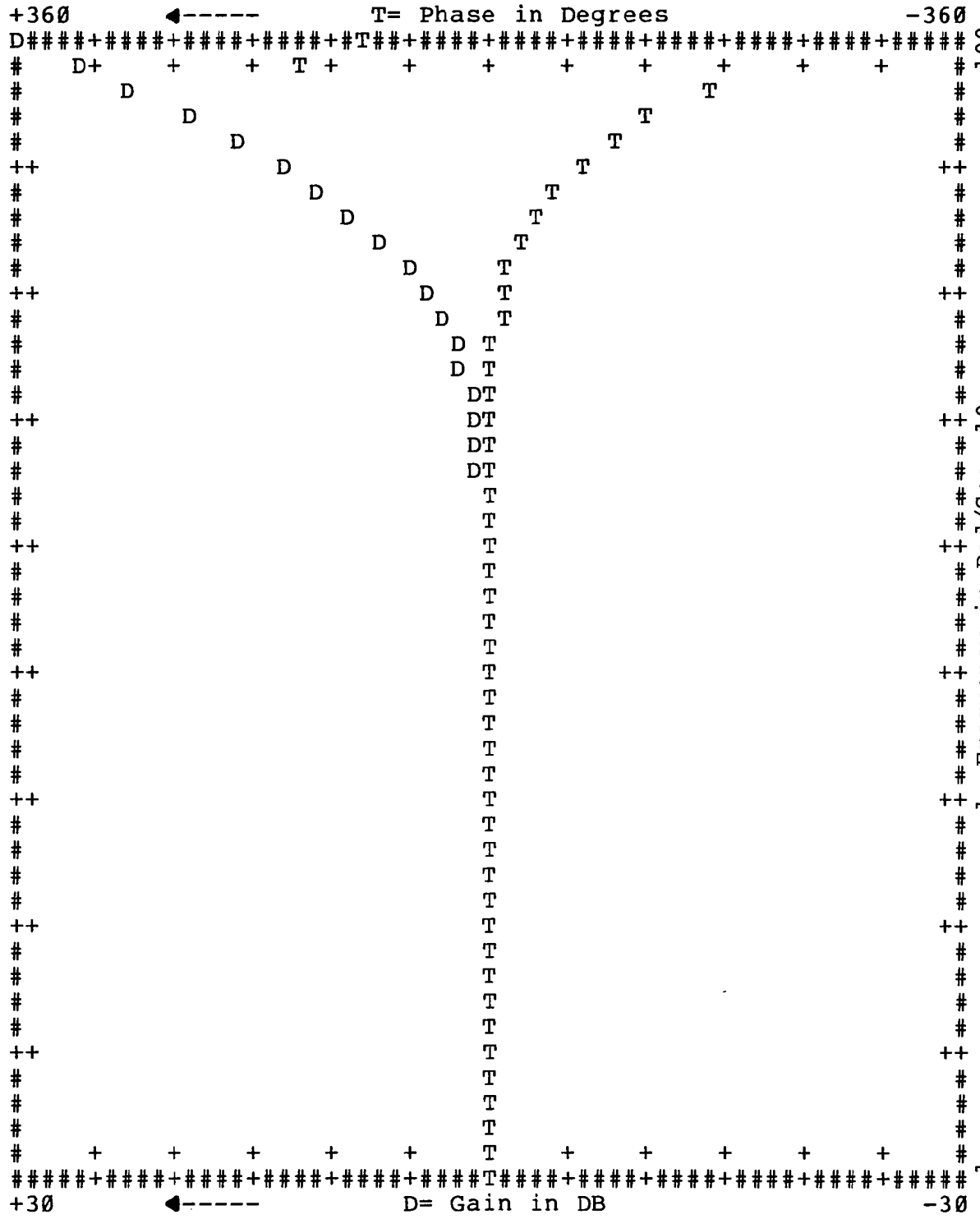

Figure 9.- Tracking Error/Aileron Bode Responses, Coordinated Dynamics.
h) $R\varepsilon_T/\delta_A$, A-B Distortion, T=.03125.

The following observations may be made from these responses and those in Appendix B.

(i) For T = .1, both integration schemes evidence the expected periodic behavior with the responses repeating at intervals of $\frac{2\pi}{.1}$ = 62.8 rad/sec. The lower sampling periods repeat beyond the range of frequencies that are plotted. This sampling effect is outside the frequency range of interest for closed-loop manual control (say ω < 10-12 rad/sec for the tasks considered here).

(ii) As expected, both integration schemes show decreases in distortion with decreases in sample period.

(iii) In the frequency range of interest, the amplitude distortion for Euler integration is greatest in the region of the oscillatory characteristic mode as a result of the reduction in damping discussed in the previous section. On the other hand, A-B integration tends to show significant amplitude distortion at frequencies greater than the characteristic frequencies, at least for T = .1. This distortion introduced by A-B integration will be discussed later.

(iv) The phase distortion for both schemes corresponds to increased phase lag at almost all frequencies. For Euler integration, the added phase lag is undoubtedly the dominant "error" introduced by discrete integration. For A-B integration the additional phase lag is almost negligible in the range of interest, but there is substantial lag at higher frequencies.

(v) For longitudinal control, both outputs that drive the visual servos, pitch angle and LOS vertical error, have the same additional phase lag as a result of the discrete integration. This is true for both CAS-OFF and CAS-ON modes. For Euler integration of the CAS-OFF configuration the additional phase lag corresponds to a transport lag, or time delay, of $\sim T$ seconds; for the CAS-ON configuration the additional delay is $\sim\frac{3T}{2}$ seconds.

(vi) For lateral control the two outputs driving the visual servos, bank angle and transverse LOS error, are also delayed by the same amount whether the CAS-OFF or CAS-ON dynamics are considered. However, unlike the longitudinal control case, the effective delays for Euler integration are the same for both CAS-ON and CAS-OFF, viz., $\sim T$ seconds. For Euler integration of the "coordinated" dynamics, the ϕ/δ transfer has an added delay of about T seconds, but the additional delay for the $R\varepsilon_T/\delta$ transfer is about $\frac{3T}{2}$ seconds.

2.3.3 Continuous Approximations of Discrete Bode Responses

We are now in a position to complete the continuous approximation to the open-loop simulator dynamics by deriving suitable approximations to D*(s) for the various conditions of interest. Because of the restrictions imposed by the OCM, we restrict the possible approximations to the following form:

$$\frac{Y_i}{u_j} = D^*_{ij}(s) \approx \tilde{D}_{ij}(s)e^{-\tau_c s} \qquad (21)$$

where $\tilde{D}(s)$ is a ratio of finite polynomials in s with numerator degree less than or equal to the degree of the denominator. Note that the same "computation" delay, τ_c is associated with each transfer function. This was seen to be a good approximation for all sets of dynamics considered here but the coordinated dynamics. The discrepancy in delays for coordinated dynamics will be accounted for by adding a first-order, rational Pade approximation to the $R\varepsilon_T/\delta$ transfer for this case. The values for τ_c for the various dynamics and the two integration schemes are given in Table 3.*

The general problem of determining a $\tilde{D}(s)$ that best approximates $D^*(s)e^{\tau_c s}$ over some frequency range (say, $0 < \omega \lesssim 12$ rad/sec) is a variant of the identification problems examined in control theory (see, e.g., [17]). A variety of sophisticated algorithms have been developed to attack the problem but no general solution exists. The application of such algorithms to the determination of $\tilde{D}$ was beyond the scope of this effort so simpler, more intuitive, schemes were employed.

The simplest approach to selecting $\tilde{D}$ is to use (18) and let

$$\tilde{D}_{ij}(s) = \Phi_{c_{ij}}(s) \tag{22}$$

From the standpoint of the OCM, this means that the state equations for the original dynamics are used and discrete integration is modeled by adding a delay determined from the phase distortion. As we have stated earlier, such an approximation probably accounts for the major source of difficulty in discrete integration. However, to employ it exclusively is to leave us somewhat uncertain as to the closed-loop significance of the amplitude distortions.

---

* The delays for A-B integration are large to offset lead introduced by an added zero to account for amplitude distortion (see below).

TABLE 3

APPROXIMATE INTEGRATION DELAYS FOR CONTINUOUS MODELING

	EULER	ADAMS BASHFORTH* (WITH ZERO INCLUDED FOR AMPLITUDE DISTORTION)
Longitudinal		
CAS-OFF	T	$\frac{3T}{2}$
CAS-ON	$\frac{3T}{2}$	$\frac{3T}{2}$
Lateral		
CAS-OFF	T	**
CAS-ON	T	**
Coordinated		
ROLL ANGLE	T	$\sim\frac{5T}{4}$
TRACKING ERROR	$\frac{3T}{2}$	$\sim\frac{5T}{4}$

* The effective delay for Adams-Bashforth in the bandwidth for manual control is virtually negligible.

** Zero-Modeling of A-B integration was not performed for Lateral Dynamics

Approximations were found that better accounted for the amplitude distortions in simulating the longitudinal control task and the lateral control task with coordinated dynamics. For Euler integration, this was accomplished by finding values for the aircraft stability derivatives that gave characteristic modes approximately equal to the principal roots obtained from the discrete integration of the original dynamics.* Table 4 shows the changes in stability derivatives necessary to match the roots of the discrete system. Figure 10 compares the resulting approximate continuous transfer functions with the discrete Bode responses for Euler integration of the longitudinal CAS-OFF dynamics. It can be seen by comparing these results with those of Figure 6 that this approximation is closer to the corresponding discrete Bode response than is the original continuous transfer. This is also true for the approximation to the pitch CAS-ON dynamics as is seen in Figure 11, although the absolute agreement between approximate CAS-ON dynamics and discrete Bode response is not as good as for the unaugmented case.

The strategy for approximating A-B integration was somewhat different. Values for stability derivatives were adjusted to match the characteristic modes as in the case of Euler integration. However, the major source of amplitude distortion in A-B integration is not the result of the relatively minor pole perturbations introduced by this scheme. Rather, the amplitude

---

* In the case of the longitudinal CAS-ON dynamics, both stability derivatives and CAS parameters were changed to obtain the requisite approximation.

TABLE 4

STABILITY DERIVATIVE CHANGES
TO MATCH DISCRETE ROOTS

Integration Scheme		Euler			Adams-Bashforth		
Sample Period	Continuous	1/32	1/16	1/10	1/32	1/16	1/10
Longitudinal							
Mq	-.487	-.346	-.194	0	-.494	-.516	-.562
Mα	-4.79	-5.00	-5.22	-5.43	-4.79	-4.86	-4.96
Coordinated							
L_p	-2.58	-2.69	-2.82	-2.98	-2.58	-2.56	-2.51
L_δ	17.24	17.95	18.83	19.91	17.24	17.07	16.74

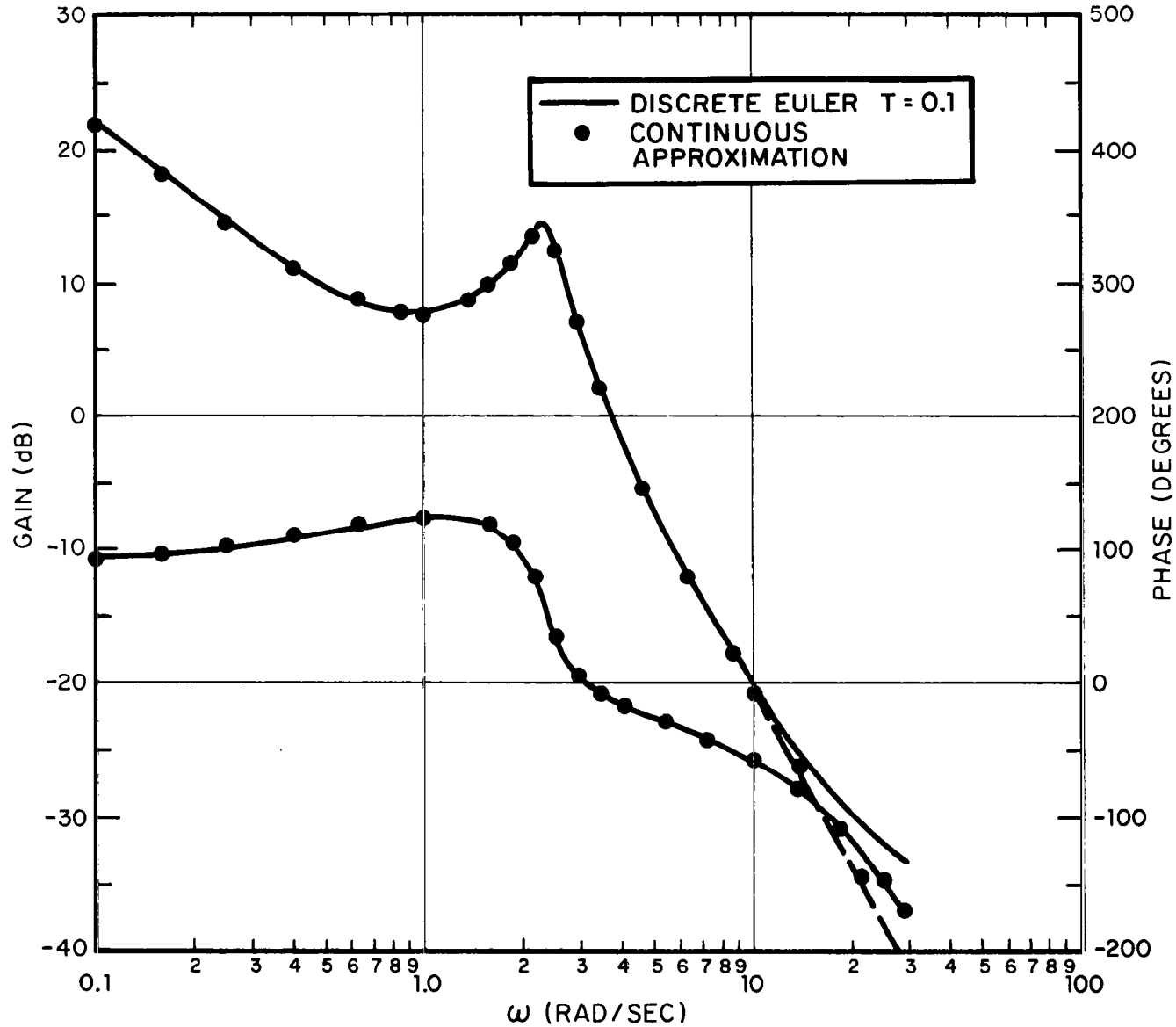

Figure 10. - Continuous Approximation to Discrete, CAS-OFF Pitch/ Elevator Bode Response (Euler integration, T=.1).

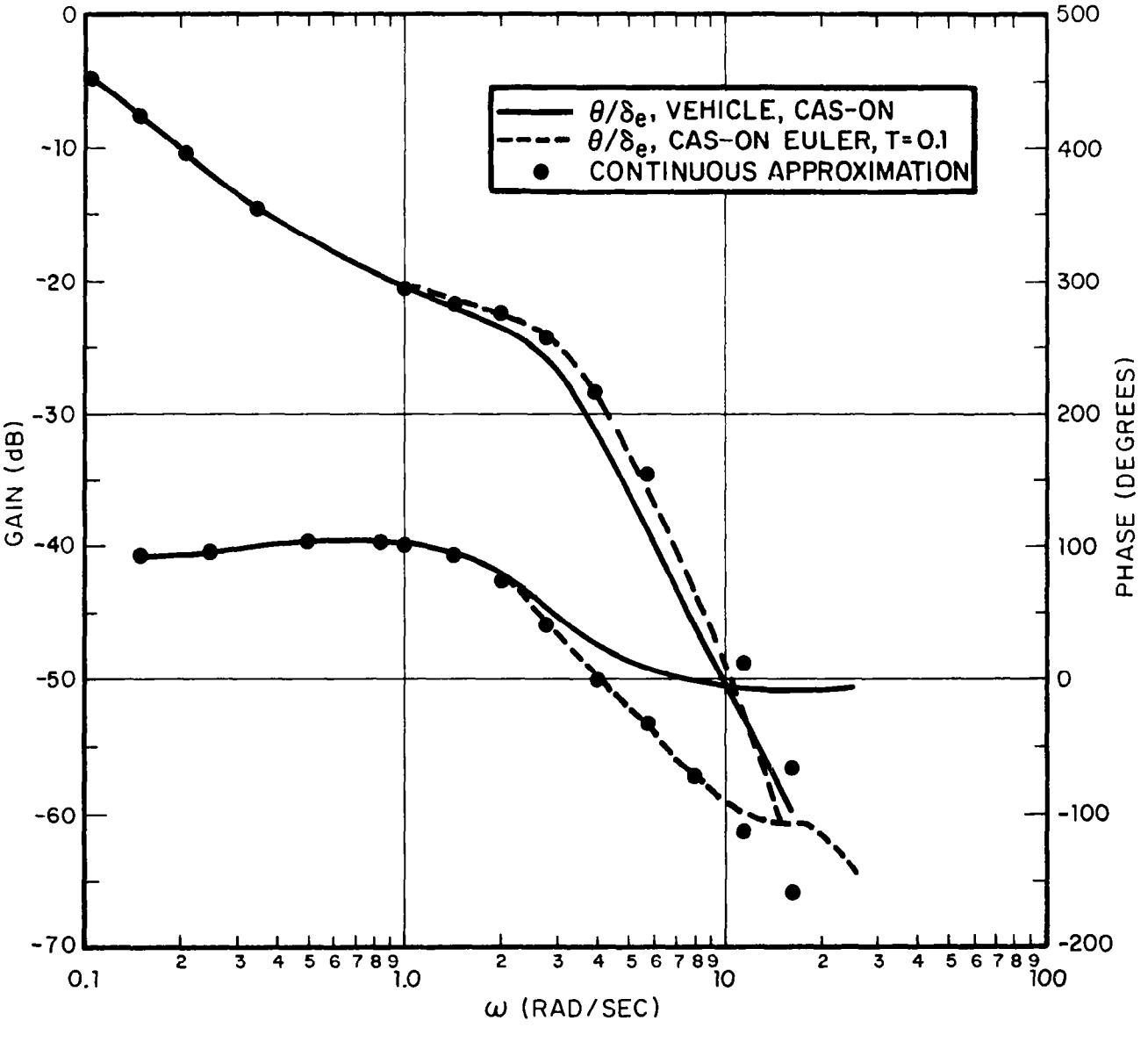

Figure 11. - Continuous Approximation to Discrete CAS-ON Pitch/ Elevator Bode Response (Euler Integration, T=.1).

distortion for A-B is characterized by the amplitude ratio not "rolling off" as rapidly as the continuous amplitude ratio in the mid- to high-frequency region (the actual frequency range depends on the sample period). This effect can be modeled by introducing an appropriately located zero in the transfer function. However, the introduction of such a zero will add phase lead that must be cancelled by adding transport lag.

Figure 12 shows the approximation to the A-B θ/δ, CAS/OFF Bode response for T = .1. The approximate transfer function was generated by introducing a zero at $\omega \approx 6.5$ rad/sec, setting τ_c = .14 seconds and perturbing the pitch damping and static stability derivatives as indicated in Table 4. Similar agreement was obtained for the longitudinal CAS/ON and coordinated A-B Bode responses and for different values of T. For the smaller values of T, the frequency of the zero increases (to ~ 22 rad/sec for T = .03125) and the amount of delay that must be added is consequently reduced. The effective delays for the A-B approximation with the zero added are given in Table 3.

The nature of the approximation for A-B integration may be understood better by comparing the z-transform for a "discrete A-B integrator" to that for the Euler integrator. These are given by (see Appendix B)

$$\text{A-B:}\quad \frac{1}{s} \rightarrow \frac{T}{2}\,\frac{(3z-1)}{z(z-1)}$$

$$\text{EULER:}\quad \frac{1}{s} \rightarrow \frac{T}{z-1} \qquad (23)$$

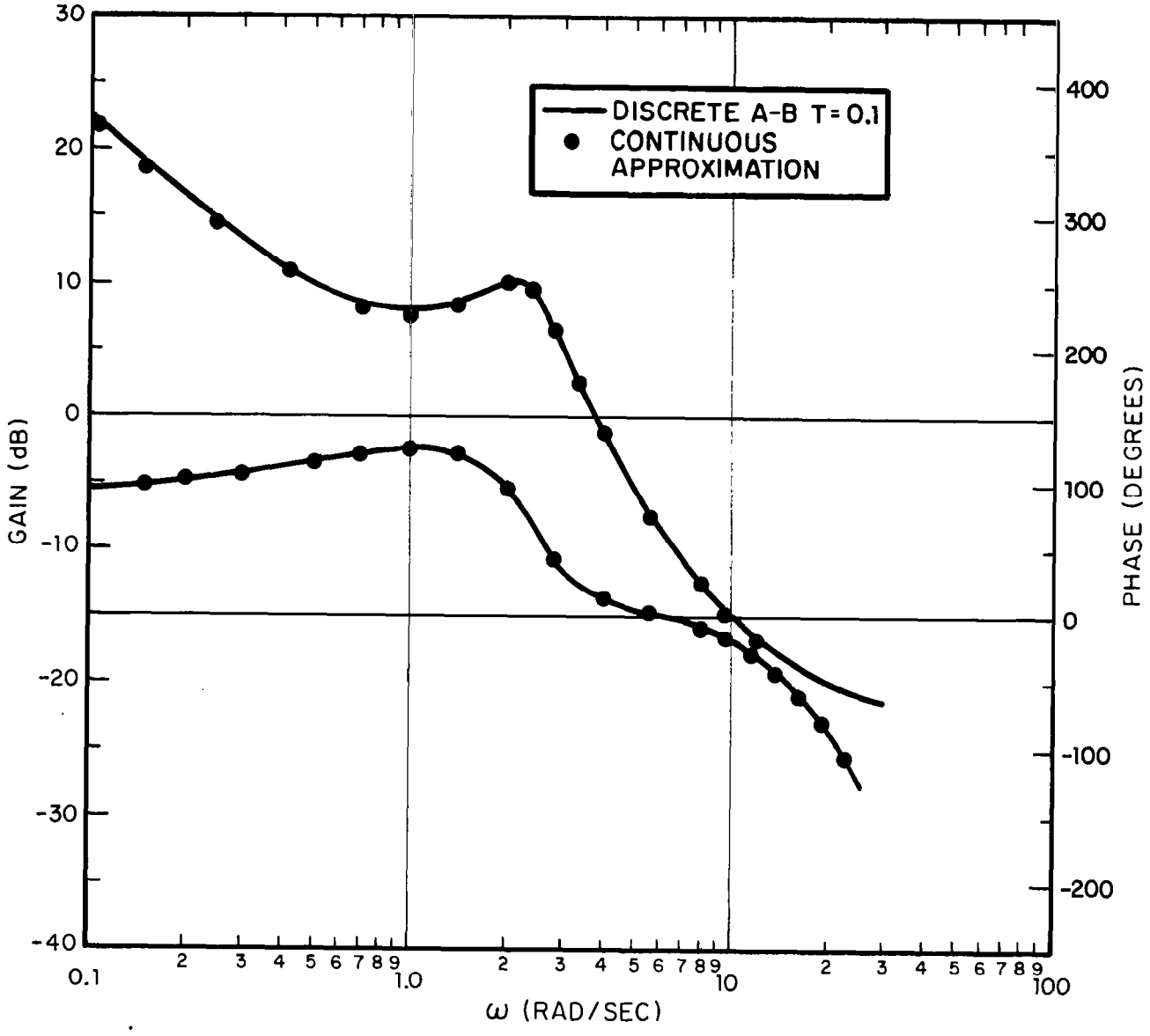

Figure 12. - Continuous Approximation to Discrete, CAS-OFF Pitch/ Elevator Bode Response (Adams-Bashforth Integration, T=.1).

When compared with Euler integration, A-B has an additional pole and zero in the z-plane. The lead introduced by the zero apparently more than compensates for any lag introduced by the added pole, thereby giving the overall desirable phase characteristic for A-B integration. However, for the continuous modeling being attempted here, if the amplitude distortion is to be accounted for by adding a zero to the continuous transfer function, then the additional delay implied by the second order denominator must also be included.

2.4 Summary

In the previous sections the open-loop dynamics for a fixed-base simulation were considered. Continuous approximations to these dynamics were developed for use in the closed-loop analysis. The basic result was that for the frequency range likely to be of interest in continuous aircraft control problems, the simulator transfer function could be modeled as

$$\frac{y(s)}{u(s)} = \tilde{D}(s)e^{-\tau_s s} \tag{24}$$

where $\tilde{D}(s)$ is an "approximation" to the Bode response for digital integration of the vehicle dynamics (denoted by $D^*(s)$). The simulator delay, τ_s, is given by

$$\tau_s = \tau_F + \tau_H + \tau_v + \tau_c \tag{25}$$

where τ_F, τ_H, τ_v and τ_c respectively, are the delays introduced by the de-aliasing filter, hold, visual servo and CPU (discrete integration).

It was found that very good approximations to discrete Bode responses could be obtained for the longitudinal control tasks and for the coordinated lateral control task to be analyzed later. These approximations involved perturbation of aircraft stability derivatives and CAS parameters to yield continuous modes that agreed with the discrete modes and, in the case of A-B integration, the introduction of a zero in the continuous vehicle transfer. Similar approximations for the full lateral dynamics, CAS-ON or CAS-OFF, were not obtained. It is anticipated, however, that by incorporating the phase lags introduced by discrete integration, the dominant effects on closed-loop performance and workload would be accounted for in these cases as well.

The approximation of Equation (24) readily lends itself to efficient application of the OCM. The system matrices corresponding to a state representation of $\tilde{D}$ (Equation 1) and the values for τ_s are easily obtained for different sample periods, etc. For each condition, a single run of the OCM is sufficient to predict the corresponding performance. Adjustment of pilot parameters, specifically observation noise levels [18], allows the sensitivity to pilot attention to be examined.

There are shortcomings in the continuous model. For example, the effects of aliasing are not considered. Thus, the degrading effects of the de-aliasing filter are included in the continuous model but not its benefits. This means that decreasing the bandwidth, ω_c, of that filter can only lead to negative results, a situation that is not obviously true, in general. Similarly, because only the delays inherent in the data holds are considered, zero-order holds will always show less degradation than first-order holds. But, in some instances, the first-order hold may provide advantages that outweigh the additional delay penalty. This type of trade-off cannot be explored with the continuous OCM. Because of these and other potential shortcomings, it was decided to develop a hybrid model. This model is discussed in the next chapter.

3. THE HYBRID MODEL FOR ANALYSIS OF CLOSED-LOOP SIMULATORS

The development of a hybrid model was motivated by two considerations: 1.) the desire to verify the results obtained with the continuous model; and 2.) the need to investigate issues not readily addressed by the continuous model. One approach to developing such a model is to derive analytic expressions for all the variables in the closed-loop following, e.g., the techniques in Appendix A that were used to develop exact transfers for the open-loop simulator dynamics. This approach was explored briefly but was abandoned because it would have required major computer program development even if it had been successful. Instead, the approach taken was to "simulate" the simulation. This involved modifying an existing program for a discrete simulation version of the OCM [19] as discussed below.

3.1 Simulation Version of OCM

To understand the nature of the hybrid model it is necessary to review the discrete simulation model of the OCM as described in [20]. The major relevant aspects of the model and some of the modeling issues are discussed below.

3.1.1 System-Display Dynamics

There are no modeling restrictions on the system being controlled, other than that a set of displayed elements y(t) at a time t be generated from:

$\underline{u}(t)$ = human's control inputs

$\underline{w}(t)$ = zero mean, white Gaussian random input disturbances or commands*

For the special case of a linear system, the system equations are (as in Equation [1])

$$\dot{\underline{x}}(t) = \underline{A}_s\underline{x}(t) + \underline{B}_s\underline{u}(t) + \underline{E}_s\underline{w}(t)$$
$$\underline{y}(t) = \underline{C}_s\underline{x}(t) + \underline{D}_s\underline{u}(t) \qquad (26)$$

where $\underline{x}(t)$ is the system state vector. The system parameters (A_s, etc.) may be time varying.

3.1.2 Human Operator Internal Model

In the OCM, the human is assumed to have an internal characterization of the input-output response of the system. This "internal model" is assumed to be linear, in state variable form,

$$\dot{\underline{x}}_m(t) = \underline{A}_m\underline{x}_m(t) + \underline{B}_m\underline{u}_m(t) + \underline{E}_m\underline{w}_m(t)$$
$$\underline{y}_m(y) = \underline{C}_m\underline{x}_m(t) + \underline{D}_m\underline{u}_m(t) \qquad (27)$$

where

$\underline{x}_m(t)$ = internal model states

$\underline{w}_m(t)$ = model Gaussian white noise inputs

etc.

---

* Actually, deterministic inputs are also allowed but are not relevant here.

The states of the "internal model" need not be the same as those of the system. Indeed, it is not even required that dimension $\{\underline{x}_m\}$ = dimension $\{\underline{x}_s\}$. Similarly, internal representation of disturbances can differ from system disturbances. On the other hand, the model inputs $\underline{u}_m(t)$ and displayed outputs $\underline{y}_m(t)$ are assumed to be the same as the actual system inputs $\underline{u}(t)$ and displays $\underline{y}(t)$ to avoid numerous conceptual problems, i.e.,

$$\underline{u}_m(t) = \underline{u}(t)$$

$$\underline{y}_m(t) = \underline{y}(t)$$

The internal model parameters (A_m, etc.) can also be time-varying.

The choice of an internal model is somewhat subjective. When the system is continuous and the operator is well-trained, a very reasonable and convenient choice is $\underline{A}_m = \underline{A}_s$, etc.; i.e., the internal model is the same as the system. This, of course, is the choice employed in the standard OCM. However, when the "system" is a simulation of a continuous system, the choice of an internal model is less obvious. Because of its generality, the hybrid model will allow us to examine alternative choices.

The internal model is used within the OCM to help generate a (continuous time) human operator control input via:

$$\dot{\underline{u}}(t) = -\underline{L}_c \begin{bmatrix} \hat{\underline{x}}_m(t) \\ \underline{u}(t) \end{bmatrix} + \underline{L}_{c2}\, \underline{v}_u(t) \qquad (28)$$

The feedback gains

$$\underline{L}_c = [\underline{T}_N^{-1}\underline{L}_{opt} | \underline{T}_N^{-1}] = [\underline{L}_{c1} | \underline{L}_{c2}] \tag{29}$$

are generated via auxiliary programs that solve the optimal control problem for the model equations. The model is also needed in the construction of the Kalman filter-predictor that generates the model state estimate $\hat{\underline{x}}_m(t)$.

3.1.3 Human Limitations

The human generates $\hat{\underline{x}}_m(t)$ on the basis of the delayed and noisy perceived information:

$$y_{pi}(t) = N_i[y_i(t-\tau)] + v_{yi}(t) \quad i=1,\ldots,NY \tag{30}$$

where

τ = the human's time delay,

$v_y(t)$ = the observation noise at time t,

and $N_i(.)$ is the non-linear observation theshold:

$$N_i(x) = \begin{cases} x-a_i & x > a_i \\ 0 & |x| \leq a_i \\ x+a_i & x < -a_i \end{cases} \tag{31}$$

In a simulation model, it is possible to implement the non-linear observations using Equations (30) and (31). However, in a human operator context we find it more meaningful and convenient to replace $N_i(.)$ by an equivalent gain, $\hat{N}_i$. The random imput describing function:

$$\hat{N}_i = \text{erfc} \frac{|x|}{a_i\sqrt{2}} \tag{32}$$

is used. $\hat{N}_i$ is interpreted as the probability that the human will respond to y_i, given its present value at time t.

Each observation noise $v_{yi}(t)$ is a zero-mean, white Gaussian noise with covariance:

$$E[v_{yi}(t)\ v_{yi}(\sigma)] = \frac{V^\circ_{yi}(t)}{f_i(t)}\ \delta(t-\sigma) \tag{33}$$

that contains both an additive and a ratioed component:

$$V^\circ_{yi}(t) = V_{yi}(t) + \pi\rho_{yi}E[y_i{}^2(t-\tau] \tag{34}$$

The quantity $f_i > 0$ is the attentional allocation to the displayed variable y_i. The f_i are constrained by:

$$\frac{1}{2}\sum_{i=1}^{NY} f_i(t) = f_T = \text{constant total attention} \tag{35a}$$

$$f_{i+1}(t) = f_i(t) \quad i-1,3,\ldots,NY-1 \tag{35b}$$

to indicate that position-velocity pairs are obtained simultaneously from the display elements, a standard OCM assumption [5].

The neuro-motor interface portion of the model is given by Equation (28). The motor noises $v_{ui}(t)$ are zero-mean white Gaussian noises, with covariance:

$$E[v_{ui}(t)\ v_{ui}(\sigma)] = V^\circ_{ui}(t)\ \delta(t-\sigma) \tag{36}$$

that contains an additive and a ratioed component,

$$V^\circ_{ui}(t)\ s\ V_{ui}(t) + \pi\rho_{ui}\ E[u_i^2(t)] \tag{37}$$

3.2 Discretized Equations for Hybrid Model

The hybrid model employs the simulation version of the OCM in a closed-loop digital Monte Carlo type computation in which "continuous" elements of the loop are updated at a rate significantly greater than discrete elements. In other words, the hybird model is a multi-rate sampling system, rather than a true hybrid system. (Informal experimentation indicates that a sample rate five times that of the discrete elements is adequate to simulate continuity for the cases considered here.) In addition, to different sample rates for continuous and discrete elements, the updating of the discrete equations of the hybrid model is different for the two kinds of elements. In particular, discrete elements are updated by means of the integration scheme and time-step specified for the simulation. The equations for continuous elements are updated at the faster rate via the transition matrix method of integration described in Appendix B. Below, we proceed around the closed-loop, starting with the digital computer, and give the basic equations for the hybrid model.

3.2.1 Vehicle Dynamics

The digital computer integrates Equations (26) using the sampled value of the output of the de-aliasing filter. Given a simulator time step T, the system equations generate outputs $y_i(k) = y_i(kT) \approx y(t)$ from the piecewise-constant inputs $u(k-1)$ and $w(k-1)$ via

$$x(k+1) = A_d x(k) + B_d u(k) + TE_d w(k)$$
$$yIk) = C_d x(k) + D_d u(k-1)$$

where A_d, etc. depend on the integration scheme and are defined for various methods in Appendix B.

3.2.2 D-A Interface

The D-A interface consists of the data hold plus visual servo. Consider first the zero-order hold. The sampled output, y_i, is held constant over a sample period. The constant value is the input to the visual servo. It is assumed that the operator observes both the servo output y_{i_d} and its rate $\dot{y}_{i_d}$. The transfer function for the visual servo is given by Equation (12).

A convenient state space model for the servo is

$$\begin{bmatrix} \dot{y}_{i_d} \\ \ddot{y}_{i_d} \end{bmatrix} = \begin{bmatrix} 0 & 1 \\ -\omega_n^2 & -2\zeta\hat{\omega}_n \end{bmatrix} \begin{bmatrix} y_{i_d} \\ \dot{y}_{i_d} \end{bmatrix} + \begin{bmatrix} 0 \\ -\omega_i{}^2 \end{bmatrix} y_i \tag{38}$$

or, with

$$\underline{x}_i' = [y_{i_d} \; \dot{y}_{i_d}], \tag{39}$$

we have

$$\dot{\underline{x}}_i = \underline{A}_v \underline{x}_i + \underline{b}_v y_i \tag{40}$$

This is simulated in the hybrid model in a subroutine called DAC via transition matrix integration of (38), i.e.,

$$\underline{x}_i(kT+\ell\Delta) = e^{\underline{A}_v\Delta}\underline{x}_i[kT+(\ell-1)\Delta] + \int_0^{\Delta} e^{\underline{A}_v\sigma}\underline{b}_v d\sigma \cdot y_i(kT) \tag{41}$$

where Δ is the time step for the faster (continuous) sample rate and

$$\ell = 1, \ldots, N_\ell = T/\Delta \tag{42}$$

Thus, the servo outputs are updated N_ℓ times over a system simulation interval T. For that simulation interval, in the case of a zero order hold, the input y_i is constant.

When the data hold is a first order hold the situation is a bit more complex. Over a simulation sample period T, $y_i(t)$ is defined by

$$y_i(t) = y_i(k) + M_k t, \quad kT \leq t \leq (k+1)T \tag{43}$$

where

$$M_k = \frac{y_i(k) - y_i(k-1)}{T}$$

To get state-equations for the servo with the input coming from a first order hold, we let

$$\underline{x}' = [y_{d_i} \; \dot{y}_{d_i} \; y_i]$$

Then

$$\dot{\underline{x}} = \tilde{\underline{A}} \, \underline{x} + \tilde{\underline{b}} \, M_k \tag{44}$$

with

$$\tilde{\underline{A}} = \left[\begin{array}{c|c} \tilde{A}_v & b_v \\ \hline \underline{0} & 0 \end{array}\right], \quad \tilde{\underline{b}} = \left[\begin{array}{c} \underline{0} \\ \hline 1 \end{array}\right] \tag{45}$$

Equation (44) will be integrated digitally, at the fast sample rate, so $y_i(t)$ must be approximated by a piecewise constant function. We do this by using average value of $y_i(t)$ over the interval $[\ell\Delta, (\ell+1)\Delta]$. Let ξ_ℓ be defined to be this average

value. Clearly,

$$\xi_{\ell+1} = \xi_{\ell} + \Delta M_k, \qquad \ell = 0,\ldots N_{\ell}-1$$

with

$$\xi_o = y(k) + \frac{\Delta}{2} M_k$$

Combining the above yields

$$\xi_{\ell+1} = y_i(k) + (\ell+1/2) \frac{y_i(k) - y_i(k-1)}{N_{\ell}} \tag{45}$$

where we have used $T = N_{\ell}\Delta$.*

Now, the same transition matrix update is used as before, but the input is changed each Δ. Thus, with $\underline{x}$ defined as in (39)

$$x[kT+(\ell+1)\Delta] = e^{A_v\sigma} x[kT+\ell\Delta] + \int_o^{\Delta} e^{A_v\sigma} b_v d\sigma . \xi_{\ell}, \quad \ell = 0, 1,\ldots,N_{\ell}-1 \tag{46}$$

3.2.3 Human Operator Model

The OCM internal model Equation must be updated every Δ seconds. This is done by the transition matrix method, so

$$\begin{aligned} \underline{x}_m(kT+\ell\Delta) &= \underline{\Phi}_m\underline{x}_m[kT+(\ell-1)\Delta]+\underline{\Gamma}_m\underline{u}[kT+(\ell-1)\Delta]+\underline{\Delta E}_m\underline{w}_m \\ \underline{y}(kT+\ell\Delta) &= \underline{C}_m\underline{x}_m[kT+\ell\Delta] + \underline{D}_m\underline{u}[kT+(\ell-1)\Delta] \end{aligned} \tag{47}$$

---

* It is interesting to note that for $N_{\ell} = 1$, $\xi_o = \frac{3y(k)-y(k-1)}{2}$ and the subsequent integration is similar to A-B integration.

where

$$\underline{\Phi}_m = e^{\underline{A}_m \Delta} \quad ; \quad \underline{\Gamma}_m = \int_0^{\Delta} e^{\underline{A}_m \sigma} \underline{B}_m d\sigma \tag{48}$$

The human operator model generates a control input $u(\ell)$, to use over the time interval $(t, t+\Delta)$, via

$$\frac{u(\ell) - u(\ell-1)}{\Delta} = -\underline{L}_1 \begin{bmatrix} \hat{\underline{x}}_m(\ell) \\ u(\ell-1) \end{bmatrix} + L_2 v_u(\ell) \tag{49}$$

where $t = kT + \ell\Delta$ and we have suppressed the Δ's in function arguments for convenience. Note that it is the control input itself that is considered to be piecewise constant for interface with the simulator model. This is in contrast to the covariance propagation approach corresponding to the standard OCM where control-rate is assumed piecewise constant with:

$$\dot{\underline{u}}(\ell) = -\underline{L}_d \begin{bmatrix} \hat{\underline{x}}(\ell) \\ \underline{u}(\ell) \end{bmatrix} + \underline{L}_{d2} \underline{v}_u(\ell) \tag{50}$$

The gains $\underline{L} = [\underline{L}_1 | \underline{L}_2]$ in Equation (49) are the discrete equivalents of the continuous gains of the standard OCM and are computed as described in [19].

The discretized observations for the human operator model are:

$$y_{pi}(\ell) = \hat{N}_i \, y_{di}(\ell-N) + v_{yi}(\ell) \tag{51}$$

where, if τ = human's time delay, N = integer $[\tau/\Delta]$. The covariance of the piecewise-constant white noise $v_{yi}(\ell)$ is $\Delta^{-1}[V^{o}_{yi}(\ell)/f_i(\ell)]$ to account for the finite time step. Similarly, the covariance of the motor noise $v_u(\ell)$ now becomes V^{o}_{ui}/Δ.

The observation and motor-noise covariances are defined by Equations (33)-(37). These equations require process (i.e., ensemble) statistics at time $\ell\Delta$. However, these are not available from a single Monte-Carlo trajectory, and their precomputation for subsequent read-in is unfeasible. The approach we have taken is to obtain temporal approximations using filtered past data. An approximation

$$\alpha(k) \doteq E[y_i^2(K-N)]$$

is obtained via lst-order filtering of $y_i^2(k-N)$,

$$\alpha(k) = e^{-\Delta/\tau_m}\alpha(k-1) + (1-e^{-\Delta/\tau_m})y_i^2(k-N) \qquad (52)$$

with initial condition $\alpha(N-1) = y_i^2(0)$. The approximate variance of $u_i^2(k-1)$ is found using a two-step procedure that estimates (through filtering) the mean and mean-square, and then computes the variance. The time constant τ_m = 0.5 sec.

The OCM includes a Kalman estimator and an optimal predictor. The estimator processes y_{p_i} to generate an a posteriori estimate of the delayed state

$$\hat{\underline{p}}(\ell/\ell) = E\{\underline{x}(\ell-N) \mid \underline{Y}_p(0),\ldots,\underline{Y}_p(kT+\ell)\}$$

according to well-known equations [19]. The predictor forms an estimate $\hat{\underline{x}}(\ell)$ from $\hat{\underline{p}}(\ell/\ell)$ using

$$\hat{\underline{x}}(\ell) = \underline{\Phi}_m^{N+P}\, \hat{\underline{p}}(\ell/\ell) + \sum_{i=0}^{N+P-1} \underline{\Phi}_m^i\, \underline{\Gamma}_m^i\, \underline{u}_c(\ell-i-1) \tag{54}$$

where u_c is the deterministic part of u. In the standard OCM, $P \equiv 0$ and the prediction compensates for the human's delay. Here, we let P be a positive parameter to be selected so as to yield the best performance, the idea being the human operator will have to compensate for simulation delays as well as his own.

3.2.4 A-D Interface

This interface consists of the de-aliasing filter, a sampler and an implicit hold corresponding to the piecewise constant input assumption associated with integration in the digital computer. The filter considered here is a third-order Butterworth filter which can be represented in state space form as

$$\dot{\underline{x}}_F = \begin{bmatrix} 0 & 1 & 0 \\ -\omega_c^2 & -2\zeta\omega_c & \omega_c^2 \\ 0 & 0 & -\omega_c^2 \end{bmatrix} \underline{x}_F + \begin{bmatrix} 0 \\ 0 \\ \omega_c^2 \end{bmatrix} u_i\ (t) \tag{55}$$

$$\triangleq \quad \underline{A}_F\, \underline{x}_F + \underline{b}_F\, u_i(t) \tag{56}$$

Equation (56) is integrated using the transition matrix method and a time step of Δ. However, only the values of the filter output at the simulation sample times, $u_1\ (kT)$ $(k=0, 1, \ldots)$, are used by the computer in subsequent updating of the vehicle dynamics.

For the third order Butterworth $\zeta = .5$ and the value of ω_c is nominally set to half the sampling frequency, but different values can be tried within the context of the hybrid model.

3.3 Steady-State Solutions

The hybrid model of the closed loop simulation is a Monte Carlo model that normally will require many solutions to obtain meaningful statistics. In the analyses to be performed in this study we are interested in the steady-state response of stationary systems. Rather than average over many Monte Carlo solutions, we have assumed ergodicity of the processes and utilized time-averaging of a single response.

Two questions arise in attempting to determine steady-state statistics via time-averaging: 1) when should the averaging process begin? and 2) what length averaging "window" is necessary? Of course, if one averages long enough the two questions become moot, but very long averaging times can be as expensive as ensemble averaging. Given the practical constraints on run-time, we want to be sure that steady-state statistics are not biased by initial transient responses and that averaging windows are sufficient to provide enough independent samples, given the correlation times of the processes.

The rationale for the choice of the "transient window" to be discarded and the "averaging window" to be selected in the Monte Carlo model is as follows. Let M_1 be the estimate of the mean of the process obtained by averaging over the first N_1 samples $y(i)$, $i = 1, N_1$ of output from a Monte-Carlo simulation. That is,

$$M_1 = \frac{1}{N_1} \sum_{i=1}^{N_1} y(i)$$

Let V_1 be the estimate of the variance, defined by

$$V_1 = \left\{\frac{1}{N_1} \sum_{i=1}^{N_1} y^2(i) - M_1^2\right\}$$

Let M_2, V_2, N_2 be defined in a similar fashion. We shall treat the first N_1 samples as the transient window to be discarded and the samples from N_1 to N_2 as the averaging window. Let M_{12} and V_{12} be estimates of mean and variance, respectively, over the averaging window, defined by

$$M_{12} = \frac{1}{N_2-N_1} \sum_{i=N_1+1}^{N_2} y(i)$$

$$V_{12} = \left\{\frac{1}{N_2-N_1} \sum_{i=N_1+1}^{N_2} y^2(i) - M_{12}^2\right\}$$

It is easy to show that

$$V_{12} = \frac{N_2V_2-N_1V_1}{N_2-N_1} + \frac{N_2M_2^2-N_1M_1^2}{N_2-N_1} - \frac{(N_2M_2-N_1M_1)^2}{(N_2-N_1)^2}$$

If we assume $M_1 = M_2$ (which is reasonable because, ideally, the process mean is zero) then

$$V_{12} = \frac{N_2V_2-N_1V_1}{N_2-N_1}$$

This formula for V_{12} was used on a representative Monte Carlo run of sufficiently long duration to check how V_{12} for various N_1 and N_2 compares with the estimate of variance obtained by

averaging over the entire run. A transient window width of 3000 samples and an averaging window width of 7500 samples was found to give satisfactory results.

Consider now the confidence that can be attached to the results obtained by the above averaging process. Assuming y(i) is a zero mean uncorrelated sequence with variance σ^2, (in steady state this is what we expect),

$$E(V_{12}) = E\left(\frac{1}{N}\sum_{i=N_1+1}^{N_2} y^2(i) - M_{12}^2\right) = \sigma^2\left(1-\frac{1}{N}\right)$$

where $N = N_2 - N_1$ and

$$\begin{aligned} Var(V_{12}) &= \left(\sigma^4 - \frac{2}{N^3}\sum E(y_i^4) + \frac{1}{N^4}\sum E(y_i^4)\right) - \sigma^4\left(1-\frac{1}{N}\right)^2 \\ &= \sigma^4\left(\frac{2}{N} - \frac{7}{N^2} + \frac{3}{N^3}\right) \ * \\ &\simeq \frac{2\sigma^4}{N} \end{aligned}$$

By Chebyshev's inequality,

$$P\left\{\left|V_{12} - E(V_{12})\right| \geq .05\sigma^2\right\} \leq \frac{2\sigma^4}{N(.05\sigma^2)^2} = \frac{800}{N}$$

Thus, N = 7500, guarantees that V_{12} will differ by less than 5% from the true σ^2 with probability roughly 90%.

---

* When $y_i \sim N(0,\sigma^2)$ the fourth moment $E(y_i^4) = 3\sigma^4$.

4. APPLICATION OF SIMULATION MODELS

In this chapter the models for closed-loop simulation are applied to an "example" simulation involving air-to-air target tracking. Results are obtained to demonstrate the effects of various simulation choices as well as problem-dependent effects.

Experiments are planned to test the validity of model predictions in the above example. Here, as a preliminary demonstration and validation of the modeling approach to analyzing simulation requirements, a comparison of model results with data obtained from an independent investigation into the effects of computation delays [20] is presented.

4.1 A Target Tracking Problem

The model of the closed loop simulation will be applied to an example to explore and analyze basic simulation effects and to (eventually) test the model's validity. The example is reasonably realistic, involving the longitudinal and roll-axis lateral dynamics of a high performance (F8) aircraft. Longitudinal and lateral tracking will be considered separately. Air-to-air target tracking is the pilot's task.

Below we define the tracking geometry, target motions, and the attacker aircraft dynamics for each tracking task. The state-variable descriptions of the system dynamics (target plus aircraft) as required for application of the models are given in Appendix C.

4.1.1 Longitudinal Tracking

The longitudinal tracking task to be considered is similar to that studied in [20], but differs in the definition of tracking error and target input. The equations for this task will be developed in an attacker-centered coordinate system with the effects of gravity neglected.

a. Geometry

Figure 13a shows the geometry of the air-to-air tracking in the longitudinal plane. The gunsight is assumed to be fixed and aligned with the aircraft body axis. For longitudinal tracking we will assume that no information concerning the target's pitch angle (or the relative aspect angle) is available. If we assume that the target velocity (V_T) and attacker velocity are nearly equal ($V_T \approx V$), then, for small (relative) angles

$$\dot{\Sigma}_{T_E} = \frac{V}{R}(\gamma_T - \gamma) = \frac{V}{R}(\dot{h}_T - \dot{h}) = \dot{\theta} + \dot{\varepsilon}_V$$

or

$$R\,\dot{\varepsilon}_V = V(\dot{h}_T - \dot{h}) - R\,\dot{\theta} \qquad (57)$$

where R is the target's range and is assumed constant and equal to 182.9m (600 ft.), as in [20].

a) LONGITUDINAL (ELEVATION)

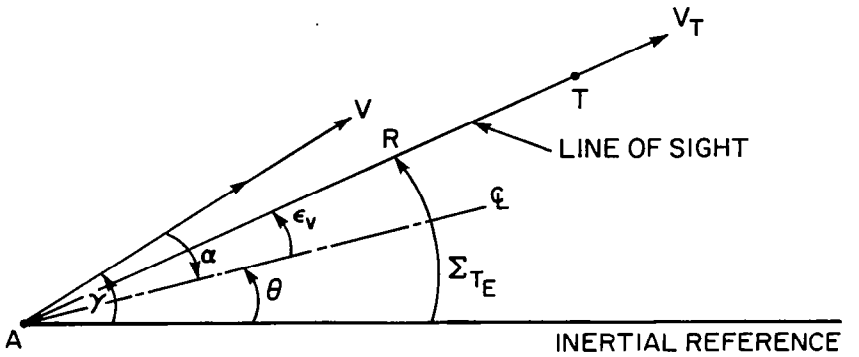

Σ_{T_E} = INERTIAL LINE-OF-SIGHT ANGLE (ELEVATION)

R = TARGET RANGE

ϵ_V = ELEVATION TRACKING ERROR = $\Sigma_{T_E} - \theta$

b) LATERAL (TRANSVERSE)

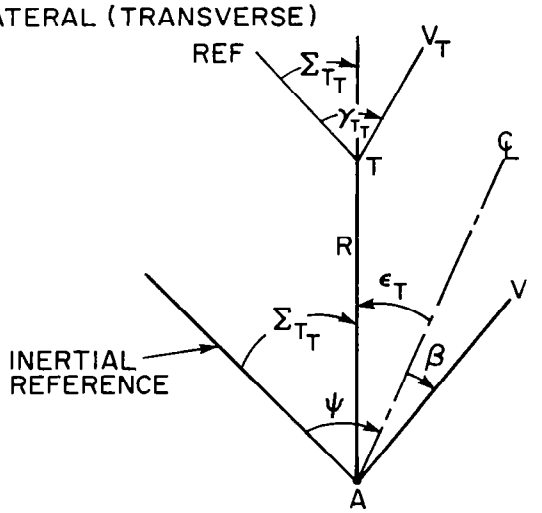

Σ_{T_T} = INERTIAL LINE-OF-SIGHT ANGLE (TRANSVERSE)

ϵ_T = TRANSVERSE TRACKING ERROR = $\Sigma_{T_T} - \psi$

ψ_{T_T} = TARGET LATERAL FLIGHT PATH

Figure 13. - Target Geometry.

b. Target Motion

The target will be assumed to execute random vertical evasive maneuvers.* In particular, target altitude variations will be generated by passing white, zero mean, gaussian noise through a third order filter as illustrated below.

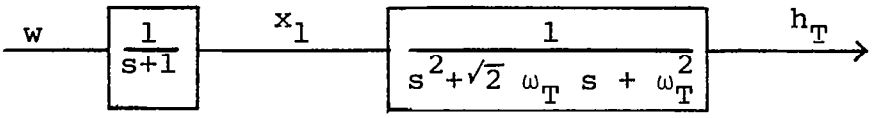

(58)

By selecting the covariance of the white noise and the cutoff frequency of the Butterworth filter, rms altitude variations and normal accelerations may be specified. Two motion variations will be considered in the longitudinal analysis as indicated below.

	ω_T	$\left(\overline{h_T^2}\right)^{1/2}$	$\left(\overline{\ddot{h}_T^2}\right)^{1/2}$
Narrowband Input	.2	81.4m (267 ft.)	$8.17\frac{m}{sec^2}$ (~.8g)
Wideband Input	.5	81.4m (267 ft.)	$30.48\frac{m}{sec^2}$ (~3.1g)

* We wish to avoid the simple sine-wave tracking task of [20].

c. Aircraft Dynamics

The longitudinal short-period dynamics of the F8 without augmentation will be the baseline dynamics.* The dynamics we will use correspond to the aircraft operating at an altitude of 6096m and a speed of 190 m/sec (flight condition #11). The short period dynamics are given by

$$\dot{q} = -.487q - 4.789\alpha - 8.743\delta_e$$

$$\dot{\alpha} = q - .836\alpha - .111\ \delta_e$$

$$n_z = [V(q-\dot{\alpha})/57.3]x\ 32.2 \qquad (59)$$

$$= .2818\alpha + .0374\ \delta_e$$

The short period dynamics have a natural frequency of $\omega_{n_{sp}} = 2.28$ and a damping of $\xi_{sp} = .29$; this represents poor short period handling qualities [20].

The state equations corresponding to the above dynamics are given in Appendix C.

d. Pitch CAS

As noted above, the short period handling characteristics of the F8 at flight condition #11 leave much to be desired. Moreover, we are interested in the effects of simulation parameters as a function aircraft dynamics. A pitch command augmentation system designed by Honeywell [16] to improve the F8

* A preliminary analysis incorporating the phugoid mode was also conducted, but the differences observed did not warrant the additional complication.

handling will be used here to generate an additional set of longitudinal handling characteristics. The pitch CAS design corresponds to a C* model-following system with angle-of-attack limiting and trim. For our linearized analysis we can modify the augmentation design of [16]. Furthermore, a substantial reduction in the order of the system needed to represent the CAS is possible by noting pole-zero cancellations.* The reduced order pitch CAS is illustrated in Figure 14. In this Figure, δ_{ep} is the pilot commanded stick (in ft/sec^2), V_{co} is the cross-over velocity in the C* specification, and the K's are system gains. K_c* is a gain scheduled with dynamic pressure. The parameters of the system have the following values:

$$V_{co} = 324$$

$$K_c^* = \frac{.158}{\bar{g}} = \frac{.158}{245} = .00064 \times 57.3 = .0369$$

$$K_{11}/K_{10} = .082$$

$$K_8/K_{10} = .72$$

With these parameter values the state equations for the augmented system are as given in Appendix C. Note the control input for these equations is the pilot input and the actual elevator deflection is an additional response variable.

* In an actual CAS implementation, this might not be desirable as the eliminated lags are needed for noise suppression, etc.

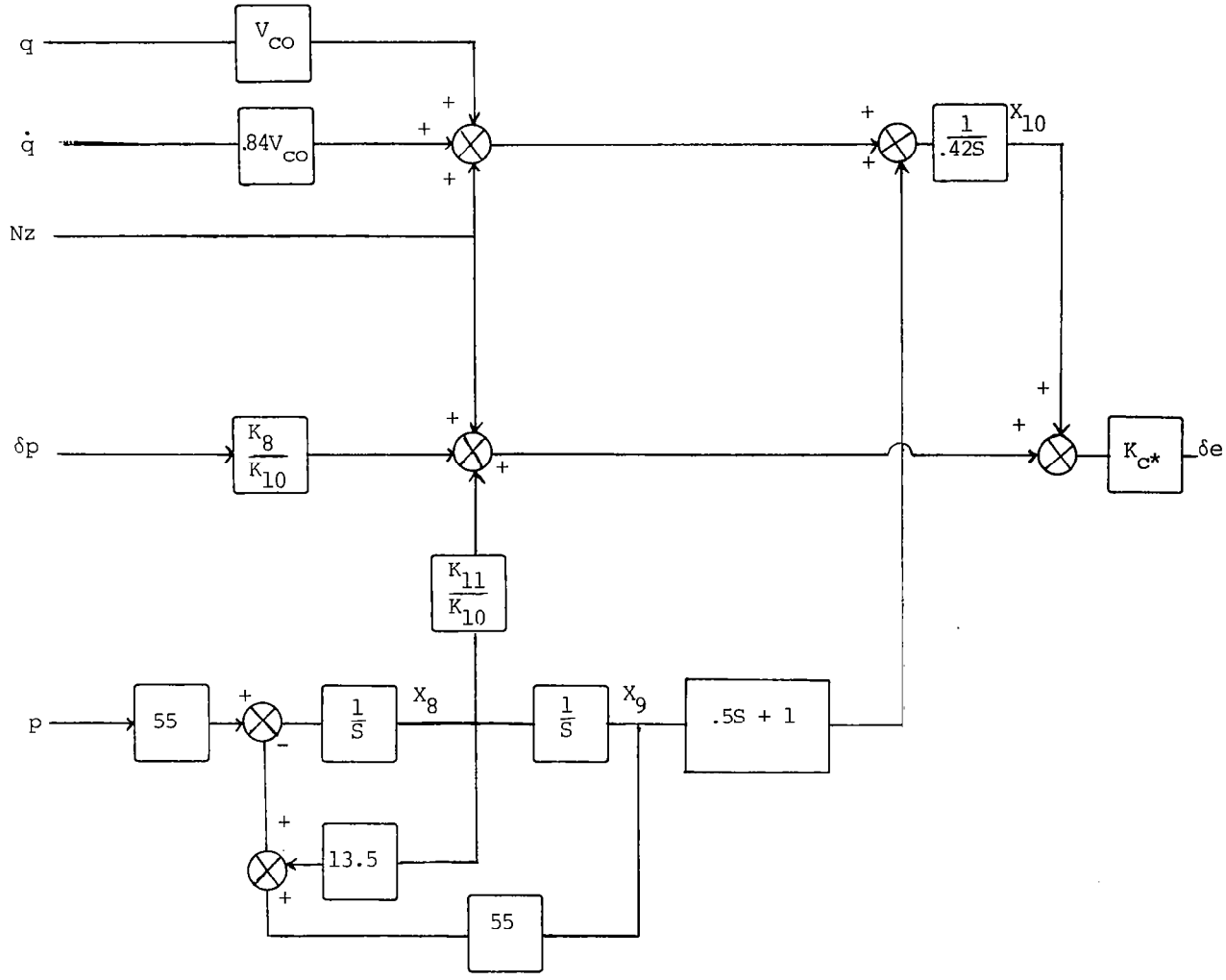

Figure 14. - Reduced-Order Pitch CAS.

The F8 with the pitch CAS has short period roots with a natural frequency of $\omega_{n_{sp}} = 2.78$ and a damping of $\xi_{sp} = .64$; this constitutes a significant improvement in the short period handling qualities.

4.1.2 Lateral Tracking

The lateral tracking task of [20] was self-excited and, therefore, somewhat difficult to analyze. We will examine an independent lateral task with target motion.

a. Geometry

The geometry for lateral tracking, or tracking in the transverse plane, is illustrated in Figure 13b. For small angles, constant and equal velocities, we obtain

$$\dot{\Sigma}_{T_T} = \frac{V}{R} \gamma_{T_T} - \frac{V}{R} (\psi+\beta) \tag{60}$$

b. Target Motion

Unlike the longitudinal tracking problem, it is important to include target attitude (roll angle) as a cue for lateral tracking (because of the essentially third-order transfer between error and control, the tracking task is extremely difficult without this information). Thus we wish to include target roll angle in the definition of random target motion. We shall assume that the target turns are all coordinated (so $\gamma_{T_T} = \psi_T$). The lateral target motion equations are then assumed to be generated by passing zero-mean, white, gaussian noise, w, through the filter.

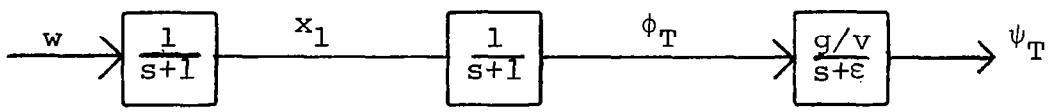

The ε (a small number) in the third filter is included to keep steady-state variance of ψ_T finite. Note that $V\dot{\psi}_T$ is the lateral acceleration of the target.

c. Lateral Aircraft Dynamics

The lateral equations of motion for the F8 at flight condition #11 are

$$\begin{aligned}
\dot{p} &= -2.58p + .251r - 37.8\beta + 17.24\delta_A + 7.016\delta_r \\
\dot{r} &= -.0753p - .273r + 4.36\beta + .816\delta_A - 3.18\delta_r \\
\dot{\beta} &= .078p - .994r - .229\beta + .05173\phi + .0456\delta_r \\
\dot{\phi} &= .997p + .078r
\end{aligned} \tag{61}$$

to which we add

$$\dot{\psi} = r$$

The roots of the lateral characteristic equation yield a roll time constant of .42 sec, a (stable) spiral time constant $\approx$ 40 sec and dutch roll frequency of $\omega_{n_d} = 2.64$ and damping of $\xi_d = .128$.

d. Lateral CAS

The lateral tracking task described above is very difficult. Furthermore, the lateral handling qualities are marginally inadequate with respect to the Dutch Roll response ($\xi_d = .128 < .19$, $\xi_d \omega_{nd} = .34 < .35$) and the roll response could also be improved. Finally, we are interested primarily in a roll-axis lateral tracking task. For these reasons we will modify the basic aircraft dynamics by incorporating a modified version of the Honeywell lateral directional CAS with Inertial Coordination [16]. The yaw-axis CAS of [16] has been simplified by assuming $|RP|<1$, ignoring the accelerometer lag and the integrator for trim ($K_{R_{nysL}} = 0$) and eliminating the aileron-to-rudder crossfeed. With these simplifications, the equations for the augmentation system are

$$
\begin{aligned}
\dot{p}_m &= -5\, p_m + 5\delta_{ap} \\
p_\varepsilon &= p_m - p \\
\hat{\dot{\beta}}_A &= r - \alpha_o\, p - \frac{g}{v}\,\phi \\
\hat{\dot{\beta}}_R &= r - \frac{g}{v}\,\phi - K_{Rp}\, p \\
\delta_{AC} &= -K_{Ae}(p_m - p) - K_{A\dot{\beta}}\,\hat{\dot{\beta}} \\
\delta_{RC} &= K'_{R\dot{\beta}}\,\hat{\dot{\beta}}_R + K_{R_{nysL}}\, n_y - K_{R_{um}}\delta_{ap} + K_{R_{pm}}\, p_m
\end{aligned}
\tag{62}
$$

The parameters and gains are

$\alpha_o = 4.5° = .0785$ rad

$g/V = .0518$ (1/sec.)

$K_{A\dot{\beta}} = (-7.29\alpha + .54) = -.03226$ (sec.)

$K_{Ae} = -.11$ (sec.)

$K_{R\dot{\beta}} = .714$ (sec.)

$K_{R_{nysl}} = .0022 \times 57.3 = .126$ deg/(ft/sec^2)

$K_{R_{um}} = (.16\alpha + .008) \times 57.3 = 1.146$ deg/deg

$K_{R_{pm}} = -.1\alpha + .012 = .00415$ (sec.)

$K_{R_p} = .54\alpha + .042 = .084$

The state equations are given in Appendix C. We have assumed that no pedal inputs are required. The characteristic roots for the augmented system yield a Dutch Roll response with $\xi_d = .62$ and $\omega_{nd} = 2.84$, a roll subsidence time constant of .23 sec and a spiral time constant of 77 sec. In addition, there is a root from the roll-rate command mode with $\tau_M = .2$ sec.

e. Coordinated Lateral Dynamics

A simplified set of dynamics incorporating turn coordination can be derived directly. These dynamics do not incorporate practical CAS features but they can be a useful, simpler alternative. They are obtained by assuming that all turns are coordinated. Thus,

$$\dot{\beta} = \beta = 0$$

$$r = \frac{g}{v}\phi = \dot{\psi} \tag{63}$$

$$\delta_r = 0$$

The state equations for these assumptions are given in Appendix C.

4.2 Parameters of OCM

Parameters for the OCM had to be chosen for the analysis. In particular, the parameters corresponding to human limitations and the cost functional weightings for the lateral control task had to be selected. The values used and their method of determination are described briefly here.

The parameters describing the human limitations are listed in Table 5. The time delay and motor noise ratio are set at nominal values used in past OCM applications [5].

Table 5

OCM MODEL PARAMETERS

Parameter	Value
Time Delay (τ)	.2 second
Neuro-Motor Time-Constant (T_N)	~.15 second
Base Observation Noise Ratio (p_{y_i})	-14 dB
Attention to Longitudinal and Lateral Tasks (f_i)	.5
Motor Noise Ratio (P_{u_i})	-25 dB
Visual Threshold:	
y_i	.05 deg. visual arc
$\dot{y}_i$	.2 deg./sec

Neuromotor time constants were selected via sensitivity analyses as described in Section 2.1.5. There is some subjectivity in selecting "operating" points from the various sensitivity curves, but a value of about .15 sec. for all the F8 tasks considered here seemed reasonable.* The base observation noise ratio of -14dB is greater than the value of -20dB nominally assigned to this parameter [5]. The nominal value curresponds to a fairly constrained laboratory situation in which the subject is highly trained, and receives substantial performance feedback and motivational input. For larger-scale simulations the same degree of training is unusual and higher noise ratios appear to be appropriate.

It was assumed that the pilots would divide their attention equally between longitudinal and lateral control tasks. Further, we assumed that there was no attention-sharing among individual display variables within a task. This corresponds to assuming that the visual presentation of target and horizon are effectively integrated. These assumptions are reasonable and are the simplest we can make; past experience with the OCM indicates that in most cases performance is not very sensitive to attentional allocation so long as a reasonable allocation is used.

The final parameters describing operator limitations are the visual thresholds. These were set at the values determined in [21]. They proved to be of negligible importance in this study.

---

* In the two-control, unaugmented lateral task the time constant associated with rudder control was ~.17 seconds. This value was a consequence of penalizing rudder control rate variances twice as much as aileron control rate variance in the quadratic cost functional.

Application of the OCM also requires specification of a quadratic cost functional embodying the task requirements. For the longitudinal tracking task, the cost functional was simply a weighted sum of tracking error and control-rate with the relative weighting selected to give the desired value of T_N. This situation is identical to that employed in laboratory tracking tasks [5] and gives reasonable results because the LOS tracking error contains both inner- and outer-loop variables (see Equation (57)).

The cost functional for lateral control tasks was more complex. For the CAS-ON and coordinated dynamics, the cost functional included a roll error term, $(\phi_T-\phi)^2$, in addition to the tracking-error and aileron control-rate terms. It was found that penalizing LOS tracking error about three times as heavily as roll error gave a reasonable mixture of response errors.

For the CAS-OFF configuration, sideslip angle and rudder control-rate terms had to be added to the cost functional. The relative penalties on LOS error and roll error were left unchanged from those for the simpler lateral tasks. Sideslip angle was penalized as heavily as LOS error and, as noted previously, the weighting on rudder control-rate variance was twice that on aileron control-rate variance.

The above parameter choices are not necessarily expected to lead to precise performance predictions. They are intended to give reasonable estimates of performance and relative work-load for the tasks considered. More importantly, predicted

changes in performance and workload as a function of simulation parameters should be relatively insensitive to small variations in OCM model parameters*, and these trends are the results of interest here.

4.3 Model Results

4.3.1 Continuous Model

The continuous model was used to analyze the effects of both simulation parameters and problem variables. With respect to the simulation, the effects of integration scheme, servo bandwidth, the order of the hold and the de-aliasing cut-off frequency are investigated for the longitudinal CAS-OFF dynamics and for the coordinated dynamics. Problem dependent effects are explored by comparing CAS-OFF and CAS-ON results for both longitudinal and lateral tracking and by changing input bandwidth for longitudinal tracking.

a. Overall Effects of Simulation

We shall define a basic simulation configuration corresponding to Figure 4 in which the cutoff of the de-aliasing filter is set at half the sample frequency, the visual servo has the DMS characteristics (ζ = .707, ω_n = 25), and a zero-order hold is used in data reconstruction.

---

* This was confirmed, at least partially, by preliminary sensitivity studies.

Figure 15 gives normalized performance for the basic configuration as a function of sample period and integration scheme for longitudinal CAS-OFF, wide-band target tracking and for lateral tracking with coordinated dynamics. Normalized performance is defined as the tracking error obtained for the simulation configuration divided by the tracking error that would be obtained in a continuous simulation with no delays (or in flight).* The normalization is determined by computing the performance utilizing the original, continuous state equations and assuming the only delay is that of the operator (.2 seconds). The scores used in normalizing the results (plus those for other variables) are given in Table 6.

Figure 15 shows substantial effects are introduced by the simulation, particularly at low sample rates. Even for the highest sample rate (T = .03125), there is a 16-20 percent performance degradation for longitudinal tracking and a 20-28 percent degradation for the lateral task. A change of this magnitude exceeds the normal intra- and inter-subject variability in manual tracking tasks and would, therefore, be expected to be significant. For the lowest sample rates the performance degradation ranges from 35-60 percent, numbers that are clearly consequential. It is clear that, from a closed-loop tracking standpoint, A-B integration is superior to Euler integration. We note, too, that the effects are somewhat more severe for lateral tracking than for the longitudinal task.

The results in Figure 15 assume that the only adjustments in pilot strategy resulting from the simulation are an increase

* As might be the case in an all analog simulation with electronic displays providing undelayed visual information.

TABLE 6

RMS PERFORMANCE SCORES PREDICTED
FOR CONTINUOUS SIMULATION

a) Longitudinal Dynamics (Wide Band Input)

VARIABLE	CAS-OFF	CAS-ON
$R\varepsilon_v$,m (ft)	23. (75.6)	22.3 (73.1)
θ, deg	16.0	16.0
n_z, g's	3.02	3.02
δ_e, deg	6.45	6.66

b) Lateral Dynamics

VARIABLE	CAS-OFF	CAS-ON	COORDINATED
$R\varepsilon_T$, m (ft)	4.9 (15.9)	7.62 (25.0)	5.8 (18.9)
$(\phi-\phi_T)$, deg	13.4	18.6	14.4
β, deg	1.39	1.86	-
ny, ft/sec^2	2.45	4.53	-
δ_A, deg	4.1	1.50*	4.9
δ_R, deg	2.33	3.54*	-

* Generated by CAS

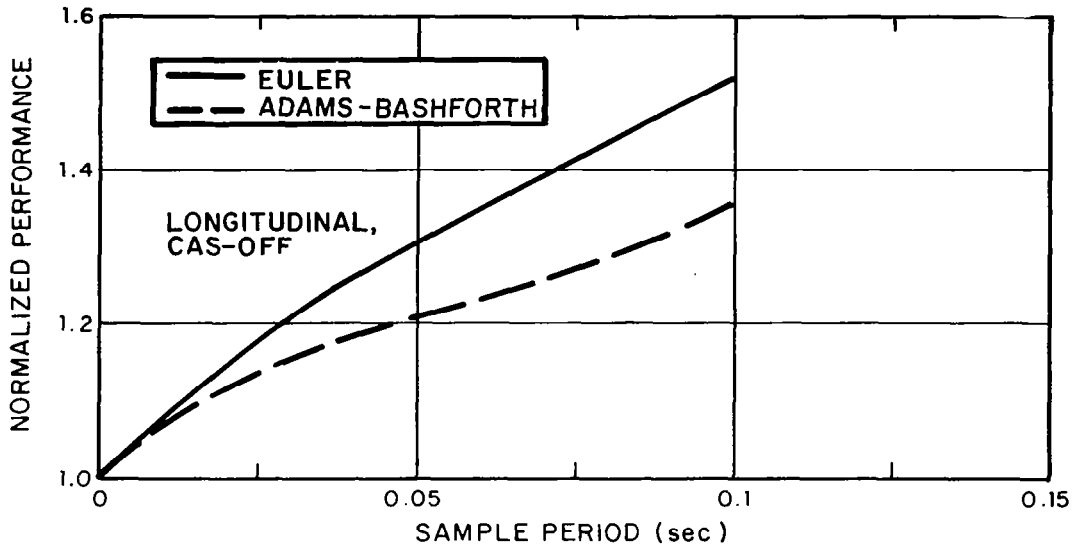

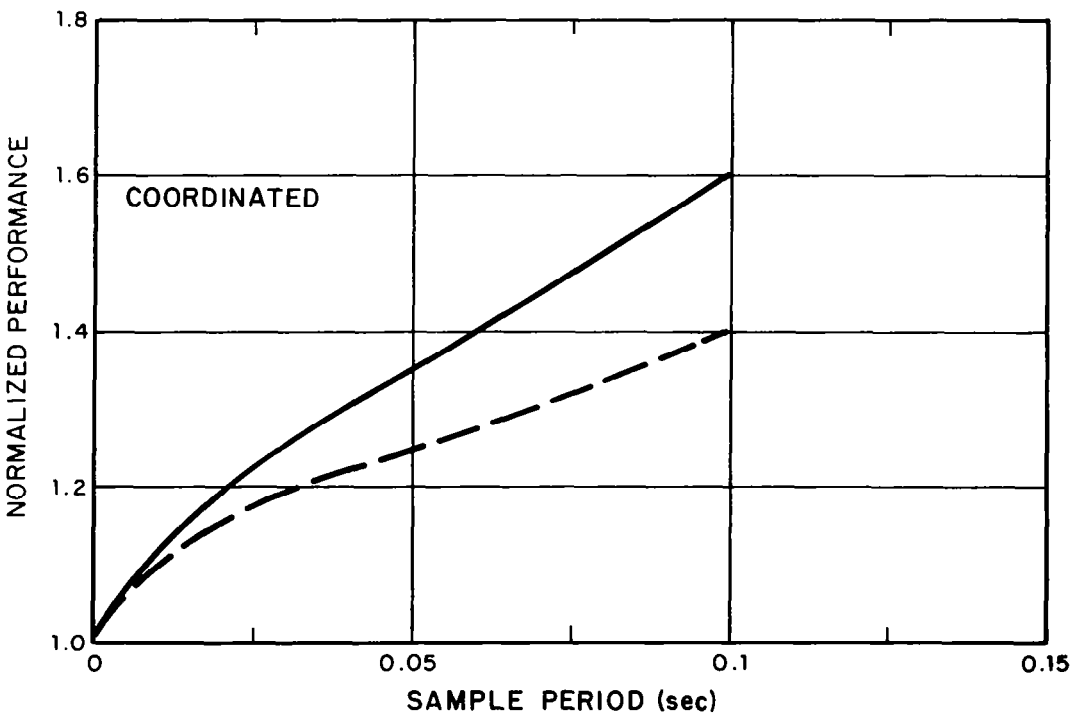

Figure 15. - Effect of Discrete Simulation on Normalized Performance.

in prediction time to compensate for simulator delays and the adoption of an internal model that accounts for the amplitude distortions (and pole perturbations) introduced by the CPU. The results are based on the assumption of a fixed level of attention throughout. However, the pilot may choose to devote more attention to the task (work harder) and, thereby, reduce tracking error. A reasonable question to ask, then, is "How much more attention to the task would be required to achieve performance levels comparable to those that could be obtained in a continuous simulation?" This question can be addressed using the model for workload associated with the OCM [18].

Figure 16 shows the sensitivity of performance to changes in attention as a function of sample period. An attention of 1 on these curves corresponds to an observation noise ratio of -14 dB (with attention shared equally between longitudinal and lateral tasks). Curves are only presented for Euler integration and longitudinal, CAS-OFF dynamics. If a horizontal line is drawn through the T = 0 curve at the point of unity attention, the intersection of this line with the remaining curves defines the attention necessary to achieve the same performance as for continuous simulation. The result of this operation is plotted in Figure 17 which also includes results for A-B integration and for lateral tracking.

It can be seen from Figure 17 that to achieve the performance equivalent to that for continuous simulation, the pilot would have to increase his attentional workload by factors up

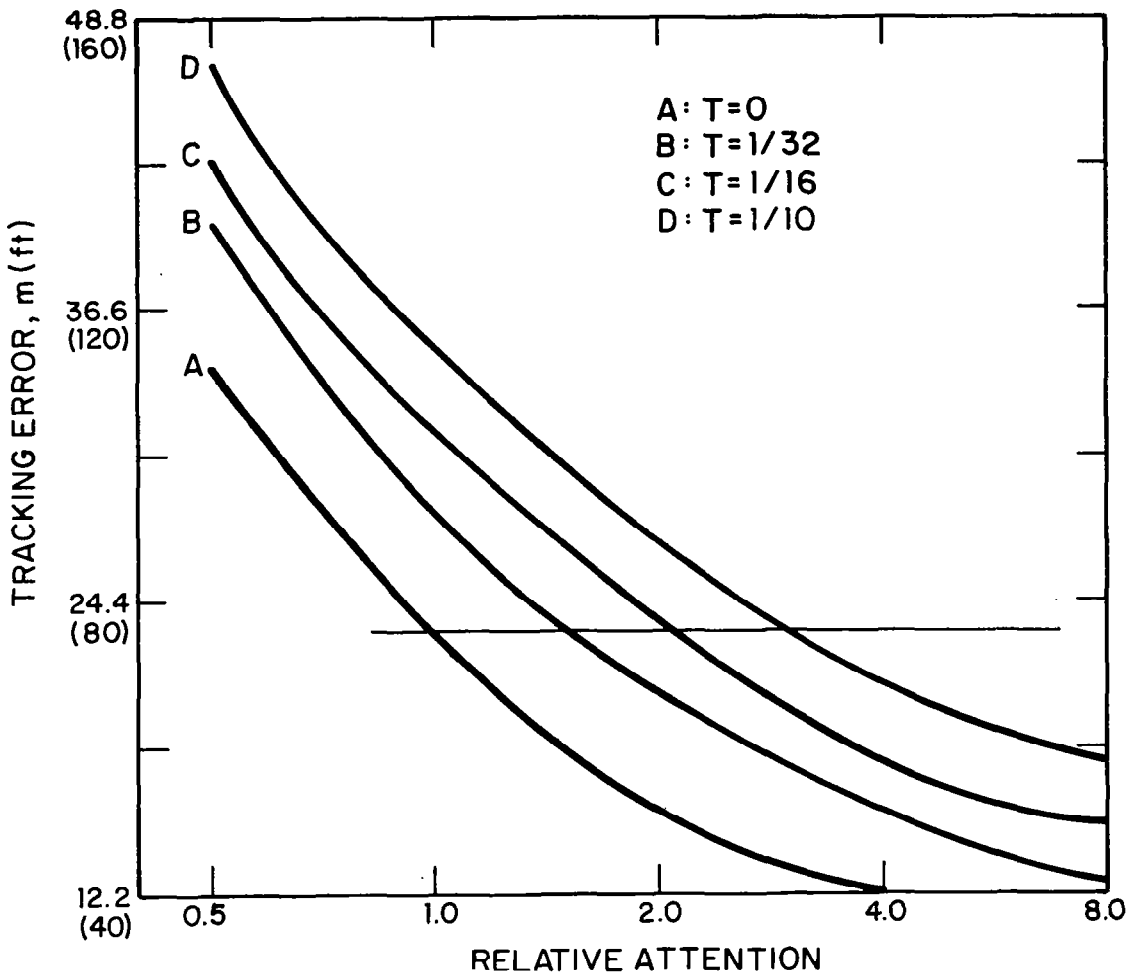

Figure 16. - Sensitivity of Performance to Changes in Attention.

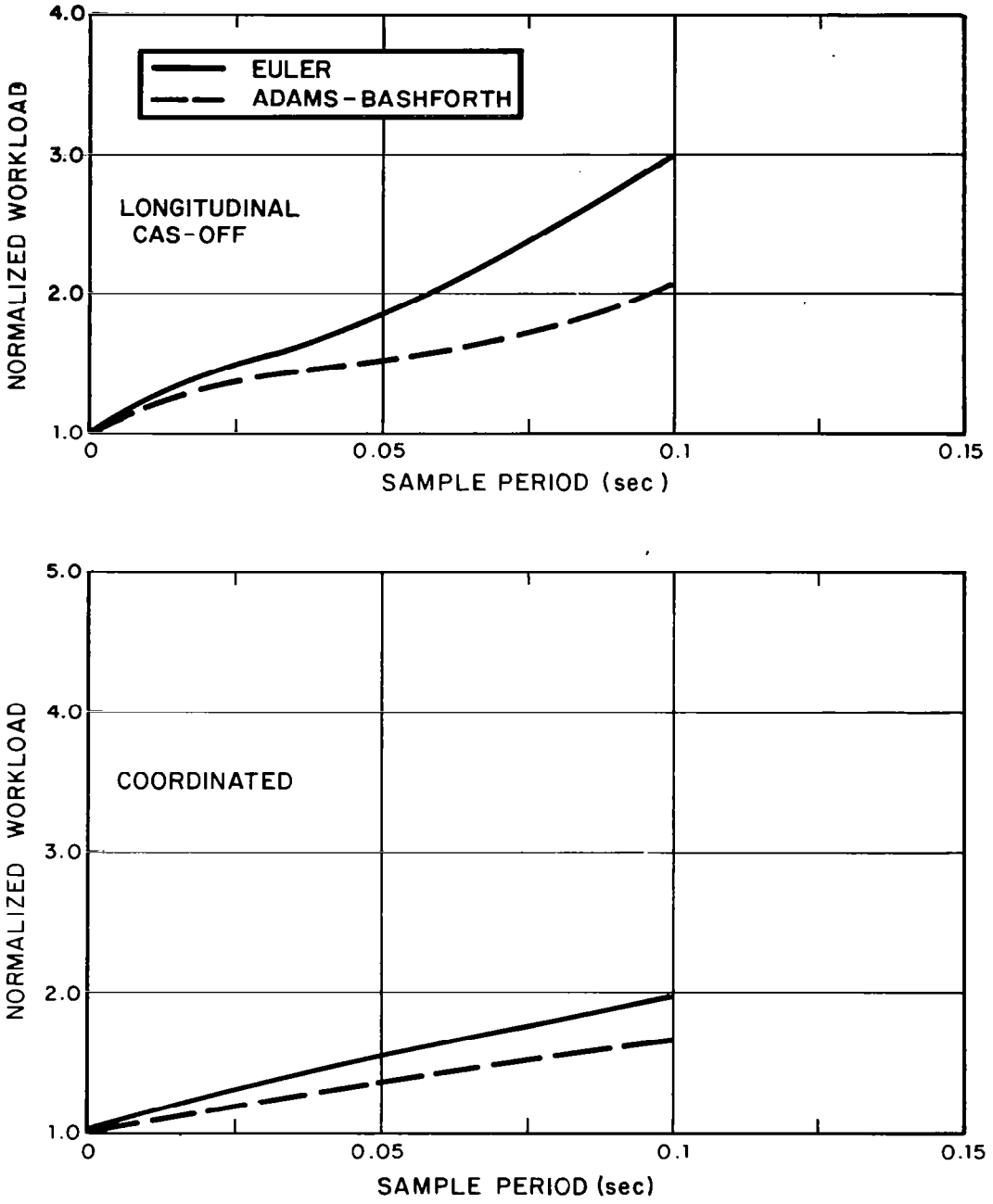

Figure 17. - Simulation Workload Penalties.

to three for the conditions considered.* This is a substantial workload penalty and it might be expected that a compromise between performance degradation and increased workload might evolve. This would be the case, especially if the pilot had not flown the vehicle or a continuous simulator in the same task so that there would be no basis for setting a criterion level of performance.

Before leaving the workload question, a further point is worth noting. In the describing function literature, it has been common practice to associate workload with the generation of lead (see, e.g., [22]). However, there has been no quantitative connection between the amount of lead and the increase in workload. In the present context, one can think of the increased prediction time necessary to compensate for simulator delays as imposing a (processing) workload analogous to that of lead generation. The measure of attentional workload given previously may then be thought of as an alternative means of quantifying the workload imposed by the requirement for additional prediction.

b. Effects of Simulation Components

We have just seen that a basic discrete simulation of an aircraft tracking problem could lead to a serious performance or workload penalty when compared with a continuous simulation with no delay. We now examine the contributions of individual

* It is interesting that the workload penalty for the coordinated lateral task is less than that for the longitudinal task. This is the reverse of the performance trend.

simulation elements to the degradation in performance. Workload is not discussed here, but it is expected that each element would contribute to the penalty in approximate proportion to its percentage contribution to the performance penalty.

Discrete Integration

The previous results show A-B integration superior to Euler integration but the differences are masked to a degree by the contributions of other elements. Figure 18 isolates the effect of the integration scheme. Performance has been computed, assuming no delays for de-aliasing filter, servo or hold, and normalized as in Figure 15. These results emphasize the advantage of A-B, especially with increased sample periods. Comparison with Figure 15 shows that at the longest sample period, the CPU accounts for 40 percent of the total change for Euler but only about 15 percent for A-B.

It is of interest to know how significant the amplitude distortion and pole perturbations are in comparison to the delay. Figure 18 also shows the result of assuming that only integration delay is important in Euler integration.* (The system model then corresponds to the continuous model plus an equivalent integration delay.) The results confirm that, for these dynamics and this task, delay is the most significant contribution to performance degradation.

---

* The amplitude distortions are minor for A-B and, as has been noted previously, it is difficult to get an appropriate estimate of the A-B delay if these distortions are ignored.

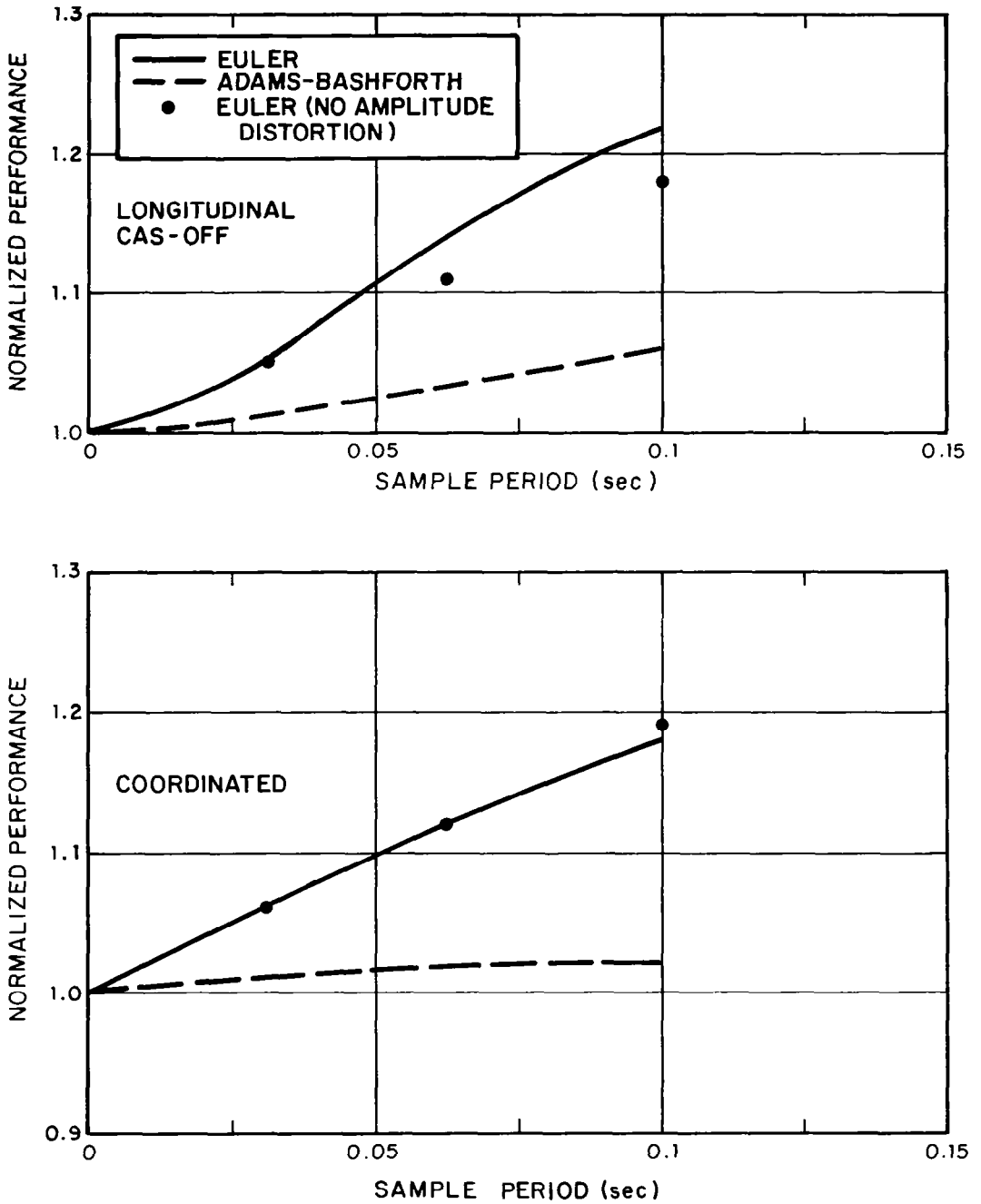

Figure 18. - Effect of Discrete Integration Scheme.

Visual Servo Dynamics

Figure 19 shows the effect of visual servo dynamics. Results are for the basic configuration and for an identical configuration with an infinite bandwidth (zero delay) servo. The visual servo dynamics contribute from 10-14 percent of the total performance loss in the simulator. The lateral task is degraded more than the longitudinal, but the differences are small. There is a slight increase in effect with sample period even though the servo delay is independent of sample period. This undoubtedly results from the fact that as the sample period is increased the system is degraded (stability margins, etc.), so that adding a fixed delay will have a more pronounced effect.

Data Hold

Figure 20 shows the effect of replacing the zero order hold in the basic configuration with a first-order hold. As noted earlier, the continuous model can only indicate a degradation in performance due to the increased delay. Figure 20 shows that the delay associated with the first-order hold has a significant effect (12 percent) only at the largest sample period. The effect is not very large, even for T=.1. Inasmuch as the benefits associated with a first order hold should increase with increasing sample period, it is possible that the differences shown in Figure 20 will be cancelled.

De-aliasing Filter

As in the case of the data hold, the continuous model will only show degradation in performance with reduction in filter

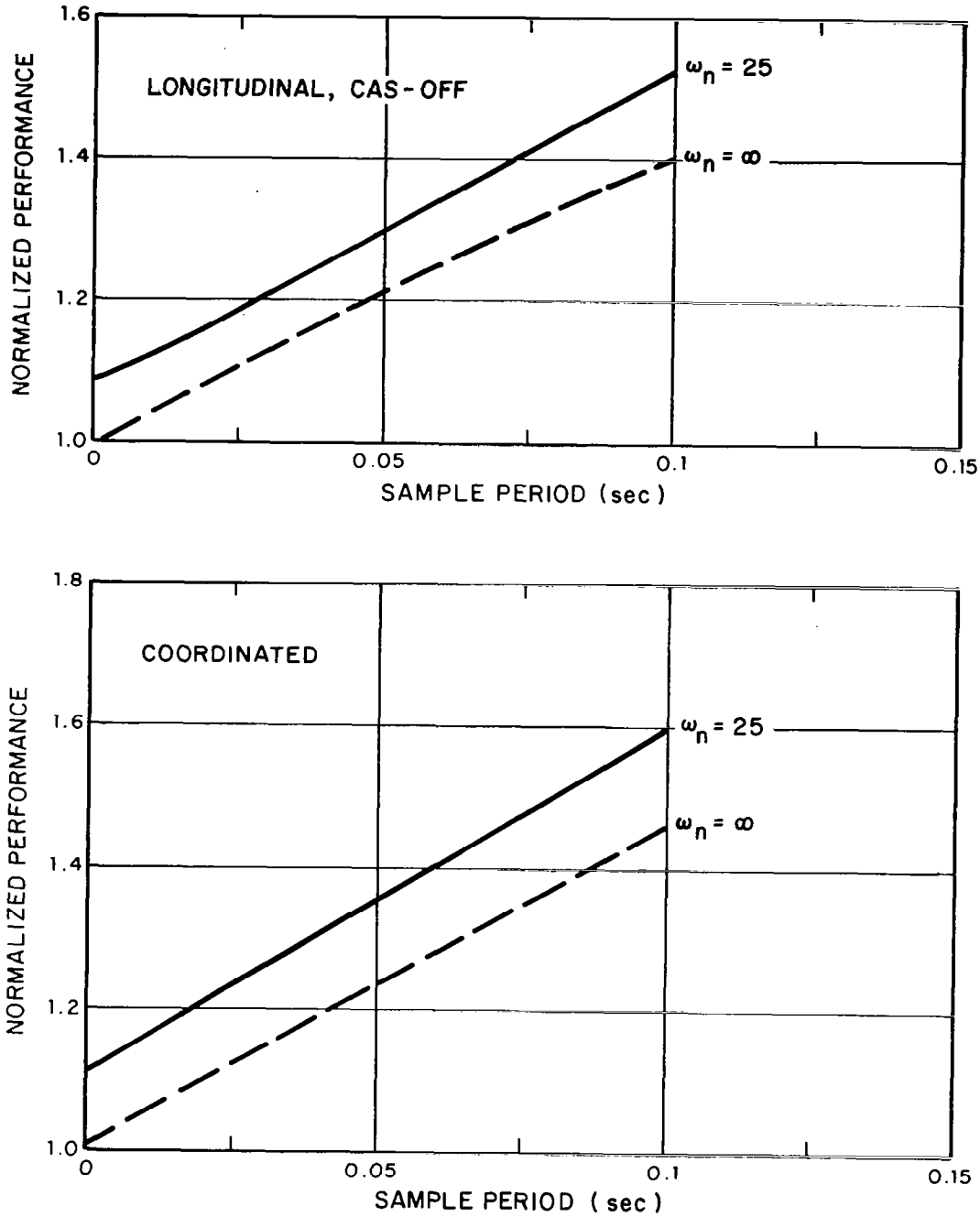

Figure 19.- Effect of Visual Servo Dynamics.

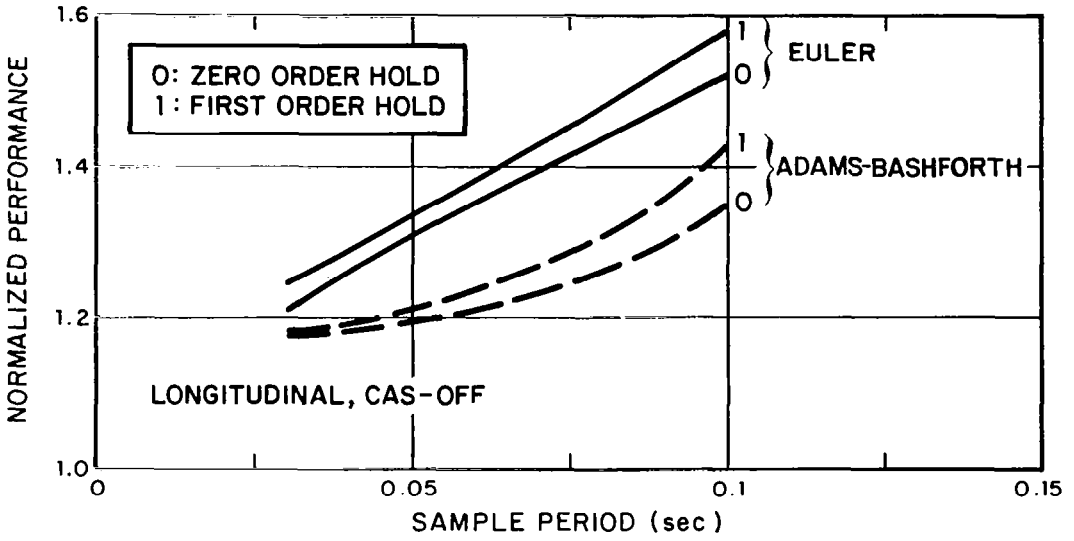

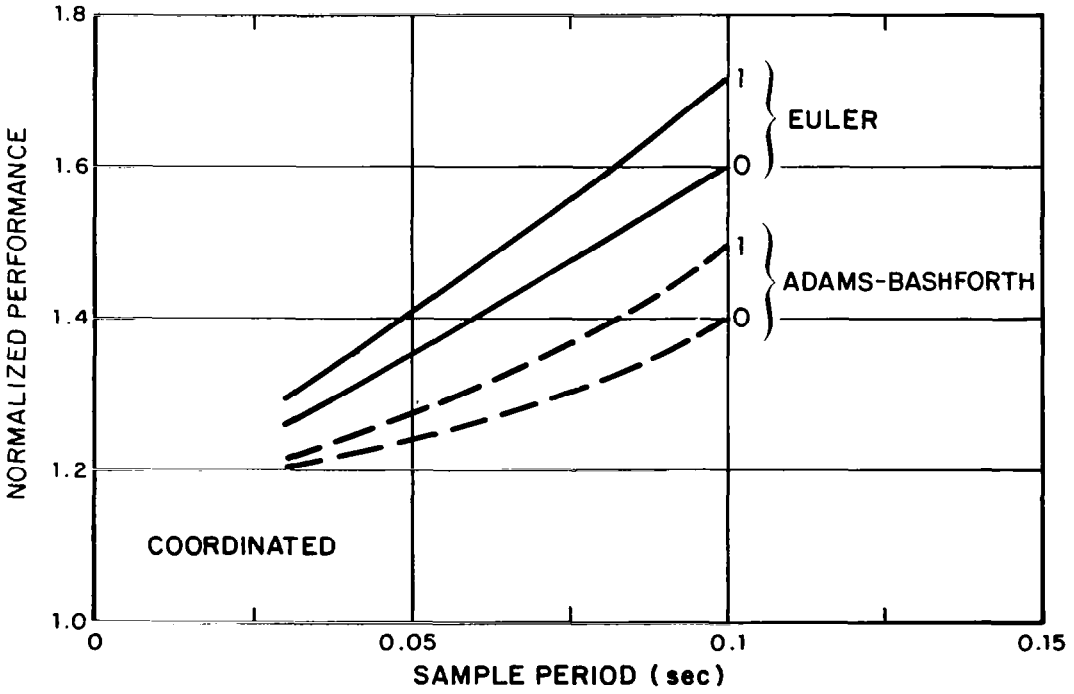

Figure 20.- Effect of Data Hold.

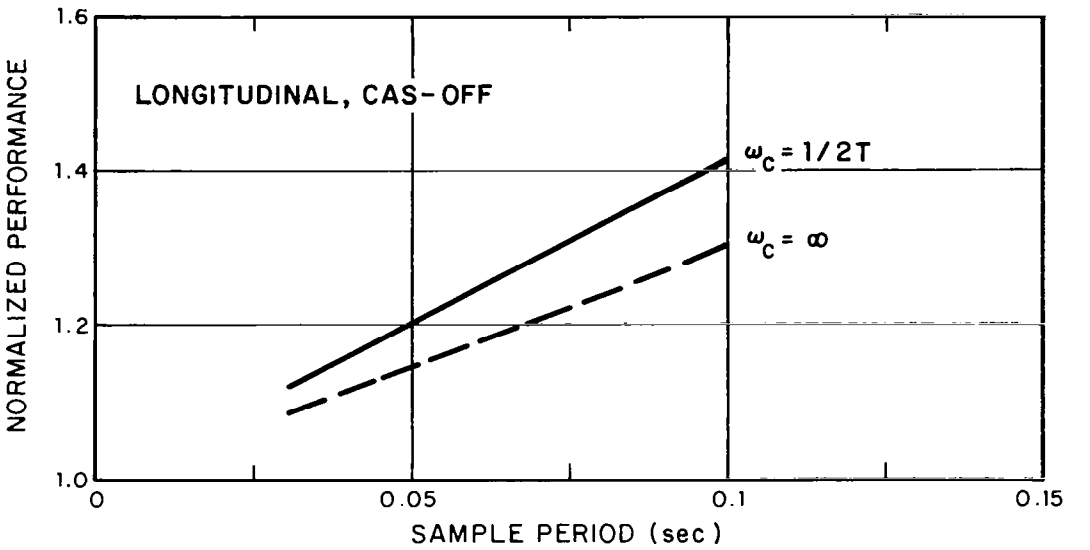

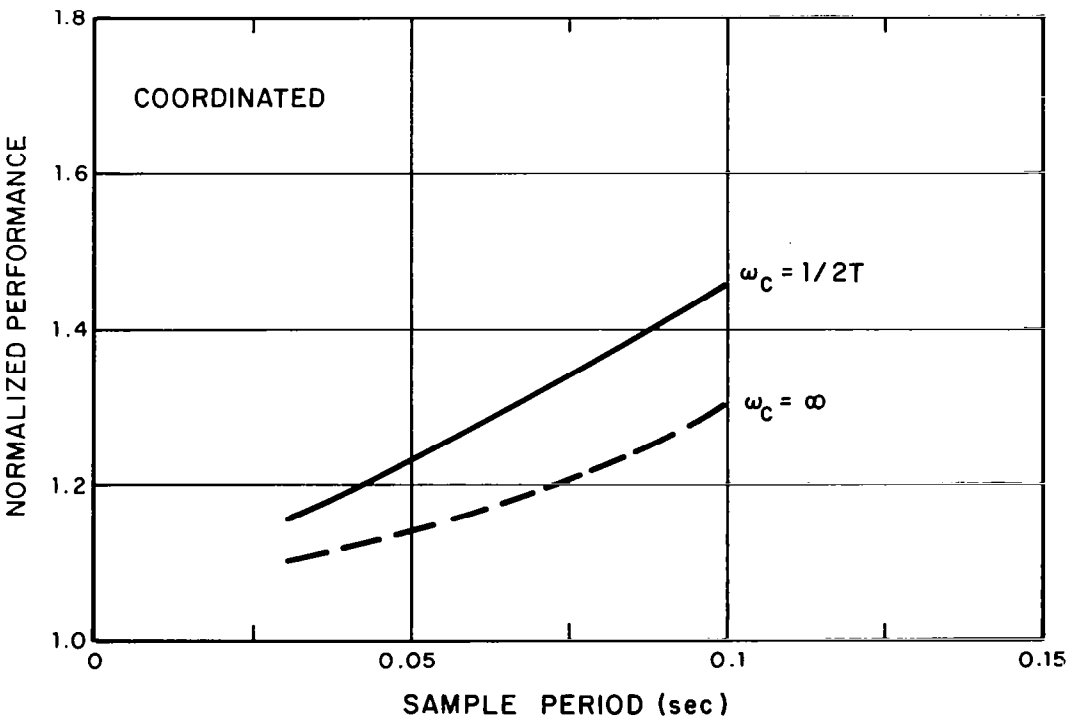

Figure 21.- Effect of Dealiasing Filter.

cut-off frequency. Figure 21 shows the magnitude of this degradation for the nominal filter cut-off of $\omega_c(\text{Hz}) = \frac{1}{2T}$ as compared with an $\omega_c = \infty$. The curves include the effect of (Euler) integration and a zero-order hold, but it is assumed that $\omega_n = \infty$. The results depend on sample period, as expected, and range from 4-16%. The lateral task suffers a somewhat greater loss in performance than the longitudinal as was the case with other simulation parameters.

Control Loading

We consider here a closed loop control loading system involving a linear control loader servo with digital feedback of spring gradient forces. Feedback of bob-weight forces is not considered. The system is based on that employed in the DMS [15]. A sampled data model for this control loading system has been developed in [23] and we will use the results obtained there in our analysis.

From the standpoint of system dynamics, the control loader introduces a second-order filter between the pilot's stick input and the elevator deflection. The filter, when implemented continuously, has a natural frequency of $\omega_n = 28$ rad/sec and a damping coefficient of $\delta = .7$. The open-loop effect of digital implementation of the control loader is to modify the frequency of this filter as shown in the table below. (The damping of the control loader is assumed to be adjusted using hardware damping, to a value of $\delta = .7$ for all sample periods; this assumption is consistent with what has become standard practice in use of the system.) [23].

EFFECT OF DIGITAL IMPLEMENTATION OF CONTROL LOADING

Sample Period	0	.03125	.0625	.1
ω_n (rad/sec)	28	19.5	12.5	8.8

The effects of digital implementation of the control loading system on closed-loop performance are shown in Figure 22. Also shown is the predicted performance for an analog implementation of the control loader. Such an implementation was suggested in [23]. For both cases, it is assumed that the rest of the simulation has the basic configuration described in Section 4.3.1.a, and that Euler integration is used. Performance is normalized to that obtained for a continuous system without control loading.

We note first, from Figure 22, that the control loading dynamics degrade tracking performance in this task, even in the continuous case. However, one should interpret this result cautiously inasmuch as the potential advantages of the kinesthetic cues provided by the loader are not considered. Essentially, the result means that adding filtering in the forward loop degrades tracking performance. Digital implementation of the control loader decreases the effective bandwidth of this filter causing further loss of performance. The overall effect can be sugnificant at low sample rates amounting to about 15% for T=.1. If control loading is necessary the analog implementation seems desirable. With this implementation, the deleterious effects decrease in significance with increasing sample period because the effects of other simulation components become dominant.

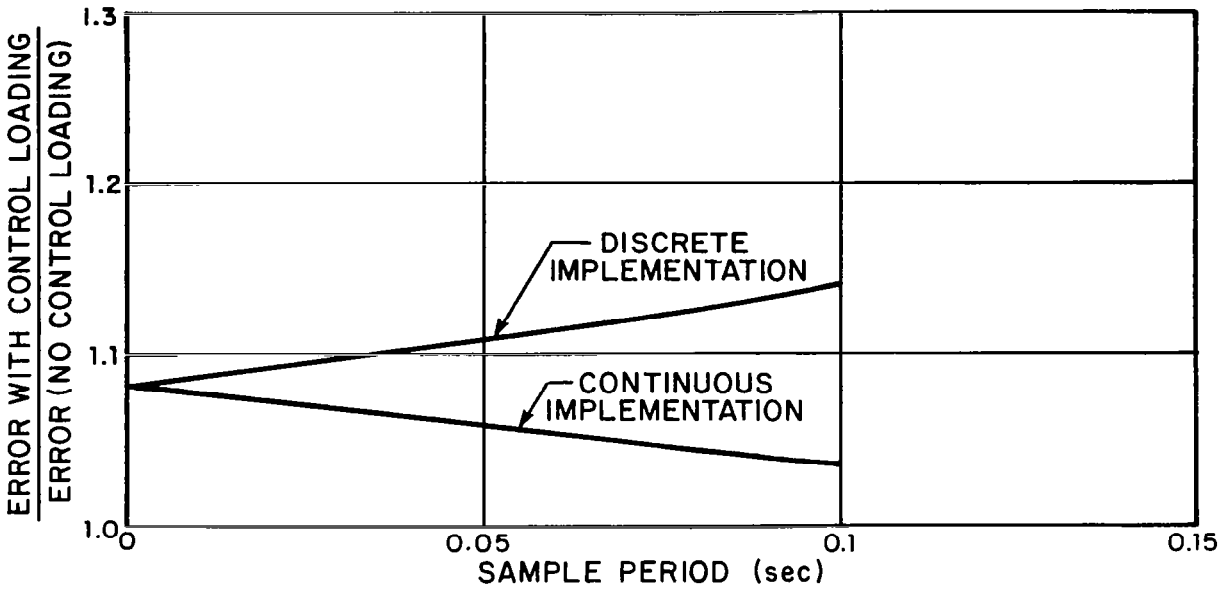

Figure 22.- Effect of Control Loading.

c. Effects of Problem Variables

It was anticipated that there would be an interaction between the effects of simulation parameters and problem variables such as vehicle handling qualities and input bandwidth. Thus, the above tasks were analyzed for different vehicle configurations* and changes in input characteristics.

Input Bandwidth

A limited investigation of the effect of input bandwidth was conducted. Longitudinal CAS-OFF dynamics and the basic simulation with Euler integration were considered. The input was the narrowband tracking input ($\omega_T \approx .2$) described in Section 4.2. The tracking error for the narrowband input was approximately one-third that for the wide band input. However, Figure 23 shows that when scores are normalized to the continuous result, the discrete simulation has a greater effect for the narrowband-input than for the wideband-input. This result is somewhat counter-intuitive. Apparently, with the wide-band input the inherent task difficulty dominates the situation and the effects of simulation delays, etc., are muted to some extent; when the input is made less demanding, the effects of the simulator on performance are emphasized by comparison.

---

* The effects of vehicle handling are also examined in Section 4.4.

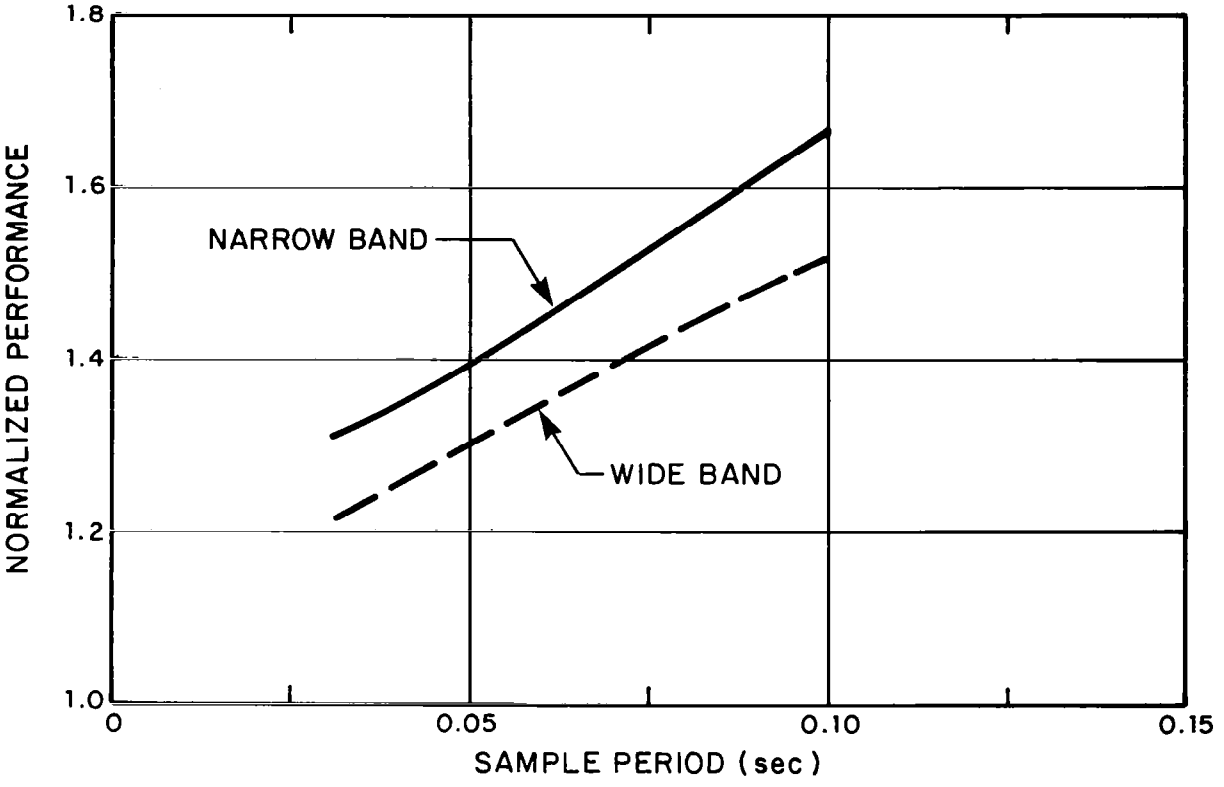

Figure 23. - Effect of Input Bandwidth.

Vehicle Dynamics

Figure 24 compares normalized longitudinal CAS-ON and CAS-OFF performance for the basic simulation. It can be seen that the CAS-ON perforamnce is degraded more by the discrete simulation than the CAS-OFF performance. These results are explained by the fact that the integration delays are larger for CAS-ON dynamics than they are for CAS-OFF dynamics (see Table 3).

The effects of longitudinal dynamics when viewed in terms of absolute performance are interesting and are also shown in Figure 24. The absolute performance for continuous simulation is better for CAS-ON than CAS-OFF (by about 3.5 percent) and the sensitivity to incremental computation delay is about the same for the two configurations. Thus, for a given simulation configuration, absolute performance for CAS-ON and CAS-OFF configurations will be about the same if Euler integration is used and the CAS-OFF configuration can give better performance if A-B integration is used. In other words, the discrete simulation washes out any improvement due to the CAS!

Figure 25 provides comparative results for the three lateral configurations considered. The results do not include any amplitude distortion or pole perturbation effects in the CAS-ON and unaugmented cases. (Recall that approximations to the discrete transfer functions for the CAS-ON and unaugmented lateral dynamics were not obtained.) Also, results are only shown for the basic simulation with Euler integration. All results are normalized by their respective continuous simulation performance.

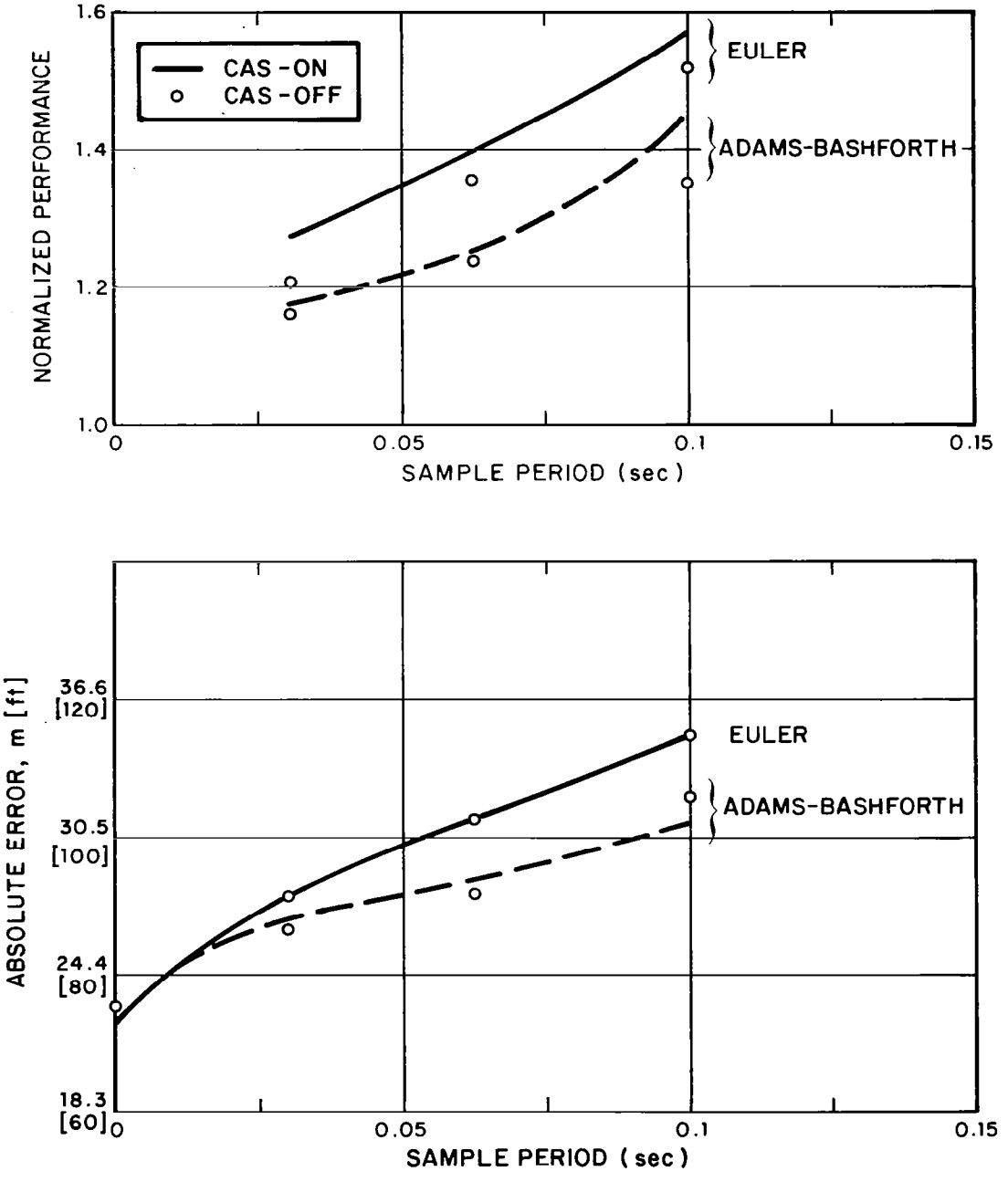

Figure 24.- Effect of Vehicle Longitudinal Dynamics.

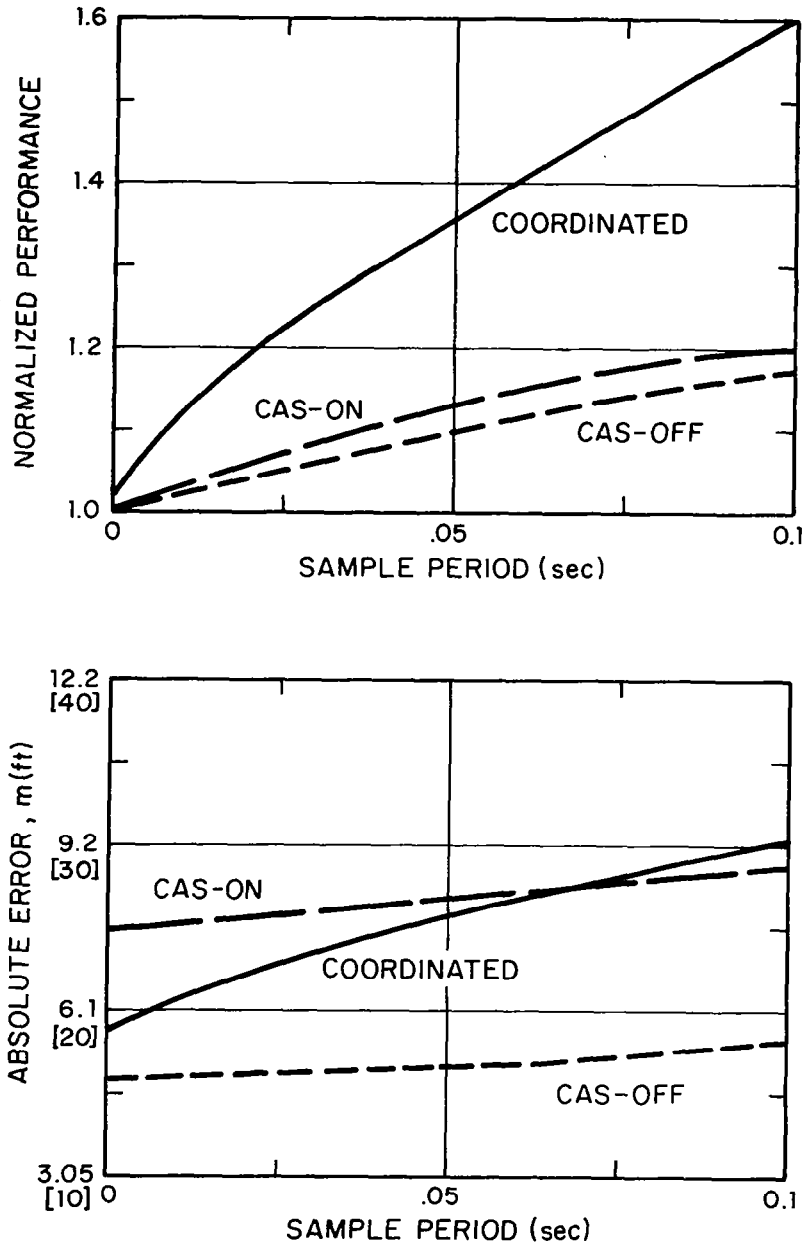

Figure 25. Effect of Vehicle Lateral Dynamics

It can be seen that the coordinated dynamics exhibit the most substantial simulation effect. This does not result from amplitude distortions but, rather, from the added delay for tracking error (see Table 3). CAS-ON and CAS-OFF configuratios display about the same sensitivity to sample period. Tracking error is smallest for the CAS-OFF configuration as is the percentage degradation due to simulation (Figure 25). The CAS-OFF configuration may give the best performance because it is the least constrained system.* However, the requirement for manual rudder control may impose a workload penalty that offsets the performance advantage for the unaugmented system.

4.3.4 Hybrid Model

The hybrid model was used to investigate several issues that could not be examined readily in the continuous model context. However, results were also obtained for conditions that would allow comparison with the continuous model. Results with the hybrid model were limited to the longitudinal unaugmented dynamics because of cost and time considerations. The results obtained are presented and discussed below.

---

* The lateral CAS attempts to keep sideslip angle and lateral acceleration small and this inhibits the transverse tracking, resulting in larger errors for the target motion considered.

Effect of Operator Prediction Time

It is reasonable to assume that a trained operator will attempt to compensate for the delays introduced by the discrete simulation. Moreover, it is expected that an optimal policy is to predict ahead a time equal to the simulation delay. In the hybrid model, operator prediction time* (in number of discrete time steps, Δ) is a parameter (see Section 3.2.3). Thus, it is possible to determine the effects of prediction time on performance.

Figure 26 shows the sensitivity of performance to prediction time (referred to as delay compensation) for the basic simulation configurations with both Euler and A-B integration and for T = .1 and T = .0625. The "internal" models for the OCM in these cases are the continuous approximations to the discrete transfers that incorporate amplitude distortion effects; however, no delay is added to the human's delay of .2 seconds to account for the simulations delays. Thus, we expect the optimal prediction times to be approximately equal to the delay introduced by the simulation. This is indeed the case as can be seen in Figure 26. For Euler integration the minima occur at ~.26 sec and ~.2 sec. for T = .1 and .0625, respectively; the corresponding simulation delays are .27 and .19.

* In excess of the basic prediction time needed to compensate for the operator's delay.

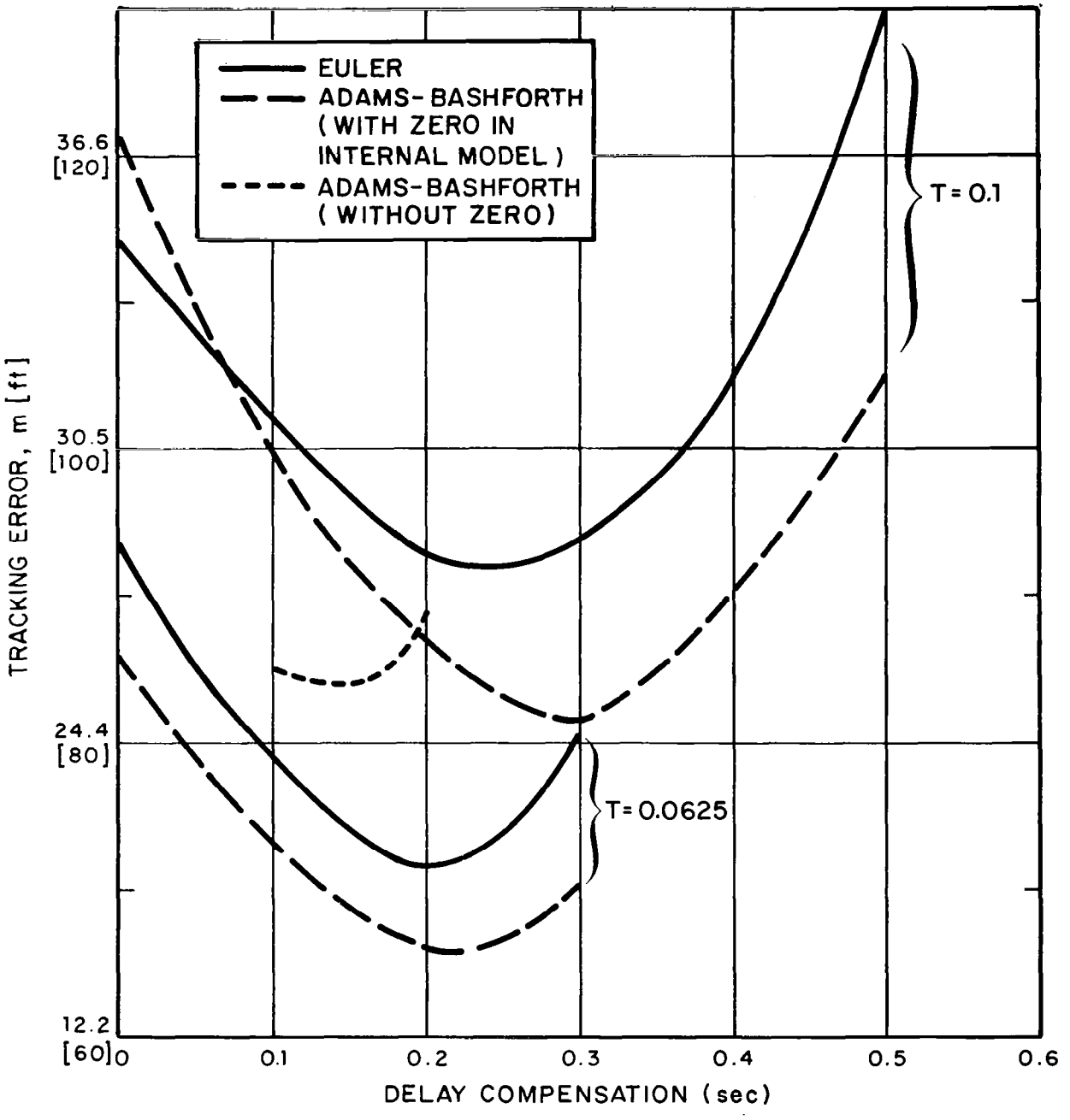

Figure 26.- Effect of Operator Prediction Time.

For A-B integration the minima are at larger compensation times than for Euler. This is consistent with the "zero-modeling" introduced to account for amplitude distortion. With T = .1, the optimal prediction time is around .3 seconds and the simulation delay is ~.32 seconds. For T = .0625, performance does not appear to be very sensitive to prediction time in the neighborhood of the optimum. The simulation delay is ~.21 seconds and performance for this prediction time is indistinguishable from optimal performance. Figure 26 also shows a curve for the case in which the operator's internal model does not include a zero to match the amplitude distortion of A-B integration. It was found that for this case a delay compensation of only .17 seconds was required. This corresponds to the delays introduced by the servo, pre-filter and zero-order hold. The optimal performance was marginally poorer than for the case with amplitude distortion included in the internal model. These results suggest that although including the zero provides a better model of the effect of A-B integration, the increased delay compensation needed to offset the extra lead should not be viewed here as a workload penalty.

These results confirm the estimates of simulation delay used in the continuous model. They also demonstrate implicitly how operators may adapt their behavior to compensate for simulator inadequacy. The added prediction required may impose a workload penalty as noted earlier.

Internal Model

Two questions concerning the pilot's internal model are of interest: 1.) What model will the trained operator adopt when "flying" the simulator?; and 2.) What is the "transfer" effect of a wrong model when transitioning from discrete simulator to continuous simulator (flight)? At least partial answers to these questions for the longitudinal dynamics and Euler integration are provided by the results shown in Figure 27.

Figure 27 gives performance vs. delay compensation for T = .1 and two internal models. One internal model is that derived to match the corresponding discrete transfer function while the other is the basic continuous model. It can be seen that better performance is obtained when the internal model corresponds to the approximate discrete model implying that this is a better model of the discrete simulation than is the original continuous model.

Figure 26 also shows the effect of using the model corresponding to T = .1 seconds in a simulation where T = .03125 seconds (i.e., nearly continuous) as compared to using the model for T - .03125 seconds (i.e., the correct one). If the operator optimizes delay compensation, performance will be degraded by about 10%. If, on the other hand, the delay compensation appropriate to T = .1 is used, a performance penalty of about 19% will be incurred. The effect is not substantial here but it might be in other tasks.

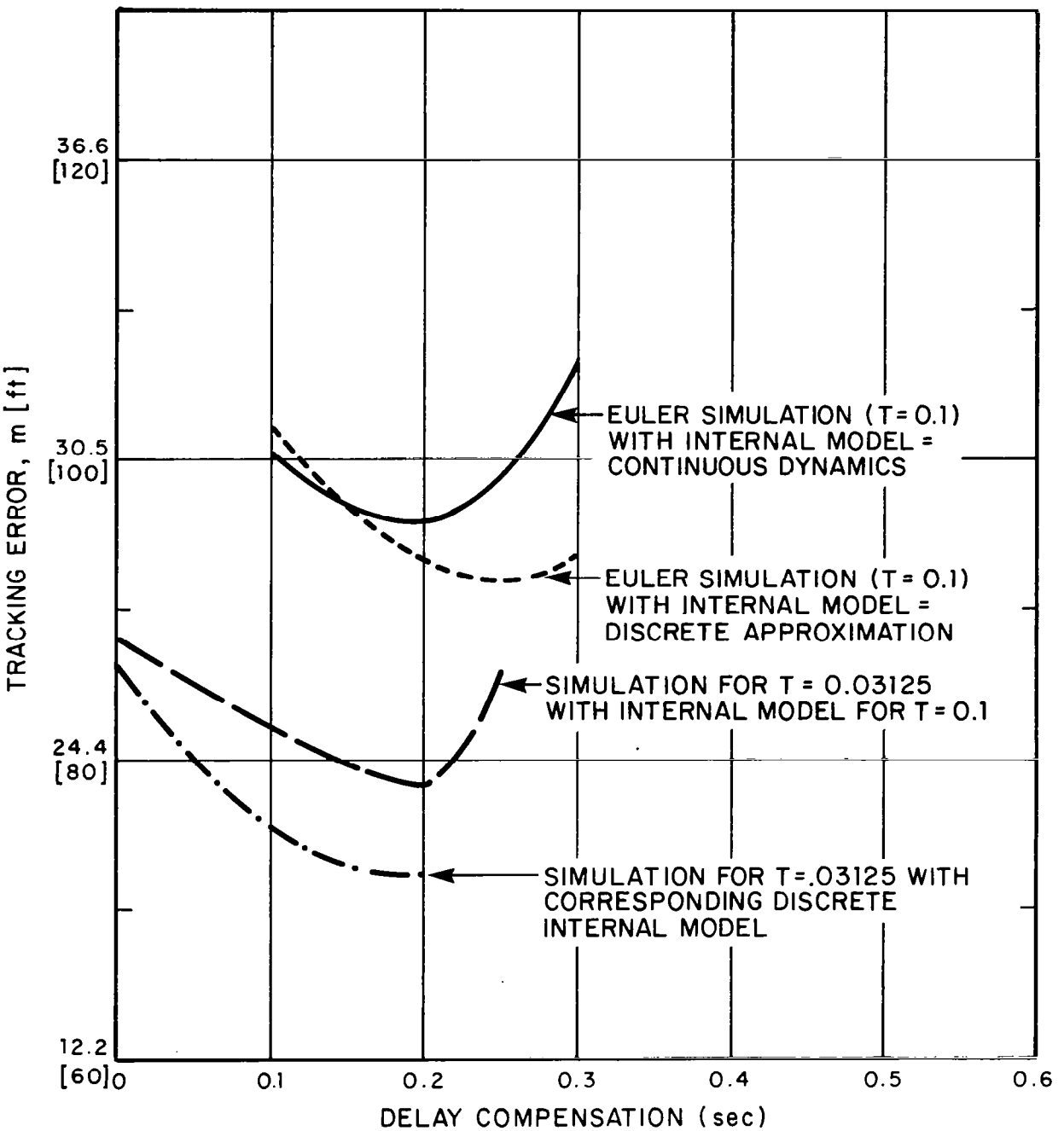

Figure 27. - Effect of Internal Model.

De-aliasing Filter

The effect of the cutoff frequency of the de-aliasing filter on performance is shown in Figure 28. Euler integration of the vehicle equations is used and other simulation parameters correspond to the basic configuration. The results are for a sample frequency of 10 Hz (T = .1) so a cutoff frequency of ω_c = 5 Hz satisfies the Nyquist requirement. Results are obtained for ω_c = 1, 5 and 20 Hz respectively. The lowest value of ω_c = 20 Hz is based on the assumption that there is not significant signal power beyond 5 Hz so there is no need to set the filter breakpoint at that frequency and incur the delay penalty.

The results in Figure 28 favor using the higher cutoff frequency, ω_c = 20 Hz, for this problem. Furthermore, there is a substantial penalty for using the low frequency cutoff. These two results imply that aliasing is not a problem here. We also note that the performance minima for ω_c = 20 Hz and 5 Hz occur at about the correct value of prediction time; the optimum prediction time for ω_c = 1 Hz is much larger but not quite so large as the estimated total simulation delay of .53 seconds.

Data Hold

The effects of using a first order hold instead of a zero order hood are shown in Figure 29 for both Euler and A-B integration at T = .1 and for Euler integration at T = .0625.

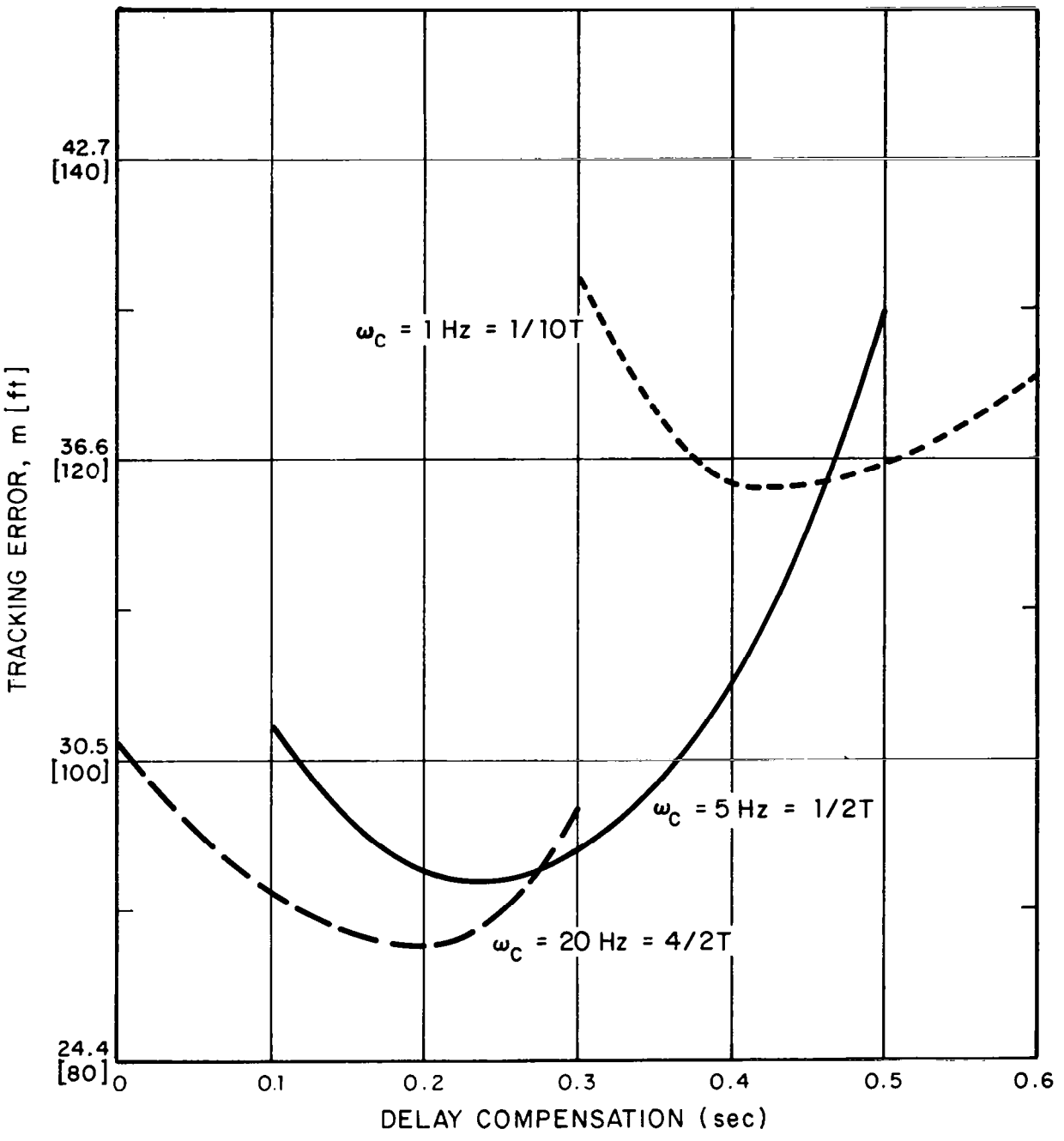

Figure 28. - Effect of Dealiasing Filter Cutoff Frequency (Hybrid Model, T = .1).

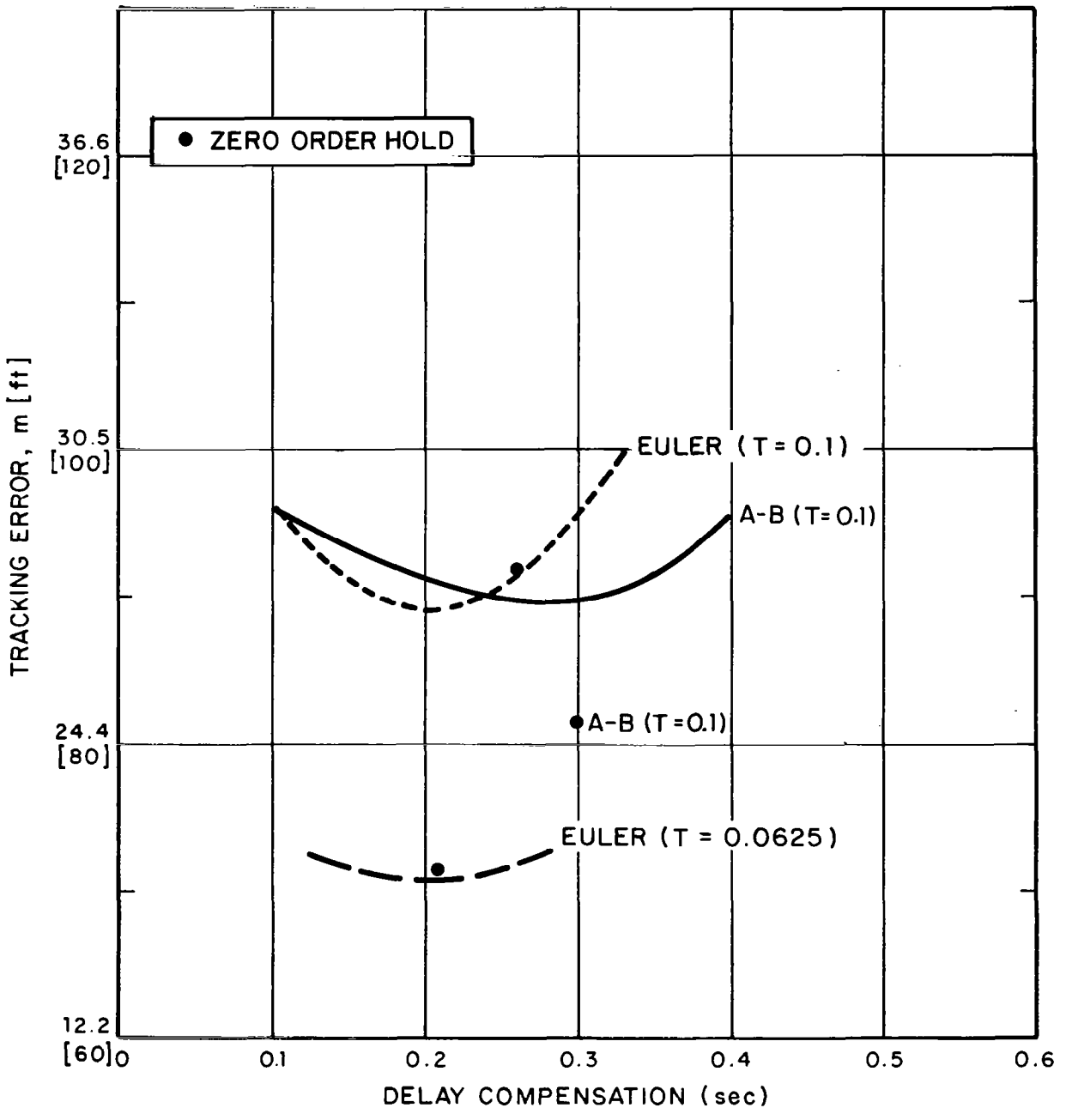

Figure 29. - Effect of First Order Hold (Hybrid Model).

The corresponding best zero order hold performance values are also shown for comparison purposes.

At a sample period of .1 seconds, slightly lower tracking errors are obtained for Euler integration with a first order hold than with a zero order hold; in addition, the minimum performance is obtained with less delay compensation. The situation for A-B integration and a .1 second sample period is the reverse of that for Euler. That is, for A-B integration the first order hold degrades performance.

A possible explanation for these results is as follows. The first order hold uses intersample information which provides some lead. For long sample periods and Euler integration, the effective lead provided is apparently more beneficial than the lag penalty associated with the higher order hold. The beneficial effects of a first order hold should decrease as the sample period decreases. This is supported by the results for T = .0625 which show no difference between the two holds.* In the case of A-B integration the added delay of the first order hold dominates. This may be due to A-B integration having an implicit first order hold at the input (See Section 3.2), thereby reducing any advantage in adding such a hold at the output.

---

* The delay for the first order hold also decreases with decreasing sample period but it remains twice as long as that for the zero order hold.

Comparison with Continuous Model

We have seen, thus far, that the trends of the hybrid model either confirm those of the continuous model or they differ in ways that are interesting but can be explained. The absolute performance predictions of the two models have not been compared yet. This is done in Table 7 and reveals that the two models do not yield the same tracking performance prediction. Moreover, the differences between the two cannot be ascribed to statistical variance associated with the Monte Carlo nature of the hybrid model.

Table 7

COMPARISON OF LONGITUDINAL TRACKING ERRORS PREDICTED BY TWO MODELS

	Euler		Adams-Bashforth	
	Continuous	Hybrid	Continuous	Hybrid
T = .1	115	92	102	81.5
T = .0625	103	71.2	94	65.0

It can be seen from Table 7 that the hybrid model gives consistently lower scores than the continuous model. In addition, for a given integration scheme, the relative change in performance as a function of sample period is substantially greater for the hybrid model than for the continuous model. (However, for a given sample period, both models predict the same relative improvement in going from Euler to A-B integration.)

It appears at this time that the OCM in the hybrid model is obtaining better rate information from the visual servo than is assumed for the continuous model. This was verified by replacing the scaling observation noise on the rate variables in the hybrid model with an additive noise equal to that obtained with the continuous model.* This makes the differences between the two model results negligible. A potential explanation for this phenomenon of better rate information lies in the nature of the data reconstruction process. The visual servo is driven by a series of step inputs from the data hold. The rate response of a continuous servo to a step is a pulse the shape of which depends on the response of the servo and the sample period. It is possible that scaling rate observation noise with this pulse signal leads to smaller effective noises than would be obtained if it were scaled with a smooth signal (as assumed in the continuous model). Alternatively, the pulse-like nature of the response may provide an onset cue (lead) that is being used by the hybrid model in an, as yet, unexplained way.

It should be noted that the hybrid model of the visual servo responds in essentially the same way as would the actual visual servo in the simulation. On the other hand, the operator may perform a smoothing operation that would result in performance closer to that of the continuous model and this smoothing is not incorporated in the hybrid model. At this time, without data, we are unable to resolve the question of which model gives better predictions of absolute performance.

---

* The additive noise in the steady-state case computed by multiplying the steady-state variance of the signal by the noise ratio.

Finally, we believe that the discrepancy between the two models in prediction of absolute performance, does not negate the comparisons made within either model.

4.4 Preliminary Validation

In this section, the continuous model is used to obtain results that can be compared with data obtained previously in an independent experiment. The goal is to show, at least in a preliminary way, that closed-loop models provide a valid means of analyzing simulation effects.

The data we shall use for comparison purposes are taken from [20]. The experiments were conducted on a fixed base simulator with the objective of studying the effects of visual delays on pilot performance and "behavior" and the interaction of those effects with vehicle handling characteristics. The piloting task was to track a target executing a sinusoidal maneuver in altitude. The pursuing aircraft had five degrees of freedom (two longitudinal, three lateral). Time delays were introduced in the visual display of target azimuth and elevation errors. An irreducible delay of .047 seconds was assumed for the simulation and delays were added in units of .03125 seconds.

Experimental details may be found in [20]. However, a few points concerning the experiment are worth mentioning prior to comparing the data with the model results. The sine wave used for the target had a frequency of .21 rad/sec which should prohibit pre-cognitive tracking. Nonetheless, given the large number of runs needed to explore all the conditions of interest it would seem that learning of the input would take place to some degree. The input for lateral tracking,

on the other hand, was completely random being self-induced by inadvertent pilot inputs to the lateral axis; in other words, lateral errors were due solely to pilot remnant. Performance measurement was in terms of altitude and transverse distance errors but the displayed errors were line-of-sight angular errors. Perhaps the most important factors to bear in mind in considering the experimental data are that almost all data are for a single subject (apparently one of the investigators) and there is considerable reason to suspect that training effects could bias the data.

The model was used to analyze only the longitudinal tracking task considered in [20]. To avoid questions about the pilot's knowledge of the sine-wave input, target altitude was assumed to be generated by passing white noise through a second-order Butterworth input. The frequency of the filter and the rms altitude deviations of its output were set to the corresponding sine-wave values of the experiment (i.e., ω = .21 rad/sec and $(\bar{h}_T^2)^{1/2}$ = 21.55m)

Because of the unknown learning effects and the fact that a single subject was used for most of the experiment, OCM model parameters were selected to match the base delay (.047 second) case for each vehicle configuration considered, as follows. Human operator time delay was fixed at .2 seconds for all cases. The neuromotor time constant was picked to match the ratio of control and control-rate scores for each configuration. The values so obtained varied from a TN = .13 sec. to TN = .22 sec., within the range that could be anticipated for this low bandwidth task. Noise ratios were selected to match error

scores (to within about one standard deviation). Motor noise-ratio was set at the "nominal" value of -25 dB for all cases except configuration 1, where a value of -22 dB was used to obtain a better match to performance. Observation noise ratios for the longitudinal task ranged from about -12 dB to about -21 dB. The noise ratios generally decrease as the configuration number increases. The observation noise ratios appear to be on the low side for the high numbered configurations given the additional tasks the operator was required to perform (lateral tracking plus a side task). The lower values may be a result of a training effect (if configurations were run sequentially)* or they may be due to the simplicity of the experimental input.

Model results were obtained for five configurations (listed in Table 8) that covered a range of longitudinal handling qualities. Configuration numbers correspond to those used in [20]. Figure 30 compares model predictions of the effects of incremental delay with the corresponding experimental results. It is important to note that the model results were matched only to the 1.5 unit delay cases. It can be seen that model predictions are generally within $\pm$ 1σ of the data for the added delay cases. Furthermore, the relative sensitivity to delay as a function of configuration tends to parellel that of the data, except perhaps for configuration 8 at the higher delays.

---

* As could be the case for the higher motor noise needed to match configuration 1.

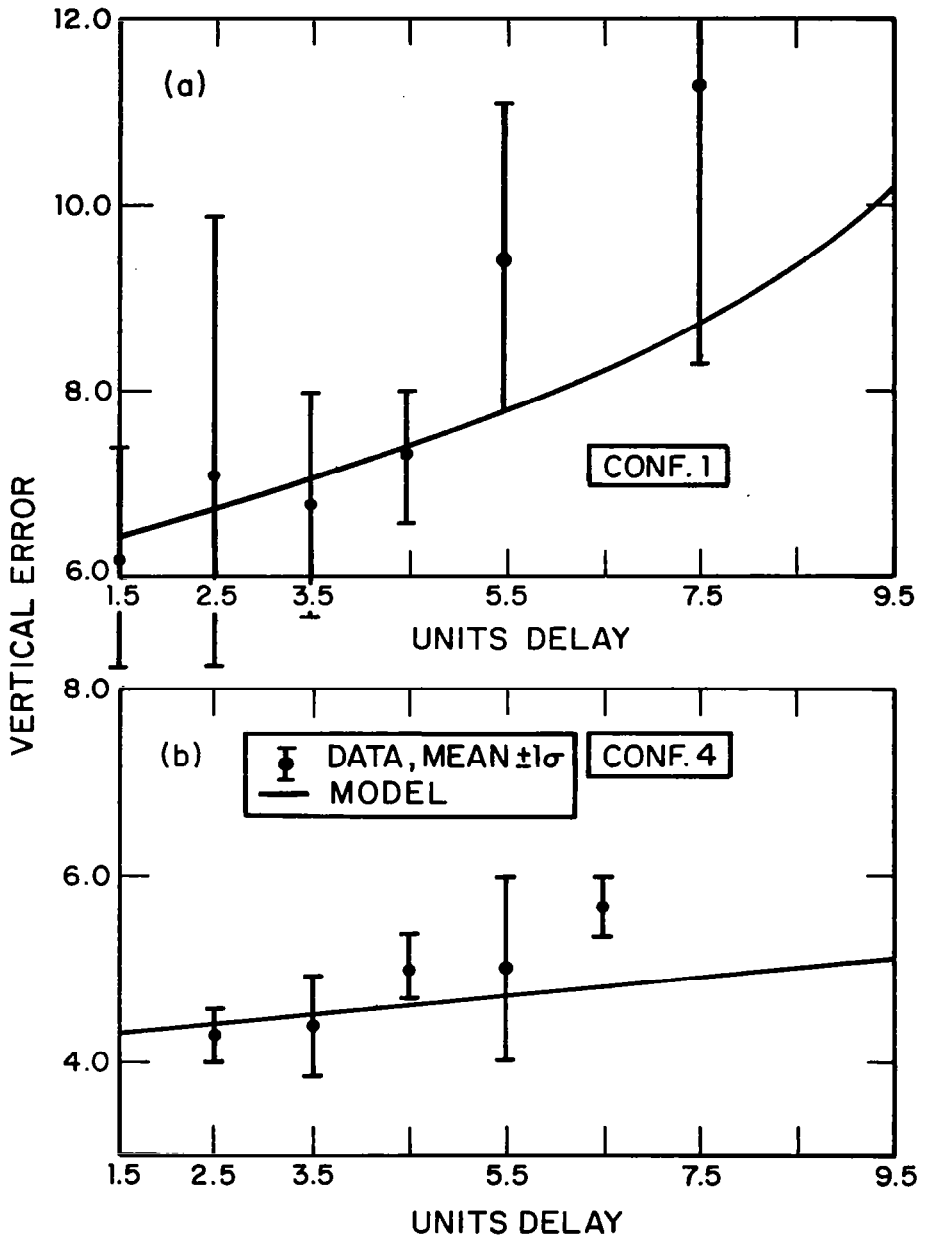

Figure 30. - Comparison of Model Results With Data of Queijo and Riley [20].

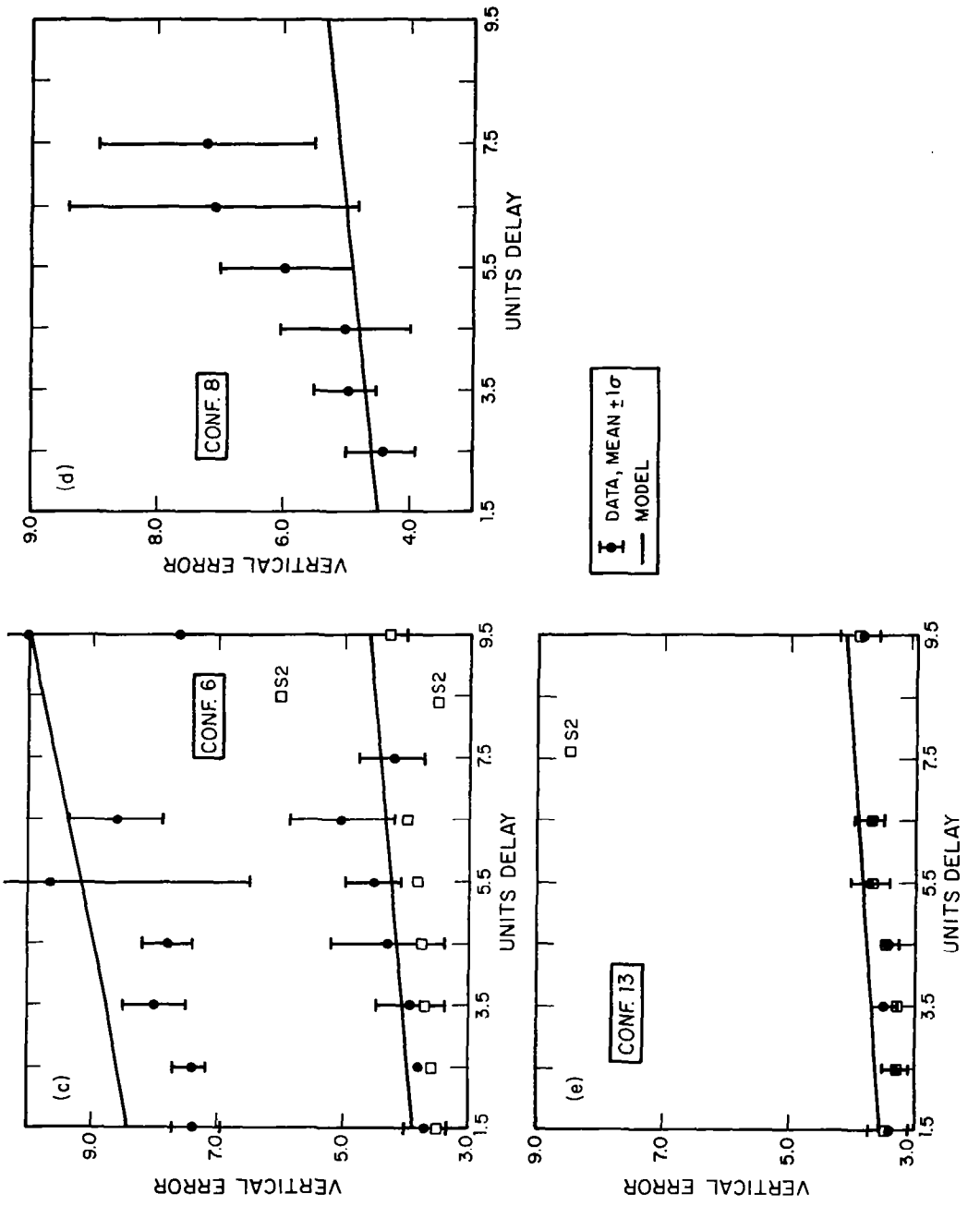

Figure 30.- Comparison of Model Results with Data of Queijo and Riley[20]. (cont.)

Table 8

LONGITUDINAL CONFIGURATIONS [20] ANALYZED

Conf. No.	ω_n	ζ	M_α	M_q	L_α
1	1.5	.3	-4.45	1.10	2.0
4	2.5	.2	-8.25	1.00	2.0
6	3.0	.7	-4.50	-2.2	2.0
8	2.83	1.59	6.00	-7.00	2.0
13	4.5	.70	-11.65	-4.3	2.0

Figure 30c demonstrates two interesting effects. First, for this configuration, data were available from two subjects and these data tend to bracket the model data. Second, data were obtained for a target frequency of twice the base frequency. To "predict" this effect the frequency of the Butterworth noise filter was doubled and all other parameters were left unchanged. The resulting predictions, though less accurate, are the right order of magnitude and capture the effect of changing target frequency.

The limited results presented in this section demonstrate that delays can have serious effects and that the magnitude or the effect depends on problem variables. They also show that a closed-loop model can predict these effects reliably. This conclusion should be tempered somewhat by the fact that it was necessary to first match the results for the individual configurations before predicting the effect of the delays.

5. SUMMARY AND CONCLUSIONS

In this report we have examined the effects of simulation parameters and components on simulator fidelity, particularly with regard to predicting operator performance and workload. Our focus has been on the dynamical aspects of simulator primarily as they relate to closed loop control. We have generally ignored questions that would necessitate inclusion of detailed models for cue perception leaving these to future study.

The human pilot in closed loop control will operate on essentially continuous outputs to generate continuous control inputs. Thus, even when digital computers are used in an aircraft simulation, it is meaningful to consider a continuous transfer function approximation to the open loop simulation dynamics. Such an approximation was developed in this study. It consisted of a rational transfer function multiplied by a transportation lag. The rational transfer function approximated the amplitude distortions introduced by discrete integration of the flight dynamics. The delay accounts for all the phase lags introduced by the simulator components. These phase lags are the major source of degraded performance and increased workload in closed loop tasks. However, the amplitude distortions can be significant for open-loop responses.

The approximate model was incorporated in the standard optimal control model for the human operator. The resulting continuous closed-loop model was used to analyze both overall simulation effects and the effects of individual elements.

The results showed that, as compared to an ideal continuous simulation, the discrete simulation could result in significant performance and/or workload penalties. The magnitude of the effects depended strongly on sample period as expected. From a closed-loop standpoint it seemed clear that A-B integration was much to be preferred. With respect to the other simulation components it can be said that any reduction in delay is desirable. Such reductions inevitably involve increased costs (hardware or software) which must be balanced against the expected improvements.

In addition to the continuous model, a hybrid model was developed to allow us to investigate situations that could not be treated adequately with the continuous model. Several interesting results were obtained with this model. It was shown that for this (fairly typical) aircraft control problem signal bandwidths were such that the de-aliasing filter cutoff frequency could be set at a value greater than half the sample frequency. Also, there appeared to be a potential under certain conditions for improved simulator performance with a first order hold (rather than a zero order hold). The model was also used to show demonstrable effects for adopting the simulator dynamics as an internal model. Predictions of tracking performance by the hybrid model did not agree with those for the continuous model. This discrepancy was not resolved but it appears to be associated with the perception of rate information from the visual servo.

A preliminary validation of the continuous model was performed by comparing model results with data obtained in an independent experiment. The model was capable of predicting

the effects of computational delays in generating visual cues, once model parameters were chosen to match basic conditions.

We believe the models developed here can be very useful in developing engineering requirements for flight simulators. These requirements will be problem dependent which is one reason why models are needed. As we see it now, the process for using the models would involve the following steps:

i) Use standard OCM to analyze ideal continuous simulation to develop baseline performance and to determine expected signal bandwidths.

ii) Analyze distortion introduced by discrete integration schemes and develop continuous models for discrete dynamics valid over the band of interest.

iii) Analyze effects of integration, cue dynamics etc. using continuous model.

iv) Use hybrid model to examine effects of data reconstruction, de-aliasing cutoff frequency etc.

Before this procedure could be used with complete confidence the models described herein need further validation and extension. It is especially important to collect data in a carefully controlled experiment to verify the individual simulation effects. It is also important to resolve the differences between hybrid and continuous models. Once these steps

are taken, the models should then be extended to account for the important issues in providing motion (and perhaps other) cues to the pilot. Finally, it would be useful for both models to develop continuous approximations corresponding to discrete integration of the lateral dynamics of an aircraft.

Appendix A

SYSTEM FUNCTION FROM STICK INPUT TO DISPLAYED OUTPUT

The system function G(s) for the simulation system under analysis may be obtained by computing its steady-state response to an input of the form e^{st}[2]. That is,

$$G(s) = \left.\frac{y_{ss}(t)}{u(t)}\right|_{u(t) = e^{st}}$$

This definition works equally well for time varying parameter systems and for fixed-parameter systems.

For the simulation system indicated in Figure 4 we have

$$y(s) = F_2(s)\ D^*(s)\ u_1^*(s)$$

where

$$u^*_1(s) = \left. u_1(z)\right|_{z=e^{sT}}$$

Using the formula

$$u_1(z) = \sum_{\text{poles of } u_1(s)} \text{residue}\left\{\frac{u_1(s)}{1-e^{sT}z^{-1}}\right\}$$

the output response of the simulation system to an input $u(t) = e^{s_o t}$ is easily computed to be

$$y(s) = F_2(s)\ D^*(s) \sum_{i=o}^{N} \frac{\{(s-s_i)F_1(s)u(s)\}_{s=s_i}}{\{1-e^{-(s-s_i)T}\}}$$

where s_i, i=1, 2, ...,N are the distinct poles* of $F_1(s)$ and $u(s)\ \frac{1}{s-s_o}$. If we drop the terms in $u_i^*(s)$ corresponding to the left half s-plane poles, we obtain the steady-state response

$$y_{ss}(s) = F_2(s)\ D^*(s)\ \frac{F_1(s_o)}{\{1-e^{-(s-s_o)T}\}}$$

To compute $y_{ss}(t)$ by inverse Laplace transformation we note the following:

i) $\frac{1}{\{1-e^{-(s-s_o)T}\}}$ has an infinity of isolated <u>simple</u> poles at $s = s_o+jn\Omega$, n=0, ±1, ±2,..., $\pm\infty$. Since $s_o = j\omega_o$ for a cissoidal input u(t), all these poles lie on the imaginary axis.

ii) The inverse Laplace transform of f(s) is

$$f(t) = \frac{1}{2\pi j} \int_{\sigma-j\infty}^{\sigma+j\infty} f(s)\ e^{st}\ ds$$

$$= \sum_{\substack{\text{poles} \\ \text{of } f(s)}} \text{residue } \{f(s)e^{st}\}$$

iii) The infinity of poles associated with $\frac{1}{\{1-e^{-(s-s_i)T}\}}$ i=1,2,...,N are all in the left half s-plane because s_i are.

* Distinct poles were assumed, in order to keep the expressions simple. Besides, the pre-filter $F_1(s)$ for the simulation system does indeed have distinct poles in the s-plane.

** Strictly, any left half s-plane poles in $F_2(s)D^*(s)$ should not be included in the exprewsion for $Y_{ss}(s)$. The final result G(s;t) will not be affected, however, because we shall not include the contribution due to such poles while computing $Y_{ss}(t)$ and then G(s;t).

iv) The inverse Laplace transform formula in (ii) is valid for a (meromorphic) function of the type in (i).

v) $s=0$ is not a pole in $y_{ss}(s)$.

vi) The residue of $\frac{1}{\{1-e^{-(s-s_o)T}\}}$ at the pole $s_o + jn\Omega$ is $\frac{1}{T}$.

Using (i) - (vi) the steady state response is

$$y_{ss}(t) = \left\{\frac{1}{T}\sum_{n=-\infty}^{\infty} F_2(s_o+jn\Omega)\ D^*(s_o+jn\Omega)e^{(s_o+jn\Omega)t}\right\}F_1(s_o)$$

Hence, the system function $G(s;t)$ from $u(s)$ to $y(s)$ is

$$G(s;t) \triangleq \left.\frac{y_{ss}(t)}{u(t)}\right|_{u(t)=e^{st}}$$

$$= \left\{\frac{1}{T}\sum_{n=-\infty}^{\infty} F_2(s+jn\Omega)D^*(s+jn\Omega)e^{jn\Omega t}\right\}\ F_1(s)$$

Since $D^*(s)$ is periodic in s with period $j\Omega$, we have

$$G(s;t) = \left\{\frac{1}{T}\sum_{n=-\infty}^{\infty} F_2(s+jn\Omega)e^{jn\Omega t}\right\}\ D^*(s)F_1(s)$$

Appendix B

ANALYSIS OF THE DISTORTIONS INTRODUCED BY DISCRETE INTEGRATION IN REAL-TIME SIMULATION OF CONTINUOUS DYNAMIC SYSTEMS

B.1. Introduction

The purpose of this Appendix is to examine the effects of various integration schemes in simulating the dynamics of a continuous system.

Consider a continuous system with state-space representation*

$$\begin{aligned} \dot{\underline{x}}(t) &= \underline{A}_c\, \underline{x}(t) + \underline{B}_c\, \underline{u}(t) \\ \underline{y}(t) &= \underline{C}_c\, x(t) \end{aligned} \tag{B-1}$$

where $\underline{x}$, $\underline{y}$, and $\underline{u}$ are, in general, vectors representing the state, output and input, respectively. For $\underline{A}_c$, $\underline{B}_c$ and $\underline{C}_c$ constant, the system Transfer Matrix is given by

$$\begin{aligned} \underline{y}(s) &= \underline{H}_c(s)\, \underline{u}(s) \\ \underline{H}_c(s) &= \underline{C}_c(s\underline{I}-\underline{A}_c)^{-1}\, \underline{B}_c \end{aligned} \tag{B-2}$$

When Equations (B-1) are "integrated" digitally, many integration schemes lead to a discrete approximation to (B-1) of the form

$$\begin{aligned} \underline{x}_{k+1} &= \underline{A}_d\, \underline{x}_k + \underline{B}_d\, \underline{u}_k \\ \underline{y}_k &= \underline{C}_d\, \underline{x}_k \end{aligned} \tag{B-3}$$

---

* The results are easily modified to include a term in the output equation that is dependent linearly on control.

The specific approximations corresponding to a number of different integration formulae are derived in Section 2. Equation (3) has the following Transfer Matrix:

$$\underline{H}_d(s) = \{\underline{C}_d[z\underline{I}-\underline{A}_d]^{-1}\ \underline{B}_d\}_{z=e^{sT}} \qquad (B-4)$$

where T is the sample period.

We are interested in two problems:

(i) Analysis Problem

How "closely" does the discrete system (3) approximate the continuous system (1)?

(ii) Synthesis Problem

Find a continuous system that approximates the continuous "simulation" system (from human control input to displayed output) in which the discrete system (4) is embedded.

The second problem is clearly related to the first one but is not identical to it. Our interest in this problem stems from the need for a "continuous" model of the simulation that can be used with existing man-machine models to analyze closed-loop performance and workload. In the remainder of this Appendix, we consider the synthesis problem only as it relates to the results of the analysis problem.

B.2. State-space Modeling of Integration Formulae

This section presents the state-space discrete equations that describe the application of various numerical integration schemes to a continuous, linear system. The original, NXC dimensional system is described by Equation B-1.

It is assumed that the input $\underline{u}(t)$ to Equation (B-1) is sampled every T sec, and it is further assumed that the integration algorithm uses

$$\underline{u}(t) = \underline{u}_k \overset{\Delta}{=} \underline{u}(kT) \quad \text{for} \quad kT \leq t < (k+1)T$$

i.e., $\underline{u}(t)$ is assumed piecewise-constant over the integration time-steps. The discrete-time equivalent of Equation (B-1) that describes the evolution of the system is given in a general form (B-3).

The dimension of the control and output vectors in the continuous and discrete-time models are the same. However, to allow for flexibility to consider high-order integration schemes we will not restrict $\underline{x}_k$ and $\underline{x}(t)$ to have the same dimension (although they often will). The matrices $\underline{A}_d$, $\underline{B}_d$ will be a function of $\underline{A}_c$, $\underline{B}_c$ and T for a given integration scheme. Generally, $\underline{C}_d = \underline{C}_c$, in cases when continuous/discrete state dimensions are compatible. Below we give formulae for $\underline{A}_d$, $\underline{B}_d$ for several commonly used integration schemes.

B.2.1 One-Step Methods

Transition Matrix Method

This is an exact integration scheme under the assumption that $\underline{u}(t)$ is piecewise-constant.

$$\underline{x}_{K+1} = e^{\underline{A}_c T}\,\underline{x}_k + \int_0^T e^{\underline{A}_c \sigma}\,\underline{B}_c\,d\sigma\;\;\underline{u}_k$$

Thus, $\dim(\underline{x}_k) = \dim(\underline{x}(t))$ and

$$\underline{A}_d = \exp(\underline{A}_c T) \tag{B-5a}$$

$$\underline{B}_d = \int_0^T \exp(\underline{A}_c \sigma)\,\underline{B}_c\,d\sigma \tag{B-5b}$$

Computation of Equation (B5) is via series summation for "small" T,

$$A_d = I + A_c T + \frac{(A_c T)^2}{2!} + \frac{(A_c T)^3}{3!} + \cdots \frac{(A_c T)^N}{N!} \tag{B-6a}$$

$$B_d = \left[I + \frac{A_c T}{2!} + \frac{(A_c T)^2}{3!} + \cdots \frac{(A_c T)^{N-1}}{N!} \right] \underline{B}_c T \tag{B-6b}$$

Euler Integration

This is perhaps the simplest integration scheme wherein $\dot{\underline{x}}(t)$ is replaced by

$$\dot{\underline{x}}(t) \rightarrow (\underline{x}_{k+1} - \underline{x}_k)/T$$

Thus,

$$\underline{x}_{k+1} = (\underline{I} + \underline{A}_c T)\ \underline{x}_k + T\underline{B}_c\ \underline{u}_k$$

so that

$$\underline{A}_d = (\underline{I} + \underline{A}_c T) \tag{B-7a}$$

$$\underline{B}_d = T\underline{B}_c \tag{B-7b}$$

Runge-Kutta

This is the most common scheme for integrating nonlinear (homogeneous) equations

$$\dot{\underline{x}} = f(\underline{x})$$

Here, $\underline{x}_{k+1}$ is computed according to

$$\underline{x}_{k+1} = \underline{x}_k + \frac{1}{6}\ [\underline{h}_1 + 2\underline{h}_2 + 2\underline{h}_3 + \underline{h}_4]$$

where

$$\underline{h}_1 = Tf(\underline{x}_k)$$

$$\underline{h}_2 = Tf(\underline{x}_k + \frac{1}{2}\ \underline{h}_1)$$

$$\underline{h}_3 = Tf(\underline{x}_h + \frac{1}{2}\ \underline{h}_2)$$

$$\underline{h}_4 = Tf(\underline{x}_k + \underline{h}_3)$$

In the linear case, assuming $\underline{u}(t)$ is constant over the interval (k, k+1),

$$f(\underline{x}) = \underline{A}_c x + \underline{B}_c\ \underline{u}_k$$

Successive substitutions of $f(\underline{x})$ into the above equations gives

$$\underline{x}_{k+1} = \left(\underline{I} + K\underline{A}_c + \frac{T^2\underline{A}_c^2}{2!} + \frac{T^3\underline{A}_c^3}{3!} + \frac{T^4\underline{A}_c^4}{4!}\right) \underline{x}_k + \left(\underline{I} + \frac{T\underline{A}_c}{2!} + \frac{T^2\underline{A}_c^2}{3!} + \frac{T^3\underline{A}_c^3}{4!}\right) T\underline{B}_c \underline{u}_k \quad \text{(B-8)}$$

Therefore, Runge-Kutta is the same as the transition matrix method where N = 4 in the summation Equation (B-6). Note that Euler method corresponds to N = 1.

Implicit Midpoint

For an arbitrary $\dot{\underline{x}} = f(\underline{x})$, implicit midpoint gives $\underline{x}_{k+1}$ according to

$$\underline{x}_{k+1} - \underline{x}_k = Tf[\tfrac{1}{2}(\underline{x}_f + \underline{x}_{k+1})]$$

For the linear case we can solve for $\underline{x}_{k+1}$ explicitly.

Substitute for $f(\underline{x}) = \underline{A}_c \underline{x} + \underline{B}_c \underline{u}$,

$$\underline{x}_{k+1} - \underline{x}_k = \frac{\underline{A}_c T}{2} \underline{x}_k + \frac{\underline{A}_c T}{2} \underline{x}_{k+1} + T\underline{B}_c \underline{u}_k$$

to obtain

$$\underline{x}_{k+1} = (\underline{I} - \underline{A}_c\, T/2)^{-1} (I + \underline{A}_c\, T/2)\underline{x}_k + (\underline{I} - \underline{A}_c\, T/2)^{-1} T\underline{B}_c \underline{u}_k \quad \text{(B-9)}$$

Thus,

$$\underline{A}_d = (\underline{I} - \underline{A}_c\, T/2)^{-1}\ (\underline{I} + \underline{A}_c\, T/2) \qquad \text{(B-10)}$$

$$= \underline{I} + \underline{A}_c T(\underline{I} - \underline{A}_c\, T/2)^{-1}$$

$$\underline{B}_d = (\underline{I} - \underline{A}_c\, T/2)^{-1}\ T\underline{B}_c \qquad \text{(B-11)}$$

Simplified Integration

In this method the transfer function for $\frac{Y(s)}{u(s)}$ is considered and the "integrators" 1/s are replaced by

$$\frac{1}{s} \rightarrow {}^{T}\left[\frac{1}{z-1}\right] \qquad \text{(B-12)}$$

thus yielding a discrete differential equation, or z transfer function. It is necessary to then find a state-space realization for the transfer. Since

$$\underline{H}(s) = \underline{C}_c(s\underline{I} - \underline{A}_c)^{-1}\ \underline{B}_c$$

substituting

$s = \frac{1}{T}\ (z-1)$ gives

$$\underline{H}(z) = \underline{C}_c[z\underline{I} - (\underline{I} + \underline{A}_c T)]^{-1}\ T\underline{B}_c$$

This z-transfer function is realized by

$$\underline{C}_d = \underline{C}_c$$

$$\underline{B}_d = T\underline{B}_c$$

$$\underline{A}_d = (\underline{I} + \underline{A}_c T)$$

i.e., the same as Euler's method--to no surprise.

Tustin Method

In this approach, a better approximation than Equation (B-12) to 1/s is used, namely

$$\frac{1}{s} \rightarrow \frac{T}{2}\left[\frac{z+1}{z-1}\right] \tag{B-13}$$

If Equation (B-13) is substituted into $\underline{H}(s)$, or equivalently into

$$s\,\underline{x}(s) = \underline{A}_c\,\underline{x}(s) + \underline{B}_c\,\underline{u}(s) \tag{B-14}$$

$$\underline{y}(s) = \underline{C}_c\,\underline{x}(s)$$

it is easy to see that both numerator and denominator terms in $\underline{H}(z)$ will have powers of z^{NXC}. This means that to find a realization of the equivalent $\underline{H}(z)$ transfer function we require

$$\underline{y}_k = \underline{C}_d\,\underline{x}_k + \underline{D}_d\,\underline{u}_k$$

i.e., we need $\underline{u}_{k+1}$ during the interval (k, k+1) in which we are computing $\underline{y}_{k+1}$. Clearly, this is not feasible in the feedback, or control context, and the Tustin method will not be pursued

any further. Note that the Tustin method is exactly equivalent to the implicit trapezoidal method where

$$\underline{x}_{k+1} - \underline{x}_k = \frac{T}{2} [f(\underline{x}_k) + f(\underline{x}_{k+1})]$$

and $$f(\underline{x}_{k+1}) = \underline{A}_c \underline{x}_{k+1} + \underline{B}_c \underline{u}_{k+1}.$$

B.2.2 Two-step Methods

It is fairly clear that implicit integration methods will not prove useful for cases when there is an independent, unknown *a priori*, input u(t). This is unfortunate since the Equation (B-13) approximates 1/s well; i.e., for low frequencies

$$\frac{T}{2} \frac{e^{sT}+1}{e^{sT}-1} \approx \frac{1+sT/2+s^2T^2/4+...}{1+sT/2+s^2T^2/6+...} \approx \frac{1}{s} \qquad \text{(B-15)}$$

Explicit Trapezoidal

The problem with the above is the need for $\underline{u}_k$ and $\underline{u}_{k+1}$ at time k. One way to amend this is to accept a one step delay and use instead $\underline{u}_{k-1}$ and $\underline{u}_k$ at time k. This scheme is referred to as the explicit trapezoidal, or modified Tustin,

$$\underline{x}_{k+1} - \underline{x}_k = \frac{T}{2} [f(\underline{x}_{k-1}) + f(\underline{x}_k)] \qquad \text{(B-16)}$$

wherein

$$\frac{1}{s} \rightarrow \frac{T}{2} \frac{(z+1)}{z(z-1)} \qquad \text{(B-17)}$$

For low frequencies,

$$\frac{T}{2}\ \frac{1+z^{-1}}{z-1} = \frac{1}{s}\ \ \frac{1-sT/2\ \ldots}{1+sT/2+\ldots}$$

i.e., an integrator with a T second delay, as anticipated.

In order to find the discrete-time state-space representation for this method, we substitute $f(\underline{x})$ into Equation (B-16)

$$\underline{x}_{k+1} - \underline{x}_k = c_1(\underline{A}_c\ \underline{x}_k + \underline{B}_c\ \underline{u}_k) + c_2(\underline{A}_c\ \underline{x}_{k-1} + \underline{B}_c\ \underline{u}_{k-1})$$

where $c_1 = T/2$, $c_2 = T/2$. Since

$$\underline{x}_{k+1} - (\underline{I} + c_1\ \underline{A}_c)\ \underline{x}_k - c_2\ \underline{A}_c\ \underline{x}_{k-1} = c_1\ \underline{B}_c\ \underline{u}_k + c_2\ \underline{B}_c\ \underline{u}_{k-1}$$

$$\underline{y}_k = \underline{C}_c\ \underline{x}_k \qquad \text{(B-18)}$$

it can be seen that the equation cannot be represented by means of an NXC-order discrete system. We need $\underline{x}_k$ and $\underline{x}_{k-1}$ at time k so that we require a 2 NXC order model. A suitable representation that is convenient for our work is

$$\underline{\chi}_{k+1} = \underbrace{\left[\begin{array}{c|c} \underline{I} + c_1\ \underline{A}_c & \underline{I} \\ \hline c_2\ \underline{A}_c & 0 \end{array}\right]}_{A_d} \underline{\chi}_k + \underbrace{\left[\begin{array}{c} c_1\ \underline{B}_c \\ \hline c_2\ \underline{B}_c \end{array}\right]}_{B_d} u_k \qquad \text{(B-19a)}$$

$$y_k = \underbrace{[C_c \vdots 0]}_{C_d}\ \underline{\chi}_k \qquad \text{(B-19b)}$$

This form is chosen so that the first NXC component of χ is the vector $\underline{x}_k$. By taking the z-transform of Equation (B-19), we can readily verify that $\underline{x}_k$ satisfies Equation (B-18) as required. Other forms of $\{\underline{A}_d, \underline{B}_d, \underline{C}_d\}$ can be obtained via similarity transformations. This approach yields some insight as to the modal structure of the discrete system--there are now two NXC modes--NXC approximate the original modes and NXC modes are "fast", i.e., of order T.

Adams-Bashforth

The idea behind this method is to ameliorate the inherent delay of the explicit trapezoidal scheme. Here, we obtain $\underline{x}_{k+1}$ according to

$$\underline{x}_{k+1} - \underline{x}_k = T(\underline{f}_k + \frac{1}{2}\,\Delta\underline{f}_k + \frac{5}{12}\,\Delta^2\underline{f}_k + \ldots)$$

where ∇ is the backward difference operator $\nabla fk = fk - fk-1$. For a two-step method we have

$$\underline{x}_{k+1} - \underline{x}_k = T\left[\frac{3}{2}\,\underline{f}(\underline{x}_k) - \frac{1}{2}\,\underline{f}(\underline{x}_{k-1})\right] \qquad \text{(B-20)}$$

which corresponds to the replacement

$$\frac{1}{s} \rightarrow \frac{T}{2}\;\frac{3z-1}{z(z-1)} \qquad \text{(B-21)}$$

For low frequencies this gives

$$\frac{T}{2}\;\frac{3-z^{-1}}{(z-1)} = \frac{1}{s}\left[\frac{1+sT/2-s^2T^2/4}{1+sT/2+s^2T^2/6}\right]$$

which is a compromise between Tustin (unachievable) and explicit trapezoidal.

To find the discrete model for the Adams-Bashforth method we substitute $\underline{f}(\underline{x}) = \underline{A}_c \underline{x} + \underline{B}_c \underline{u}$ into Equation (B-20) and expand. If we define

$$c_1 = 3T/2, \; c_2 = -T/2$$

the resulting equations are in exactly the form of Equation (B-18). Thus, Equations (B-19a)-(B-19b) serve as the discrete model, with the proper definitions of c_1 and c_2. Note that we can model any integrator replacement of the form

$$\frac{1}{s} \rightarrow \frac{c_1 z + c_2}{z(z-1)}$$

by the above method.

B.3 The Analysis Problem

The analysis problem is to determine how well the discrete integration schemes (operating at fixed sample-rates due to real-time constraints) mimic the continuous system. One approach to this analysis is to consider the difference between outputs of the "actual" and "simulated" systems for a given input. This kind of "error analysis" is carried out, for example, in Rosko [2]. The difficulty with this approach is that it is input dependent. We would like results that do not depend explicitly on the input and, moreover, that are relevant to closed-loop analysis. For these reasons, we examine the relationship between the continuous and discrete transfer functions.

We define the "distortion function", $D_{ij}(s)$, introduced by the discrete integration scheme by the following relation

$$D_{ij}(s) = H_{d_{ij}}(s)/H_{c_{ij}}(s) \qquad \text{(B-22)}$$

where H_d and H_c are defined in (B-2) and (B-4) and the subscripts i and j refer to output and input, respectively. That is, H_{ij} is the transfer function relating the i^{th} output to the j^{th} input. The definition of Equation (B-22) is straightforward with respect to single input systems, whether they involve a single output or multiple outputs. Furthermore, the determination of the distortion function in these cases may be helpful in solving the corresponding synthesis problem, especially if the distortion function is of a simple form (e.g., a constant gain and pure delay). For the case of multiple inputs, the definition provides analytic insight but it does not address the synthesis problem because it ignores interactions that are essential to reproducing the overall input/output relations.*

It should be noted that because the definition is in terms of transfer functions, the distortion will be independent of the state-space representation.

---

* For this case, it is probably best to approximate H_d directly without attempting to relate the approximation to the original continuous transfer matrix H_c.

B.4 Results

A computer program was developed to compute distortion results for several of the integration schemes discussed in section B.2. The results are summarized below. The following shorthand notation is used in the sequel to identify the integration schemes:

EU : Euler
TM : Transition Matrix
RK : Runge-Kutta
IM : Implicit Midpoint
AB : Adams-Bashforth

B.4.1 Integration ($H_c(s) = \frac{1}{s}$)

Here $A_c = 0$, $B_c = C_c = 1$. Simple analysis of the integration schemes shows that the TM, EU, RK and IM methods yield identical discrete transfer function $H_d(s)$ and should yield identical distortion results D(s). This was verified to be the case. The magnitude and phase distortion results obtained are plotted vs. a normalized frequency in Figure B-1. For this case, the normalized magnitude and phase distortion results are independent of the sampling frequency.

B.4.2 Computation of D(s) for $H_c(s) = \frac{1}{s+p}$

The details of computation will, of course, depend on the integration scheme used. For illustrative purposes, let us consider the Euler scheme. Any other scheme may be worked out similarly. Here we are approximating

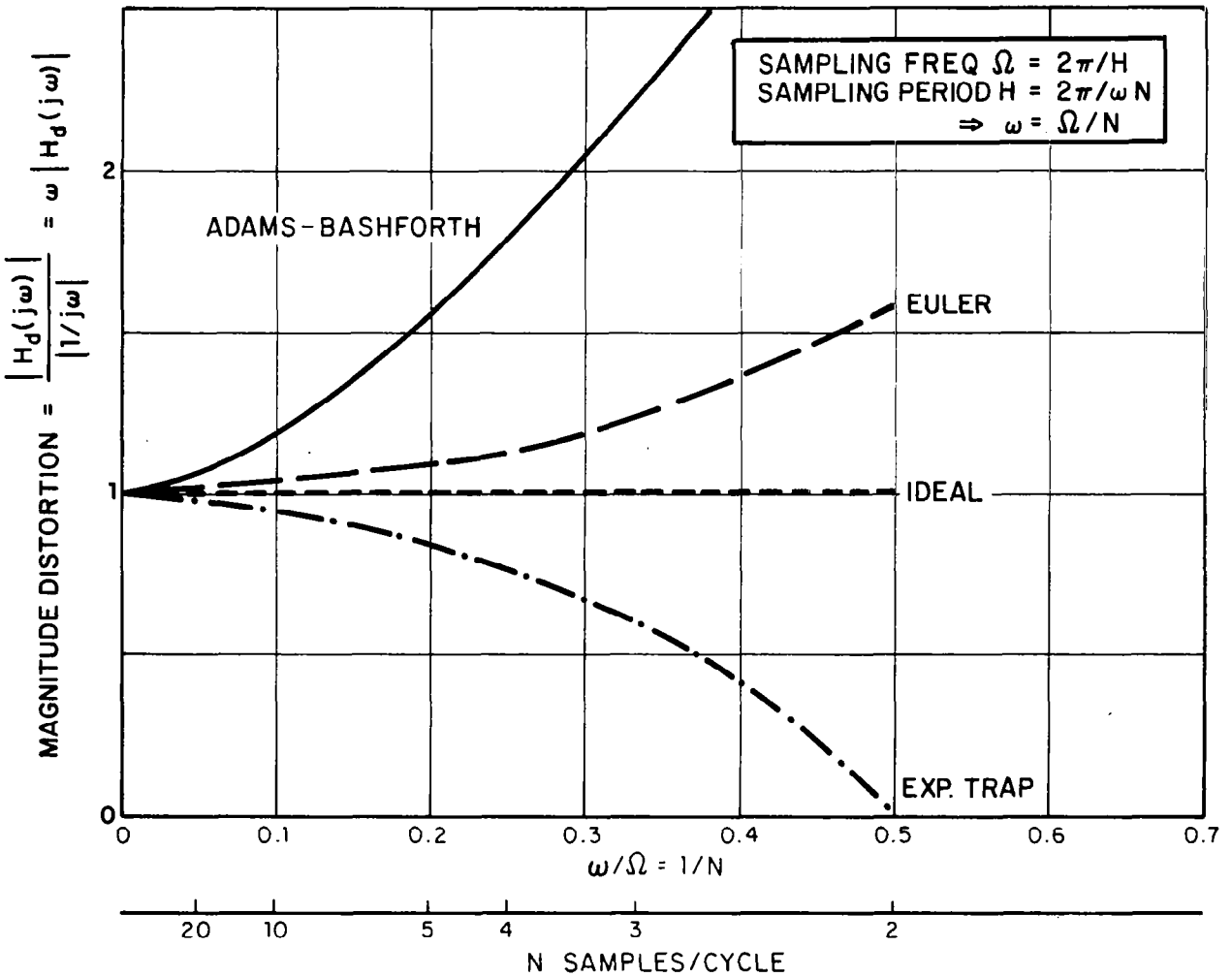

Figure B1A. - Distortion Results for Integration ($H_c(s) = 1/s$).

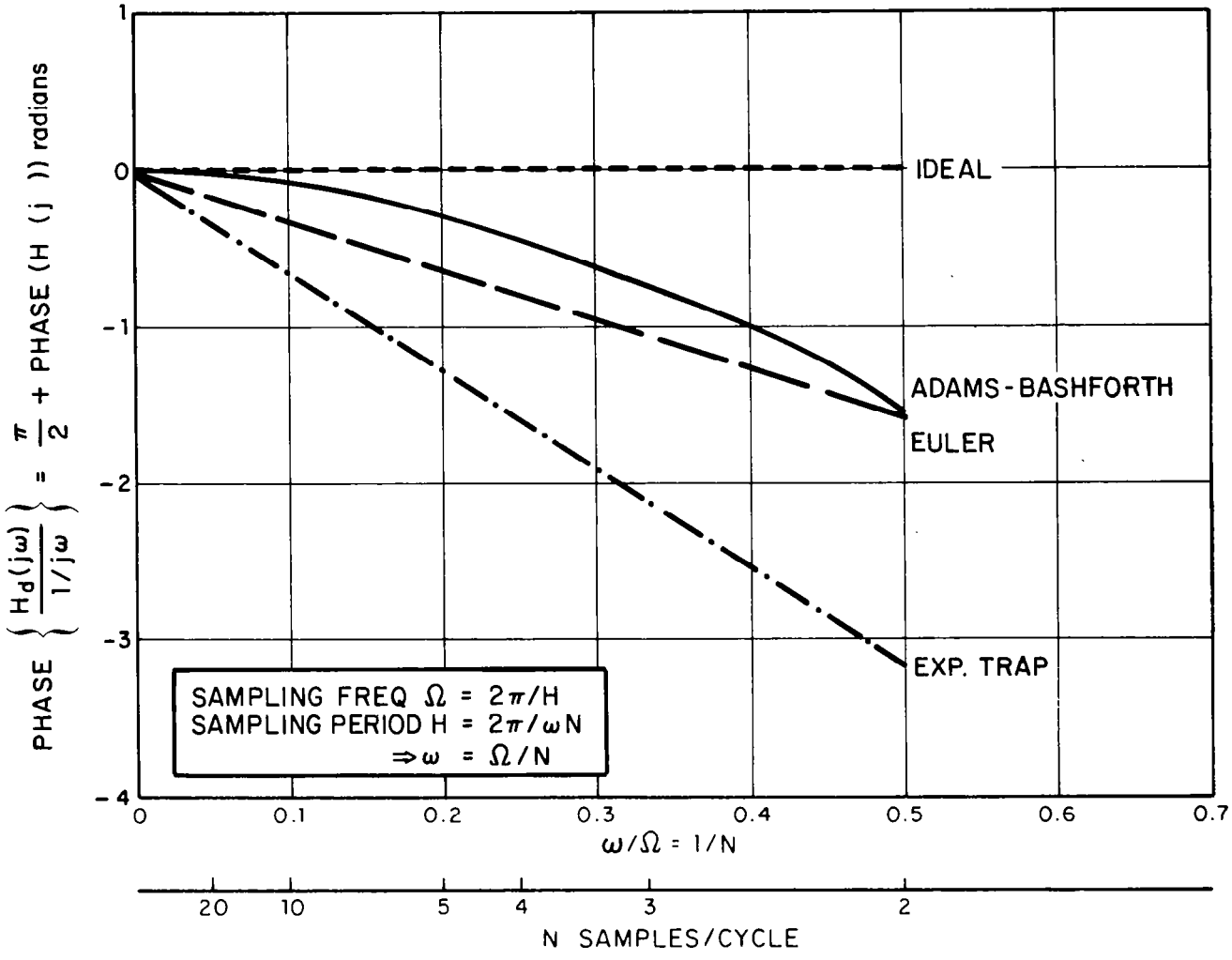

Figure B1B. - Distortion Results for Integration ($H_c(s) = 1/s$).

$$\dot{y} = - py + u$$

by

$$y_{k+1} = y_k + (-py + u)T$$

Thus

$$H_c(s) = \frac{1}{s+p}$$

and

$$H_d(s) = \frac{T}{z-1 + pT}\Big|_{z=\exp(sT)}$$

so that

$$D(s) = \frac{(s+p)T}{\exp(sT)-1+pT}$$

From

$$D(j\omega) = \frac{(j\omega T+pT)}{\exp(j\omega T)-1+pT} \qquad \text{(B-23)}$$

it is easy to compute the magnitude and phase distortions as

$$D_m(j\omega) = \left| D(j\omega) \right|$$

$$D_p(j\omega) = \text{Arctan}\{\frac{\text{Imag. part } D(j\omega)}{\text{Real part } D(j\omega)}\}$$

These are plotted in Figure B.2.

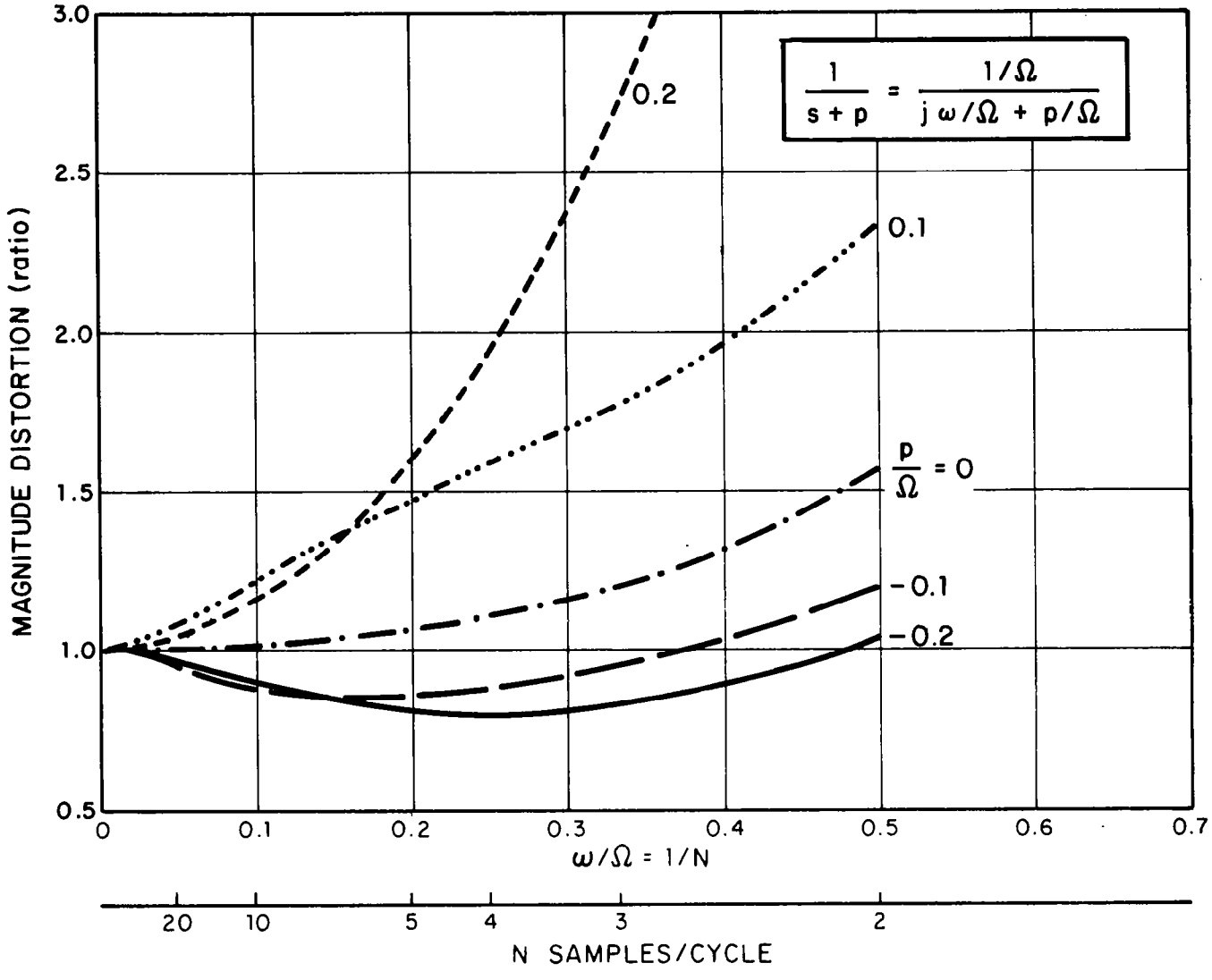

Figure B2A. - Distortion Results for First Order Dynamics ($H_c(s) = 1/s+p$).

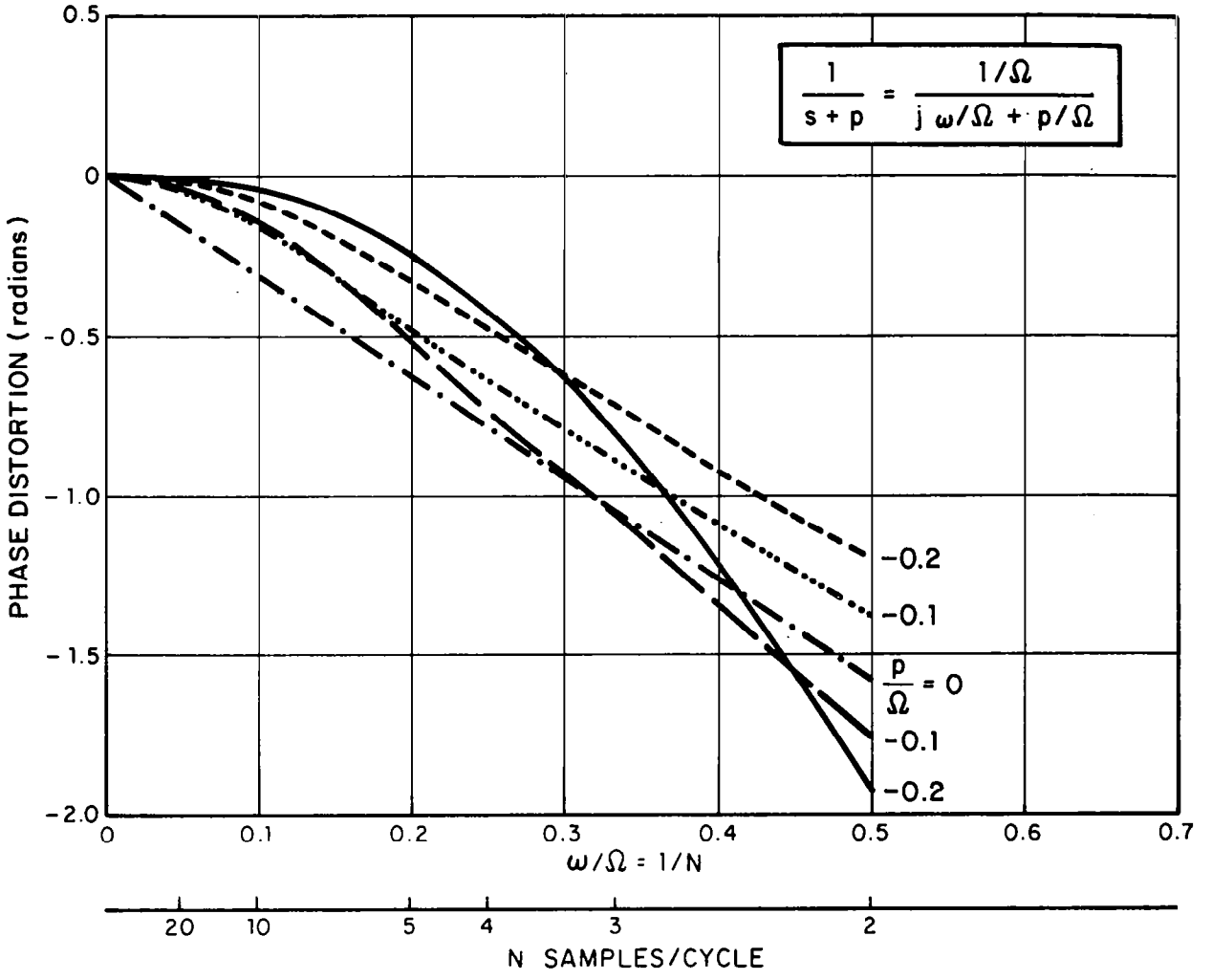

Figure B2B. - Distortion Results for First Order Dynamics ($H_c(s) = 1/s+p$).

B.4.3 Computation of D(s) for $H_c(s) = (s+z)$

Again we shall illustrate only the Euler scheme. We are approximating

$$\dot{u} = - zu + y$$

by

$$u_{k+1} = u_k + (y_k - zu_k)T$$

It follows that

$$D(s) = \frac{e^{sT}-1+zT}{(s+z)T} \qquad \text{(B-24)}$$

which is simply the reciprocal of the result for $H_c = \frac{1}{s+p}$ with $p \equiv z$. Hence, the magnitude distortion for a zero is simply the reciprocal of that for a pole; the phase distortion for a zero is negative of that for a pole.

B.4.4 Computation of D(s) for any $H_c(s)$

We note that any $H_c(s)$ may be written in the factored form

$$H_c(s) = \frac{K \prod_{i=1}^{m} (s+z_i)}{\prod_{j=1}^{n} (s+p_j)} \qquad \text{(B-25)}$$

Some of the z_i and p_j may be zero or complex, the latter, of course, occurring in conjugate pairs. It then follows easily that*

$$D_m(H_c(s)) = \prod_{j=1}^{n} D_m\left(\frac{1}{s+p_j}\right) \Big/ \prod_{i=1}^{m} D_m\left(\frac{1}{s+z_i}\right) \tag{B-26}$$

$$D_p(H_c(s)) = \sum_{j=1}^{n} D_p\left(\frac{1}{s+p_j}\right) - \sum_{i=1}^{m} D_p\left(\frac{1}{s+z_i}\right) \tag{B-27}$$

The result in (B-23), of course, is true for p real, complex or zero. Writing $p = \bar{\sigma} + j\bar{\omega}$ we have

$$D_m \frac{1}{s+p} = \sqrt{\frac{(\bar{\sigma}T)^2 + ((\omega+\bar{\omega})T)^2}{(\bar{\sigma}T-1+\cos\ \bar{\omega}T)^2 + (\bar{\omega}T+\sin\ \bar{\omega}T)^2}} \tag{B-28}$$

and

$$D_p \frac{1}{s+p} = \text{Arctan}\ \{\frac{(\omega+\bar{\omega})T}{\bar{\sigma}T} \tag{B-29}$$

$$-\text{Arctan}\ \{\frac{\bar{\omega}T+\sin\ \bar{\omega}T}{\bar{\sigma}T-1+\cos\ \bar{\omega}T}\} \tag{B-30}$$

We may hence also compute the effective time delay τ_d for any transfer function using (B-29) as

---

* We abuse notation here and write $D_m(H_c(s))$ to denote $D_m(\omega)$ for the transfer function $H_c(s)$ and similarly for $D_p(H_c(s))$.

$$\tau_d(H_c(s)) = \sum_{j=1}^{n} \tau_d \left(\frac{1}{s+p_j}\right) - \sum_{i=1}^{m} \tau_d \left(\frac{1}{s+z_i}\right) \qquad \text{(B-31)}$$

where $\tau_d \frac{1}{s+p_j}$ is the effective delay associated with a pole at p_j, etc.

Thus, the effective delay for transfer function $H_c(s)$ can be bounded by

$$-m\ \tau_d \left(\frac{1}{s}\right) \leq \tau_d(H_c(s)) \leq n\ \tau_d \left(\frac{1}{s}\right)$$

B.4.5 F-8 Dynamics

The aforementioned computer program was used to obtain distortion results for various unaugmented configurations of the F-8 dynamics corresponding to Flight Condition #11 [21]. Results for the various integration schemes are given as a function of frequency in Figures B-3 - B-6* where the plot symbols E, A, T and X respectively denote Euler, Adams-Bashforth, Transition matrix and Explicit trapezoidal integration. (Transition matrix and explicit trapezoidal results are shown only for the longitudinal short period dynamics.)

* The use of a normalized frequency is not convenient for dynamics other than pure integration
distortion versus normalized frequency is no longer covariant with sample frequency.

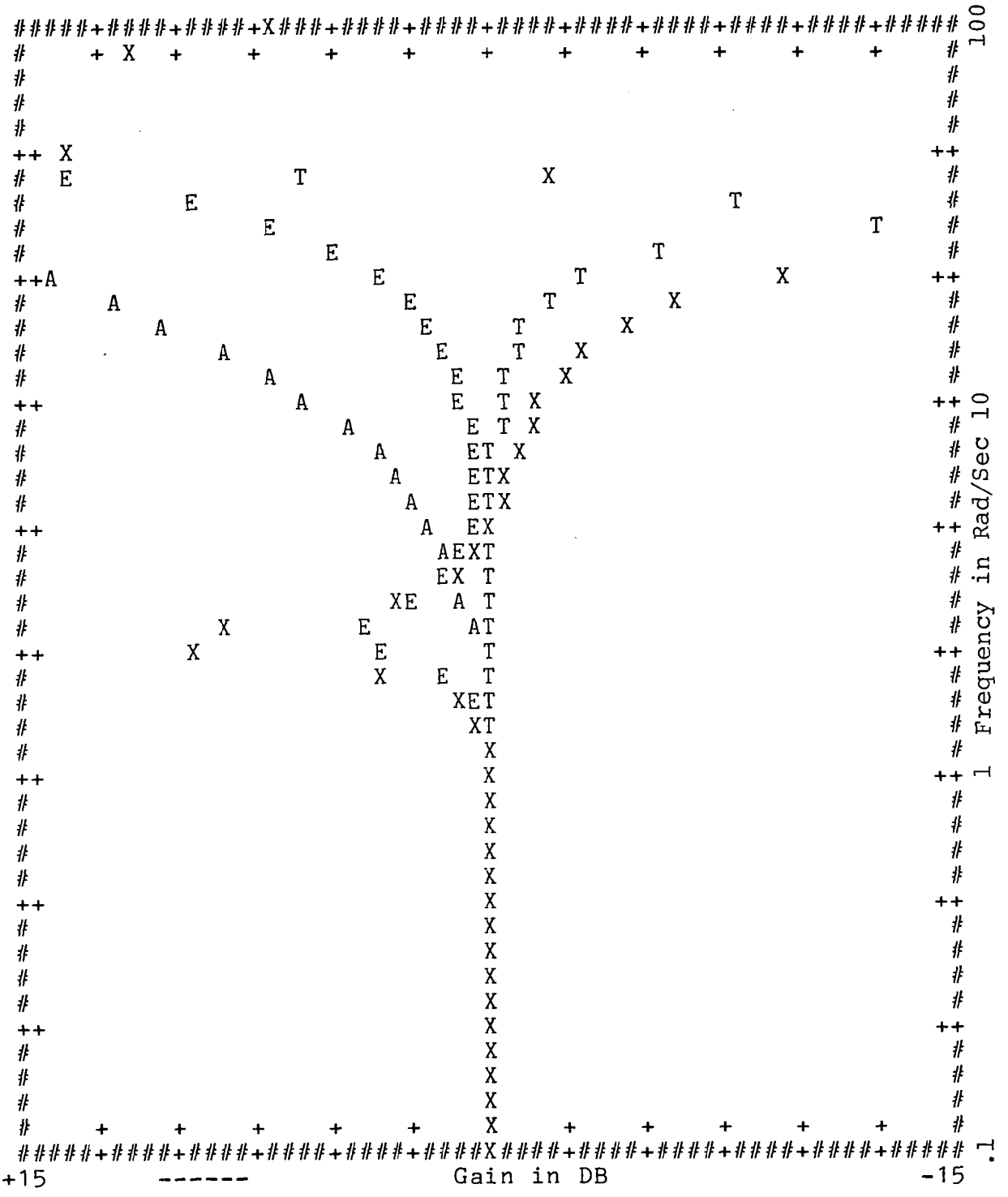

Figure B3. - Distortion Results for Longitudinal F8 Dynamics.
a) Pitch/Elevator Magnitude Distortion at T = 1/10.

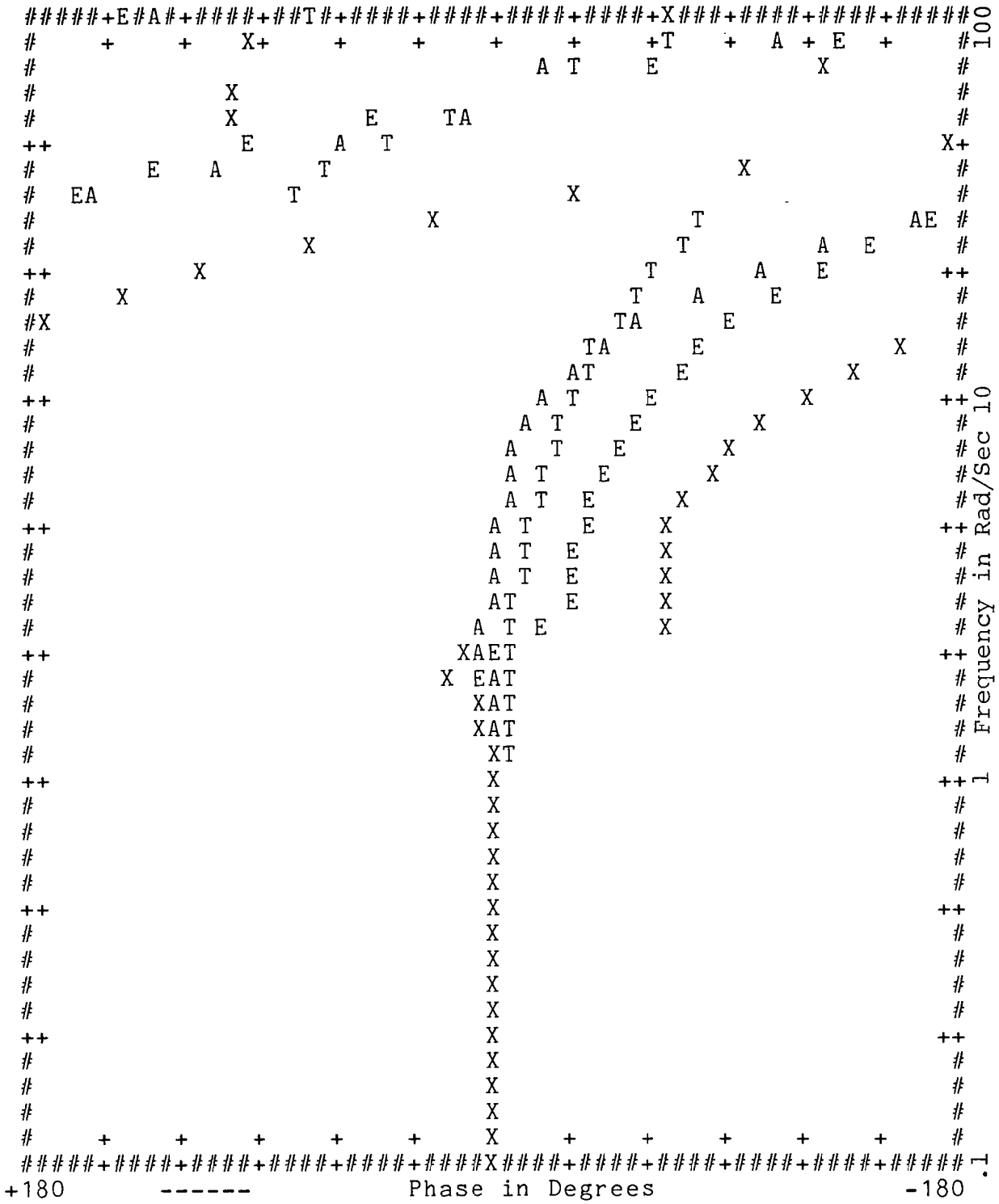

Figure B3. - Distortion Results for Longitudinal F8 Dynamics,
b) Pitch/Elevator Phase Distortion at T = 1/10.

Figure B3. - Distortion Results for Longitudinal F8 Dynamics.
c) Pitch/Elevator Magnitude Distortion at T = 1/32.

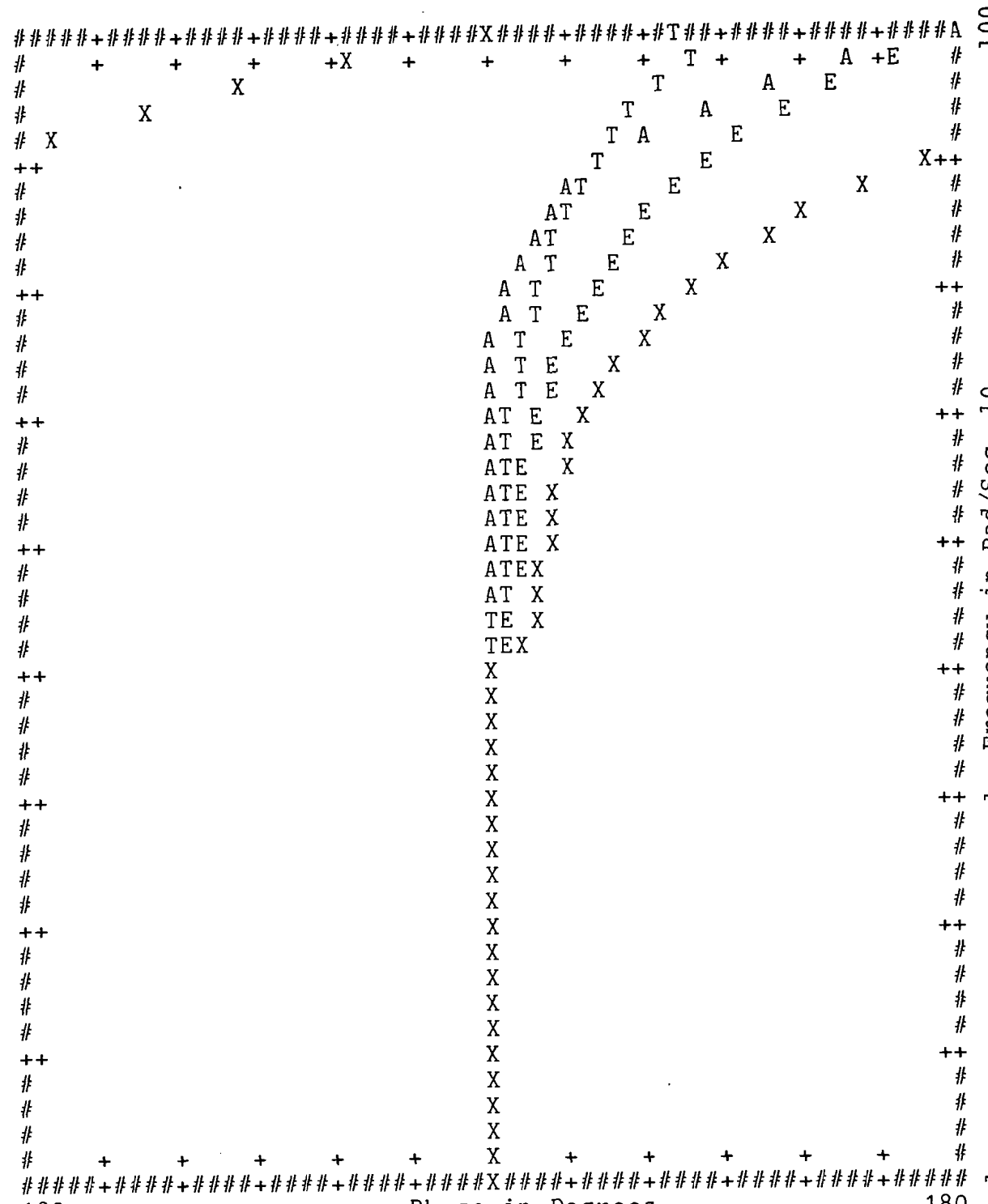

Figure B3. - Distortion Results for Longitudinal F8 Dynamics.
d) Pitch/Elevator Phase Distortion at T = 1/32.

Figure B4. - Distortion Results for Lateral CAS-OFF F8 Dynamics.
a) Roll Angle/Aileron Magnitude Distortion at T = 1/10.

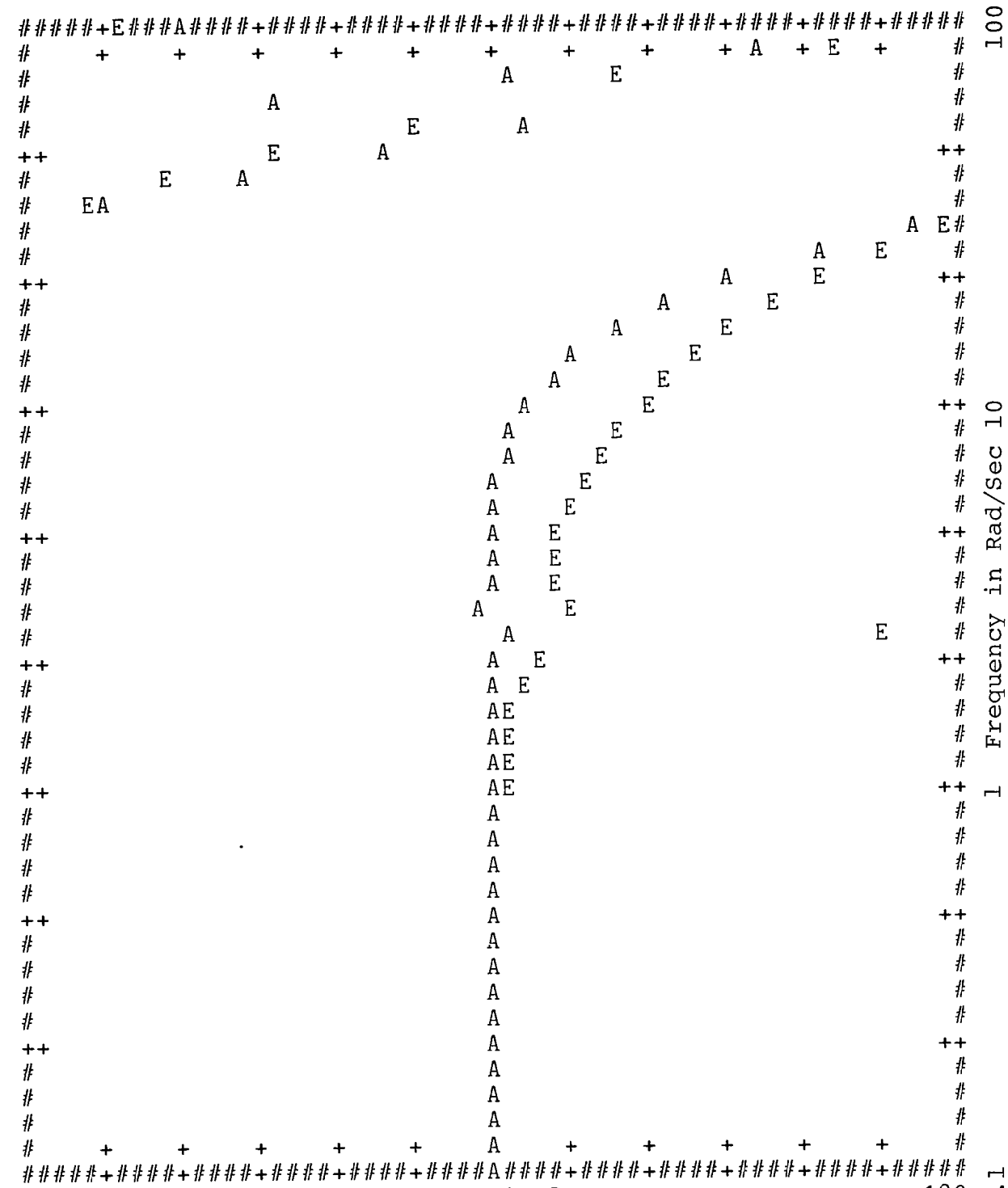

Figure B4.- Distortion Results for Lateral CAS-OFF F8 Dynamics.
b) Roll Angle/Aileron Phase Distortion at T = 1/10.

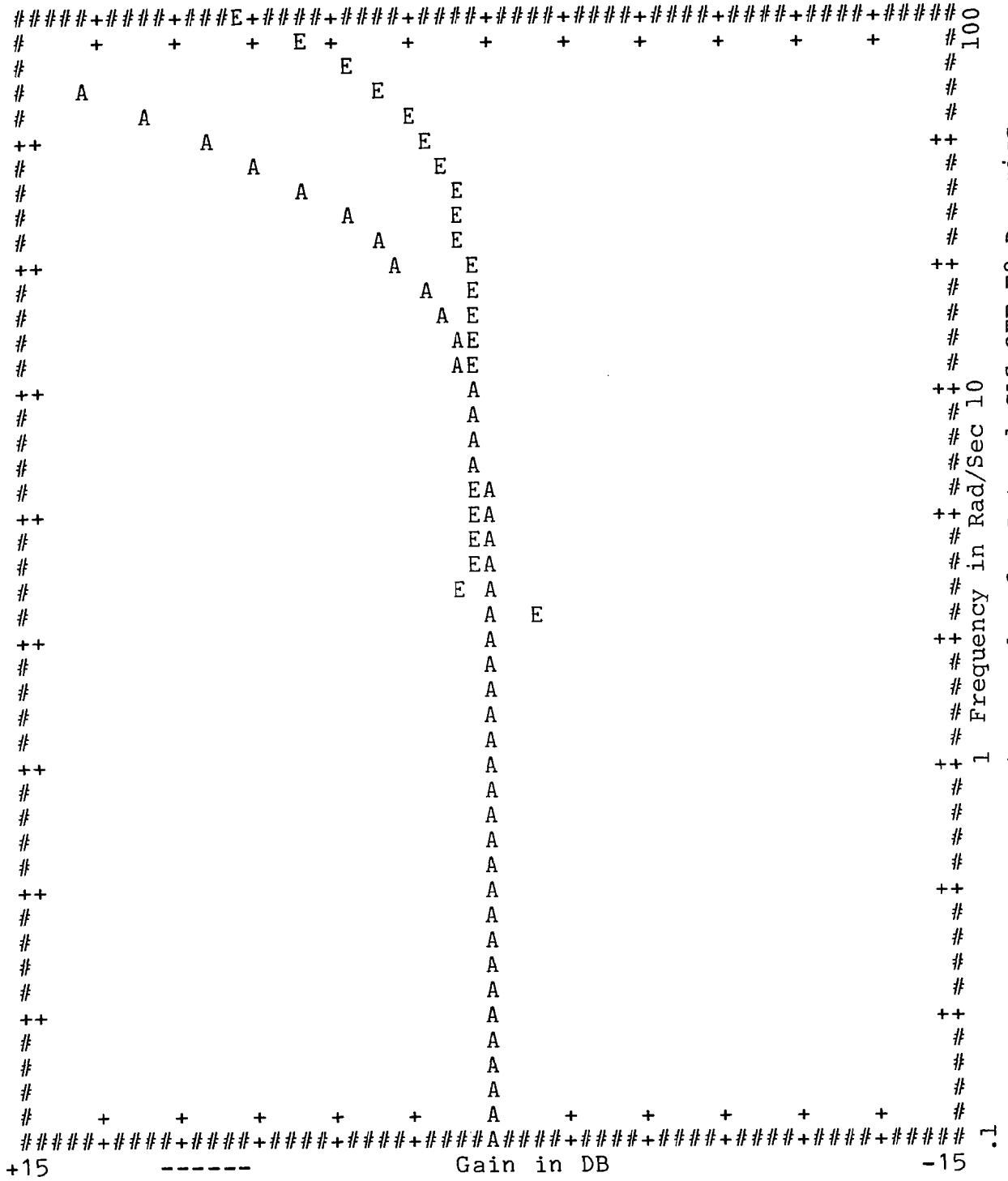

Figure B4. - Distortion Results for Lateral CAS-OFF F8 Dynamics.
c) Roll Angle/Aileron Magnitude Distortion at T = 1/32.

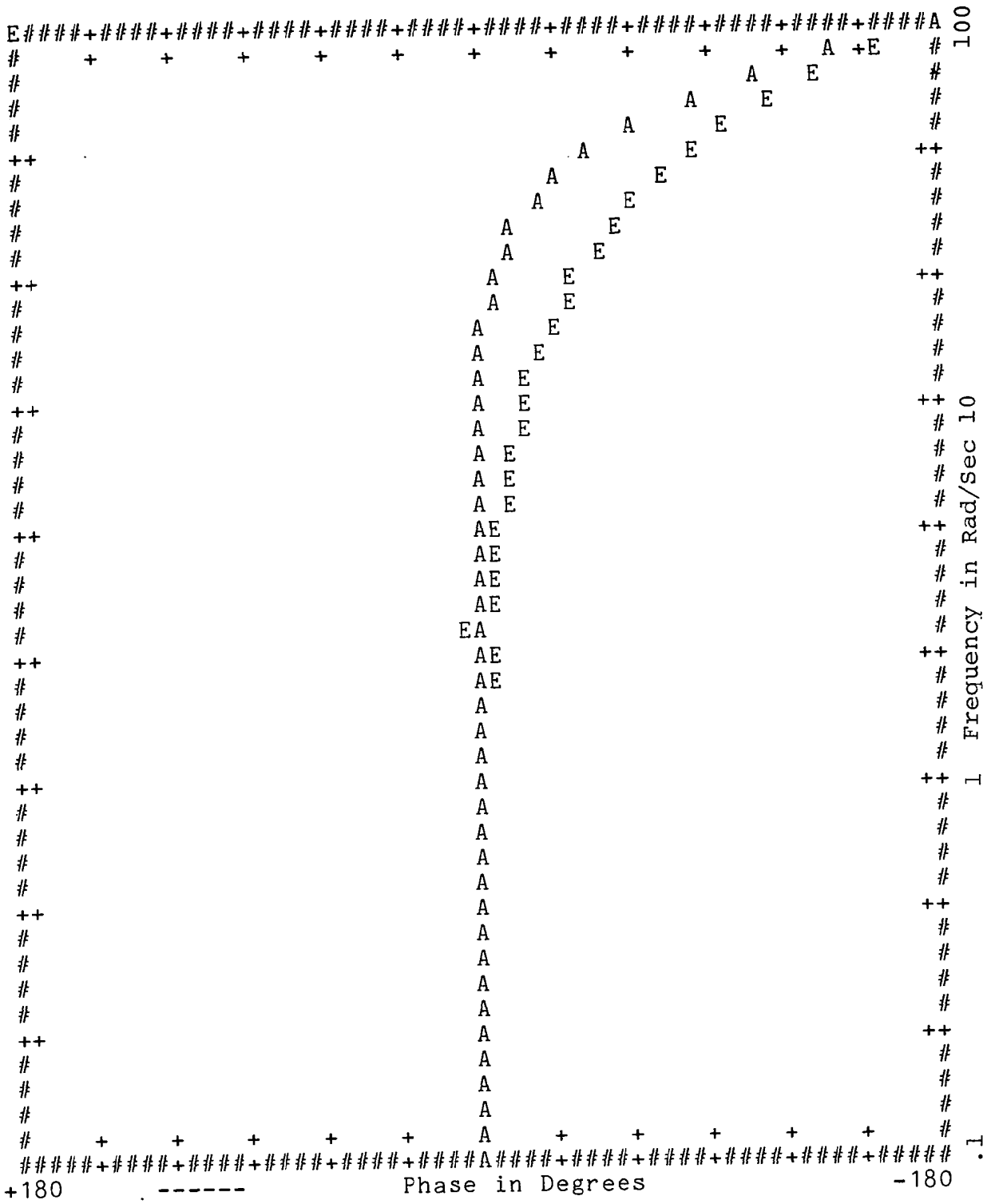

Figure B4. - Distortion Results for Lateral CAS-OFF F8 Dynamics.
d) Roll Angle/Aileron Phase Distortion at T = 1/32.

Figure B5.- Distortion Results for Lateral CAS-OFF F8 Dynamics.
a) Roll Error/Rudder Magnitude Distortion at $T = 1/10$.

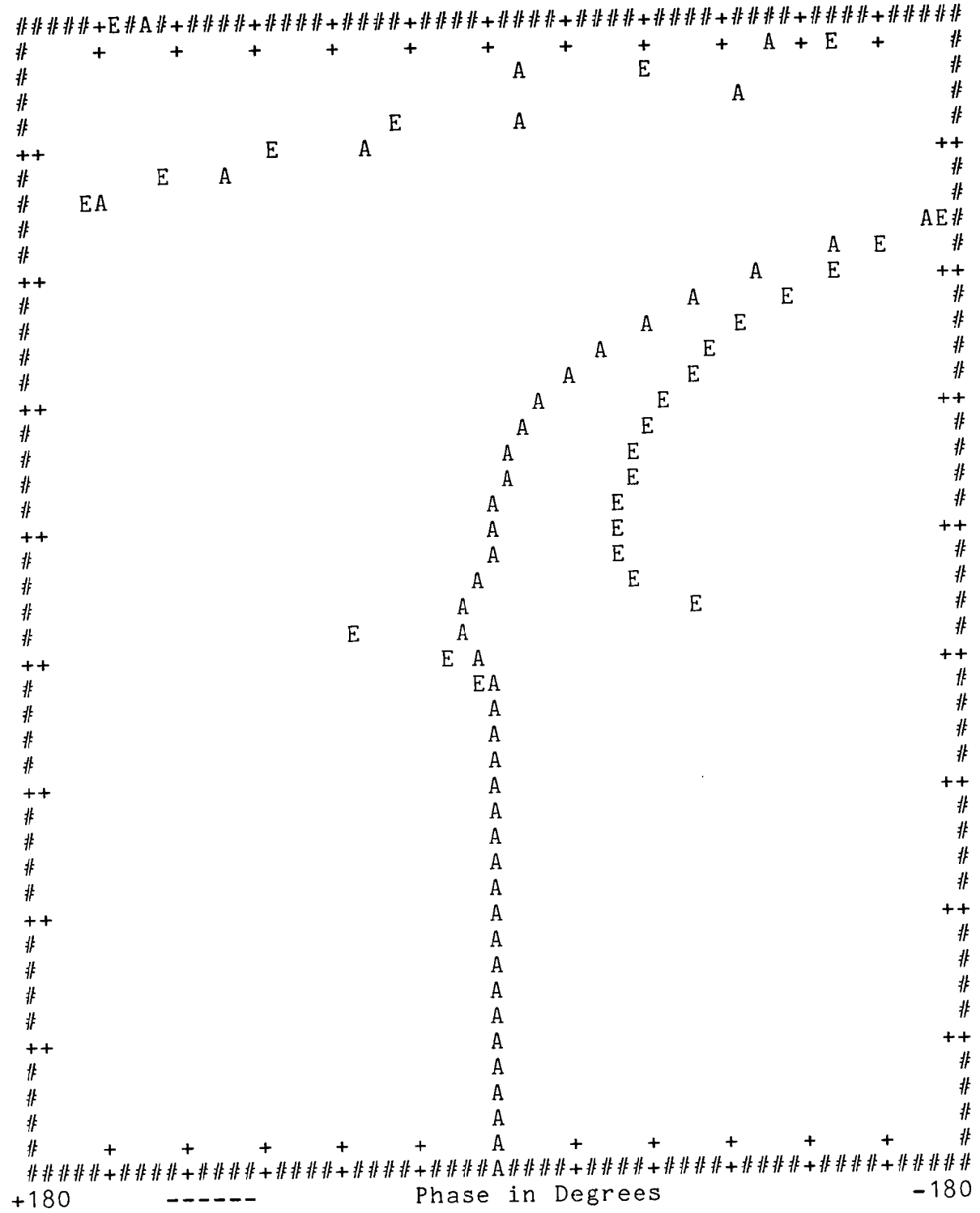

Figure B5. - Distortion Results for Lateral CAS-OFF F8 Dynamics.
b) Roll Error/Rudder Phase Distortion at T = 1/10.

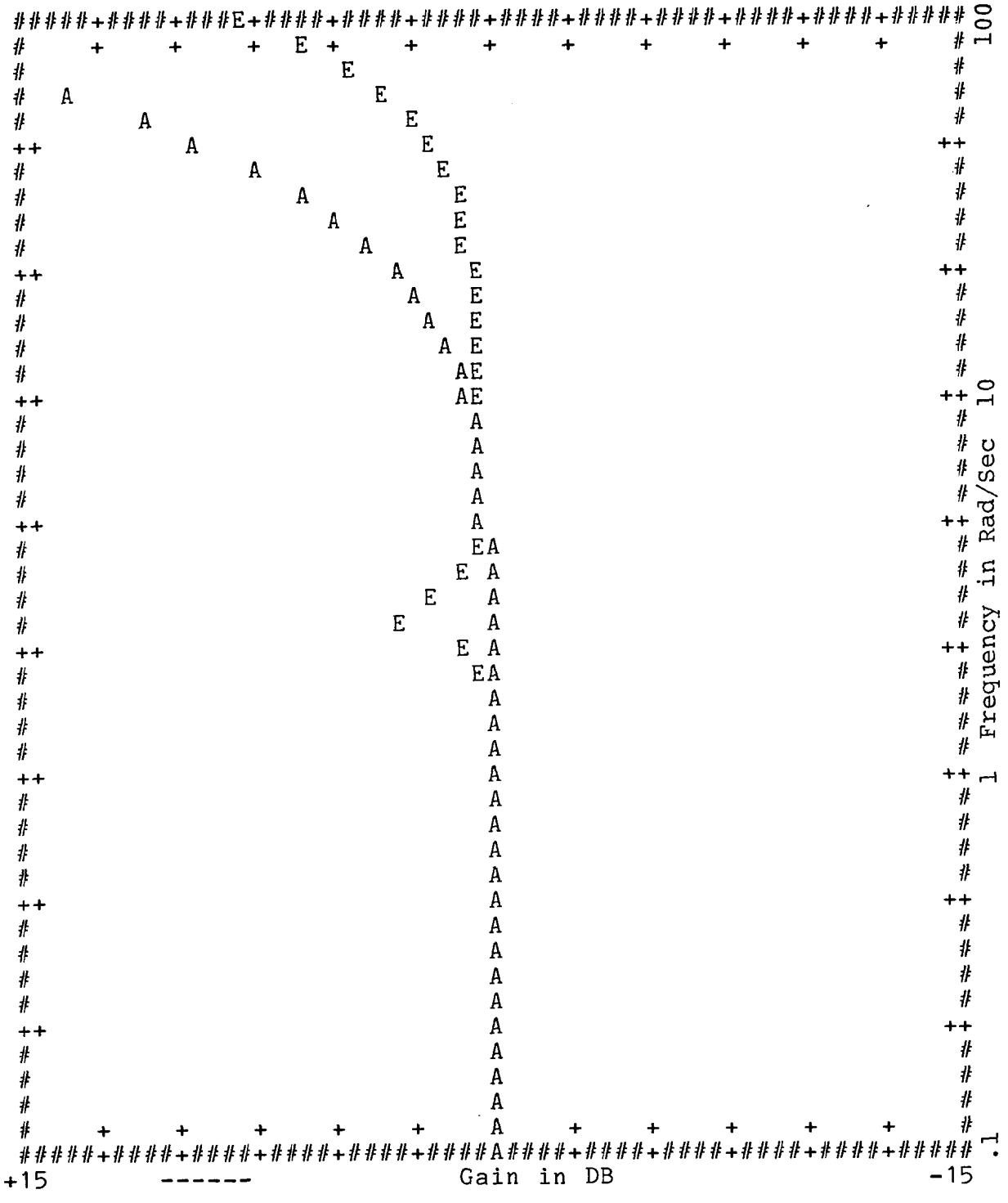

Figure B5. - Distortion Results for Lateral CAS-OFF F8 Dynamics.
c) Roll Error/Rudder Magnitude Distortion at T = 1/32

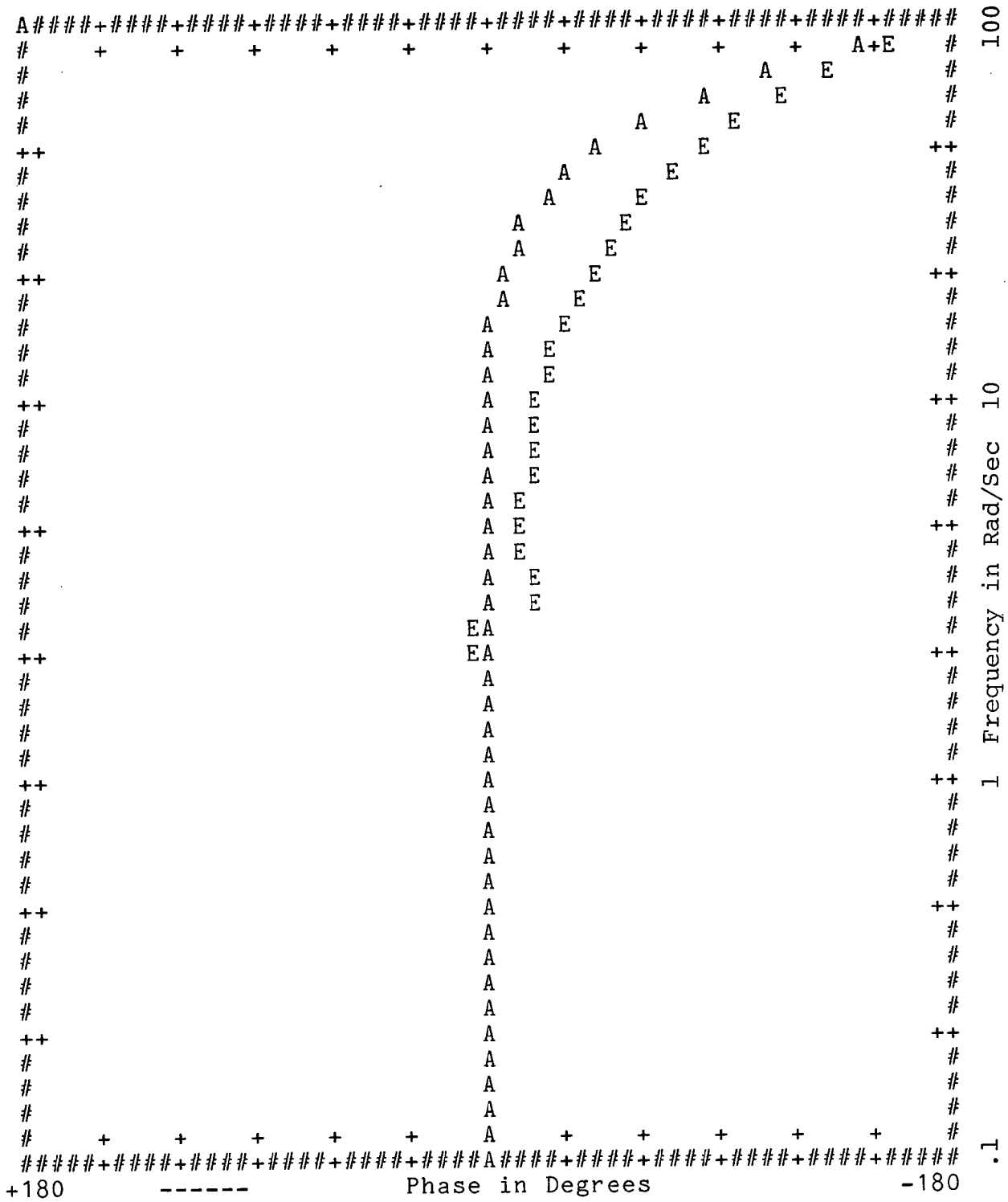

Figure B5. - Distortion Results for Lateral CAS-OFF F8 Dynamics.
d) Roll Error/Rudder Phase Distortion at T = 1/32.

Figure B6. - Distortion Results for Coordinated F8 Dynamics.
a) LOS Error/Aileron Magnitude Distortion at τ = 1/10.

Figure B6. - Distortion Results for Coordinated F8 Dynamics.
b) LOS Error/Aileron Phase Distortion at τ = 1/10.

Figure B6. - Distortion Results for Coordinated F8 Dynamics.
c) LOS Error/Aileron Magnitude Distortion at T = 1/32.

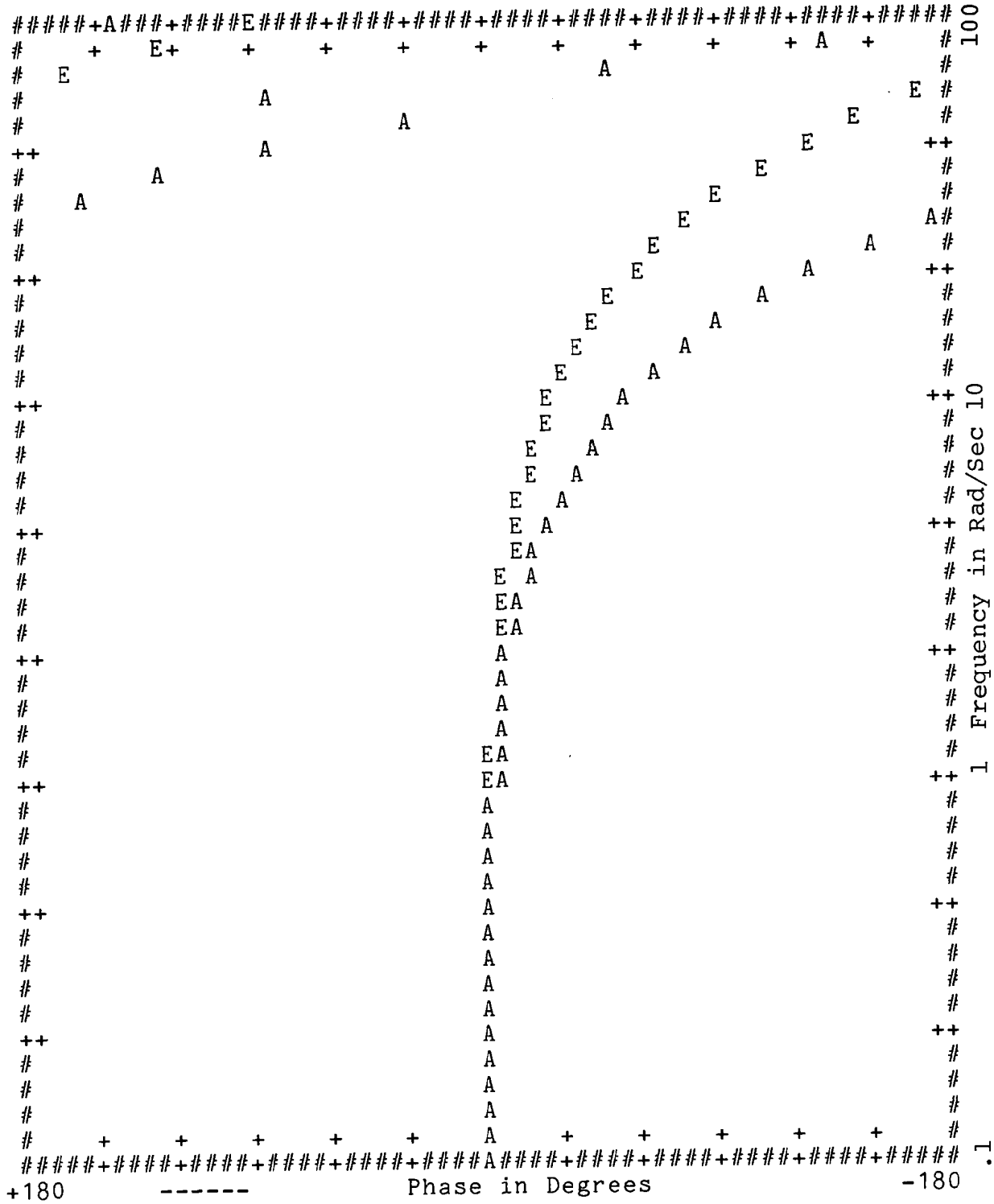

Figure B6. - Distortion Results for Coordinated F8 Dynamics.
d) LOS Error/Aileron Phase Distortion at T = 1/32.

Figure B6. - Distortion Results for Coordinated F8 Dynamics.
e) Roll Angle/Aileron Magnitude Distortion at T = 1/10.

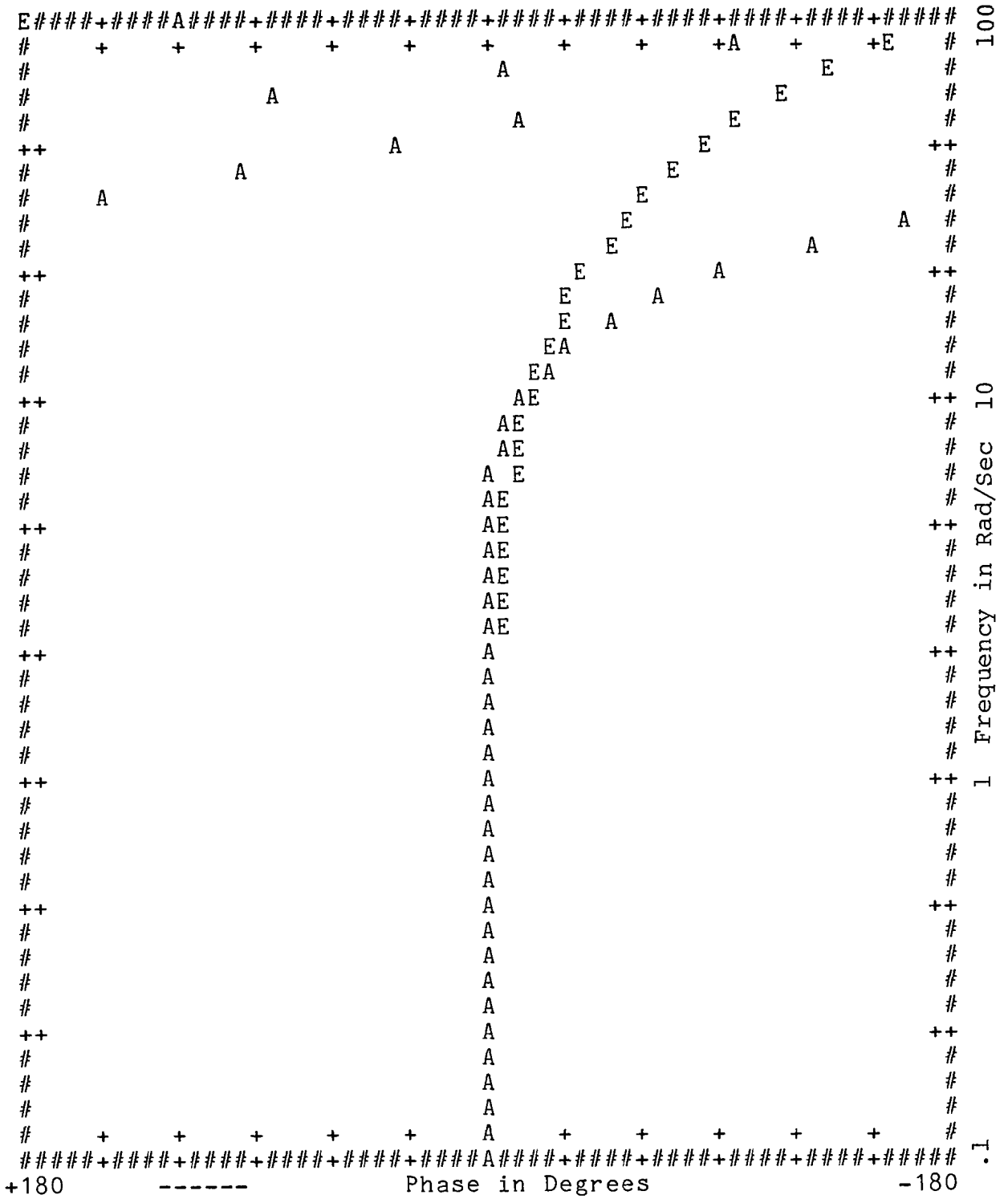

Figure B6. - Distortion Results for Coordinated F8 Dynamics.
f) Roll Angle/Aileron Phase Distortion at T = 1/10.

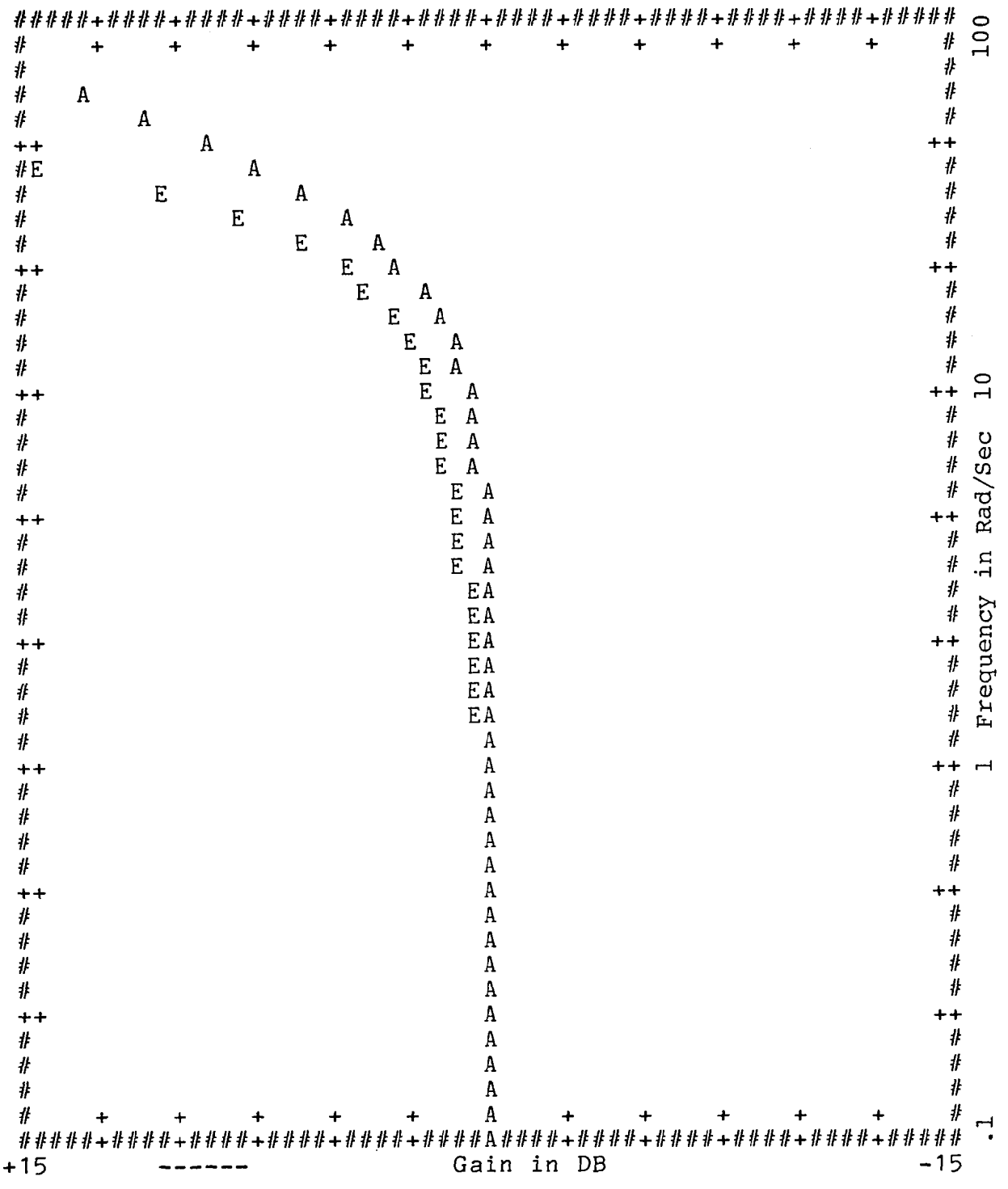

Figure B6. - Distortion Results for Coordinated F8 Dynamics.
g) Roll Angle/Aileron Magnitude Distortion at T = 1/32.

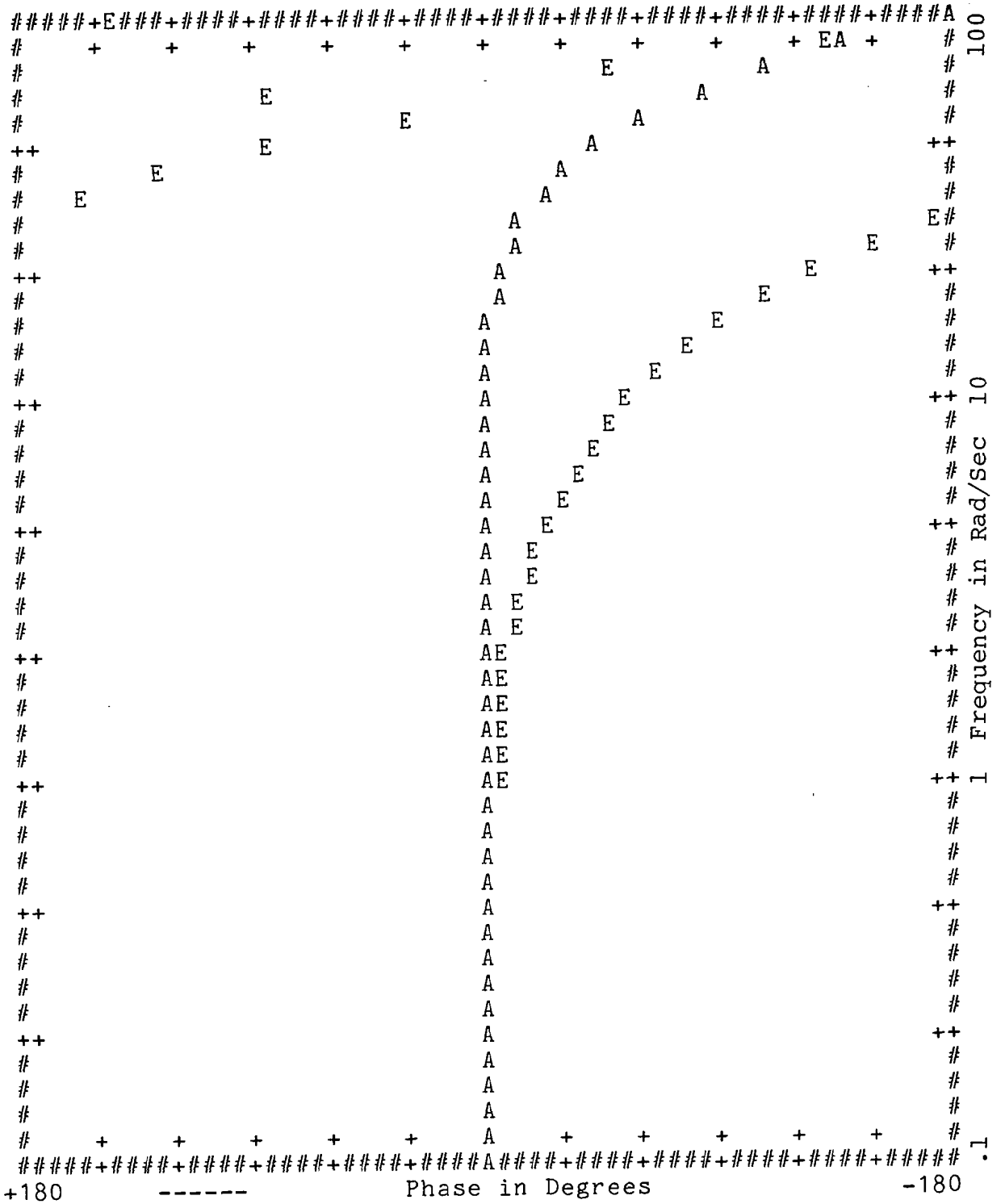

Figure B6.- Distortion Results for Coordinated F8 Dynamics.
h) Roll Angle/Aileron Phase Distortion at T = 1/32.

APPENDIX C

STATE EQUATIONS FOR F-8 DYNAMICS

In this Appendix, the state variables and state equations for the various F-8 configurations analyzed in the text are presented. In general, the state variable description is

$$\dot{\underline{x}} = \underline{A}\,\underline{x} + \underline{B}\,\underline{u} + \underline{E}\,\underline{w}$$

$$\underline{y} = \underline{C}\,\underline{x} + \underline{D}\,\underline{u} \qquad \text{(C-1)}$$

The state and output variables are not unique and may be defined in various ways. The definitions used in the analyses conducted here and the appropriate system matrices for (C-1) are given below.

C.1 Longitudinal Dynamics

x_1: dummy variable (used in generating target motion)

x_2: h_T (ft)

x_3: $\dot{h}_T$ (ft/sec)

x_4: q (deg/sec)

x_5: α(deg): angle of attack

x_6: θ(deg): pitch angle

x_7: h (ft): deviation from nominal altitude

The output variables were selected to be

$y_1 = R\,\varepsilon_v$: tracking error (ft.)

$y_2 = R\,\dot{\varepsilon}_v$: tracking error-rate (ft/sec)

$y_3 = \theta$ (deg): pitch angle

$y_4 = q$(deg/sec): pitch rate

$y_5 = n_z(q)$: normal acceleration

$y_6 = h_T(\text{ft/sec}^2)$: target normal acceleration

For the analysis $y_1 - y_4$ are observed by the pilot. Normal acceleration n_z, is a response variable of some interest and the target's normal acceleration is included as an output for convenience.

The state equations corresponding to the above definitions are given in Figure C-1 for the wideband target motions. For the narrowband target motion the equations are modified simply by letting

$$a_{32} = -.04,\ a_{33} = -.2828,\ c_{62} = .04,\ c_{63} = .2828.$$

The system matrices for the longitudinal CAS-ON dynamics are given in Figure C-2. The three additional states $x_8 - x_{10}$ are CAS-states. The remaining variables are defined as before, except the pilot's input now has units of ft/sec^2.

C.2 Lateral Dynamics

The states, controls and outputs are defined as follows for lateral tracking with unaugmented dynamics.

x_1 = dummy variable

$x_2 = \phi_T$ (deg)

$x_3 = \psi_T$ (deg)

x_4 = p (deg/sec)

x_5 = r (deg/sec)

$x_6 = \beta$ (deg)

$x_7 = \phi$ (deg)

$x_8 = \psi$ (deg)

$x_9 = R\,\varepsilon_T$ (ft)

$u_1 = \delta_a$ (deg)

$u_2 = \delta_r$ (deg)

$y_1 = \phi_T - \phi_A$ (deg)

$y_2 = \dot{\phi}_T - \dot{\phi}_A$ (deg/sec)

$y_3 = R\,\varepsilon_T$ (ft)

$y_4 = R\,\dot{\varepsilon}_T$ (ft/sec)

$y_5 = \phi$ (deg)

$y_6 = \dot{\phi}$ (deg/sec)

$y_7 = n_y$ (ft/sec^2)

$y_8 = r$ (deg/sec)

The corresponding system matrices are displayed in Figure C-3.

For the lateral CAS, one state is added for model-following $x_{10} = p_m$ (deg/sec). Two output responses are added to those above, viz.

$y_9 = \delta_{AC}$ (deg)

$y_{10} = \delta_{RC}$ (deg)

The resulting system matrices are given in Figure C-4.

Finally, for the coordinated dynamics, the system matrices are given in Figure C-5, where

$x_1 - x_4$ defined as above

$x_5 = \phi$ (deg)

$x_6 = \psi$ (deg)

$x_7 = R\ \varepsilon_T$ (ft)

$y_1 - y_6$ defined as above

```
TOTAL NOISE STATES=  3
 A    MATRIX:
   -1.000E+00     0.            0.            0.            0.
    0.            0.
    0.            0.            1.000E+00     0.            0.
    0.            0.
    1.000E+00    -2.500E-01    -7.070E-01     0.            0.
    0.            0.
    0.            0.            0.           -4.870E-01    -4.789E+00
    0.            0.
    0.            0.            0.            1.000E+00    -8.360E-01
    0.            0.
    0.            0.            0.            1.000E+00     0.
    0.            0.
    0.            0.            0.            0.           -1.086E+01
    1.086E+01     0.
 B    MATRIX:           E    MATRIX:
    0.                      1.000E+00
    0.                      0.
    0.                      0.
   -8.743E+00               0.
   -1.110E-01               0.
    0.                      0.
    0.                      0.
 C    MATRIX:
    0.            1.000E+00     0.            0.            0.
   -1.047E+01    -1.000E+00
    0.            0.            1.000E+00    -1.047E+01     1.086E+01
   -1.086E+01     0.
    0.            0.            0.            0.            0.
    1.000E+00     0.
    0.            0.            0.            1.000E+00     0.
    0.            0.
    0.            0.            0.            0.           2.818E-01
    0.            0.
   -1.000E+00     2.500E-01     7.070E-01     0.            0.
    0.            0.

 D    MATRIX:
    0.
    0.
    0.
    0.
    3.735E-02
    0.
```

Figure C1.- State Representation for Longitudinal Wide-Band Tracking Task (CAS-OFF).

TOTAL NOISE STATES= 3

A MATRIX:

-1.000E+00	0.	0.	0.	0.
0.	0.	0.	0.	0.
0.	0.	1.000E+00	0.	0.
0.	0.	0.	0.	0.
1.000E+00	-2.500E-01	-7.070E-01	0.	0.
0.	0.	0.	0.	0.
0.	0.	0.	-4.870E-01	-4.789E+00
0.	0.	-2.645E-02	0.	-3.226E-01
0.	0.	0.	1.000E+00	-8.360E-01
0.	0.	-3.359E-04	0.	-4.096E-03
0.	0.	0.	1.000E+00	0.
0.	0.	0.	0.	0.
0.	0.	0.	0.	-1.086E+01
1.086E+01	0.	0.	0.	0.
0.	0.	0.	0.	0.
0.	0.	-1.350E+01	-5.500E+01	0.
0.	0.	0.	0.	0.
0.	0.	1.000E+00	0.	0.
0.	0.	0.	7.957E+00	-3.251E+01
0.	0.	8.997E-01	2.380E+00	-3.540E+00

B MATRIX:

0.
0.
0.
-2.323E-01
-2.949E-03
0.
0.
5.500E+01
0.
-2.549E+00

E MATRIX:

1.000E+00
0.
0.
0.
0.
0.
0.
0.
0.
0.

Figure C2.- State Representation for Longitudinal Wide-Band Tracking Task (Pitch CAS-ON).

C MATRIX:

0.	1.000E+00	0.	0.	0.
-1.047E+01	-1.000E+00	0.	0.	0.
0.	0.	1.000E+00	-1.047E+01	1.086E+01
-1.086E+01	0.	0.	0.	0.
0.	0.	0.	0.	0.
1.000E+00	0.	0.	0.	0.
0.	0.	0.	1.000E+00	0.
0.	0.	0.	0.	0.
0.	0.	0.	2.086E-12	2.818E-01
0.	0.	1.130E-04	0.	1.378E-03
0.	0.	0.	0.	0.
0.	0.	3.026E-03	0.	3.690E-02

D MATRIX:

0.
0.
0.
0.
9.922E-04
2.657E-02

Figure C2. - State Representation for Longitudinal (cont.) Wide-Band Tracking Task (Pitch CAS-ON).

```
TOTAL NOISE STATES=  3
 A    MATRIX:
   -1.000E+00     0.             0.             0.             0.
    0.            0.             0.             0.
    1.000E+00    -1.000E+00      0.             0.             0.
    0.            0.             0.             0.
    0.            5.173E-02     -1.000E-02      0.             0.
    0.            0.             0.             0.
    0.            0.             0.            -2.580E+00      2.510E-01
   -3.778E+01     0.             0.             0.
    0.            0.             0.            -7.530E-02     -2.730E-01
    4.360E+00     0.             0.             0.
    0.            0.             0.             7.800E-02     -9.940E-01
   -2.290E-01     5.173E-02      0.             0.
    0.            0.             0.             9.970E-01      7.800E-02
    0.            0.             0.             0.
    0.            0.             0.             0.             1.000E+00
    0.            0.             0.             0.
    0.            0.             1.086E+01      0.            -1.047E+01
   -1.086E+01     0.            -1.086E+01      0.
 B    MATRIX:                      E    MATRIX:
    0.            0.                  1.000E+00
    0.            0.                  0.
    0.            0.                  0.
    1.724E+01     7.016E+00           0.
    8.160E-01    -3.180E+00           0.
    0.            4.560E-02           0.
    0.            0.                  0.
    0.            0.                  0.
    0.            0.                  0.
```

Figure C3. – State Representation for Unaugmented Lateral Dynamics.

```
C     MATRIX:
    0.              1.000E+00      0.              0.              0.
    0.             -1.000E+00      0.              0.
    1.000E+00      -1.000E+00      0.             -9.970E-01      -7.800E-02
    0.              0.             0.              0.
    0.              0.             0.              0.              0.
    0.              0.             0.              1.000E+00
    0.              0.             1.086E+01       0.             -1.047E+01
   -1.086E+01       0.            -1.086E+01       0.
    0.              0.             0.              0.              0.
    0.              1.000E+00      0.              0.
    0.              0.             0.              9.970E-01       7.800E-02
    0.              0.             0.              0.
    0.              0.             0.              0.              6.510E-02
   -2.486E+00       0.             0.              0.
    0.              0.             0.              0.              1.000E+00
    0.              0.             0.              0.
D     MATRIX:
    0.              0.
    0.              0.
    0.              0.
    0.              0.
    0.              0.
    0.              0.
    0.              4.950E-01
    0.              0.
```

Figure C3. – State Representation for Unaugmented Lateral Dynamics. (cont.)

```
TOTAL NOISE STATES=  3
 A    MATRIX:
   -1.000E+00     0.             0.             0.             0.
    0.            0.             0.             0.             0.

    1.000E+00    -1.000E+00      0.             0.             0.
    0.            0.             0.             0.             0.

    0.            5.173E-02     -1.000E-02      0.             0.
    0.            0.             0.             0.             0.

    0.            0.             0.            -4.962E+00      6.026E+00
   -4.012E+01    -3.054E-01      0.             0.             1.927E+00

    0.            0.             0.             3.595E-02     -2.687E+00
    5.422E+00     1.240E-01      0.             0.             7.569E-02

    0.            0.             0.             7.509E-02     -9.591E-01
   -2.442E-01     4.993E-02      0.             0.             2.018E-04

    0.            0.             0.             9.970E-01      7.800E-02
    0.            0.             0.             0.             0.

    0.            0.             0.             0.             1.000E+00
    0.            0.             0.             0.             0.

    0.            0.             1.086E+01      0.            -1.047E+01
   -1.086E+01     0.            -1.086E+01      0.             0.

    0.            0.             0.             0.             0.
    0.            0.             0.             0.            -5.000E+00

 B    MATRIX:      E    MATRIX:
    0.                 1.000E+00
    0.                 0.
    0.                 0.
   -8.575E+00          0.
    3.887E+00          0.
   -5.573E-02          0.
    0.                 0.
    0.                 0.
    0.                 0.
    5.000E+00          0.
```

Figure C4. - State Representation for Augmented Lateral Dynamics.

```
C    MATRIX:
    0.            1.000E+00     0.            0.            0.
    0.           -1.000E+00     0.            0.            0.

    1.000E+00    -1.000E+00     0.           -9.970E-01    -7.820E-02
    0.            0.            0.            0.            0.

    0.            0.            0.            0.            0.
    0.            0.            0.            1.000E+00     0.

    0.            0.            1.086E+01     0.           -1.047E+01
   -1.086E+01     0.           -1.086E+01     0.            0.

    0.            0.            0.            0.            0.
    0.            1.000E+00     0.            0.            0.

    0.            0.            0.            9.970E-01     7.820E-02
    0.            0.            0.            0.            0.

    0.            0.            0.           -3.157E-02     4.439E-01
   -2.651E+00    -1.951E-02     0.            0.            2.191E-03

    0.            0.            0.            0.            1.000E+00
    0.            0.            0.            0.            0.

    0.            0.            0.           -1.122E-01     2.352E-02
    0.           -1.672E-03     0.            0.            1.100E-01

    0.            0.            0.           -6.377E-02     7.653E-01
   -3.341E-01    -3.941E-02     0.            0.            4.426E-03
D    MATRIX:
    0.
    0.
    0.
    0.
    0.
    0.
   -6.050E-01
    0.
    0.
   -1.222E+00
```

Figure 4.- State Representation for Augmented Lateral Dynamics. (cont.)

```
TOTAL NOISE STATES=  3
 A    MATRIX:
   -1.000E+00     0.            0.            0.            0.
    0.            0.
    1.000E+00    -1.000E+00     0.            0.            0.
    0.            0.
    0.            5.173E-02    -1.000E-02     0.            0.
    0.            0.
    0.            0.            0.           -2.580E+00     1.300E-02
    0.            0.
    0.            0.            0.            9.970E-01     4.100E-03
    0.            0.
    0.            0.            0.            0.            5.173E-02
    0.            0.
    0.            0.           1.086E+01      0.           -5.420E-01
   -1.086E+01     0.
 B    MATRIX:     E    MATRIX:
    0.                1.000E+00
    0.                0.
    0.                0.
    1.724E+01         0.
    0.                0.
    0.                0.
    0.                0.
 C    MATRIX:
    0.            1.000E+00     0.            0.           -1.000E+00
    0.            0.
    1.000E+00    -1.000E+00     0.           -9.970E-01    -4.100E-03
    0.            0.
    0.            0.            0.            0.            0.
    0.            1.000E+00
    0.            0.           1.086E+01      0.           -5.420E-01
   -1.086E+01     0.
    0.            0.            0.            0.            1.000E+00
    0.            0.
    0.            0.            0.            9.970E-01     4.100E-03
    0.            0.
 D    MATRIX:
    0.
    0.
    0.
    0.
    0.
    0.
```

Figure C5. - State Representation for Coordinated Lateral Dynamics.

REFERENCES

1. Gum, D. R. and W. B. Albury, "Time-Delay Problems Encountered in Integrating the Advanced Simulator for Undergraduate Pilot Training," Journal of Aircraft, Vol. 14, No. 4, April 1977.

2. Rosko, J. S., "Digital Simulation of Physical Systems" Addison-Wesley Publishing Co., Reading, Mass., 1972.

3. Smith, J. M., "Recent Developments in Numerical Integration," Journal of Dynamic Systems, Measurement and Control, March 1974.

4. Fowler, M. E., "A New Numerical Method for Simulation," Simulation, No. 14, 1965.

5. Kleinman, D. L., S. Baron and W. H. Levison, "An Optimal Control Model of Human Response," Automatica, Vol. 6, No. 3, pp. 367-384, May 1970.

6. Kleinman, D. L. and S. Baron, "Manual Vehicle Systems Analysis by Means of Modern Control Theory," NASA CR-1753, June 1971.

7. Baron, S., "A Model for Human Control and Monitoring Based on Modern Control Theory," Journal of Cybernetics and Information Science, Vol. 1, No. 1, Spring 1976.

8. Gaskill, R. A., "Fact and Fallacy in Digital Simulation," Simulation: The Dynamic Modeling of Ideas and Systems with Computers, Ed. by J. McLeod, McGraw Hill Book Co., N. Y., 1968.

9. Levison, W. H. and A. M. Junker, "A Model for the Pilot's Use of Motion Cues in Roll-Axis Tracking Tasks," AMRL-TR-77-40, Wright-Patterson AFB, Ohio, June 1977.

10. Kleinman, D. L. and S. Baron, "Analytic Evaluation of Display Requirements for Approach to Landing," NASA CR-1952, November 1971.

11. Kleinman, D. L. and T. Perkins, "Modeling the Human in a Time-Varying Anti-Aircraft Tracking Loop," IEEE Trans. on Auto. Control, AC-19, pp. 297-306, 1974.

12. Levison, W. H., S. Baron and D. L. Kleinman, "A Model for Human Controller Remnant," IEEE Trans. on Man-Machine Systems, MMS-10, No. 4, 1969.

13. Baron, S. and J. Berliner, "The Effects of Deviate Internal Representations in the Optimal Model of the Human Operator," Proceedings of Thirteenth Annual Conference on Manual Control, M.I.T., Cambridge, Mass. June 1977.

14. Parrish, Russell V., "Effect of Digitally Computed Drives on Performance of Continuous Linear Systems. NASA TN D-8518, 1977.

15. Ashworth, B. R. and W. M. Kahlbaum, Jr., "Description and Performance of the Langley Differential Maneuvering Simulator," NASA TN D-7304, NASA, Langley Research Center, June 1973.

16. Hartmann, G. L., J. A. Hauge and R. C. Hendrick, "F-8C Digital CCV Flight Control Laws," NASA CR-2629, February 1976.

17. "Special Issue on System Identification and Time-Series Analysis," IEEE Trans. on Auto Control, Vol. AC-19, No. 6, December 1974.

18. Levison, W. H., J. I. Elkind and J. L. Ward, "Studies of Multi-Variable Manual Control Systems: A Model for Task Interference," NASA CR-1746, May 1971.

19. Kleinman, D. L., S. Baron and J. Berliner, "MCARLO: A Computer Program for Generating Monte-Carlo Trajectories in a Time-Varying Man-Machine Control Task," U.S. Army Missile Research and Development Command, Tech. Report TD-CR-77-2, Redstone Arsenal, Ala., June 1977.

20. Queijo, M. J. and D. R. Riley, "Fixed-Base Simulator Study of the Effect of Time Delays in Visual Cues on Pilot Tracking Performance," NASA TN D-8001, October 1975.

21. Levison, W. H., "The Effects of Display Gain and Signal Bandwidth on Human Controller Remnant," Wright-Patterson Air Force Base, AMRL-TR-70-93, March 1971.

22. Anderson, R. O., "A New Approach to the Specification and Evaluation of Flying Qualities," Wright-Patterson Air Force Base, AFFDL-TR-69-120, June 1970.

23. Parrish, R. V. and B. R. Ashworth, "The Effect of Digital Computing on the Performance of A Closed-Loop Control-Loading System", NASA TN D-8371, NASA Langley Research Center, December 1976.

1. Report No.	2. Government Accession No.	3. Recipient's Catalog No.
NASA CR-2965		

4. Title and Subtitle	5. Report Date
Closed Loop Models for Analyzing Engineering Requirements for Simulators	February 1980
	6. Performing Organization Code

7. Author(s)	8. Performing Organization Report No.
Sheldon Baron, Ramal Muralidharan, and David Kleinman	
	10. Work Unit No.

9. Performing Organization Name and Address	11. Contract or Grant No.
Bolt Beranek and Newman, Inc. 50 Moulton Street Cambridge, MA 02138	NAS1-14449
	13. Type of Report and Period Covered
12. Sponsoring Agency Name and Address	Contractor Report
National Aeronautics and Space Administration Washington, DC 20546	14. Army Project No.

15. Langley Technical Monitor: Russell V. Parrish
Final Report
Permission has been granted to use U.S. Customary Units in Appendix C.

16. Abstract

The development of engineering requirements for man-in-the loop simulation is a complex task involving numerous trade-offs between simulation fidelity and costs, accuracy and speed, etc. For real-time digital simulation with a pilot in the loop, the design problem involves specification of conversion equipment (A-D and D-A) as well as of the discrete model of the system dynamics.

The objective of the work reported here was to develop a closed loop analytic model, incorporating a model for the human pilot, (namely, the optimal control model) that would allow certain simulation design tradeoffs to be evaluated quantitatively and to apply this model to a realistic flight control problem. The resulting model is used to analyze both overall simulation effects and the effects of individual elements. The results show that, as compared to an ideal continuous simulation, the discrete simulation can result in significant performance and/or workload penalties.

17. Key Words (Suggested by Author(s))	18. Distribution Statement
closed loop analytic model simulation fidelity optimal control model	Unclassified – unlimited Subject Category 05

19. Security Classif. (of this report)	20. Security Classif. (of this page)	21. No. of Pages	22. Price*
Unclassified	Unclassified	231	$9.50

*For sale by the National Technical Information Service, Springfield, Virginia 22161

NASA-Langley, 1980